Universidad de Alcalá

Escuela Politécnica

Departamento de Electrónica

Development of III-nitride-based waveguides for application in all-optical integrated circuits at 1.55 μm

Tesis Doctoral presentada por

Laura Monteagudo Lerma

2015

Universidad de Alcalá

Escuela Politécnica

Departamento de Electrónica

Development of III-nitride-based waveguides for application in all-optical integrated circuits at 1.55 μm

Tesis Doctoral presentada por

Laura Monteagudo Lerma

Directores:

Dr. Miguel González Herráez

Dr. Fernando B. Naranjo Vega

Alcalá de Henares, 2015

Abstract

The development of new all-optical technology for data processing in future telecommunication networks has attracted a great interest since the last decade. This technology is aimed at the full exploitation of the large bandwidth of the optical fiber, avoiding the optical-electrical-optical conversion at each node of the traditional communication networks. This new all-optical technology requires different optical components which must be optically controlled. These devices are obtained by different semiconductor materials and are implemented in a miniaturized size within an all-optical integrated circuit operating at 1.55 μm, improving the reliability of the system while reducing costs.

Since III-nitride materials have demonstrated a great potential for optical communication applications at 1.55 μm, the purpose of this work is the development of novel all-optical devices based on III-nitrides for their further integration in an ultrafast photonic integrated circuit operating at telecom wavelengths.

Several all-optical waveguide devices based on different III-nitride structures on sapphire substrates and working at 1.55 μm have been developed during this Thesis. Firstly, different optical waveguides based on GaN/AlN quantum wells and quantum dots are optimized to act as saturable absorbers via their intersubband transitions. These waveguides could be used in all-optical switching processes. Secondly, the growth of AlN material by RF sputtering is optimized. The use of this material for fabricating passive optical waveguides is demonstrated. The linear optical behavior of the sputtered-AlN waveguides shows their suitability to act as low-cost passive interconnections within the all-optical integrated circuit. Finally, two sputtered-InN-based optical waveguides are optimized to operate as reverse saturable absorbers via two photon absorption processes. The obtained nonlinear

optical response of both waveguides opens the possibility of using them for all-optical limitation applications at telecom wavelengths.

Resumen

El desarrollo de una nueva tecnología todo-óptica para el procesado de datos en las futuras redes de telecomunicación está generando un gran interés desde hace una década. Esta tecnología está encaminada al total aprovechamiento del gran ancho de banda que proporciona la fibra óptica, evitando la conversión entre los dominios óptico y eléctrico necesario en cada nodo de las redes de comunicaciones actuales. Esta nueva tecnología todo-óptica requiere de diferentes componentes ópticos que puedan ser controlados ópticamente. Estos dispositivos se obtienen a partir de distintos materiales semiconductores y se implementan de forma miniaturizada en un circuito todo-óptico integrado operando a 1.55 μm, mejorando de esta forma la fiabilidad del sistema y reduciendo su coste.

Teniendo en cuenta que los nitruros del grupo III son materiales que han demostrado un gran potencial para aplicaciones en comunicaciones ópticas a 1.55 μm, el objetivo de este trabajo es el desarrollo de nuevos dispositivos todo-ópticos basados en éstos para su futura implementación en circuitos fotónicos integrados ultrarrápidos operando a longitudes de onda de telecomunicación.

Durante esta Tesis se han desarrollado varios dispositivos de guía de onda basados en diferentes estructuras de nitruros del grupo III sobre substratos de zafiro y funcionando a 1.55 μm. En primer lugar, se han optimizado diferentes guías de onda ópticas basadas en pozos y puntos cuánticos de GaN/AlN para trabajar como absorbentes saturables a través de sus transiciones intersubbanda. Estas guías de onda podrían utilizarse en procesos de conmutación todo-óptica. En segundo lugar, se ha optimizado el crecimiento de AlN por *sputtering* de radiofrecuencia permitiendo su uso para la fabricación de guías de onda pasivas. El comportamiento óptico lineal de las guías de AlN por *sputtering* muestra su idoneidad para actuar como interconectores pasivos de bajo coste en un circuito todo-óptico integrado. Por último,

se han optimizado dos tipos de guías de onda basadas en InN por *sputtering* para funcionar como absorbentes saturables inversos mediante procesos de absorción de dos fotones. La respuesta óptica no lineal de ambas guías abre la posibilidad de utilizar estos dispositivos para aplicaciones en limitación todo-óptica a longitudes de onda de telecomunicación.

Contents

1 Introduction **1**

1.1 Motivations 1

1.2 Objectives 6

1.3 Outline of this Thesis 8

2 Growth of III-nitrides **11**

2.1 Structural and morphological properties 11

2.1.1 Crystalline structure 11

2.1.2 Polarization in wurzite nitrides 14

2.2 Optical properties 19

2.3 Film synthesis techniques 22

2.3.1 Plasma assisted molecular beam epitaxy (PAMBE) 22

2.3.1.1 Plasma-Assisted MBE system used in this work . . . 25

2.3.2 Sputtering 27

2.3.2.1 RF magnetron sputtering system used in this work . 33

2.3.3 Substrates 34

3 Nitrides characterization techniques **39**

3.1 Structural and morphological characterization 40

3.1.1 High-resolution x-ray diffraction (HRXRD) 40

3.1.2 Atomic force microscopy (AFM) 46

3.1.3 Field emission scanning electron microscopy (FESEM) 47
3.2 Linear optical characterization 48
3.2.1 Visible/NIR transmittance measurements 48
3.2.2 Photoluminiscence (PL) measurements 50

4 Optical waveguides: Beam propagation, fabrication and optical characterization 53

4.1 Introduction to modal guiding in planar waveguides 54
4.1.1 Geometric optics: Ray approach 54
4.1.2 Electromagnetic description: Wave equation. Matrix formalism 58
4.1.2.1 Wave equation 61
4.1.2.2 Light polarizations: TE and TM cases 65
4.1.2.3 Guided modes 70
4.2 Optical waveguide types 71
4.3 Numerical analysis: Finite-difference Beam Propagation Method . . . 73
4.4 Waveguide design and fabrication 76
4.4.1 Optical design 76
4.4.2 Lithography 77
4.4.2.1 UV lithography or Photolithography 77
4.4.2.2 e-beam lithography 79
4.4.3 Etching techniques 80
4.4.3.1 ICP-RIE 82
4.4.3.2 Sputtering etching 83
4.4.4 Facet polishing 83
4.5 Waveguide optical characterization 85
4.5.1 Experimental setup 85
4.5.2 Optical characterization procedure 86

4.5.3 Propagation and coupling losses: Cut-back method 88

5 Nonlinear optical absorption saturation in GaN/AlN QW- and QD-based waveguides 91

5.1 Introduction 92

5.2 Optical and electrical design 96

5.3 Structure growth and waveguide fabrication 102

5.4 Linear and nonlinear optical measurements 105

5.4.1 Theory of nonlinear optical absorption 105

5.4.2 Optical results at linear and nonlinear regimes 109

5.4.2.1 Linear optical experiments: Cut-back method 110

5.4.2.2 Nonlinear optical absorption saturation measurements 112

5.5 Conclusions 115

6 Passive sputtered-AlN-based optical waveguides 117

6.1 Introduction 118

6.2 AlN films synthesized by RF reactive sputtering 121

6.2.1 Effect of RF power 122

6.2.2 Effect of substrate temperature 126

6.2.3 Effect of substrate bias 127

6.2.4 Two-step deposition method 132

6.3 Sputtered-AlN-based optical waveguides 134

6.3.1 Waveguide optical design 135

6.3.2 AlN film deposition 137

6.3.3 Waveguide fabrication 138

6.3.4 Optical transmittance at 1.55 μm at linear and nonlinear regimes 139

6.4 Conclusions 142

7 Nonlinear TPA process in sputtered-InN-based waveguides 145

7.1 Introduction 146

7.2 InN deposition using AlN buffers by RF reactive sputtering 148

7.2.1 Structural, morphological and optical characterization 149

7.2.1.1 Structural characterization 150

7.2.1.2 Morphological analysis 151

7.2.1.3 Optical properties 153

7.3 Sputtered-InN-based optical waveguides 155

7.3.1 Waveguide optical design 155

7.3.1.1 Columnar InN/AlN waveguide 156

7.3.1.2 Compact InN waveguide 157

7.3.2 Waveguide fabrication 160

7.4 Linear and nonlinear optical characterization of sputtered-InN-based waveguides 162

7.4.1 Linear optical experiments: Cut-back method 165

7.4.2 Nonlinear optical measurements 166

7.5 Conclusions 169

8 Conclusions and future work 173

8.1 Conclusions 173

8.2 Future work 180

List of Figures

1.1 Evolution of the telecommunication networks from EICs based on Si-technology with transistors, resistors... to PICs consisting of different optical components such as lasers, detectors, switches, modulators... fabricated by diverse materials. 2

1.2 Direct band gap energies versus in-plane lattice constant for group-III-nitrides [Bau07]. 5

2.1 Wurtzite structure of III-nitrides. Its primitive unit cell (dotted contour) is defined by the lattice vectors $\vec{a_1}$, $\vec{a_2}$ and $\vec{c}$. 12

2.2 (Left) Stacking sequence for wurtzite ABABA... planes along the $\langle 0001 \rangle$ axis. (Right) Staking sequence for cubic ABCABCA... planes along the $\langle 111 \rangle$. 13

2.3 Different polarities on wurtzite III-nitrides with the corresponding spontaneous polarization directions: (a) metal-polarity and (b) N-polarity. 15

2.4 Scheme of the spontaneous and piezoelectric polarizations and the induced electric field in a [0001]-wurzite metal-face GaN well pseudomorphically grown on AlN. 19

2.5 Different atomic processes that can take place at the surface during MBE growth [Das12]. 23

2.6 Morphology of a growing film depending of the growth mode: Frank van der Merwe, Volmer-Weber and Stranski-Krastanow for various stages of the growth depending on the film thickness. 25

2.7 Scheme of the PAMBE equipment used for the growth of the MBE samples analyzed in this Thesis. 26

2.8 (a) Schematic representation of the physical sputtering process. (b) Possible processes during material sputtering. 28

2.9 Scheme of the bombardment process in a sputtering system in planar diode configuration [Alb03]. 29

2.10 Schematic diagram of the electrodes in a planar magnetron. 30

2.11 Hysteresis process in reactive sputtering. 32

2.12 Schematic of the substrate biasing method used in this work for sputtering deposition. 33

2.13 RF magnetron sputtering system used in this work together with the gas installation in the GRIFO facilities at the University of Alcalá. . . 33

2.14 (a) Illustration of the Si structure with (100) cubic plane and highlighted (111) hexagonal plane. The red-dashed triangle shows the relationship between silicon cubic and hexagonal phases. The hypotenuse corresponds to the lattice parameter of the hexagonal phase, $a_{Si(111)}$, and the length of each side is half of the cubic phase lattice parameter, $a_{Si(100)}/2$. (b) Scheme of the epitaxial relationship between III-nitrides and sapphire in (0001) plane. 35

2.15 Experimental linear optical transmittance measurements of Si(111) and sapphire substrates in the visible/NIR range. 37

2.16 AFM images of the substrates used in this work: (a) sapphire and (b) AlN-on-sapphire template. 38

3.1 Bragg's reflection corresponding to two consecutive planes separated a distance d [Alb03]. 41

3.2 Scheme of x-ray diffraction configurations: symmetrical and asymmetrical. The vector $\mathbf{s}$ is the scattering vector whose direction is given by the difference between the incident ($\mathbf{k}_0$) and diffracted ($\mathbf{k}_z$) beams. 41

3.3 Scheme of the rocking curve diffraction measurement. The materials grains responsible of the diffracted beam are highlighted in each case (blue color) [Nar03]. 42

3.4 Schematic representation of the $2\theta/\omega$-scan. The diffracted planes responsible of the detected beam are highlighted in each case (blue color) [Nar03]. 43

3.5 Example of a typical XRR scan of an AlN thin film pointing the critical angle (θ_c) together with the estimation of the layer thickness in the inset. 44

3.6 Scheme and real image of the diffractometer used during this work. . 45

3.7 Schematic representation of the AFM setup and FESEM image of the used tips. 46

3.8 Linear optical transmittance setup ranging from 350 nm to 1700 nm [VF11]. 49

3.9 Schematic representation of the PL setup [Lah09]. 51

4.1 Schemes of the behavior of an incident ray which travels from a certain medium (n_1) to another with lower refractive index ($n_2 < n_1$) as a function of the angle of incidence: (a) $\theta_i = \theta_c$, (b) $\theta_i < \theta_c$ and (c) $\theta_i > \theta_c$. 55

4.2 Geometry of an asymmetric planar waveguide consisted of substrate (n_2), guiding-layer (n_1) and cover (n_3). The refractive indices follow the relation: $n_1 > n_2 > n_3$. (Red) Relationship between the light wavevector and the propagation constant. 57

4.3 Scheme of the planar waveguide infinitely extended along the x- and z-direction. 62

4.4 Schemes of the electric and magnetic fields in the case of TM- and TE-polarized light propagating along the positive direction of z-axis. 65

4.5 Schematic of several designs used for rectangular waveguides. 72

4.6 Schematic of the transverse grid points and the propagation step in the finite difference method. 74

4.7 (Left) Example of the transverse distribution of the real part of the refractive index at the input facet of a strip-loaded waveguide. (Right) Example of the contour map of the light mode amplitude at the output of the same waveguide. 76

4.8 Scheme of the UV lithography process using negative photoresist under contact exposured. 79

4.9 Procedure etching for the fabrication of ridge-type waveguides by using as the engraving protection layer (a) the developed photoresist and (b) the deposited metal. 81

4.10 Different dry etching techniques depending on the working pressure and the excitation energy of the plasma together with the evolution of the figures of merit such as the etching anisotropy and the selectivity. 82

4.11 Polishing tools used in this work: (a) Apiezon wax piece and metal cylinders with (b) angled and (c) straight slots in which samples are fixed, together with the supporting pieces for the cylinders, (d) and (e). 84

4.12 Scheme of the experimental setup for optical characterization of the waveguides by monitoring the optical mode at the output of the structure. Inset: Scheme of a typical tapered lensed fiber (supplied by *OZ Optics*) used in this setup. 86

4.13 Scheme of the experimental setup for linear and nonlinear optical transmittance measurements of the waveguides. 87

4.14 Representation of the different scattering sources which likely produce propagation losses [Wu05]. 88

5.1 (a) Scheme of the parabolic CB and VB in a semiconductor. Confinement geometric format and plot of the density of states, *g(E)*, as a function of the excitation energy for (b) bulk material (0D), (c) QW nanostructure (1D) and (d) QD nanostructure (3D). 96

5.2 (a) Scheme of the energy levels for electron and holes in an ideal QW system along the confinement direction, z. (b) Cross-section of the E-k relation of a QW compared to that of the semiconductor bulk (dashed line). The energy levels in the CB are labeled as e_1 and e_2, and h_1 in the VB [VF11]. 98

5.3 Scheme of the GaN/AlN waveguide format together with the dimensions susceptible to optimize. The active region can be based on QWs or QDs of GaN embedded in AlN barriers. 99

5.4 (a-c) Cross-section of the waveguide and normalized modal amplitude color maps at the output of GaN/AlN waveguides with different ridge widths: 2, 5 and 10 μm, respectively. 100

5.5 Representative optical simulations which demonstrate the optimized ridge height for a 2-μm-wide waveguide leading to 350 nm. (Left) Normalized output modal amplitude profile with different ridge etching depths: 100, 200 and 350 nm. (Right) Estimated effective mode area as a function of the etching depth. 101

5.6 (Left) Normalized output modal amplitude profile for both 5-μm- and 2-μm-wide waveguides with 350-nm-deep ridges. Black vertical lines indicate the location of the QD/QW regiones in the experimental structures. (Right) Conduction band profile of the active GaN/AlN superlattice considering the whole waveguide structure designed to obtain a resonant ISB transition at $\sim$ 1.55 μm. Dot-dashed line shows the depletion of the active structure when growing the QWs directly on the AlN template. Solid line illustrates the avoiding of the depletion of the QWs when introducing a minimum GaN buffer layer $\sim$25 nm. . 102

5.7 HRTEM images of the active region of the samples containing 3 layers of (a) Si-doped GaN/AlN QWs and (b) Si-doped GaN/AlN QDs. . . 103

5.8 Photolithography masks used for the definition of (left) the waveguide patterns and (right) the metallization patterns of the GaN/AlN-based waveguides. Orange regions correspond to the UV opaque chrome zones of the masks. 104

5.9 FESEM images of a 2-μm-wide GaN/AlN waveguide (a) tilted 45° and (b) in plane view. 105

5.10 Scheme of the optical absorption saturation phenomenon in a two-electronic-level system at resonant energies ($E_{gap} \sim h\nu$). 108

5.11 Near-field images taken with the IR camera of the obtained optical modes at the output of the (a) 5-μm-wide and (b) 2-μm-wide QD-based waveguides. 110

5.12 Cut-back method: Experimental TE-TM transmittance at minimum incident power (-12 dBm) as a function of the waveguide length for the devices under study (S1-S3). The experimental points correspond to the average of transmittance measurements in three waveguides for each waveguide length. 111

5.13 Transmittance for TE- and TM-polarized light (left) and transmittance increase for TM-polarized light (right) versus control pulse energy in (a,b) a 1-mm-long 5-μm-wide QW-based WG (S1), (c,d) a 1.5-mm-long 5-μm-wide QD-based WG (S2), and (e,f) a 1.5-mm-long 2-μm-wide QD-based WG (S3). 114

6.1 (a) HRXRD $2\theta/\omega$-scans and (b) ω-scans of AlN films deposited on c-sapphire substrates at 100% N_2, 0.47 Pa, 400 °C and floating substrate as a function of the RF power. 123

6.2 Growth rate for AlN films deposited on c-sapphire at a sputering pressure of 0.47 Pa, T_{subs} = 400 °C and pure nitrogen atmosphere as a function of the RF power applied to the Al target. 124

6.3 (Left) rms surface roughness measured by AFM on 1×1 μm^2 scanned area as a function of the RF power for the AlN layers under study. (Right) AFM images depending on the RF power: (a) 100 W, (b) 125 W, (c) 150 W and (d) 175 W. 125

6.4 Linear fitting of the experimental square absorption coefficient of the optimized AlN layer deposited at 150 W presenting an estimated band gap energy of 6.02 eV. Inset: Linear optical transmittance spectrum of the AlN sample in the wavelength range from 190 nm to 2500 nm. . . 126

6.5 FWHM of the rocking curve of the AlN(0002) x-ray reflection and grain size as a function of substrate temperature for AlN layers deposited at 150 W, 0.47 Pa and 100% N_2. 127

6.6 (a) Real-time evolution of the current I_c during the AlN deposition process for 2 h for different values of substrate bias. (b) Saturation intensity, I_s, as a function of the bias applied to the substrate during the AlN deposition process. 128

6.7 Estimated growth rate and film density by means of XRR measurements of the AlN samples deposited under different substrate bias. 129

6.8 FWHM of the rocking curve of the AlN(0002) reflection and grain size as a function of the substrate bias. Best results of the FWHM and grain size for AlN deposited under unbiased conditions are 1.91° and 40.5 nm, respectively. 130

6.9 (a) HRXRD $2\theta/\omega$-scans of AlN films deposited at T_{subs} = 450 °C and P_{RF} = 150 W as a function of the substrate bias together with the unbiased AlN layer (F.S.). (b) HRXRD $2\theta/\omega$-scan of the AlN sample consisting of a thin buffer layer (30 nm) biased at -15 V followed by a 240-nm-thick unbiased AlN layer (red line). This diffractogram is shown in comparison to the 120-nm-thick unbiased AlN film (black line). 131

6.10 (a) HRXRD $2\theta/\omega$-scans of AlN films deposited under various substrate bias conditions: 120-nm-thick AlN at -15 V, two-step AlN with 15-nm and 30-nm-thick unbiased buffer layer followed by 120-nm-thick AlN at -15 V, and 120-nm-thick unbiased AlN. (b) HRXRD rocking curve around the AlN(0002) reflection peak for all the AlN films described in the previous caption. 133

6.11 AFM images of 120-nm-thick AlN deposited on *c*-sapphire (a) at floating substrate conditions; (b) at -15 V of substrate bias; and (c) at -15 V biased substrate conditions on top of 30-nm-thick unbiased AlN buffer layer (optimized two-step method). The rms surface roughness of the layers is 0.6, 0.7 and 0.4 nm, respectively. 134

6.12 (a),(c) Simulated waveguide cross-sections and normalized transverse modal amplitudes at the output facet for 2-μm- and 5-μm-wide waveguides, respectively. (b),(d) Normalized light amplitude color maps when propagating along the waveguide for 2-μm- and 5-μm-wide waveguides, respectively. 136

6.13 (a) 45°-tilted FESEM and (b) 2×2 μm^2 AFM images of the 570-nm-thick AlN layer deposited on sapphire for the development of the waveguides. The obtained rms is ∼1 nm. 137

6.14 Linear optical transmittance of the optimized AlN bulk material (black line) and theoretical calculations (red line) together with the dispersion relation for the ordinary refractive index estimated for this AlN layer. 138

6.15 (Left) Scheme of the photomask used in the UV lithography process for the patterning of the AlN waveguides. (Right) FESEM image of the cross-section and surface of the fabricated 2-μm-wide AlN waveguide. 139

6.16 (a) Experimental optical transmittance of the 2-μm-wide and 1.8-mm-long AlN waveguides for TE- and TM-polarizations at linear and nonlinear regimes at 1.55 μm. (b) Cut-back method: Experimental relative optical transmittance between TE and TM polarizations at minimum incident optical power (-12 dBm) as a function of the waveguide lengths under study. 140

6.17 Normalized amplitude at the output of the 2-μm-wide and 1.8-mm-long AlN waveguide exhibiting lower collected output light with the 8-μm-diameter-core optical fiber in the case of TE polarization compared to propagated TM light. 141

7.1 Calculated apparent optical band gap as a function of the free carrier concentration by considering the Burstein-Moss effect and including the conduction band nonparabolicity [Wal04]. Typical limit values of the band gap for the sputtered InN films are also shown. 146

7.2 (a) HRXRD $2\theta/\omega$-scan of sample S4 showing the (0001)-preferred growth orientation together with the AlN(0002) reflection corresponding to the thickest AlN buffer layer among the analyzed samples. (b) HRXRD rocking curves of the InN(0002) reflection peak of the InN layers (S1-S4). 150

7.3 AFM images (2×2 μm^2 scanned area) of the InN layers under study (S1-S4). 151

7.4 FESEM images of all the InN films deposited on c-sapphire. 152

7.5 RT squared absorption coefficient (solid line) with a linear fit (dot-dashed line) as a function of the photon energy for the set of InN layers under study. 153

7.6 Normalized RT PL emission spectra depending on the excitation photon energy for the analyzed InN samples (S1-S4). 154

7.7 Optical simulations for the 2-μm-wide and 2-mm-long columnar InN waveguide: (Left) Effective area of the mode at the output of the single mode waveguide considering etching depths from 50 nm to 200 nm. (Right) Cross-section of the waveguide and normalized modal amplitude color maps at the output of the device considering 100 nm of etching depth. 156

7.8 (Left) AFM and (Right) FESEM images of the compact InN layer deposited directly on the sapphire substrate by RF reactive sputtering. 158

7.9 Optical simulations for the 2-μm-wide and 2-mm-long compact InN waveguide: (Left) Normalized output modal amplitude profile for different etching depths from 50 nm to 350 nm. (Right) Plane view of the waveguide format together with the color maps of the normalized modal amplitude of light propagating along the 250-nm-deep waveguide confirming its multimode behavior. 158

7.10 (Left) Cross-section of the waveguide and normalized modal amplitude color maps at the output of the deviced with the optimized etching depth of 350 nm. (Right) Normalized modal amplitude profile obtained at the output of the two optimized InN-based waveguides. Vertical solid lines indicate the thickness for the InN layer in each case. 159

7.11 Designed InN-based waveguides with the detailed dimensions: (Left) Columnar InN on double AlN buffer waveguide and (Right) Compact InN waveguide. 160

7.12 FESEM images of the fabricated columnar InN/AlN waveguides: (Left) surface view of the 2-μm-wide waveguide and (Right) cross-section and suface view of the 5-μm-wide waveguide. 161

7.13 FESEM images of the fabricated compact InN waveguides: (Left) surface view of the 5-μm-wide waveguide and (Right) cross-section of facet of the 2-μm-wide waveguide. 161

7.14 Comparison of the linear optical transmittance of the original InN layer grown on sapphire, the single sapphire substrate and the InN layer after the Ar plasma etching. The agreement between the spectra of the etched InN and that of the sapphire substrate confirms the total etching of the original InN layer. 162

7.15 Scheme of the TPA process in a two-electronic-level semiconductor. . 163

7.16 Cut-back method: Experimental TE-TM transmittance at low incident optical power (-2 dBm) as a function of the device length for (Left) the columnar InN/AlN waveguide and (Right) the compact InN waveguide. The experimental points correspond to the average of transmittance measurements in three similar waveguides for each length. 165

7.17 (Left) Transmittance and (Right) optical loss increase for TE- and TM-polarized light versus the input pulse energy in (a,b) a 1.84-mm-long columnar InN-on-double-AlN waveguide and (c,d) a 2.07-mm-long compact InN waveguide. 167

List of Tables

2.1 Lattice parameters at 300 K of bulk wurzite AlN, GaN and InN [Vur03] and deviation ratios from the ideal structure. 12

2.2 Spontaneous polarization for metal-face wurtzite III-nitrides [Vur03]. 15

2.3 Values of the elastic coefficients [Vur03] and piezoelectric coefficients [Vur01] of AlN, GaN and InN. 18

2.4 Commonly accepted values of the band gap energies at low and room temperature, $E_g(0)$ and $E_g(300\ K)$, respectively, and Varshni constants α and β, of wurzite AlN, GaN and InN. 20

2.5 Commonly accepted values of the ordinary and extraordinary refractive indices of AlN, GaN, InN and sapphire at 1.55 μm. Values with an asterisk have been estimated from our samples at 1.55 μm. The values used for the simulations of the optical structures and devices investigated in this work are underlined. 22

2.6 Lattice mismatch between AlN, GaN and InN and Si(111) and sapphire substrates at 300 K. Δa_{epi} is the difference between lattice parameters of the layer and the substrate, obtained taking into account the epitaxial relationship explained in the text. The in-plane lattice parameters of Si(111) and sapphire are 3.840 $\mathring{A}$ and 4.758 $\mathring{A}$, respectively [Fen08]. 36

5.1 Summary of the GaN/AlN-based waveguides under study concerning the implemented active nanostructures and ridge widths. 110

5.2 Summary of the experimental input pulse energy required for reaching 3-dB and 10-dB of optical transmittance contrast for TM light for the three samples under study. 112

6.1 Sputtering parameters investigated for the deposition of AlN films. . . 122

7.1 Summary of the conditions for the four buffers under study: type of buffer, RF power applied to the substrate during the buffer layer deposition and buffer thickness. The sputtering pressure and substrate temperature are kept at 0.47 Pa and 450 °C for all the material deposition in this study together with the nitrogen atmosphere. The optimized substrate bias for the biased-AlN buffer is -15 V. 149

7.2 Summary of the structural and morphological properties of the analyzed InN films depending on the buffer used in terms of crystal quality, density of columns, columns size and rms surface surface. . . 151

7.3 Summary of optical characterization results obtained using transmittance and PL measurements at RT for all the analyzed samples. 154

7.4 Results for the parameters related to the linear and nonlinear optical absorption for both sputtered-InN-based waveguides under study. . . 169

Chapter 1

Introduction

This chapter presents a brief overview of the current technological limitations and challenges which arise in the future telecommunication networks. The main motivation in this field is focused on profiting the extremely large bandwidth that optical domain brings. In this work, different optical waveguide devices based on III-nitrides are developed with the aim of advancing in technology of future all-optical integrated circuits. This chapter also explains the three specific objectives of this study. The organization of the manuscript is introduced in the last part of the chapter.

1.1 Motivations

Moving towards all-optical integrated circuits

Electronic integration combines different electronic components on a chip forming the well-known electronic integrated circuit (EIC). Equally, photonic integration provides a possibility to combine active and passive optical components within the so-called photonic integrated circuit (PIC). While transistors, capacitors and resistors are typically integrated in EICs, these components are replaced in PICs by optical devices such as lasers, modulators, switches, multiplexers/demultiplexers, photodetectors, etc. Furthermore, like in electronics, a PIC provides cost, space, power and reliability advantages compared to the use of discrete single-function devices since connections are printed directly onto the chip. Thus, the development

of PICs allows to reach compact and cost-efficient structures which include a wide variety of optical functions for a broad range of applications, such as optical communications, sensing, biophotonics, spectroscopy, etc.

During the last decades, the evolution from EICs to PICs arises as one of the most important future needs and challenges in the development of telecommunication networks. The beginnings of EICs came from J. Kilby when first integrated several transistors into a germanium-based single device in the late 60's [Kil64]. Since then, the objective was to integrate more transistors and other electronic devices delivering exponentially greater data processing power while lowering the cost per device, improving reliability and reducing space and power requirements. Nevertheless, the wide functionality of EICs is not enough for covering the increasing bandwidth demand in telecommunication networks. The best solution would be the implementation of both types of devices integration, electronic and photonic, taking profit of their wide functionality. In fact, EICs provide many value-added functions in optical networks at a very low cost per device, such as switching, monitoring data transmission, system management and performance enhancement. The basis of telecom networks has significantly changed during the last decades, and nowadays the maximum bandwidth of the copper wire wants to be multiplied by 1000 through the use of PICs leading to ∼1 Tbps of data transmission rate per channel. In this sense, photonics is seen as the future of signal transfers because of the speeds that can be achieved.

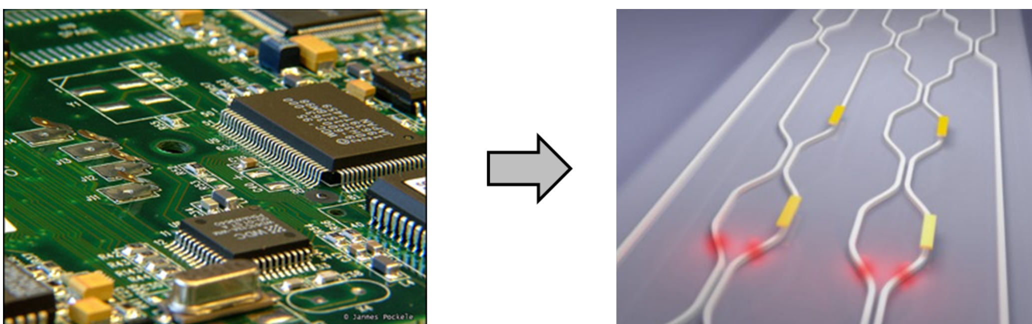

Figure 1.1: Evolution of the telecommunication networks from EICs based on Si-technology with transistors, resistors. . . to PICs consisting of different optical components such as lasers, detectors, switches, modulators. . . fabricated by diverse materials.

However, even considering the almost unlimited bandwidth provided by optical fibers, in current optical communication networks the limitation comes directly through the optical-to-electrical-to-optical (OEO) conversions. Despite the benefits in functionality and throughput that electronics can introduce within optical networks, the fact is that OEO conversion at each node is so expensive that its generalized use is not cost-effective. Thus, the tendency is moving towards the all-optical domain in telecom networks even taking into account that all-optical technologies are more expensive and complex than electronic Si-based technologies. Hence, in all-optical integrated circuits (ICs), electronic processing with the corresponding OEO conversion would be just relegated to the edges of the network while all the data transmission and switching processes would be performed in the optical domain.

Because of these reasons, much effort has been put into the development of PICs, mainly addressing their use in all-optical communication at 1.55 μm. The PICs can be classified depending on their functionality (active or passive), their dimensions (large- or small-scale), the number of working wavelengths in use (single- or multi-channel) and the type of integration (hybrid or monolithic). The hybrid integration is based on multiple single-function optical devices assembled into a single package usually involving different materials and being possible to associate with EICs. At the same time, monolithic integration comprises many functions or devices into a single photonic material. This latter type of integration is the best solution in terms of simplicity and reliability since it includes optical components into a single device based on a single material. The capability of integrating as many different optical functions into a single material platform can be considered as the figure of merit of a PIC.

Nowadays, optical components are fabricated by using different materials such as InP, GaAs, $LiNbO_3$, Si, SiO_2/Si, group-III-nitrides, etc. Among these different materials, most of them have not shown the capability of performing the most basic opto-electronic functions required in an optical transport network such as light generation, amplification, modulation and detection. Particularly, GaAs presents a limited working wavelength at $\sim$850 nm while $LiNbO_3$ can not implement lasing and detection operations. On the other hand, although silicon is a low-cost material compatible with the CMOS-technology which presents high refractive index attractive for optical waveguiding, it also presents an indirect band gap which induces

a low light emission efficiency; besides, detection is not possible for wavelengths above ∼1.1 μm. Up to date, InP is the unique material platform which has been used for implementing large-scale monolithically integrated PICs. This material can provide both active and passive opto-electronic functions such as light generation, amplification, detection, wavelength multiplexing and demultiplexing, switching, etc. and integrate them in a single substrate leading in turn to costs reduction. Furthermore, the coupling losses between different-material packages or fiber-device couplings are completely avoided, thus, improving the reliability of the system. Concerning the industry's production of these PICs, *Infinera Corporation* presented the first PIC achieving a capacity of 1 Tbps on a single photonic integrated chip. All the optical components were monolithically integrated onto an InP-based PIC operating with 10 channels at 100 Gbps of data rate per wavelength [Lal11]. Despite the benefits of the InP-platform, the drawback arises from its operation speed which is limited up to ∼500 Gbps per channel.

The best way is to fabricate the PIC by using a single photonic material, but most of times it is not possible to provide many functions just with one material. In these cases, it is desirable to integrate different components by using materials from the same family, at least, taking profit of the better lattice- and thermal-expansion-matching between them. A promising alternative is the implementation of a PIC based on III-nitrides. In fact, ambitious researches are currently being carried out focusing on all-optical signal processing technologies at 1.55 μm. Using this material family, further implementation of ultrafast all-optical ICs working at data transmission rates ≥1 Tbps per wavelength channel could be reached.

Why III-nitrides?

Group-III-nitrides have emerged as attractive material constituents for photonic devices due to many reasons. First of all, the widespread direct band gap that III-nitride alloys can reach, ranging from the near infrared (NIR at ∼1.9 μm) for InN to the ultraviolet (UV at ∼200 nm) for AlN. This feature makes III-nitrides excellent semiconductors for efficient light emission within a wide spectral range thanks to the band gap engineering through alloys, heterojuntions and quantum-based

heterostructures. Figure 1.2 shows the direct band gap energy of wurtzite GaN, AlN and InN compounds and related ternary alloys (solid lines) as a function of the structural in-plane lattice parameter. It has to be pointed out that the tunable optical band gap gives advantage on the enhancement of nonlinear material properties when exciting at resonant energy.

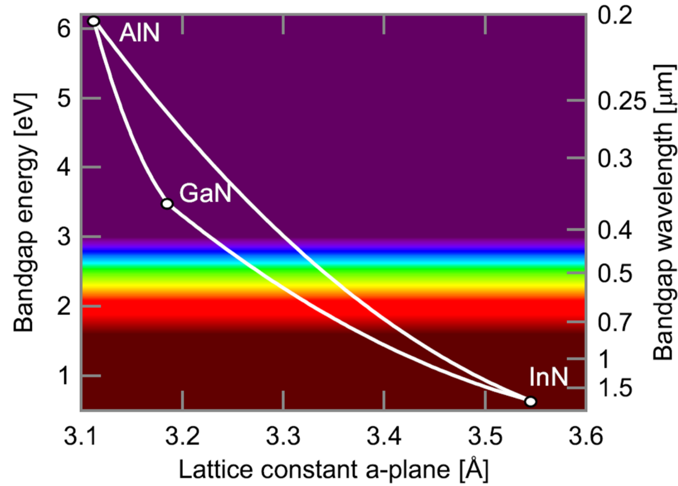

Figure 1.2: Direct band gap energies versus in-plane lattice constant for group-III-nitrides [Bau07].

On the other hand, III-nitride semiconductors present electron mobilities about four times larger than silicon. Furthermore, the high bond energy between N and metal (Ga, Al, In) leads to materials with high thermal and chemical stability which are suitable for using in a wide variety of applications such as environmental applications, sensing and communication fields. In other respects, an important advantage of III-nitrides with respect to InP-based alloys is the better light coupling between silica optical fibers and III-nitride devices. This better coupling is due to the lower difference between refractive indices at 1.55 μm of III-nitrides ($\sim$2-2.3) and optical fiber ($\sim$1.46) than between InP ($\sim$3) and fibers. Thus, the coupling losses due to Fresnel's reflection are lower in the case of III-nitrides.

Several optical components based on III-nitrides have been developed during the last two decades. The large conduction-band offset in the GaN/AlN quantum heterostructures ($\sim$1.8 eV [Tch06]) may allow the fabrication of intersubband-based (ISB) emitters and detectors operating at 1.55 μm. In fact, several photodetectors have been developed based on quantum GaN/Al(Ga)N

heterostructures [Hof03][Var08]. On the contrary, up to date, it has not been reported any light emitter based on ISB transitions in III-nitrides working at 1.55 μm. On the other hand, 3-dB optical waveguide couplers at 1.55 μm have been developed based on GaN/AlGaN heterostructures [Hui03].

III-nitride semiconductors are definitely very promising materials for implementation in PICs aimed at all-optical communication applications at 1.55 μm since they cover the third window of telecommunications (1.53-1.57 μm) with different possibilities. The first one is based on the ultrafast intersubband transition ($\sim$100 fs [VF08] in GaN/AlN quantum-based heterostructures while the second alternative approach comes from the interband transition of InN/InGaN heterostructures with relaxation lifetimes of a few ps [VF12a]. At the same, it is possible to operate at 1.55 μm through InN material whose optical bang gap is comprised within the C-band [Nar07]. In addition, the nonlinear two-photon-absorption (TPA) effect at 1.55 μm achieved in bulk InN by sputtering with subpicosecond recovery times [VF12b] can be also taken into account for active functions in optical communications. Furthermore, AlN and GaN are excellent candidates for passive optical waveguide devices at 1.55 μm since they are transparent within the visible/NIR range. It has to be noted that the implementation of these types of III-nitride waveguides on sapphire substrates would avoid the light absorption by the substrate due to its high transparency at telecommunications wavelengths.

On the other hand, it has to be pointed out that III-nitrides can be deposited by sputtering taking profit of the low-cost solution it brings. In addition, this technique enables the regrowth of material at not harmful temperatures on previously deposited nitride-based devices, avoiding the likely damage due to high deposition temperatures by other techniques.

1.2 Objectives

Taking into account the previous reasons, the main objective of this work is to investigate the optical response of different III-nitride-based waveguides performing

different functions for their implementation in further developed all-optical ICs. Thus, particularly, the objectives of this Thesis can be summarized in these three:

- To design optical waveguides based on GaN/AlN QWs and QDs heterostructures grown by MBE. Once the waveguides are designed and fabricated, the main objective is to investigate their optical response at linear and nonlinear regimes focusing on the input pulse energy required to reach a 3-dB of transmittance increase of each structure via nonlinear saturable absorption at 1.55 μm. Special interest is given to the application of these devices in ultrafast all-optical switching functions.

- To investigate the optical response of sputtered-AlN-based waveguides at low and high input optical powers. For this purpose, optimization of the deposition conditions for the growth of AlN films by RF sputtering is firstly required together with the optical design and fabrication of the waveguides. The final aim is to demonstrate that these devices act as low-cost passive interconnecting pathways for being introduced in all-optical ICs at 1.55 μm.

- To analyze the nonlinear optical behavior of sputtered-InN waveguides. Within this premise, efforts are firstly dedicated to the optimization of the deposition of InN films by RF sputtering. After that, optical simulations for performing the design of the waveguides and their fabrication are required. The aim is to obtain InN devices capable of acting as low-cost all-optical limiters operating at telecom wavelengths via the two-photon absorption phenomenon.

This work has been developed within the framework of several projects from different institutions:

- CISTER (TEC2012-37958-C02-01) and FASTCOM (TEC2009-14423-C02-02), from Spanish Government calls.

- FACTOTEM2 (S2009/ESP-1781) and SINFOTON (S2013/MIT-2790), from Comunidad de Madrid calls.

- DIBOS (UAH2011/EXP-024) and DESLAP (CCG2013/EXP-052), from University of Alcalá calls.

1.3 Outline of this Thesis

This manuscript is divided in two main blocks. The first one includes Chaps. 2 to 4 and comprises the theoretical basis necessary for the comprehension of the study carried out in this Thesis. Particularly, the second chapter focuses on the material properties of wurzite III-nitride semiconductors (AlN, GaN, InN) in terms of structural, morphological and optical properties. The growth techniques used within the framework of this Thesis are also described there. Furthermore, Chap. 3 summarizes the different experimental techniques used along this work for the characterization of group-III-nitrides. The fourth chapter aims at being a basic guide on the theoretical concepts of integrated optics. A large section is dedicated to the analytic study of light modal guiding in planar waveguides as well as the numerical analysis technique used for investigating more complex non-planar optical devices. Furthermore, the theory of design and fabrication of optical waveguides is also treated while the description of the experimental setup used for optical characterization of the devices in the linear and nonlinear regimes is also described.

On the other hand, the second block comprises Chaps. 5 to 7. They are focused on the experimental results obtained within this Thesis for the different optical waveguides under study, coinciding with the main three objectives expected in this work. Each chapter of this block describes the step-by-step process from the growth of the III-nitride materials and the design and fabrication of the waveguides until their optical characterization. Namely, Chap. 5 is dedicated to the investigation of the nonlinear optical absorption saturation presented in waveguides based on GaN/AlN QWs and QDs at 1.55 μm. These optical waveguides are intended to be promising active devices for implementing all-optical switching functions in III-nitride-based PICs. At the same time, Chap. 6 presents the growth and optimization of AlN films by RF reactive sputtering together with the design and fabrication of the AlN waveguide devices. The experimental results describe the capability of using these structures in III-nitride PICs as passive light pathways for interconnections between different devices. Likewise, the development of sputtered-InN-based optical waveguides is presented in Chap. 7. The nonlinear behavior of these InN-based structures at 1.55 μm is described via two-photon absorption processes demonstrating its usefulness as active all-optical power limiters in future III-nitride PICs.

Finally, Chap. 8 indicates the conclusions achieved along this study while providing new ideas for further improvement of the work presented in this manuscript.

Chapter 2

Growth of III-nitrides

This chapter presents a general overview of group-III nitride properties including a brief explanation of the two main thin film growth techniques which take part in this Thesis. Firstly, structural, morphological and optical properties are summarized for wurzite (Al, Ga, In)N compounds giving data about lattice parameters, elastic coefficients, polarization values, semiconductor band gap energies, refractive indices, etc. On the other hand, thin film deposition methods as molecular beam epitaxy (MBE) and sputtering are described. In addition, details of the growth equipment used during this work are also given.

2.1 Structural and morphological properties

2.1.1 Crystalline structure

(Al, Ga, In)N and their alloys crystallize in three different structures: hexagonal wurtzite (α-phase), cubic zinc-blende (β-phase) and rocksalt (γ-phase). While the wurtzite structure is the thermodynamically most stable at room temperature and atmospheric pressure, group-III nitrides can also be grown in the metastable zinc-blende structure and less commonly in the rocksalt one. The latter can be obtained only at very high pressures and cannot be stabilized by the epitaxial growth. This work only focuses on binary wurtzite-type nitrides.

The wurtzite structure is determined by three main parameters: the edge length of the basal hexagon in the plane (0001) (in-plane lattice constant, a), the height of the hexagonal prism along the $\langle 0001 \rangle$ axis (out-of-plane lattice constant, c) and an internal parameter u defined as the metal-nitrogen bond length along the $\langle 0001 \rangle$ axis (see Fig. 2.1). In an ideal wurtzite crystal, the c/a and u/c ratios are 1.633 and 0.375, respectively. The real nitride structure presents a certain deviation from these expected values, which depends on the nature of the metal cation.

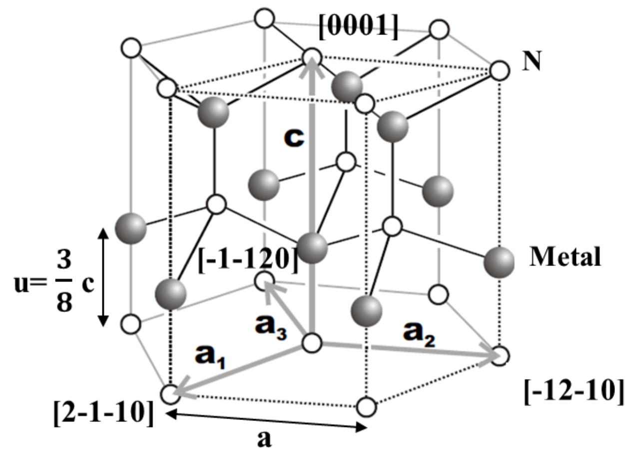

Figure 2.1: Wurtzite structure of III-nitrides. Its primitive unit cell (dotted contour) is defined by the lattice vectors $\vec{a_1}$, $\vec{a_2}$ and $\vec{c}$.

The lattice parameters of binary wurtzite AlN, GaN and InN at 300 K are indicated in Table 2.1.

Parameter	AlN	GaN	InN
a (Å)	3.112	3.189	3.545
c (Å)	4.982	5.185	5.703
c/a	1.601	1.626	1.612
u/c	0.380	0.376	0.377

Table 2.1: Lattice parameters at 300 K of bulk wurzite AlN, GaN and InN [Vur03] and deviation ratios from the ideal structure.

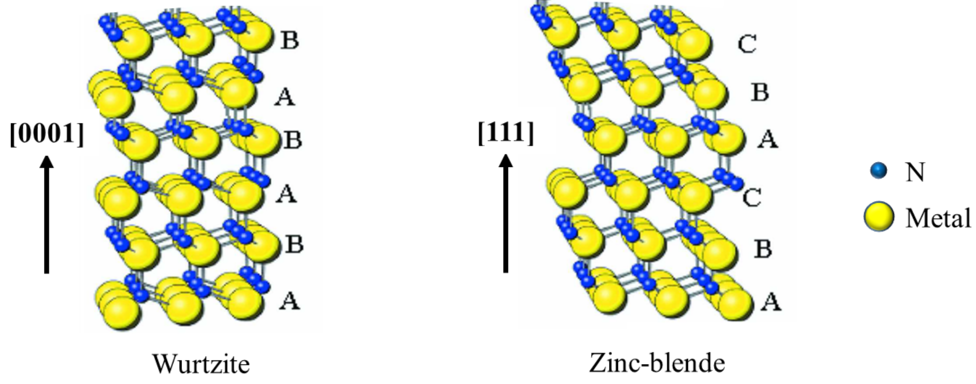

Figure 2.2: (Left) Stacking sequence for wurtzite ABABA... planes along the ⟨0001⟩ axis. (Right) Staking sequence for cubic ABCABCA... planes along the ⟨111⟩.

For ternary compounds like $A_xB_{1-x}N$, considering A and B as the metal elements and x as the concentration of metal A, the lattice parameters of a ternary alloy can be estimated using a linear interpolation of the lattice constants of the two forming binary alloys with respect to the concentration x (Vegard's Law):

$$a_{A_xB_{1-x}N}(x) = xa_{AN} + (1-x)a_{BN} \quad (2.1)$$

$$c_{A_xB_{1-x}N}(x) = xc_{AN} + (1-x)c_{BN} \quad (2.2)$$

The wurtzite structure shows hexagonal symmetry with the associated space group $P6_3mc(C^4_{6\nu})$. It consists of two hexagonal-close-packed (hcp) intertwined sublattices of metal (Ga, Al or In) and nitrogen (N) atoms, respectively, ideally shifted each other a ratio of $3/8c$ along the ⟨0001⟩ axis. By contrast, the zinc-blende structure presents a cubic symmetry with the associated space group F43m (T^2_d) consisting of two interconnected face-centered cubic (fcc) metal-nitrogen sublattices and shifted each other a ratio 1/4 of the cubic diagonal (⟨111⟩) length. In both hexagonal and cubic phases, the atoms are tetrahedrically bonded. The major aspect which differentiates the wurtzite and cubic crystalline structures is the stacking sequence. The wurtzite phase stacks along the ⟨0001⟩ axis plane following an ABABA... sequence as illustrated in Fig. 2.2(left) and the cubic phase exhibits an ABCABCA... stacking sequence along the ⟨111⟩ axis shown in Fig. 2.2(right).

In a hexagonal system, the three-index notation for crystallographic directions and planes has a equivalent one based on the Miller-Bravais indices. The Miller notation uses four indices, they being related to the projection of the considered direction on the vectors of the basic cell $\{\vec{a_1},\vec{a_2},\vec{a_3},\vec{c}\}$ (see Fig. 2.1). Since $\vec{a_3}$=-($\vec{a_1}$+$\vec{a_2}$), a (*hkl*) plane is equivalent to (*hkil*) under Miller notation where *i=-(h+k)* and [*hkil*] defines the direction perpendicular to the (*hkil*) plane. This four-index notation takes into account that there are three equivalent symmetry axes $\vec{a_1}$, $\vec{a_2}$ and $\vec{a_3}$ in the plane perpendicular to the principal *c*-axis. Hence, the equivalency of, for example, planes such as (-1-120) and (2-1-10) is clearly shown in Fig. 2.1.
The interplanar distance is given by the following equation:

$$\frac{1}{d_{hkl}^2} = \frac{4}{3}\frac{h^2 + k^2 + hk}{a^2} + \frac{l^2}{c^2} \tag{2.3}$$

2.1.2 Polarization in wurzite nitrides

The wurtzite structure does not present inversion symmetry along the *c*-axis leading to two different polarity configurations of these anisotropic uniaxial materials. A stretching out of the tetrahedrons is induced due to the difference in electronegativity between nitrogen and metal atoms which form the covalent bond. Since N presents higher electronegativity (∼3.0) than Al, Ga or In atoms (∼1.6-1.8), nitrogen atoms have higher tendency to attract the valence electrons from the metal atoms. Thus, an electrostatic dipole is induced in each tetrahedron. Then, due to the lack of symmetry along the *c*-axis of the wurtzite structure, the [0001] and [000-1] directions are not equivalent.

The contribution of each tetrahedron to the total dipole leads to the generation of a macroscopic spontaneous polarization ($\mathbf{P}_{sp}$). The terminology used for determining the different material polarities is: metal-polarity (Ga-, Al- and In-face) when growing along the [0001] direction leading to metal atoms at the end of the bilayer and nitrogen-polarity (N-face) when growing along the [000-1] direction finishing with nitrogen atoms at the bilayer. The sign of the polar axis is determined to be positive in the case of metal polarities and negative when dealing with nitrogen polarities. Figure 2.3 illustrates the difference between both types of polarity.

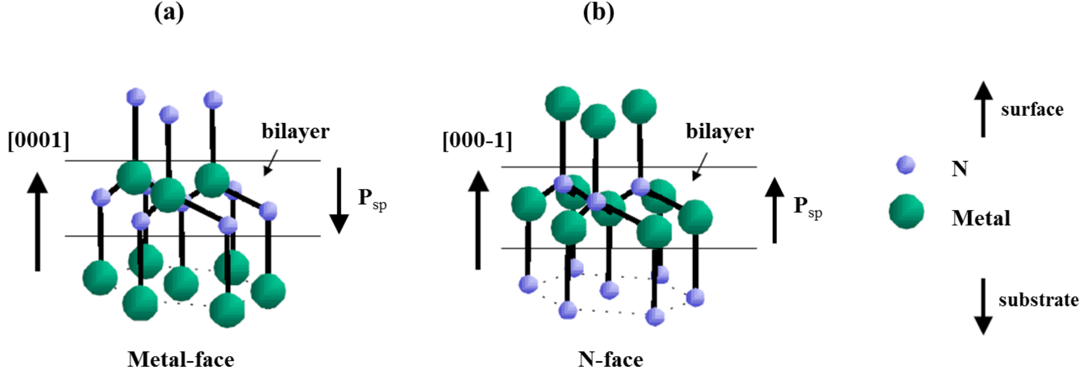

Figure 2.3: Different polarities on wurtzite III-nitrides with the corresponding spontaneous polarization directions: (a) metal-polarity and (b) N-polarity.

It must be pointed out that structures with different polarity are not at all equivalent showing large variations in physical and chemical properties. As an example, in the case of GaN, the N-face material presents a more reactive surface and worse crystalline quality compared to the Ga-face [Dim00][Mas05]. Since the spontaneous polarization vector points from the least to the most electronegative atom, *i.e.*, from the metal- to the N-atom, its value is negative for metal-face structures and positive for N-face crystals.

Table 2.2 indicates the calculated spontaneous polarization for metal-face AlN, GaN and InN. AlN structure presents a larger value of the P_{sp} compared to those calculated for GaN and InN. This difference is related to the large deviation of the AlN crystal from the ideal wurtzite structure (see c/a and u/c ratios in Table 2.1). Hence, the larger the deviation of the structure from the ideal wurtzite, the higher the value of the spontaneous polarization.

	AlN	**GaN**	**InN**
$\boldsymbol{P}_{sp}$ (C/m^2)	-0.090	-0.034	-0.042

Table 2.2: Spontaneous polarization for metal-face wurtzite III-nitrides [Vur03].

On the other hand, a piezoelectric polarization ($\mathbf{P}_{pz}$) can appear due to an induced distortion of the tetrahedrons when applying a mechanical stress. Nitride layers can not be obtained through homoepitaxial growth due to the lack of suitable

lattice-matched substrates with the same thermal expansion coefficients as nitrides. Thus, nitrides are mainly heteroepitaxially synthesized on substrates as sapphire, SiC or Si inducing strain within the layer during the growth. The piezoelectric polarization is related to the induced crystal strain, ε_{ij}, through the piezoelectric tensor by:

$$\vec{P_{pz}} = \begin{pmatrix} 0 & 0 & 0 & 0 & e_{15} & 0 \\ 0 & 0 & 0 & e_{15} & 0 & 0 \\ e_{31} & e_{31} & e_{33} & 0 & 0 & 0 \end{pmatrix} \times \begin{pmatrix} \varepsilon_{xx} \\ \varepsilon_{yy} \\ \varepsilon_{zz} \\ \varepsilon_{yz} \\ \varepsilon_{zx} \\ \varepsilon_{xy} \end{pmatrix} \tag{2.4}$$

where e_{ij} are the piezoelectric coefficients. Considering the symmetry in wurtzite crystals, there are only three independent piezoelectric constants: e_{15}, e_{31} and e_{33}. Since the material is usually grown along the [0001] direction on a substrate with different a lattice parameter, deformations along [0001] direction (ε_{zz}) and in the plane perpendicular to $\langle 0001 \rangle$ axis (ε_{xx}, ε_{yy}) are induced. These deformations or strains are defined by the following equations:

$$\varepsilon_{zz} = \frac{c - c_0}{c_0} \tag{2.5}$$

$$\varepsilon_{xx} = \varepsilon_{yy} = \frac{a - a_0}{a_0} \tag{2.6}$$

where c_0 and a_0 are the out-of-plane and the in-plane lattice parameters, respectively, of fully relaxed bulk material. Accordingly to Hooke's Law, the stress σ_{ij} is related to the strain ε_{ij} through the tensor of the elastic module C_{ij}. In the case of hexagonal crystal symmetry, five of the six elastic coefficients containing in the 6×6 matrix are independent as indicated by the following expression:

$$\begin{pmatrix} \sigma_{xx} \\ \sigma_{yy} \\ \sigma_{zz} \\ \sigma_{yz} \\ \sigma_{zx} \\ \sigma_{xy} \end{pmatrix} = \begin{pmatrix} C_{11} & C_{12} & C_{13} & 0 & 0 & 0 \\ C_{12} & C_{11} & C_{13} & 0 & 0 & 0 \\ C_{13} & C_{13} & C_{33} & 0 & 0 & 0 \\ 0 & 0 & 0 & C_{44} & 0 & 0 \\ 0 & 0 & 0 & 0 & C_{44} & 0 \\ 0 & 0 & 0 & 0 & 0 & \frac{C_{11}-C_{12}}{2} \end{pmatrix} \times \begin{pmatrix} \varepsilon_{xx} \\ \varepsilon_{yy} \\ \varepsilon_{zz} \\ \varepsilon_{yz} \\ \varepsilon_{zx} \\ \varepsilon_{xy} \end{pmatrix} \quad (2.7)$$

In this work, the crystal is grown along the [0001] direction. The in-plane stress is uniform (σ_{xx}=σ_{yy}) and there is no stress along the c-axis (σ_{zz}=0). In this case, ε_{yz}=ε_{zx}=ε_{xy}=0 leading to a simplified diagonal deformation tensor referred by Eq. 2.8. Table 2.3 indicates the mechanical parameters of AlN, GaN and InN.

$$\begin{pmatrix} \sigma_{xx} \\ \sigma_{yy} \\ 0 \end{pmatrix} = \begin{pmatrix} C_{11} & C_{12} & C_{13} \\ C_{12} & C_{11} & C_{13} \\ C_{13} & C_{13} & C_{33} \end{pmatrix} \times \begin{pmatrix} \varepsilon_{xx} \\ \varepsilon_{yy} \\ \varepsilon_{zz} \end{pmatrix} \quad (2.8)$$

Under these conditions, the in-plane and the out-of-plane deformation are related by:

$$\varepsilon_{zz} = -\frac{2C_{13}}{C_{33}}\varepsilon_{xx} \quad (2.9)$$

and, taking into account Eq. 2.4, the piezoelectric polarization in the (0001) plane is nule, *i.e.*, P^X_{pz}=P^Y_{pz}=0, and the strain-induced piezoelectric polarization along the [0001] direction can be expressed as:

$$P^Z_{pz} = 2\frac{a-a_0}{a_0}(e_{31} - e_{33}\frac{C_{13}}{C_{33}}) \quad (2.10)$$

Since [e_{31}-$e_{33}C_{13}/C_{33}$]<0 for group III-nitrides assuming metal-face polarization (see Table 2.3), the piezoelectric field is positive (points to the [0001] direction) if the

material is under compressive strain ($a<a_0$) or negative (oriented along the [000-1] direction) when the material is under a tensile strain ($a>a_0$).

Finally, in the case of a strained crystal, the total polarization (P_{tot}) is the sum of both spontaneous and piezoelectric contributions and induces a total internal electric field within the material given by

$$E_{tot} = -\frac{P_{tot}}{\varepsilon_0 \varepsilon_r} \tag{2.11}$$

where ε_0 is the vacuum permittivity and ε_r is the relative permittivity or dielectric constant of the material.

	AlN	**GaN**	**InN**
C$_{11}$ (GPa)	396	390	223
C$_{12}$ (GPa)	137	145	115
C$_{13}$ (GPa)	108	106	92
C$_{33}$ (GPa)	373	398	224
e$_{31}$ (C/m^2)	-0.50	-0.35	-0.57
e$_{33}$ (C/m^2)	1.79	1.27	0.97

Table 2.3: Values of the elastic coefficients [Vur03] and piezoelectric coefficients [Vur01] of AlN, GaN and InN.

The growth of heterostructures along the polar [0001] direction leads to polarization discontinuities at the interfaces that induce polarization charge densities (σ_{pol}), resulting thus in the generation of an internal electric field. For example, in quantum well (QW) heterostructures the charge density induced by the total polarization is equal to the difference of polarization between the barrier and the well:

$$\sigma_{pol} = P_{tot}^{well} - P_{tot}^{barrier} \tag{2.12}$$

Then, an internal electric field is induced within the well which is proportional to the charge density accumulated at the interface of the layers:

$$E_{well} = \frac{-\sigma_{pol}}{\varepsilon_0 \varepsilon_r} \tag{2.13}$$

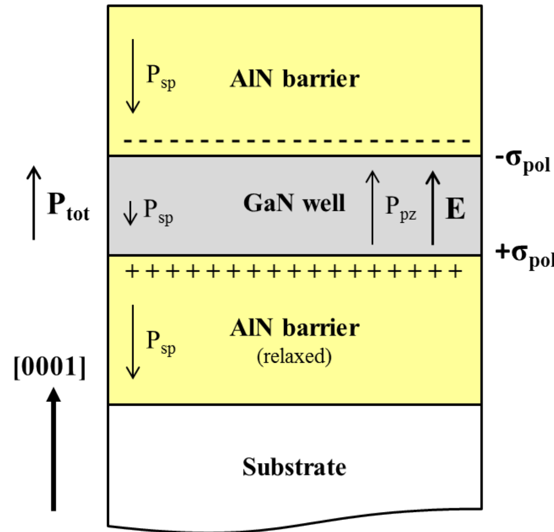

Figure 2.4: Scheme of the spontaneous and piezoelectric polarizations and the induced electric field in a [0001]-wurzite metal-face GaN well pseudomorphically grown on AlN.

Figure 2.4 shows the case of a metal-polarity GaN well pseudomorphically grown on a relaxed AlN barrier thus suffering a compressive strain. The directions and contributions of the spontaneous and piezoelectric polarizations, and the generated internal electric field are also indicated. This structure will be deeply studied in Chapter 5.

2.2 Optical properties

Group III-nitride semiconductors present direct band gap which imply that the maximum of the valence band and the minimum of the conduction band are centered at the Brillouin zone. At this point, direct band-to-band absorption and emission processes can take place just involving photons with energies higher than the band gap. Ternary alloys allow to work within a wide spectral range. The band gap energy of the compounds can be tuned from the near infrared of the InN ($\sim$0.64 eV, $\sim$1.9 μm) to the ultraviolet ($\sim$6.2 eV, $\sim$200 nm) corresponding to the AlN, by changing the metal content.

	E$_g$(0) (eV)	α (meV/K)	β (K)	**E$_g$ (300 K)** (eV)	**Ref.**
AlN	6.25	1.799	1462	6.14	[Vur03]
GaN	3.51	0.909	830	3.43	[Vur03]
InN	0.69	0.414	454	0.64	[Wu03]

Table 2.4: Commonly accepted values of the band gap energies at low and room temperature, $E_g(0)$ and $E_g(300\ K)$, respectively, and Varshni constants α and β, of wurzite AlN, GaN and InN.

The band gap dependence on the alloy composition is modeled using a quadratic polynomial equation whose nonlinear coefficient is called the bowing parameter, b. This parameter takes into account the deviation from the linear interpolation given by the Vegard's Law. Then, for a ternary nitride compound as $A_xB_{1-x}N$, the band gap energy can be expressed as a function of the alloy composition as:

$$E_{g,A_xB_{1-x}N}(x) = xE_{g,AN} + (1-x)E_{g,BN} - b(1-x)x \tag{2.14}$$

The commonly accepted values of the band gap energy at low, *E_g(0)*, and room temperature, *E_g(300 K)*, are summarized in Table 2.4. In general, the temperature dependence of the band gap energy of semiconductors can be described by the Varshni's Equation (Eq. 2.15). By fitting the experimental values of the *E_g(T)* to this equation, the optical parameters related to the band gap can be obtained. In this equation, *E_g(0)* is the band gap energy at 0 K, α is a constant and β is a parameter associated with the Debye temperature of the crystal [Var67].

$$E_g(T) = E_g(0) - \frac{\alpha T^2}{\beta + T} \tag{2.15}$$

Concerning the InN semiconductor, at the beginning, Tansley and Foley presented a value of the fundamental absorption edge for InN of 1.89 eV at room temperature which seemed to be well-established [Tan86]. This InN was grown by RF sputtering on glass substrates leading to polycrystalline films with residual carrier concentrations above $\sim 10^{19}$ cm^{-3}. Nevertheless, a controversy was raised when different groups suggested that the band gap energy values of InN grown mostly by MBE were in the

range of 0.65-0.90 eV [Wu02][Mat02][Sai02]. Among them, Davydov *et al.* reported a band gap value of 0.9 eV for high quality InN films through different characterization techniques as optical absorption and PL spectroscopies [Dav02]. This value has converged to ∼0.64 eV [Wu03]. The difference between both ranges of band gap values for InN may be attributed to the crystalline quality of the InN films. InN grown by MBE and MOVPE presents high structural quality and low residual carrier concentration ($\sim 10^{16}$ cm^{-3}). Larger band gap energies in the range of ∼1.6-1.9 eV have been obtained for InN films deposited by sputtering usually presenting high doping levels in the order of $\sim 10^{20}$-10^{21} cm^{-3} [Guo98][Sai01][VF12c]. This high free carrier concentration which induces the Burstein-Moss effect is one of the commonly accepted reasons of the InN large band gap together with the presence of oxygen and other dopant sources within the layers.

As well as the band gap energy, the refractive index, $\widetilde{n}(\lambda)$, and the absorption coefficient, $\alpha_0(\lambda)$, are crucial parameters for the application of these materials in optoelectronics and photonics. The refractive index is given by the following complex relationship:

$$\widetilde{n}(\lambda) = n_0(\lambda) + i\kappa(\lambda) \tag{2.16}$$

where $\widetilde{n}$ is the complex index of refraction, $n_0(\lambda)$ is the real part of the refractive index which indicates the speed at which an electromagnetic wave propagates through the material while $\kappa(\lambda)$ is the imaginary part called extinction coefficient which gives information about the amount of light which is absorbed when propagates through the material and its value is given by:

$$\kappa(\lambda) = \frac{\alpha_0(\lambda)\lambda}{4\pi} \tag{2.17}$$

Since the group III-nitrides in wurzite phase and sapphire are anisotropic uniaxial materials, they present two different refractive indices depending on the vibration direction of the light. They exhibit a certain refractive index when light vibrates parallel to the c-axis (extraordinary index, $n_e(\lambda)$) and another when light vibrates perpendicular to the c-axis (ordinary refractive index, $n_o(\lambda)$) which is the same in all 360°.

	AlN	**GaN**	**InN** [Web10]	**Sapphire** [Mal72]
n_0	2.120[Pas66] 2.042[Ozg01] 1.85*	2.317[Bar73] 2.279[Ozg01]	2.28*	1.746 1.74*
n_e	2.160[Pas66] 2.089[Ozg01]	2.305[Bar73] 2.315[Ozg01]	2.09	1.738

Table 2.5: Commonly accepted values of the ordinary and extraordinary refractive indices of AlN, GaN, InN and sapphire at 1.55 μm. Values with an asterisk have been estimated from our samples at 1.55 μm. The values used for the simulations of the optical structures and devices investigated in this work are underlined.

Table 2.5 summarizes the widely accepted values of the real part of the ordinary and extraordinary refractive index for AlN, GaN, InN and sapphire at the wavelength of interest for this study, 1.55 μm. Furthermore, values estimated from our samples are also included and highlighted with an asterisk.

2.3 Film synthesis techniques

Thin film deposition techniques are mainly classified in four groups depending on the type of the involved process: evaporative processes as in plasma-assisted molecular beam epitaxy (PAMBE), glow-discharge as in sputtering, gas-phase chemical processes as in chemical vapor deposition (CVD) and liquid-phase chemical processes [Ses02]. The choice of the growth technique plays an important role in the properties of the obtained thin films. During the development of this Thesis, AlN and InN thin films have been deposited by sputtering and the quantum-confined heterostructures based on GaN/AlN have been grown by PAMBE. Thus, a general view of these two methods for the deposition of III-nitrides is given in this section.

2.3.1 Plasma assisted molecular beam epitaxy (PAMBE)

Epitaxial growth can be considered as the deposition of single crystal films which maintains a certain lattice alignment with respect to the single crystal substrate

below. Particularly, heteroepitaxial growth is defined as the deposition of a material different from the substrate material. On the contrary, if both film and substrate materials are the same, the growth is considered homoepitaxial.

PAMBE technique consists of the growth of a material under ultra-high vacuum through the interaction between evaporated atomic or molecular fluxes and the growing sample surface. The evaporated atoms impinge on a properly heated substrate where they condense and grow epitaxially. Group III-nitrides are provided by effusion cells and the gas flux is provided by a radio frequency (RF) N_2 plasma cell.

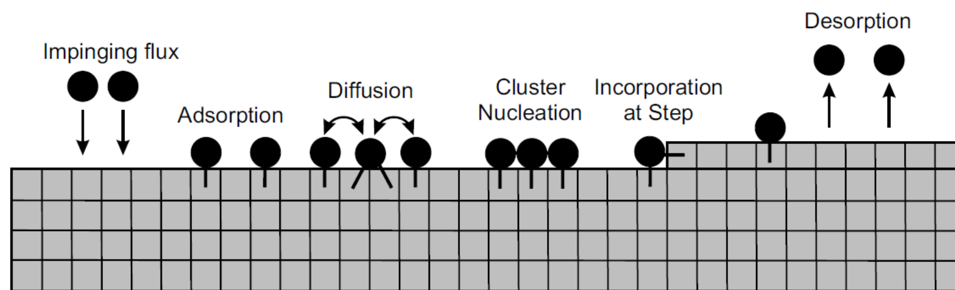

Figure 2.5: Different atomic processes that can take place at the surface during MBE growth [Das12].

The main parameters to control the growth kinetics and thermodynamics are the material cells temperature, which determines the atomic fluxes limiting the arrival rate of atoms, and the substrate temperature, which controls the different processes that can occur at the substrate surface during the epitaxial growth. Figure 2.5 depicts the multiple surface processes that can take place during the epitaxial growth. Adsorption of the impinging fluxes can be occurred at the growing surface by chemical process (chemisorption through impinging atoms and surface atoms chemical bond sharing electrons) and by physical process (physisorption through Van der Waals forces). Difussion and desorption of species can be occurred due to the mobility of the atoms at a certain substrate temperature. These species will not be incorporated to the layer. Nevertheless, others will incorporate either by step-edge growth forming atomic terraces, or by cluster nucleation.

PAMBE presents several advantages over other growth techniques as:

- Growth under ultrahigh vacuum (10^{-11} mBar).
- In-situ growth control by Reflection High-Energy Electron Diffraction (RHEED).
- Good layer thickness control due to low growth rate (less than one monolayer per second) and excellent smooth surface morphology, thanks to the RHEED system.
- Precise control of the beam fluxes.
- Growth of complex heterostructures with many different layers and high abrupt interfaces.
- Not very high growth temperature (700-750 °C).

It has to be pointed out that the RHEED allows to real-time monitor the evolution of the growing material. In particular, the number of the monolayers grown, the change of its lattice parameter, its surface morphology and the likely transitions between different dimensional growth 2D-3D can be measured. The RHEED system is based on the collection of the electrons diffracted by the growing surface under ultrahigh vacuum by means of a fluorescent screen. Streaky diffraction patterns correspond to flat surfaces (∼2D) on the growing sample while rough surfaces (∼3D) present spotty diffraction patterns. PAMBE is widely used for the synthesis of nanometer-scaled structures based on different materials, like quantum wells (QWs), quantum dots (QDs) and nanowires (NWs).

Depending on the substrate temperature and the relation between III-V elements, three different heteroepitaxial growth modes can be performed (see Fig. 2.6). The growth mode characterizes the nucleation and growth processes, and there is a direct correspondence between the growth mode and the film properties. The growth modes are the following:

- Frank van der Merwe growth [Fra49]: This growth is carried out layer by layer resulting 2D structures. Atoms have enough mobility on the surface forming 2D

islands and extending them until cover the previous monolayer. Dislocations can appear to overcome the likely lattice mismatch. This growth method has been used for the synthesis of multi-quantum-well (MQW) structures presenting in this Thesis, where abrupt and flat interfaces are required.

- Volmer-Weber growth [Vol26]: This method is characterized by the nucleation of small material 3D islands on the surface at the first stages of the growth due to the very low mobility of the atoms leading to a non-completely covered surface. These emerged islands are easily formed when the surface presents defects, impurities or roughness.

- Stranski-Krastanow [Str38]: This type is a combination of layer and island growth modes. The deposition begins layer by layer but when a critical thickness (Θ_{lim}) is reached, this 2D growth becomes energetically unfavorable and the growth continues with the formation of 3D islands. This growth method has been performed for the deposition of the multi-quantum-dot (MQD) structures analyzed in this work.

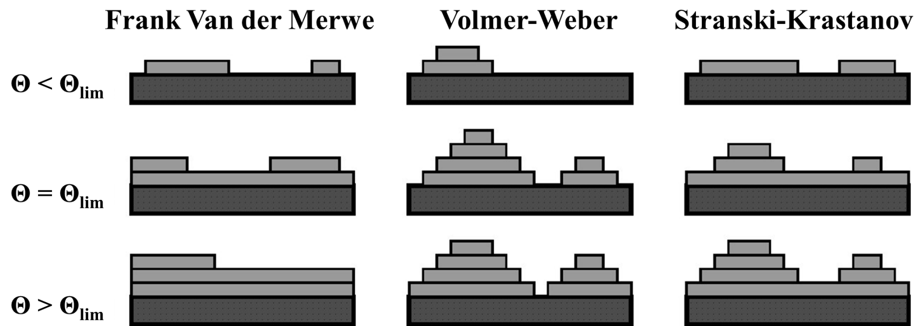

Figure 2.6: Morphology of a growing film depending of the growth mode: Frank van der Merwe, Volmer-Weber and Stranski-Krastanow for various stages of the growth depending on the film thickness.

2.3.1.1 Plasma-Assisted MBE system used in this work

The growth of the MBE samples analyzed in this work was carried out in the INAC-SP2M laboratories in CEA-Grenoble under the supervision of Dr. Eva Monroy.

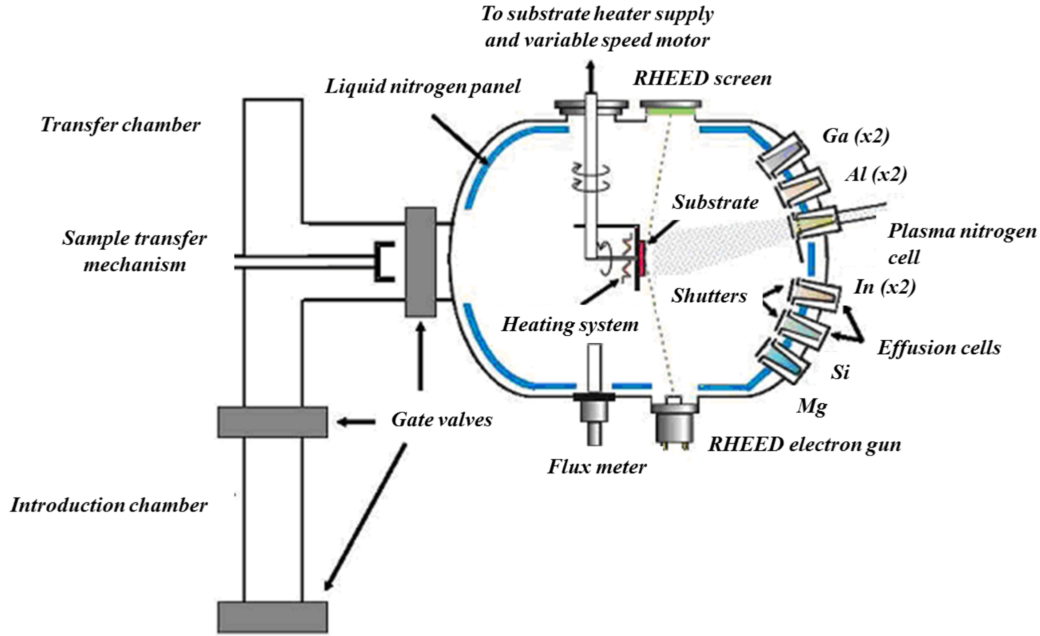

Figure 2.7: Scheme of the PAMBE equipment used for the growth of the MBE samples analyzed in this Thesis.

Figure 2.7 depicts the schematic of the PAMBE equipment which has been used for the growth of the MBE samples studied in this work. It consists of three chambers individually pumped and separated by gate valves: introduction, transfer and growth chambers. The substrates are indium-glued on the sample holder and introduced in the machine through the introduction chamber. This chamber is pumped by means of both turbomolecular and ionic pumping systems reaching a pressure of $\sim 10^{-8}$ mBar. Afterwards, the substrates are carried out to the transfer chamber through a cart. Both introduction and transfer chambers are separated by a gate valve increasing the vacuum in the transfer chamber achieving a pressure of $\sim 10^{-10}$ mBar with another ionic pump. Once the substrates are under high vacuum in the transfer chamber, they are introduced in the growth chamber. They are located in the center and facing the effusion cells which provides the elements for the epitaxial growth. This chamber is kept under ultrahigh vacuum in the pressure range of $\sim 10^{-11}$ mBar. The substrates are heated with a hot filament and controlled in temperature with a thermocouple placed in contact with the substrate holder. Furthermore, the substrate holder rotates to ensure an homogeneous deposition. In this case, effusion cells provides group-III

metals (Al, Ga, In) and dopants (Si, Mg) while active nitrogen is provided by an RF plasma (13.56 MHz) cell where N_2 molecules are excited and dissociated.

2.3.2 Sputtering

Sputtering is one of the most widely used thin film fabrication techniques of metals, insulating materials and semiconductors. It is also used as a physical etching method for surface cleaning and pattern definition. Sputtering presents the advantage of being a low-cost technique in terms of equipment and maintenance which allows the deposition of thin films in a wide range of temperatures, even at room temperature, and on both rigid and flexible substrates. Sputtering deposition is a process in which ionized atoms from a plasma are accelerated into a surface (target) in order to eject atoms from it. When the plasma ions impact to the target atoms, a transference of kinetic momentum occurs ejecting them as shown in Fig. 2.8(a). These ejected or sputtered atoms can then be condensed under the right deposition conditions onto a substrate to nucleate a thin film of that material. The bombardment of the target by the plasma ions not only produces the pulverization of the target but also the emission of energetic secondary electrons which are accelerated towards the plasma enabling the maintenance of the plasma discharge. This process takes place in a high vacuum deposition chamber with a base pressure of $\sim 10^{-7}$ mBar in order to minimize the amount of impurities in the growing films.

The discharge gas is typically an inert gas with high atomic mass in order to increase the transference of kinetic momentum to the target atoms. The most commonly gas used is Ar taking profit besides of its low price. The efficiency of sputtering depends mainly on the energy of the incident ions to the target. The objective is to maximize the knocking off of target surface atoms while minimizing the implantation of the incoming ions. The parameter which express this efficiency is the sputtering yield being defined as the average number of atoms ejected from the target per incident ion. This parameter depends on the angle, energy and mass of the incident ion and the surface binding energy of atoms in the target. When these positive ions reach the target surface with an energy above the surface binding energy, atoms can be ejected and then travel towards the substrate to create the film. Nevertheless, if low energetic ions reach the target, they can be reflected or can produce surface damage and surface migration. On the contrary, if ions with too much energy reach the target,

the probability of ion implantation process increases. Figure 2.8(b) depicts all the processes that can occur when sputtering a material.

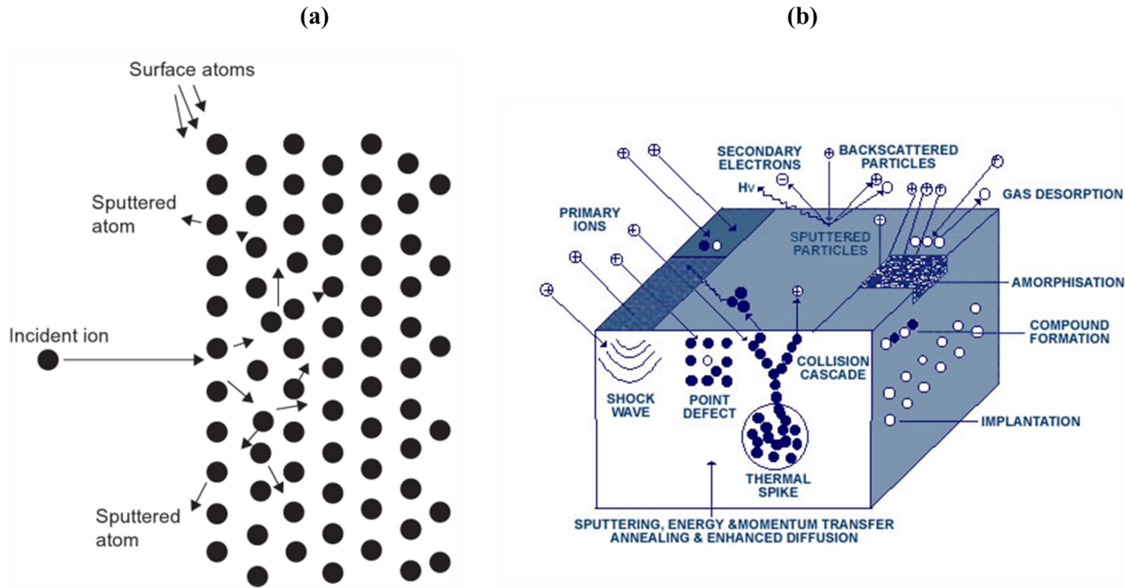

Figure 2.8: (a) Schematic representation of the physical sputtering process. (b) Possible processes during material sputtering.

In the sputtering technique, the ejected atoms can reach the substrate from different directions due to the several collisions with the particles of the chamber atmosphere. The mean free path of the ejected particles is inversely proportional to sputtering pressure. Thus, working pressure has to be optimized in order to obtain the maximum mean free path as possible of the sputtered atoms. Ideally, this mean free path should be at least similar to the target-substrate distance in the sputtering system.

Sputtering deposition is mainly based on four elements: a target made of the material to be deposited, a gas atmosphere under controlled pressure, an electric power source to sustain the plasma and a substrate for the deposition of the desired material. Although these elements can be arranged in different configurations and with additional parts like magnets and electrodes, only the relevant configurations for this work are summarized. The simplest one is the planar diode actuated with a static potential according to the scheme in Fig. 2.9. In this scheme, the target of the material to be deposited is bombarded with accelerated ionized gas atoms generated in the plasma. Atoms from the target are removed by collisions of the

incident ions and are subsequently deposited on, mainly, the substrates surface. In the planar diode sputtering configuration, high pressure (10^{-1} mBar) and high voltage (a few kV) are required which induce low deposition rates and low thin film crystal quality. Thus, the sputtering technology evolved towards the use of magnetrons to confine the plasma. Among the different geometries of magnetron, the most used is the planar magnetron which allows deposition at lower pressures (10^{-3} mBar) and weaker voltages (∼300-500 V). Under these conditions, the structural quality and the growth rate of the films increase while the ejected particles reach high energies what improve the adhesion to the substrate without increasing its temperature.

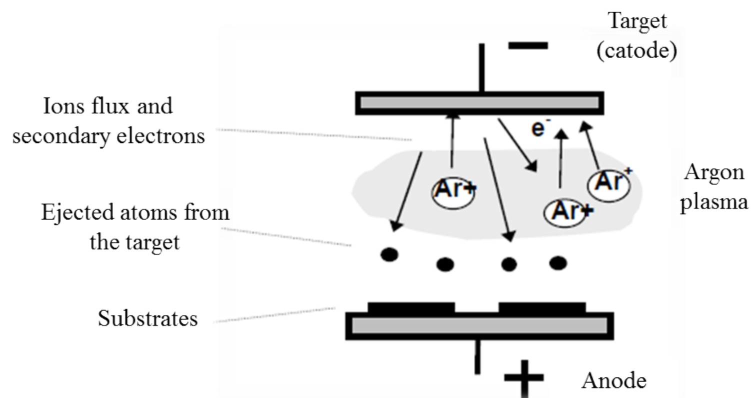

Figure 2.9: Scheme of the bombardment process in a sputtering system in planar diode configuration [Alb03].

The sputtering system used during this Thesis presents the planar magnetron configuration. The magnetrons are formed by a cathode connected to a power supply. The target based on the desired material to deposit is located below the cathode. Above the cathode, permanent magnets produce a magnetic confinement ring-shaped zone leading to the effective confinement of the electrons near the target. And the anode is placed surrounding the target. When the plasma is present, electrons from the plasma and secondary electrons from the target suffer helicoidal movements because of the Lorentz's force from the electric field between the electrodes and the magnetic field. Since plasma ions are much more massive than electrons, the effect of the same magnetic field on them can be considered negligible. Thus, only the electrons follow the helicoidal orbits [Alb03]. The objective of this concentration of electrons in the vicinity of the target is to provide them with larger mean path. Thus, the plasma density in that zone is enhanced which induces a higher sputtering rate.

Besides, in this way, it is possible to avoid the electrons not to arrive to the substrate. Most electrons are confined in regions where the magnetic field lines are parallel to the target surface leading to a higher ionization of the gas atoms in that region and, subsequently, inducing a higher sputtering rate in the target areas immediately in front of the confined regions (see Fig. 2.10). The growth rate (GR) is calculated by the following equation:

$$GR = \frac{d}{t_s} \tag{2.18}$$

where d is the layer thickness and t_s is the sputtering time.

Magnetron sputtering has the following advantages compared to planar diode configuration: higher ionization efficiency, lower power discharge, plasma confinement in the target area and possibility of working at lower pressures leading to higher deposition rates.

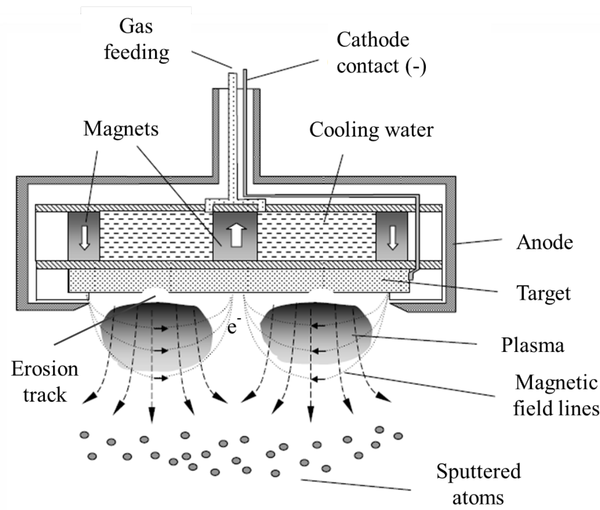

Figure 2.10: Schematic diagram of the electrodes in a planar magnetron.

Another sputtering parameter is the power supply for plasma generation. The plasma can be generated under both direct (DC) and alternating (RF) voltage application. The simplest way to generate the electrical discharge is the application of a DC voltage at the cathode electrode. Nevertheless, to sustain a DC glow discharge, the target

has to be conductive. When the target is non-conductive, the electrode is charged up due to the accumulation of positive charges, and the discharge extinguishes. The application of an RF voltage is the solution for maintaining the sputtering process in insulating materials. This alternating voltage compensates the positive charges accumulated in a semi-cycle by the negative charges accumulated in the previous cycle. So, the target electrode acts alternately as the cathode and the anode. In an RF plasma, electrons are oscillating with the same frequency of the driving field (usually 13.56 MHz) while ions, due to their much larger mass, are not involved in the oscillations. As the RF plasma maintains the sputtering process only by semi-cycles, the material deposition rate in this configuration is lower than in the case of DC sputtering. In fact, at the same applied power, lower deposition rates ($\sim$50% of DC rates) are expected to be achieved.

As well as plasmas generated from noble gases, it is possible to create plasmas from molecular gases N_2, O_2, etc. In that case a reactive plasma is generated due to the dissociation of molecules leading to reactive chemical species. The sputtering technique used under this configuration is called reactive sputtering and can be used to obtain compounds. The compounds are formed by reactive processes between the sputtered material and the gas in the chamber either on the target surface, in-flight or on the substrate depending on the deposition conditions. The AlN and InN thin films obtained during this work have been deposited under reactive gas conditions by means of sputtering metallic Al and In targets, respectively, in a nitrogen plasma.
A drawback to take into account is the possibility of target poisoning when reactive processes take place with the atoms in the target surface. A thin film of compound can be formed on the target surface decreasing the sputtering growth rate. This phenomenon can lead to a positive feedback loop: the more the poisoning of the sputtering target, the more the growth rate is reduced. Hence, more reactive gas is needed for reaching a certain compound and, in turn, for increasing the growth rate. Thus, resulting in a higher target poisoning. This positive feedback is seen as a target hysteresis based on sudden changes in the thin film deposition rate as observed in Fig. 2.11. For low reactive gas flow (up to A), the reactive gas is not enough for reaching the stoichiometric compound since most of the sputtered metal atoms do not react with the gas. At this situation, the growing film is formed by the metal and the gas diluted within the layer. To prevent this metallic mode, the reactive gas flow has to be increased (from A to B). Hence, the reactive mode begins accompanied by

a significant decrease of the growth rate (C) because of the target poisoning while the compound is formed and deposited onto the substrate. In order to avoid a higher target poisoning, the reactive gas flow is decreased to a certain flow (D) where the reactive gas is not enough to continue forming the compound. Thus, the poisoning of the target disappears and the deposition rate suddenly increases beginning the metallic mode deposition again.

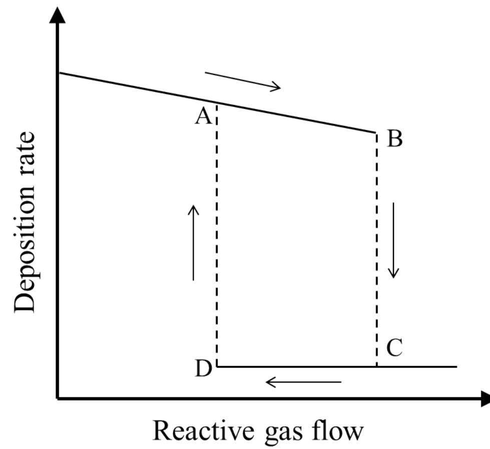

Figure 2.11: Hysteresis process in reactive sputtering.

The technique used to grow the samples during the development of this Thesis is the radio-frequency reactive magnetron sputtering due to its simplicity, versatility and suitability to deposit polycrystalline AlN and InN with high quality and in a low cost procedure. The main steps towards the optimization of layer synthesis consisted in studying the effect of the different deposition parameters on the layer properties. These sputtering parameters can be the RF power, sputtering pressure, substrate temperature, gases ratio, sputtering time and substrate bias. The substrate bias is an external parameter which is induced during deposition by using a DC voltage source connected to the substrate holder through a resistor (56.2 Ω). A negative bias applied to the substrate is critical to improve the crystalline quality of the layers due to the arrival of highly accelerated positive ions (Al^+, N^+, N_2^+) to the substrate which influences the mobility of the atoms in the layer [Seo10]. Figure 2.12 shows a simple scheme of the substrate biasing setup used in our sputtering system.

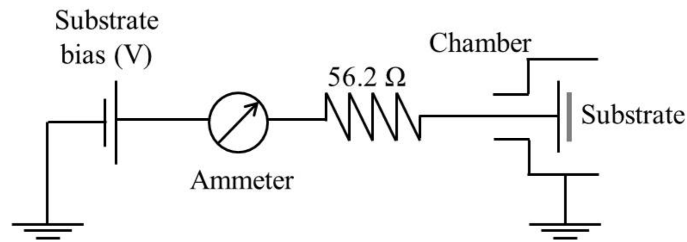

Figure 2.12: Schematic of the substrate biasing method used in this work for sputtering deposition.

2.3.2.1 RF magnetron sputtering system used in this work

All the sputtered samples studied in this Thesis were grown in an RF sputtering system ATC ORION-3-HV from AJA International (see Fig. 2.13). The base pressure reached in its chamber is $\sim 10^{-8}$ mBar.

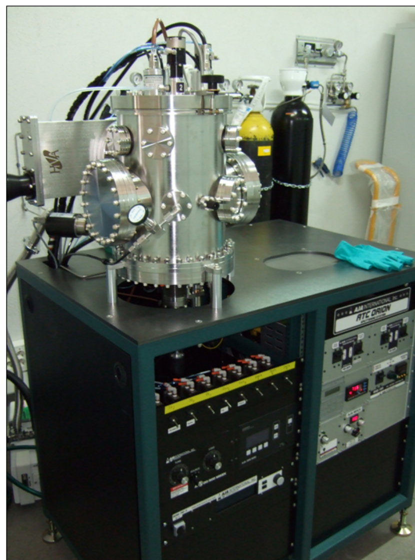

Figure 2.13: RF magnetron sputtering system used in this work together with the gas installation in the GRIFO facilities at the University of Alcalá.

This system consists mainly of the following parts:

- High-vacuum valve for controlling the pressure in the chamber.
- Pump system formed by a turbomolecular pump (up to 210 l/s) and a rotatory pump (up to 12 m^3/h).

- A low-base pressure gauge ($\sim 10^{-8}$ mBar) based on ionization method and a convectron gauge for pressures close to atmospheric pressure.
- A baratron gauge for measuring pressures under plasma atmosphere in the range of $\sim 10^{-4}$-10^{0} mBar.
- Gas sources: Ar(5N) and N_2(6N).
- Mass-flow controllers to monitor the flow of the gases introduced into the sputtering chamber.
- Variable leak valve for chamber venting with nitrogen.
- Three 2-inch diameter confocal magnetron cathodes with integrated shutters and gas distribution system.
- Metal targets: Al(5N) and In(4N5).
- Two RF power sources (up to 300 W) with impedance matching unit and a DC power supply (up to 750 W).
- A 4-inch substrate holder with automatic rotatory system for optimized heating and thin film deposition homogeneity.
- Two quartz lamps placed under the substrate holder to heat the substrates up to 850 °C.
- One K-type thermocouple placed 2 mm below the substrate holder and controlled by a PID with a resolution of ±1 °C for monitoring the substrate temperature during the deposition process.
- Closed-cycled cooling system for keeping cool the magnetrons and the substrate heater.

2.3.3 Substrates

As it has been mentioned previously, the lack of appropriate lattice- and thermal-expansion-matched substrates makes III-nitrides to be grown heteroepitaxially. Thus, they are mainly grown on a variety of substrates, such as sapphire (Al_2O_3), silicon (Si), silicon carbide (SiC), gallium arsenide (GaAs),

zinc oxide (ZnO), etc. The choice of the substrate to grow either thin films or heterostructures considers the reduction of lattice and thermal expansion mismatches between layer and substrate. Furthermore, the desired crystal orientation, defect density, surface morphology and substrate cost will depend on the further material application.

Concerning the variety of substrates used for the growth of III-nitrides, Si is the best choice since it is obtained by well-established growth procedure, at low cost and in large substrate areas. Moreover, devices and layers grown on this substrate can be easily integrated into the existent Si technology. Cubic silicon presents hexagonal symmetry within the plane perpendicular to the [111] direction, allowing the growth of wurtzite nitrides. The epitaxial relationship between nitrides and Si(111) comprises the alignment of the [0001] and [1000] directions of the III-nitride compound and the [111] and [110] of the Si, respectively.

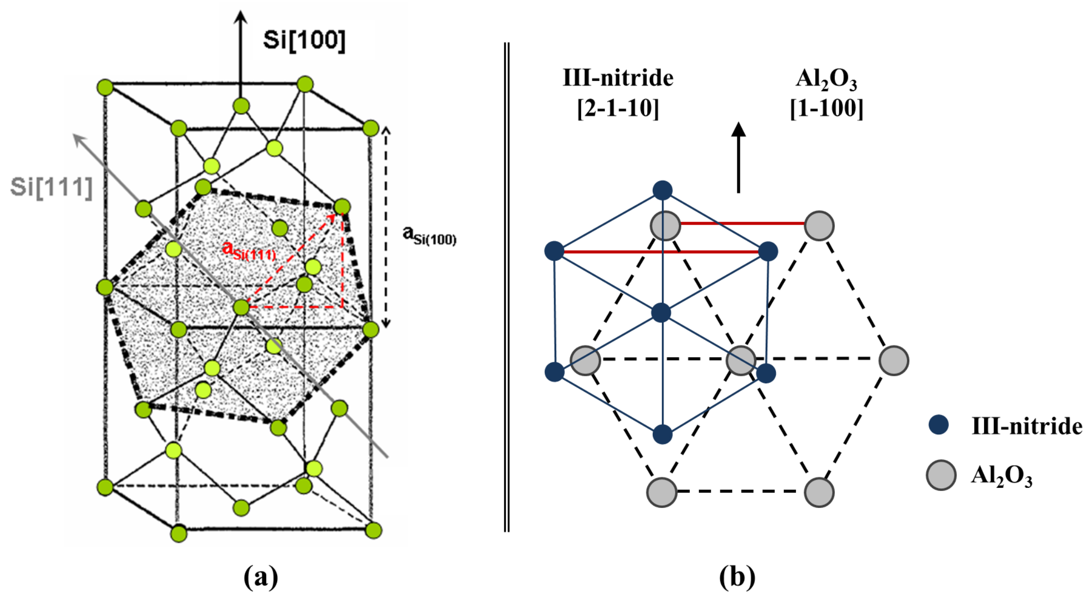

Figure 2.14: (a) Illustration of the Si structure with (100) cubic plane and highlighted (111) hexagonal plane. The red-dashed triangle shows the relationship between silicon cubic and hexagonal phases. The hypotenuse corresponds to the lattice parameter of the hexagonal phase, $a_{Si(111)}$, and the length of each side is half of the cubic phase lattice parameter, $a_{Si(100)}/2$. (b) Scheme of the epitaxial relationship between III-nitrides and sapphire in (0001) plane.

Figure 2.14(a) depicts the relation between cubic plane (100) and hexagonal plane (111) of Si. Particularly, the red-dashed triangle shows the lattice parameters relationship which should be considered for the growth of hexagonal nitrides on Si(111). In this triangle, the hypotenuse is the in-plane lattice parameter of the silicon hexagonal phase, $a_{Si(111)}$, and the length of the sides coincides with half of the cubic phase lattice parameter, $a_{Si(100)}/2$. Thus, the relationship is given by:

$$a_{Si(111)} = \frac{a_{Si(100)}}{\sqrt{2}} \tag{2.19}$$

Table 2.6 shows the lattice mismatch between Si(111) substrates and (Al, Ga, In)N compounds obtained using the Eq. 2.19.

	$a(\AA)$	$\Delta a_{epi}/a_{Si(111)}$ (%)	$\Delta a_{epi}/a_{sapphire}$ (%)
AlN	3.112	-19.0	13.3
GaN	3.189	-17.0	16.1
InN	3.545	-7.7	29.0

Table 2.6: Lattice mismatch between AlN, GaN and InN and Si(111) and sapphire substrates at 300 K. Δa_{epi} is the difference between lattice parameters of the layer and the substrate, obtained taking into account the epitaxial relationship explained in the text. The in-plane lattice parameters of Si(111) and sapphire are 3.840 $\AA$ and 4.758 $\AA$, respectively [Fen08].

Concerning the case of sapphire substrates, this material crystallizes in a hexagonal structure but the lattice parameter is quite higher than those of the III-nitrides structure. As it is schemed in Fig. 2.14(b), when III-nitrides grow on sapphire, the nitride crystal structure is rotated 30° with respect to the sapphire one. Then, [2-1-10] nitride direction and [1-100] sapphire direction are aligned. This rotation leads to an effective lattice parameter of III-nitride when growing on sapphire. This effective lattice parameter is given by the following equation:

$$a'_{III-nitride} = \sqrt{3}a_{III-nitride} \tag{2.20}$$

As it is observed in Table 2.6, III-nitrides grow under tensile strain on Si(111) substrates and under compressive strain when growing on sapphire substrates.

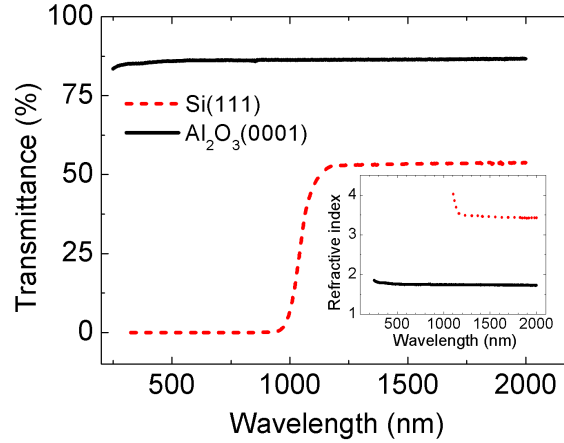

Figure 2.15: Experimental linear optical transmittance measurements of Si(111) and sapphire substrates in the visible/NIR range.

Among the mentioned variety of substrates to grow III-nitrides, just sapphire-based substrates have been used in this work. Sapphire is transparent in the near-infrared (NIR) range (E_g ~9.9 eV ~125 nm) as depicted in Fig. 2.15 compared to the transmittance of the Si substrate. Besides, as presented previously in Table 2.5, sapphire has a refractive index lower than those of III-nitrides. Thus, developed nitride materials can be applied in optical waveguiding at 1.55 μm taking advantage of the contrast between sapphire and layer which leads to a better light modal guiding. The optical waveguiding using Si as a substrate is not possible due to its refractive index of ~3.5 at 1.55 μm, which is higher than those of III-nitrides. At the same time, although the lattice mismatch between InN and sapphire is much larger than that between InN and Si(111), it can be easily reduced by introducing AlN buffer layers while not affecting the absorption of the structure for application at 1.55 μm.

During the development of this Thesis, two types of substrates have been used for the growth of different nitrides:

- **Sapphire substrates**: They have been grown by Czochralski method and supplied by Semiconductor Wafer, INC. The sapphire substrate consists of double side polished ~500-μm-thick [0001]-oriented Al_2O_3 with 3-inch diameter. Its AFM image is presented in Fig. 2.16(a).

- **AlN-on-sapphire templates**: These substrates have been grown by MOVPE and supplied by DOWA. The template consists of ∼1-μm-thick [0001]-oriented AlN with a dislocation density ∼5×10^9 cm^{-2} grown on ∼430-μm-thick c-axis sapphire substrate. AFM image of this substrate is presented in Fig. 2.16(b).

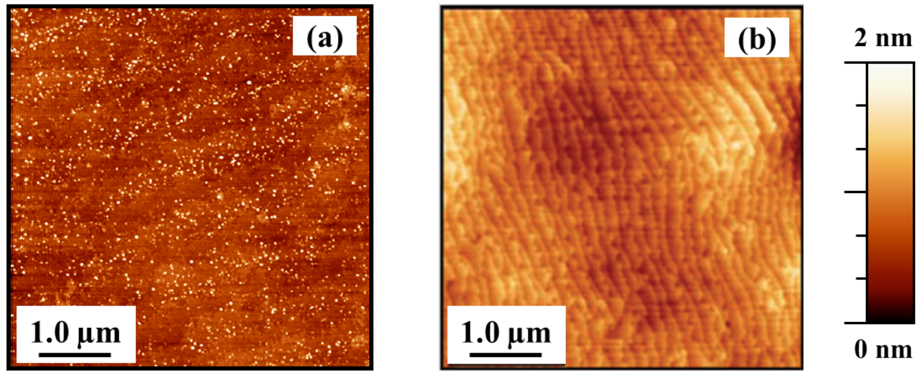

Figure 2.16: AFM images of the substrates used in this work: (a) sapphire and (b) AlN-on-sapphire template.

Chapter 3

Nitrides characterization techniques

The growth of III-nitrides and the material characterization process run in parallel during the development of this Thesis. The material properties obtained from the characterization measurements are the basis for reaching the optimized growth conditions.

This chapter describes the experimental techniques used for the analysis of the nitride structures obtained in this work. They are mainly aimed at determining structural and morphological properties as well as defining the optical and electrical behavior of the material. The structural and morphological techniques used are high-resolution x-ray diffraction (HRXRD), atomic force microscopy (AFM) and field-emission scanning electron microscopy (FESEM). Meanwhile, the layer optical characterization is focused on linear optical experiments consisting of transmittance (Tr) and photoluminiscence (PL) measurements.

PL, AFM and FESEM characterization measurements were carried out in the CEA-Grenoble facilities under the supervision of Dr. Eva Monroy while HRXRD analysis was performed at the X-ray Diffraction Techniques Laboratory at the ICMM-CSIC in Madrid under the supervision of Dr. Ana Ruiz. Linear optical transmittance measurements were carried out in our facilities in the Electronics Department of the University of Alcalá.

3.1 Structural and morphological characterization

Structural characterization techniques not only provide information about the structure and crystalline quality of the layers but also they can bring understanding of surface morphology, interface quality and film density. This section describes the main methods used in this work to characterize the structural and morphological properties of the group III-nitride layers.

3.1.1 High-resolution x-ray diffraction (HRXRD)

Diffraction techniques are based on the principle of interference between electromagnetic waves. In a general explanation, in order to get information about dimensions of a material formed by items, two conditions are required: a periodic distribution of items and incident waves with wavelengths similar to the distance between those items.

In the case of crystalline semiconductors where atoms, ions and molecules are positioned in a periodic-spatial distribution, x-ray diffraction techniques are used for determining the detailed structure of the analyzed material. The x-ray wavelength is in the range of angstroms (typically, from 0.1 $\AA$ to 100 $\AA$) which covers the typical interatomic distance in the semiconductor. As observed in Fig. 3.1, the diffraction effect is produced when x-radiation beams reflect with a periodic structure with parallel and equidistant (with $d \sim \lambda$) atomic planes. The diffraction peak is obtained when a constructive interference between reflected x-radiation beams is produced following the Bragg's Law:

$$2dsen\theta = m\lambda \tag{3.1}$$

where d is the distance between two consecutive atomic planes, θ is the angle between the incident beam and the planes diffracting it, m is an integer called the diffraction order and λ is the radiation wavelength.

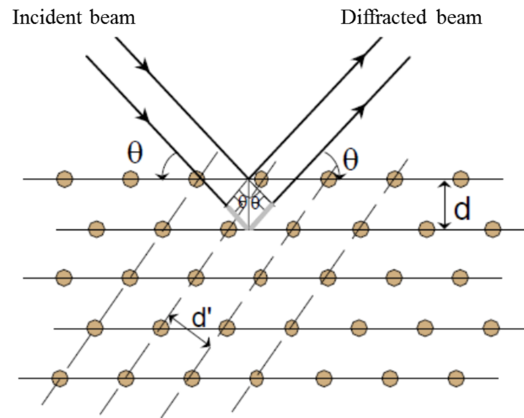

Figure 3.1: Bragg's reflection corresponding to two consecutive planes separated a distance d [Alb03].

Thus, x-ray diffraction measurements used along this Thesis are based on the registration of x-ray intensity reflected from the material under study depending on the angles of the incident and diffracted beams. In this way, the exploration of different distances and periodicities in the sample can be obtained.

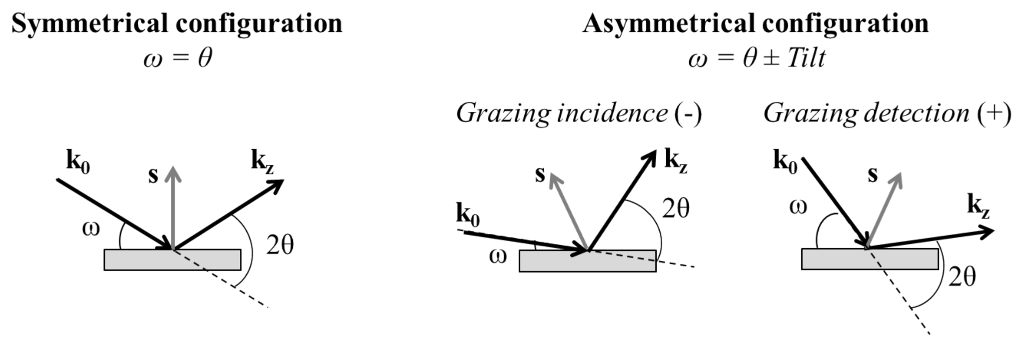

Figure 3.2: Scheme of x-ray diffraction configurations: symmetrical and asymmetrical. The vector **s** is the scattering vector whose direction is given by the difference between the incident ($\mathbf{k}_0$) and diffracted ($\mathbf{k}_z$) beams.

Two configurations can be performed for HRXRD measurements as represented in Fig. 3.2: symmetrical (the angle formed between the detector and the sample is equal to that formed between the incident beam and the sample) and asymmetrical (the angle between the detector and the sample differs from that formed between the incident beam and the sample).

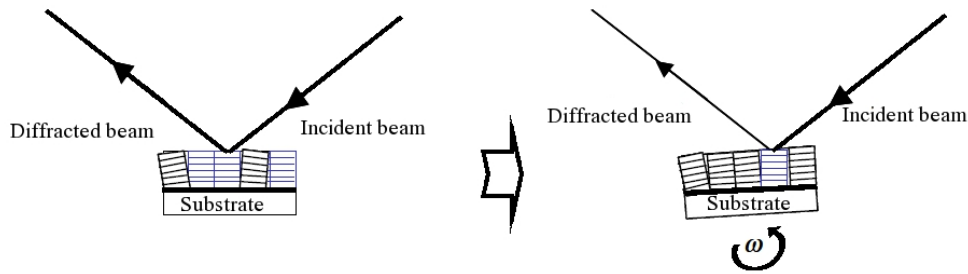

Figure 3.3: Scheme of the rocking curve diffraction measurement. The materials grains responsible of the diffracted beam are highlighted in each case (blue color) [Nar03].

In this study three types of diffractograms under symmetrical configuration were performed: ω-scan (rocking curve), $2\theta/\omega$-scan and reflectivity (XRR).

- **ω-scan (rocking curve):** In this configuration, both the x-ray source and the detector are kept fixed and the sample rotates around the Bragg's condition angle. Figure 3.3 shows an scheme of the rocking curve scan. A perfect single crystal produces a very sharp peak, observed only when the crystal is properly tilted so that the diffraction condition is fulfilled. In this case, the rocking curve presents a minimum FWHM due just to the instrument broadening and the intrinsic width of the crystal material. Larger broadening of the rocking curve of a material can be due to different contributions like tilt (angular grain inclination with respect to the substrate while keeping the same in-plane lattice parameter, a), strain surrounding dislocations and grain size broadening. Thus, the FWHM of the rocking curve of the diffraction beam provides information about the degree of misorientation of the grains in the material and, therefore, its structural quality. The broader the FWHM of the rocking curve around the Bragg's angle, the worse the crystal quality of the material layer.

- **$2\theta/\omega$-scan:** In this type of scan, the x-ray source remains fixed and when the sample rotates an angle ω, then the detector rotates twice compared to the sample movement, 2θ (see Fig. 3.4). This measurement is sensitive to interplanar distance variation. Thus, the position of the diffraction peaks obtained by these measurements provides an estimation of the out-of-plane lattice parameter, c, of the material which is directly related to the degree of deformation (tensile or compressive strain) of the layer along the c-axis and its composition. The peaks intensity are usually proportional to the volume of material which produces diffraction. Furthermore, this scan allows the

estimation of the average grain size, G, from the Scherrer's formula for spherical particles [Pat39]:

$$G = \frac{0.9\lambda}{\Delta 2\theta} cos\theta \tag{3.2}$$

where λ is the x-ray wavelength and θ and $\Delta 2\theta$ are the Bragg's diffraction angle and the FWHM of the diffraction peak, respectively.

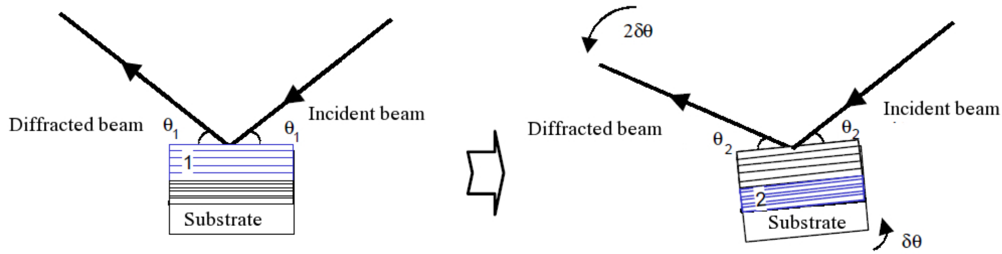

Figure 3.4: Schematic representation of the $2\theta/\omega$-scan. The diffracted planes responsible of the detected beam are highlighted in each case (blue color) [Nar03].

- **x-ray reflectivity (XRR):** This technique is widely used in thin films and multilayer structures characterization. It is based on an specific $2\theta/\omega$-scan selecting low incident beam angle (grazing incidence). This angle is significantly lower than the first Bragg diffracted one, thus the intensity peaks related to the diffraction by the different family planes is not observed. Under these conditions, the material can be considered as a continuous medium with a certain density. In this way, the x-ray reflected intensity is due to the difference in density at the interfaces: air-layer, layer-layer and layer-substrate. Thus, intensity variations induced by the several beam reflections on the thin film surface and on the interfaces are obtained. These variations lead to noteworthy information about the thickness, interface roughness and density of the topmost layer. Successful estimated values of the film thickness can be provided within different ranges depending on the optical resolution of the equipment.
  In this study, XRR measurements were carried out for estimating the thickness and the density of the AlN thin layers. It has to be noticed that the HRXRD used in this work can provide information about layer thicknesses below 200 nm [Yas10]. The film thickness has been obtained through the spacing between maximums of the reflectivity together with the Bragg's equation as shown in

the inset of Fig. 3.5. An estimation of the material density of the layer can be achieved through the analysis of the critical angle (θ_c) obtained as the angle from which the reflected intensity strongly decays (see Fig. 3.5). As a first approach, the value of the critical angle is related to the material density (ρ) through the following equation [Yas10]:

$$\rho = \frac{\theta_c^2 \pi}{r_0 \lambda^2 N_A} \frac{\sum x_i A_i}{\sum x_i Z_i} \tag{3.3}$$

where A_i, x_i and Z_i are the molar mass, atomic ratio and atomic number, respectively, of the i-th atom. Besides, r_0 is the classical radius of the electron and N_A is the Avogadro's number.

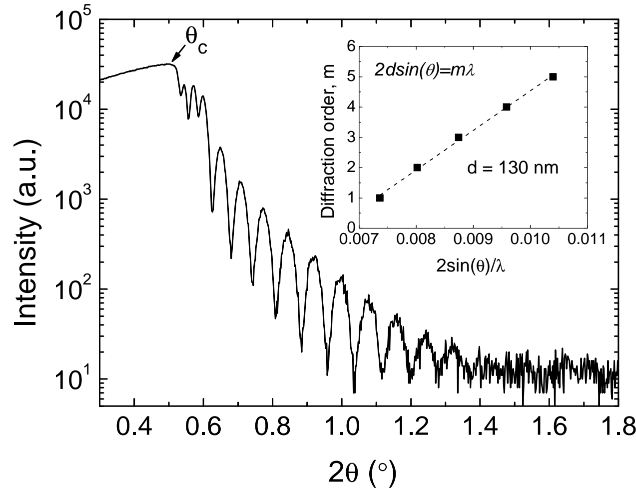

Figure 3.5: Example of a typical XRR scan of an AlN thin film pointing the critical angle (θ_c) together with the estimation of the layer thickness in the inset.

Furthermore, reciprocal space maps can be obtained when both ω- and $2\theta/\omega$-scans for a diffraction peak is represented in two dimensions. When performing the reciprocal space map of an asymmetric reflection together with a diffraction peak of reference, it is possible to obtain both in-plane and out-of-plane lattice parameters of the film and, in turn, its strain state. Furthermore, in the case of ternary compounds, information about the composition and strain can be achieved simultaneously.

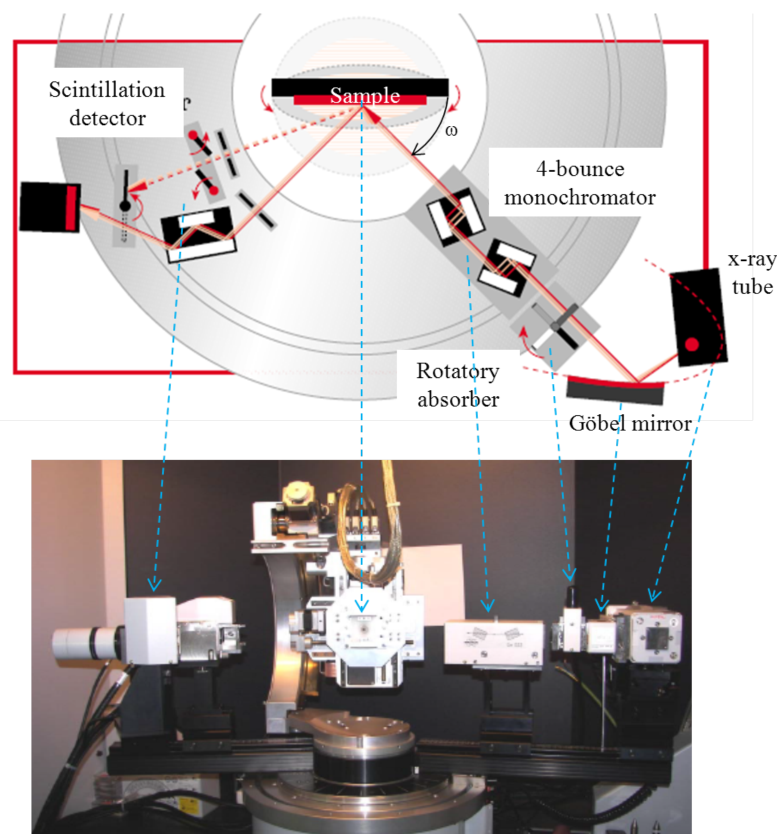

Figure 3.6: Scheme and real image of the diffractometer used during this work.

A Bruker D8-4C Advance x-ray diffractometer was used to perform the measurements (see Fig. 3.6). This diffractometer is based on 3-axis (x, y, z) and 4-circles (2θ, ω, φ, χ) movements. X-ray are generated by bombarding a Cu target with electrons in an evacuated tube. The primary beam coming from the x-ray tube is divergent and polychromatic with wavelengths corresponding to the Cu K$\alpha_{1,2}$ and Cu Kβ emission lines. Thus, the beam is collimated using a Göbel mirror removing, at the same time, the Cu Kβ radiation. The remaining radiation is led to a rotatory absorber which protects the detector varying the absorption factor in a previously set or an automatic mode. Afterwards, the beam passes through a Ge(220) 4-bounce monochromator that only retained the Cu Kα_1 radiation ($\lambda = 1.5406$ $\mathring{A}$) and, finally, the beam comes into contact with the sample. The diffracted beam from the material gets the detector and the beam intensity is monitored during the measurement. There are two different detectors: a scintillation detector with a Ge(002) analyzer with selectable divergence slit as well as a position sensitive detector working in linear or punctual mode.

3.1.2 Atomic force microscopy (AFM)

AFM is a commonly used technique that provides a topographic image of the surface of an analyzed sample. This image gives information about the surface morphology in terms of root-mean-square (rms) surface roughness, the average grain size and, even, a grain density estimation. AFM is based on the attraction and repulsion forces (Van der Waals forces) that a tiny silicon probe tip mounted at the end of a cantilever experiences when approaching to the surface of the material under study. Figure 3.7 exhibits a scheme of an AFM system together with an image taken by FESEM of the morphology and geometry of the used probe tips. The cantilever is mounted to a piezoelectric actuator and a laser beam is reflected by the cantilever (coated by aluminum) and collected by a position sensitive photodetector. The deflection of the cantilever (given by the signal in the photodetector) is used as input to a circuit based on the piezoelectric actuator that moves the cantilever along the z-axis.

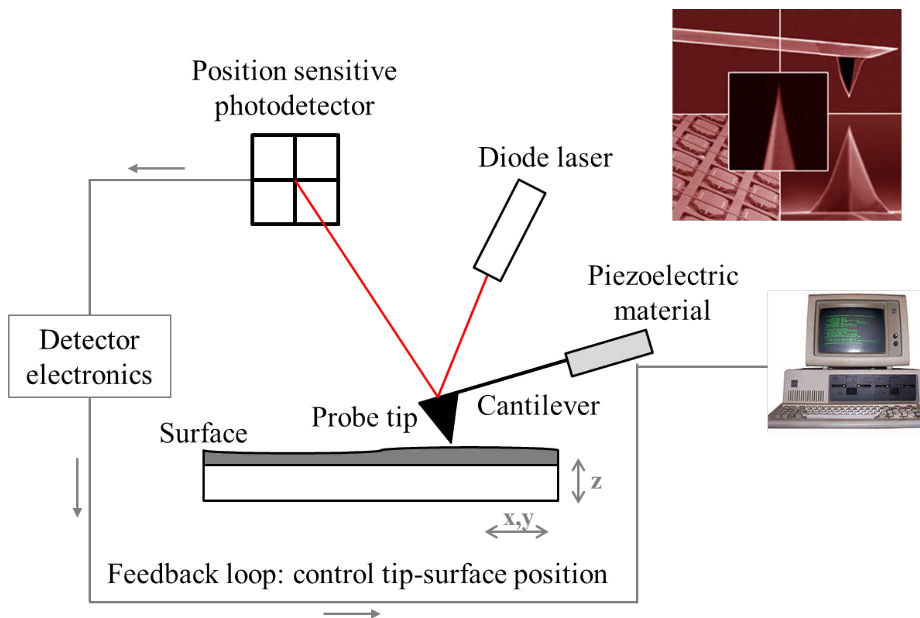

Figure 3.7: Schematic representation of the AFM setup and FESEM image of the used tips.

Among the different measurement modes, the contact mode is based on the interaction between the sample and the tip at distances below 1 $\AA$. The force between the tip and the sample surface is kept constant during the scanning of the area under study by maintaining a constant deflection of the cantilever.

On the other hand, in the tapping mode operation, the probe tip is not in contact with the sample surface. Instead, the tip is oscillating with a fixed frequency at near its resonance, while the amplitude of the oscillation is monitored. Starting from free oscillation amplitude, the tip is approached to the sample until its amplitude is reduced to the set point value, which is selected to reduce the damage to the sample. When the oscillating tip is close enough to the surface (less than 10 nm), Van der Waals interaction (repulsive and attractive forces) between sample atoms and tip atoms arises. Then, the oscillation amplitude is kept at the set point and the z-position is now controlled by the feedback mechanism. The variations of the z-position of the tip during scanning are plotted as a function of the position of the tip on the xy plane to create the surface height image.

In this work, the AFM measurements were performed in the tapping mode with a Veeco Dimension 3100 microscope and probe tips Bruker OTESPA with a resonant frequency of 300$\pm$50 kHz. Data visualization and processing were performed by using the WSxM software [Hor07].

3.1.3 Field emission scanning electron microscopy (FESEM)

In this type of microscopy, the surface of the sample is scanned point by point with a high-energy focused beam of electrons. The interaction between the electrons and the sample produces both secondary and backscattered electrons. The latters, which are more energetic than secondary electrons, are detected leading to the formation of an image which contains information about the surface morphology of the layers. In this study, FESEM images of the cross-section and the surface of the layers have been taken providing information about the type of growth (columnar or compact) while allowing the estimation of the layer thickness and, in turn, the material growth rate.

Two different FESEM equipments were used for taking the images exhibited in this Thesis: a Zeiss Ultra55 Plus microscope and a FEI Nova NanoSEM 230 microscope. Both systems consist of a high resolution in-lens secondary detector which allows high contrast topographic imaging working in both secondary and backscatter modes. Furthermore, they can analyzed non-conductive materials without a previous metallization process.

3.2 Linear optical characterization

In this study, both linear optical transmittance (Tr) and photoluminiscence (PL) measurements are the techniques used in optical characterization of semiconductors. They give information about the band gap energy and its relation with impurities and crystal defects. At the same time, it is possible to estimate both the refractive index and absorption coefficient of the semiconductor from Tr spectra. The knowledge of these optical properties is fundamental for optimizing the material growth process.

3.2.1 Visible/NIR transmittance measurements

Linear optical transmittance measurements provide information about the linear absorption of a semiconductor film, its linear refractive index and the band gap energy. The evolution of light with wavelength λ travelling through an absorptive medium along the x-direction is given by the Lambert-Beer's Law as:

$$I(\lambda, x) = I_0(\lambda) e^{-\alpha(\lambda) x} \tag{3.4}$$

where $I(\lambda, x)$ is the light intensity detected after passing through the sample, $I_0(\lambda)$ is the intensity which enters the sample without considering the input interface, *i.e.*, at x=0, $\alpha_0(\lambda)$ is the absorption coefficient of the sample material and x is the position within the absorptive layer. The transmittance coefficient of the sample with a thickness of L is defined as $Tr(\lambda, L)=I(\lambda, L)/I_0(\lambda)$.

The experimental values of the linear refractive index and linear absorption coefficient used in this Thesis were estimated by fitting the experimental transmittance results by theoretical calculations using the transfer matrix method [Ber99][Nar07]. For energies well below the band gap energy, the extinction coefficient κ can be neglected compared to the real part of the refractive index leading to an scalar refractive index, $\widetilde{n}(\lambda)=\mathrm{n}_0(\lambda)$. First-order Sellmeier dispersion formula was considered for modeling the dependence of the index of refraction as a function of the wavelength within the transparent region as:

$$n_0^2(\lambda) = P + \frac{A_1 \lambda^2}{\lambda^2 - A_2^2} \tag{3.5}$$

where P, A_1 and A_2 are fitting parameters [Bor99].

On the other hand, it is straightforward to estimate the absorption coefficient of the materials through the following relation which neglects the reflection losses at the different interfaces in the sample and light scattering from the surface:

$$\alpha(E)L = -ln[Tr(E)] \tag{3.6}$$

The effective optical band gap energy, $E_{g,opt}$, of the sample under study can be estimated assuming a sigmoidal approximation of the absorption coefficient by:

$$\alpha(E) = \frac{\alpha_0}{1 + e^{\frac{E_{g,opt} - E}{\Delta E}}} \tag{3.7}$$

which takes into account the constant absorption at energies well above the band gap energy, α_0, and also contains information about the absorption band edge broadening, ΔE.

Experimentally, sputtered InN and AlN films have been studied in the spectral range from 350 nm to 1700 nm. In the case of sputtered InN layers, it is possible to completely fit the function $-ln[Tr(E)]$ from absorption region to transparency region and estimate the linear absorption coefficient. Nevertheless, for sputtered AlN films and sapphire substrates, they can be considered non-absorptive in the experimental wavelength range analyzed in the transmittance measurements, *i.e.*, $\alpha_0 \sim \kappa \sim 0$.

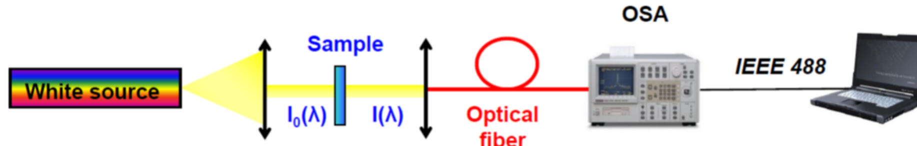

Figure 3.8: Linear optical transmittance setup ranging from 350 nm to 1700 nm [VF11].

Figure 3.8 illustrates the optical transmittance setup in the visible/NIR range used in this work. The light source is a white broadband lamp whose emission is collimated and driven through the sample at normal incidence. The light transmitted by the sample is focused with a 20× magnification microscope objective into a 600-μm-diameter optical fiber connected to an optical spectrum analyzer (OSA). The OSA is provided by two detectors (Si an InGaAs) which allow the light detection in the visible/NIR range from 350 nm to 1700 nm. Performing the measurements with sample and without sample (reference optical signal), the transmittance spectra of the sample under study is obtained by means of a software tool developed by our group. This software processes the experimental data transmitted from the OSA to the computer through GPIB communication protocol.

3.2.2 Photoluminiscence (PL) measurements

This technique is based on the detection of the photon emission from a material which is optically excited. The laser wavelength is chosen so that the excitation energy is higher than the band gap of the material, in order to populate as many energy levels as possible via the electron-hole pairs generation. Photon emission is achieved through radiative recombinations when electron-hole pairs return to equilibrium. The emission energy depends on the difference between the energy levels of the electron and the hole.

The photoluminiscence (PL) spectra provide information not only about intrinsic transitions of the material involving the band gap levels but also about extrinsic transitions which involves doping levels within the band gap. These doping levels mainly appear due to the presence of impurities or crystal defects. Furthermore, the intensity and broadening of the PL peaks can be related to the crystalline quality and homogeneity of the sample. In this sense, high-quality materials present an intense and sharp PL emission. PL measurements as a function of the temperature of the samples also provide information about the thermal activation energy of the involved recombination process. Besides, this technique gives an estimation of the Stoke's shift when comparing the obtained band gap energy from PL with that achieved from Tr spectra at the same temperature.

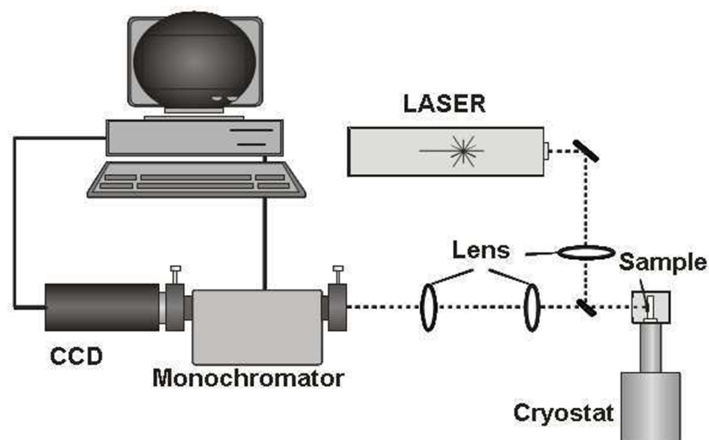

Figure 3.9: Schematic representation of the PL setup [Lah09].

Figure 3.9 illustrates the PL setup used in this work. The excitation source is a power-controlled laser diode ($\lambda = 405$ nm) providing an optical power of 7 mW focused onto a 50-μm-diameter spot. The emission is collected into a 45-cm-focal-length Jobin-Yvon monochromator and detected by a charge-coupled-device (CCD) camera.

Chapter 4

Optical waveguides: Beam propagation, fabrication and optical characterization

This chapter is intended to be a guide for understanding the basis and theoretical concepts of light propagation through optical waveguides. At the same time, information involving the process of design, fabrication and experimental characterization of the different waveguides is also given.

The first part of this chapter focuses on the ray- and wave-approaches of the problem of light guiding in planar waveguides. The second part deals with the different types of optical waveguides depending mainly on the refractive index profile. The basis of the numerical analysis used to solve the distribution of light through the waveguides under study is presented. Furthermore, a brief overview of the waveguide fabrication methods is performed considering both lithography and etching techniques together with facets final processing. Finally, the experiment used for performing the optical characterization of the waveguides is described while the experimental measurement protocol is detailed.

4.1 Introduction to modal guiding in planar waveguides

In this first section of the chapter, we describe the two main analytic treatments of the light propagation problem in planar waveguides. It is a general overview of the problem considering both the model of ray-optics and the wave approach. The theoretical treatment is based mainly on several high-quality books in general photonics, optics and guided-optics fields [Sal91][Kas01][Iiz02][Agr04][Kaw04][Liu05].

4.1.1 Geometric optics: Ray approach

Optical waveguiding devices are the basic elements for confinement and transmission of light. Among them, optical fibers allow light transmission in a macroscopic distance scale up to thousands of kilometers while integrated optical waveguides (WG) transmit light in a microscopic scale up to few millimeters. Both types of waveguides can be partially described by a geometric optics approach.

Geometric optics describes the propagation of light rays through an optical system. The basic concept of optical modal guiding is quite simple: a medium of a determined refractive index embedded in a medium of lower refractive index acts as a light "trap" within which optical rays remain confined by multiple total internal reflections (TIR) at the boundaries. The Snell's Law given by Eq. 4.1 describes the relation between the incident and refracted or transmitted ray paths when passing through a boundary between two isotropic media with different refractive index, n_1 (medium 1) and n_2 (medium 2):

$$n_1 \, sin(\theta_i) = n_2 \, sin(\theta_t) \tag{4.1}$$

where θ_i and θ_t are the angles of the incident and the transmitted (refracted) rays, respectively, with respect to the normal of the media interface (see Fig. 4.1). It has to be noticed that the refractive indices dependence on the light frequency has been removed for simplicity.

Thus, if $n_1 > n_2 \Rightarrow \theta_i < \theta_t$, hence, there is an incident angle for light traveling through medium 1 called the critical angle (θ_c) which leads to light transmission through the interface of both considered media, *i.e.*, $\theta_t = \pi/2$, preventing the reflected beam and

the transmitted light into medium 2 [see Fig. 4.1(a)]. In the case of incident angles lower than the critical one ($\theta_i < \theta_c$), incident light is divided into a transmitted and a reflected rays when reaching the media interface as indicated in Fig. 4.1(b). On the other hand, for higher angles than the critical one ($\theta_i > \theta_c$), TIR is reached showing no transmitted ray from medium 1 to medium 2 and leading to the completely reflection of light [see Fig. 4.1(c)].

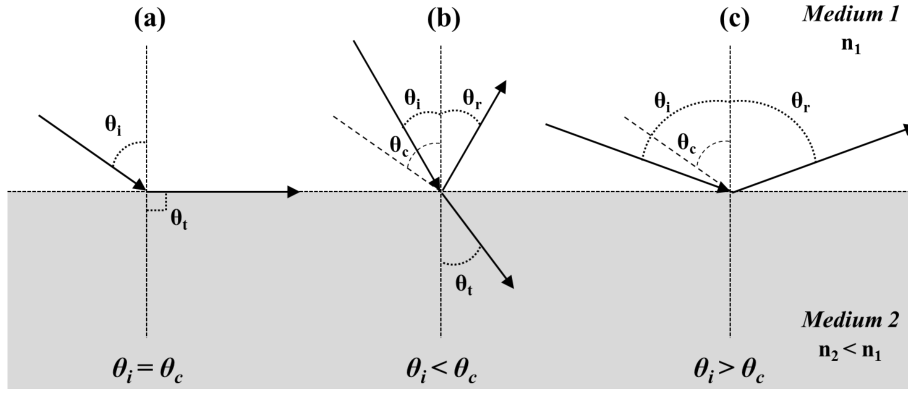

Figure 4.1: Schemes of the behavior of an incident ray which travels from a certain medium (n_1) to another with lower refractive index ($n_2 < n_1$) as a function of the angle of incidence: (a) $\theta_i = \theta_c$, (b) $\theta_i < \theta_c$ and (c) $\theta_i > \theta_c$.

The simplest way to fabricate a waveguide is by using planar structures. An asymmetric three-layer-structured waveguide consisted of substrate (n_2)/guiding-layer (n_1)/cover (n_3) is presented in Fig. 4.2, as an example. Often, air is considered as the cover layer. It is considered that this waveguide does not present any losses due to absorbance or light scattering. Light guidance can exist when the refractive index of the guiding layer is higher than those corresponding to the substrate and the cover. Furthermore, light must reach the boundary of both media with an angle (θ) higher than the critical in both guiding-layer/substrate (θ_{c2}) and guiding-layer/cover (θ_{c3}) interfaces.

$$\theta_{c2} = arcsin\left(\frac{n_2}{n_1}\right) \qquad \theta_{c3} = arcsin\left(\frac{n_3}{n_1}\right) \tag{4.2}$$

Another basic concept within guided-optics is the acceptance angle. Considering the scheme of the asymmetric waveguide in Fig. 4.2, there is a maximum angle of a ray impinging on the guiding layer (related to the waveguide axis) called the acceptance

angle (θ_a) which allows the incident light to be guided through the guiding layer. Light injected with angles higher than the acceptance angle will be lost through radiation effects through the substrate and the cover. When injected light at the acceptance angle, the transmitted ray presents an angle ($\pi/2 - \theta_c$). Thus, applying the Snell's Law, θ_a is given by

$$\theta_a = arcsin\left(\frac{1}{n_0}\sqrt{n_1^2 - n_2^2}\right) \tag{4.3}$$

where n_0 is the refractive index of the outside medium and the TIR is studied between the guiding layer (n_1) and the substrate (n_2) in the asymmetric planar waveguide. According to this, the numerical aperture (NA) is a commonly-given parameter in optical waveguides, mainly in optical fibers, which is related to the acceptance angle as follows:

$$NA = n_0 sin\theta_a = \sqrt{n_1^2 - n_2^2} \tag{4.4}$$

A monochromatic plane wave with optical frequency f is considered to be propagated along the guiding-layer (n_1). When a monochromatic wave propagates through media of different refractive indices, its frequency remains the same ($\omega = 2\pi f$), but its velocity (v), wavelength (λ) and wavenumber (k) are altered. In the case of a light ray propagating along the longitudinal direction through the i-layer within the system, its wavevector is given by $\mathbf{k}_i = n_i\mathbf{k}_0$ where k_0 is the wavenumber of light in free space ($k_0 = \frac{2\pi}{\lambda}$) and it coincides with the optical ray direction. The wavelength of the light is also modified when propagating through a medium different from vacuum being $\lambda_i = \frac{\lambda}{n_i}$, where λ is the wavelength of light in free space. Besides, the phase velocity of the light through the medium is $v_i = \frac{\omega}{k_i} = \frac{c}{n_i}$.
It has to be noticed that a light ray (or wave) is totally defined by the light propagation constant (β) which corresponds to the z-component of the wavevector as illustrated in Fig. 4.2. Hence, the value through the guiding-layer is $\beta = k_0 n_1 sin\theta$. The phase that a plane wave accumulates during its propagation is $\phi = \mathbf{kr}$ and an additional phase shift is induced when light is reflected by a medium. This latter phase shift depends on the polarization of the light.

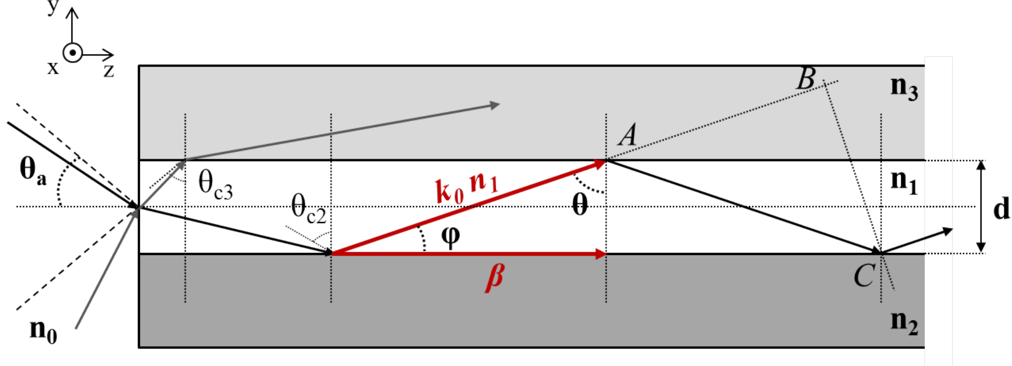

Figure 4.2: Geometry of an asymmetric planar waveguide consisted of substrate (n_2), guiding-layer (n_1) and cover (n_3). The refractive indices follow the relation: $n_1 > n_2 > n_3$. (Red) Relationship between the light wavevector and the propagation constant.

It has to be pointed out that only certain internal reflection angles (θ) are susceptible to be guided. An additional requirement must be followed by the optical ray: the self-consistency condition (Eq. 4.5). According to the self-consistency condition, the wave must reproduce itself after two consecutive reflections. Taking into account the path of the ray propagating through the guiding layer in Fig. 4.2, the phase shift produced between A and B and that produced between A and C must be an integer (m) multiple of 2π in order to achieve constructive propagation along the z-direction:

$$\frac{2\pi}{\lambda} n_1\, 2d cos\theta = \varphi_2(\theta) + \varphi_3(\theta) + m2\pi \tag{4.5}$$

where the term on the left describes the phase shift due to the difference in travelled path way between $\overline{AC}$ and $\overline{AB}$, and $\varphi_2(\theta)$ and $\varphi_3(\theta)$ are the phase shifts associated with the internal reflections of light at the lower and upper interfaces, respectively. From this resonance condition, only certain discrete values of the incident angle are allowed, θ_m, resulting in discrete values of the propagation constant, β_m. The fundamental mode is given by $m = 0$ and corresponds to the highest value of β (β_0). All of the $m > 0$ lead to high-order modes.

On the other hand, additionally to the guided modes in the waveguide, substrate radiation modes can exist if TIR only occurs at its upper interface but not at the lower interface ($\theta_{c2} > \theta > \theta_{c3}$). At the same time, radiation modes can exist at both substrate and cover layers when $\theta_{c2} > \theta_{c3} > \theta$. Substrate and cover radiation modes are associated with real values of β belonging to a continuum range between the limits indicated by both critical angles.

In addition, there are also evanescent radiation modes which suffer an exponential decay of the intensity along the z- direction since these modes are associated to non-discrete pure imaginary values of β.

In summary, in geometric optics, a waveguide mode is associated to a discrete value of the light propagation constant along the waveguide. Thus, an effective refractive index can be associated to a propagating optical mode through the guiding-layer being defined as:

$$n_{eff} = \frac{\beta}{k_0} = n_1 sin\theta \tag{4.6}$$

This modal n_{eff} will be included in the range between the refractive index of the guiding-layer and that corresponding to the covering medium which presents the highest refractive index (typically the substrate since the cover is usually air). The existence of a series of solutions (modes) which follow the self-consistency condition does not imply the propagation of all of them through the waveguide and neither with the same power since it depends on the coupling of the light into the waveguide.

When the thickness of the guiding layer (d) is much larger than the light wavelength (λ), diffraction effects can be neglected and the problem can be studied in an intuitive and visual way through geometric optics as briefly discussed up to now. Nevertheless, when $d \approx \lambda$ the investigation of the waveguide modes based on the theory of electromagnetic optics is also needed by solving the Maxwell's equations.

4.1.2 Electromagnetic description: Wave equation. Matrix formalism

As all electromagnetic processes, propagation of light in a waveguide is governed by the Maxwell's equations which characterize both the space- and time-dependence of the electromagnetic field in a certain medium. Optical modes refer to specific solutions of the Maxwell's equations satisfying the boundary conditions and maintaining their spatial distribution and polarization with propagation along the waveguide axis. It has to be pointed out that the structures investigated during this work are considered

to be non-conductive leading to negligible current densities and free charges, $\mathbf{J}$=0 and ρ=0. In this case, the Maxwell's equations can be written as:

$$\nabla\cdot\mathbf{D} = 0 \tag{4.7}$$

$$\nabla\cdot\mathbf{B} = 0 \tag{4.8}$$

$$\nabla\times\mathbf{E} = -\frac{\partial\mathbf{B}}{\partial t} \tag{4.9}$$

$$\nabla\times\mathbf{H} = \frac{\partial\mathbf{D}}{\partial t} \tag{4.10}$$

where $\mathbf{D}$ is the electric displacement field, $\mathbf{E}$ is the electric field, $\mathbf{B}$ is the magnetic induction and $\mathbf{H}$ is the magnetic field. $\mathbf{E}$ and $\mathbf{H}$ are fundamental microscopic fields while $\mathbf{D}$ and $\mathbf{H}$ are macroscopic fields that include the response of the medium to an electromagnetic excitation. Actually, these four fields are related to one another through the constitutive relations which take into account the polarization, $\mathbf{P}$, and magnetization, $\mathbf{M}$, generated in the medium by the response to the electric and magnetic fields, respectively.

$$\mathbf{D} = \epsilon_0\mathbf{E} + \mathbf{P} \tag{4.11}$$

$$\mathbf{B} = \mu_0\mathbf{H} + \mathbf{M} \tag{4.12}$$

where $\epsilon_0 = 8.85 \times 10^{-12}\ Fm^{-1}$ and $\mu_0 = 4\pi \times 10^{-7}\ Hm^{-1}$ are the permittivity and the permeability of free space, respectively. Due to the non-magnetic nature of the materials under study, magnetization can be assumed as zero and, thus, $\mathbf{B}$=$\mu_0\mathbf{H}$. Nevertheless, the spatial and temporal relation between $\mathbf{P}(\mathbf{r},t)$ and $\mathbf{E}(\mathbf{r},t)$ is characterized by the electric susceptibility tensor, $\tilde{\chi}$, through the following equation:

$$\mathbf{P}(\mathbf{r},t) = \epsilon_0 \int_{-\infty}^{+\infty} \tilde{\chi}(\mathbf{r}, t-t') \cdot \mathbf{E}(\mathbf{r}, t')\, dt' \tag{4.13}$$

Since the response of a medium to an external electric field is not instantaneous, the polarization response at a given time t, $\mathbf{P}(t)$, is the superposition of the effects of $\mathbf{E}(t')$ at any previous time $t' \leq t$. Mathematically, this delay is represented by the convolution of the parameter which gives information of the medium response ($\tilde{\chi}$) with the external electric field.

By means of the Fourier transform, the polarization and the excitation field can be translated from the time domain to the frequency domain leading to the following expression of $\mathbf{P}$:

$$\mathbf{P}(\mathbf{r},\omega) = \epsilon_0 \tilde{\chi}(\mathbf{r},\omega)\mathbf{E}(\mathbf{r},\omega) \tag{4.14}$$

Consequently, considering Eq. 4.11, the electric displacement field can be written in the frequency domain as

$$\mathbf{D}(\mathbf{r},\omega) = \epsilon_0[1+\tilde{\chi}(\mathbf{r},\omega)]\mathbf{E}(\mathbf{r},\omega) = \tilde{\epsilon}(\mathbf{r},\omega)\mathbf{E}(\mathbf{r},\omega) \tag{4.15}$$

where $\tilde{\epsilon}(\mathbf{r},\omega)$ is the electric permittivity of the medium. From now on, the frequency and spatial dependence of the variables and the tilde over them indicating their tensor nature are avoided for simplicity. The relative permittivity or dielectric constant, ϵ_r, relates the permittivity of the medium and that corresponding to the free space by the following equation:

$$\epsilon_r = \frac{\epsilon}{\epsilon_0} = 1 + \chi \tag{4.16}$$

Besides, the refractive index of the medium is related to the relative permittivity through $n = \sqrt{\epsilon_r}$. In general, for media with losses or gain, the relative electric permittivity is complex $\epsilon_r = \epsilon_r{}' + j\epsilon_r{}''$ (see Eq. 4.17). Hence, Eq. 4.18 indicates the relation between the real and imaginary parts of both the permittivity and the index of refraction. The extinction coefficient, κ, gives information about the absorption coefficient of the medium, α, by means of $\alpha = \dfrac{4\pi\kappa}{\lambda}$.

$$n^2 = (n' + j\kappa)^2 = \epsilon_r{}' + j\epsilon_r{}'' \tag{4.17}$$

$$\begin{aligned} \epsilon_r{}' &= n'^2 - \kappa^2 \\ \epsilon_r{}'' &= 2n'\kappa \end{aligned} \tag{4.18}$$

The electric susceptibility and, consequently, the electric permittivity are parameters which characterize the optical behavior of a material when responding to an electromagnetic excitation. Thus, if the medium is isotropic, $\tilde{\chi}$ and $\tilde{\epsilon}$ are scalar as $\tilde{\chi} = \chi$ and $\tilde{\epsilon} = \epsilon$. Nevertheless, for anisotropic media (like many crystals treated in this work), $\tilde{\chi}$ and, in turn, $\tilde{\epsilon}$ are tensors being both vector $\mathbf{P}$ and $\mathbf{D}$ not parallel to $\mathbf{E}$. Taking into account the spatial or temporal homogeneity of the

material, all optical structures present spatial inhomogenities which varies the electric permittivity and, consequently, the refractive index with the material point position. In optical waveguides, this parameter variation makes possible the confinement of the light along the guiding material. Thus, both the electric susceptibility and permittivity depend on the position, $\chi(\mathbf{r})$ and $\epsilon(\mathbf{r})$. Furthermore, it is possible to deal with nonlinear materials in which optical parameters depend on the electric field magnitude, $\chi = \chi(\mathbf{E})$ and $\epsilon = \epsilon(\mathbf{E})$. On the other hand, when the medium of propagation is dispersive, the optical parameters depend on the frequency of the propagating light, *i.e.*, $\chi = \chi(\omega)$ and $\epsilon = \epsilon(\omega)$.

4.1.2.1 Wave equation

A simple way to calculate the optical modes is to assume a monochromatic wave in which the electric and magnetic fields vary with time as $e^{-j\omega t}$

$$\begin{aligned} \mathbf{E}(\mathbf{r},t) &= \mathbf{E}(\mathbf{r})e^{-j\omega t} + c.c. \\ \mathbf{H}(\mathbf{r},t) &= \mathbf{H}(\mathbf{r})e^{-j\omega t} + \; c.c. \end{aligned} \tag{4.19}$$

It is assumed in this work that the waveguide structure is infinite and invariant along the z-direction, thus, the optical modes propagating through it will vary with the z-coordinate as $e^{j\beta z}$.

The electric and magnetic fields can be expressed by means of the transverse fields together with the evolution of propagation along z and the temporal dependence:

$$\begin{aligned} \mathbf{E}(\mathbf{r},t) &= \mathbf{e}(x,y)e^{j\beta z}e^{-j\omega t} \\ \mathbf{H}(\mathbf{r},t) &= \mathbf{h}(x,y)e^{j\beta z}e^{-j\omega t} \end{aligned} \tag{4.20}$$

Taking into account the format of the electromagnetic field and that $c = \dfrac{1}{\sqrt{\epsilon_0\mu_0}}$, $\omega = k_0 c$, $k_0 = \dfrac{2\pi}{\lambda}$ and that the impedance of the vacuum is given by $Z_0 = \sqrt{\dfrac{\mu_0}{\epsilon_0}}$,

Eqs. 4.9 and 4.10 can be rewritten as

$$\nabla \times \mathbf{E} = jZ_0k_0\mathbf{H} \tag{4.21}$$

$$\nabla\times\mathbf{H} = -j\frac{k_0n^2}{Z_0}\mathbf{E} \tag{4.22}$$

by using the constitutive relation given by Eq. 4.15.

For simplicity, a general study of the behavior of the electromagnetic field propagating through a linear, isotropic and dielectric planar waveguide is presented here. It is assumed that the structure under study can be divided in several sandwiched homogeneous substructures each with its own constant refractive index, n_i, and different thickness, d_i, for $i = [1, 2, ...N - 1]$ where n_0 is the refractive index of the substrate and n_N corresponds to that of the surrounding air. It has to be pointed out that the planar waveguide is considered to be infinite along the x-direction and, hence, the electric and magnetic fields do not present any dependence with the x-variable. Thus, the x-derivatives can be removed. A scheme of the structure of the infinitely planar waveguide is shown in Fig. 4.3.

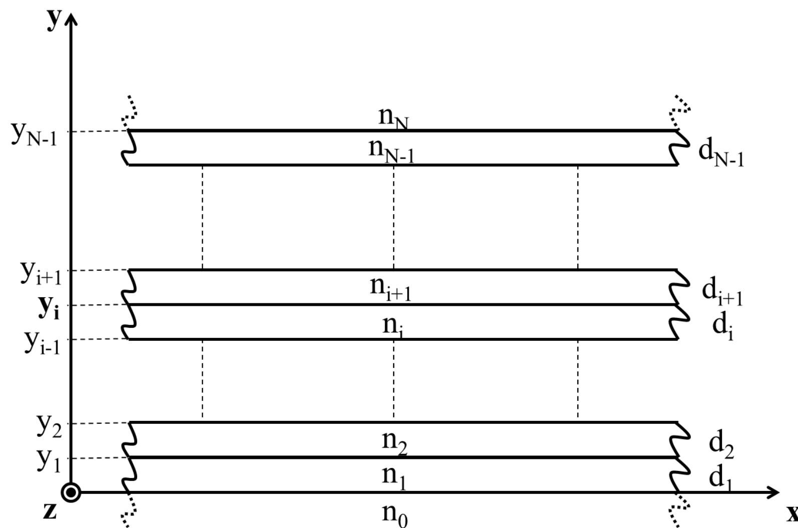

Figure 4.3: Scheme of the planar waveguide infinitely extended along the x- and z-direction.

Considering that the optical fields in the waveguide have the form of Eq. 4.20 and also the fields x-variable-independence ($\partial/\partial x = 0$), Maxwell's equations can be written as:

$$\begin{array}{c||c}
\frac{dE_z}{dy} - j\beta E_y = jZ_0k_0H_x & \frac{dH_z}{dy} - j\beta H_y = -jk_0\frac{n^2}{Z_0}E_x \\
j\beta E_x = jZ_0k_0H_y & j\beta H_x = -jk_0\frac{n^2}{Z_0}E_y \\
-\frac{dE_x}{dy} = jZ_0k_0H_z & -\frac{dH_x}{dy} = jk_0\frac{n^2}{Z_0}E_z
\end{array} \tag{4.23}$$

Hence, from Eq. 4.23, the transverse components of the electric and magnetic fields in this study can be expressed in terms of the longitudinal components as:

$$\begin{aligned}
E_x &= \frac{jk_0Z_0}{k_0^2n_i^2 - \beta^2}\frac{dH_z}{dy} \\
E_y &= \frac{j\beta}{k_0^2n_i^2 - \beta^2}\frac{dE_z}{dy} \\
H_x &= \frac{jk_0n_i^2}{Z_0(k_0^2n_i^2 - \beta^2)}\frac{dE_z}{dy} \\
H_y &= \frac{j\beta}{k_0^2n_i^2 - \beta^2}\frac{dH_z}{dy}
\end{aligned} \tag{4.24}$$

Therefore, in a waveguide, once the longitudinal field components, E_z and H_z, are known, all field components can be obtained. The common approach to find the longitudinal field components is to solve the wave equations together with boundary conditions. First of all, the wave equation for the electric field through the region i is obtained by taking the curl of Eq. 4.21 and using Eq. 4.22.

$$\nabla \times \nabla \times \mathbf{E} = k_0n_i^2\mathbf{E} \tag{4.25}$$

The left part of the equation above can be modified by means of the vector identity $\nabla \times \nabla \times \mathbf{E} = -\nabla^2\mathbf{E} + \nabla(\nabla\mathbf{E})$. Taking into account that $\nabla \cdot \mathbf{D} = \nabla \cdot (\epsilon\mathbf{E}) = 0$ and assuming that the considered substructures are spatially homogeneous, *i.e.*, $\nabla\epsilon = 0$, the wave equations for $\mathbf{E}$ and $\mathbf{H}$ in each homogeneous region are given by

$$\begin{aligned} \nabla^2\mathbf{E} + (k_0^2 n_i^2 - \beta^2)\mathbf{E} = 0 \\ \nabla^2\mathbf{H} + (k_0^2 n_i^2 - \beta^2)\mathbf{H} = 0 \end{aligned} \tag{4.26}$$

The solutions of the wave equations must satisfy the boundary conditions at each interface between two consecutive regions (i and $i{+}1$). At this point, for the case of dielectric media, Eqs. 4.27–4.30 must be obeyed, where the two firsts relations (Eqs. 4.27–4.28) represent the continuity of the normal components of, respectively, the magnetic induction and electric displacement fields at the interface considering media free of any charges. At the same time, Eqs. 4.29 and 4.30 indicate the continuity of the tangential components of the magnetic and the electric field, respectively, due to the absence of currents at the interface between consecutive regions.

$$\widehat{\mathbf{n}}(\mathbf{B}_{i+1} - \mathbf{B}_i) = 0 \tag{4.27}$$

$$\widehat{\mathbf{n}}(\mathbf{D}_{i+1} - \mathbf{D}_i) = 0 \tag{4.28}$$

$$\widehat{\mathbf{n}} \times (\mathbf{H}_{i+1} - \mathbf{H}_i) = 0 \tag{4.29}$$

$$\widehat{\mathbf{n}} \times (\mathbf{E}_{i+1} - \mathbf{E}_i) = 0 \tag{4.30}$$

where $\widehat{\mathbf{n}}$ is the unit vector perpendicular to the interface.

Finally, the expressions for the longitudinal components of $\mathbf{E}$ and $\mathbf{H}$ are obtained by solving the wave equation:

$$\left\{\frac{d^2}{dy^2} + k_0^2 n_i^2 - \beta^2\right\} \begin{bmatrix} E_z \\ H_z \end{bmatrix} = 0 \tag{4.31}$$

The Poynting vector defined as $\mathbf{S} = \mathbf{E} \times \mathbf{H}$ represents the direction of the power flow of the electromagnetic field. The magnitude of this flux is given by the module of $\mathbf{S}$.

Nevertheless, most of times it is useful to know the light intensity I that the wave carries. The intensity is obtained through the module of the time-averaged Poynting vector as:

$$I = |\overline{S}| = \frac{1}{T}\int_0^T |\mathbf{E} \times \mathbf{H}| dt \tag{4.32}$$

4.1.2.2 Light polarizations: TE and TM cases

In this type of dielectric structures, two different sets of linearly polarized modes can propagate along the waveguide: the transverse electric (TE) and transverse magnetic (TM) modes. TE-light is characterized by the absence of the longitudinal component of the electric field, $E_z = 0$. Considering Eqs. 4.24, TE polarized light entails zero-components of the electromagnetic field as $E_y = 0$ and $H_x = 0$. In turn, TM-light does not present the longitudinal component of the magnetic field, $H_z = 0$ leading to components $E_x = 0$ and $H_y = 0$. This formalism describes the TM-mode propagation when the electric field only vibrates parallel to the growth axis, *i.e.*, within the *(y,z)* plane, while TE-light corresponds to the electric field vibrating perpendicular to the growth axis, *i.e.*, within the *(x,z)* plane.

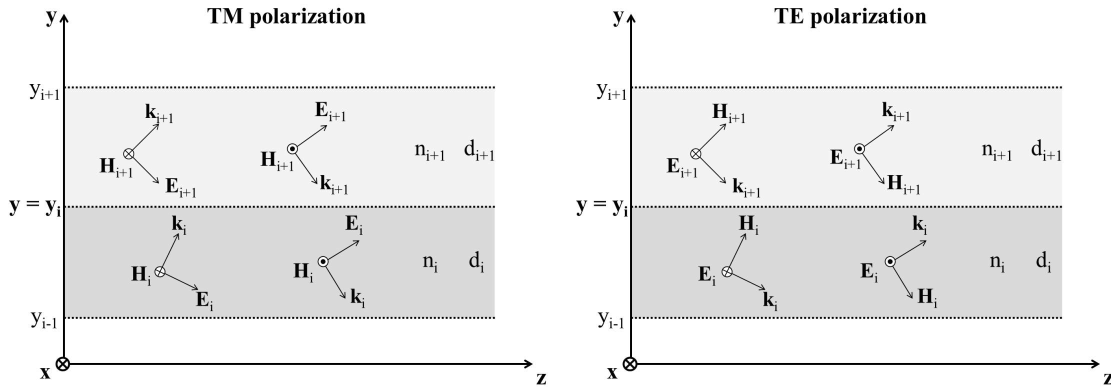

Figure 4.4: Schemes of the electric and magnetic fields in the case of TM- and TE-polarized light propagating along the positive direction of z-axis.

This subsection deals with the case of propagation of TE- and TM-polarized waves through the waveguide. Beginning with the TM-light case, and using the cartesian nomenclature, the magnetic field vector presents the following format $\mathbf{H} = (H_x, 0, 0)$

and the electric field is like $\mathbf{E} = (0, E_y, E_z)$. Hence, considering the i region, the wave equation adapted from Eq. 4.31 is given by:

$$\left\{\frac{d^2}{dy^2} - \chi_i^2\right\} E_z^i(y) = 0, \quad y_{i-1} < y < y_i \tag{4.33}$$

where $\chi_i = \sqrt{\beta^2 - k_0^2 n_i^2}$.

The general solution of this wave equation in the i-layer is represented by the sum of a forward and a backward propagating electric field through the y-transverse direction:

$$E_z^i(y) = A_1^i e^{\chi_i(y-y_i)} + A_2^i e^{-\chi_i(y-y_i)} \tag{4.34}$$

where A_1^i an A_2^i are constant parameters which represents the field amplitude in the medium i. Once the general equation is known for the longitudinal component of the electric field, it is straightforward from Eqs. 4.24 to express the general solution for the non-zero components, *i.e.*, $E_y^i(y)$ and $H_x^i(y)$:

$$E_y^i(y) = -\gamma_i \left\{ A_1^i e^{\chi_i(y-y_i)} - A_2^i e^{-\chi_i(y-y_i)} \right\} \tag{4.35}$$

$$H_x^i(y) = -\gamma_i' \left\{ A_1^i e^{\chi_i(y-y_i)} - A_2^i e^{-\chi_i(y-y_i)} \right\} \tag{4.36}$$

The two new constants $\gamma_i = j\frac{\beta}{\chi_i}$ and $\gamma_i' = j\frac{k_0 n_i^2}{Z_0 \chi_i}$ are introduced in order to simplify the notation. Thus, the y- and z-dependent electric and magnetic fields for TM polarization are given by:

$$E_{TM}^i(y,z) = \left\{ A_1^i \begin{bmatrix} 0 \\ -\gamma_i \\ 1 \end{bmatrix} e^{\chi_i(y-y_i)} + A_2^i \begin{bmatrix} 0 \\ \gamma_i \\ 1 \end{bmatrix} e^{-\chi_i(y-y_i)} \right\} e^{j\beta z} \tag{4.37}$$

$$H_{TM}^i(y,z) = \left\{ A_1^i \begin{bmatrix} -\gamma_i' \\ 0 \\ 0 \end{bmatrix} e^{\chi_i(y-y_i)} + A_2^i \begin{bmatrix} \gamma_i' \\ 0 \\ 0 \end{bmatrix} e^{-\chi_i(y-y_i)} \right\} e^{j\beta z} \tag{4.38}$$

Similarly to the solution of the case of TM polarized light, the same procedure can be followed for TE light in order to obtain the solution of the associated electric and magnetic fields (recalling that $\mathbf{E} = (E_x, 0, 0)$ and $\mathbf{H} = (0, H_y, H_z)$, respectively). The wave equation to solve is the following:

$$\left\{\frac{d^2}{dy^2} - \chi_i^2\right\} H_z^i(y) = 0, \quad y_{i-1} < y < y_i \tag{4.39}$$

Considering a similar general solution for $H_z^i(y)$ as the used for $E_z^i(y)$ in Eq. 4.34, the electric and magnetic field expressions for TE light polarization are given by:

$$E_{TE}^i(y,z) = \left\{ A_1^i \begin{bmatrix} -\gamma_i'' \\ 0 \\ 0 \end{bmatrix} e^{\chi_i(y-y_i)} + A_2^i \begin{bmatrix} \gamma_i'' \\ 0 \\ 0 \end{bmatrix} e^{-\chi_i(y-y_i)} \right\} e^{j\beta z} \tag{4.40}$$

$$H_{TE}^i(y,z) = \left\{ A_1^i \begin{bmatrix} 0 \\ -\gamma_i \\ 1 \end{bmatrix} e^{\chi_i(y-y_i)} + A_2^i \begin{bmatrix} 0 \\ \gamma_i \\ 1 \end{bmatrix} e^{-\chi_i(y-y_i)} \right\} e^{j\beta z} \tag{4.41}$$

where $\gamma_i'' = j\dfrac{k_0 Z_0}{\chi_i}$ for simplifying the notation.

As χ_i includes a square root that can be complex, it is considered that when χ_i is pure imaginary, the exponential terms with positive sign represent waves propagating along the negative direction of the y-axis. Contrarily, negative exponential terms are related to waves propagating along the positive direction of the y-axis. The obtained solutions must follow the boundary conditions at the interface between consecutive media ($y = y_i$) given by Eqs. 4.27–4.30. The continuity of the tangential components of the electric and magnetic fields are imposed for each light polarization (see Fig. 4.4) as follows:

$$TM \Longrightarrow \begin{cases} E_z^i(y_i) = E_z^{i+1}(y_i) \\ H_x^i(y_i) = H_x^{i+1}(y_i) \end{cases} \quad 0 \le i \le N-1 \tag{4.42}$$

$$TE \Longrightarrow \begin{cases} E_x^i(y_i) = E_x^{i+1}(y_i) \\ H_z^i(y_i) = H_z^{i+1}(y_i) \end{cases} \qquad 0 \leq i \leq N-1 \tag{4.43}$$

The relation between the field amplitudes at the interface y_i of two close layers can be expressed in a matrix formalism as [Ane99][Est06]:

$$\begin{bmatrix} A_1^i \\ A_2^i \end{bmatrix} = P(i)\, T(i, i+1) \begin{bmatrix} A_1^{i+1} \\ A_2^{i+1} \end{bmatrix} \tag{4.44}$$

$$P(i) = \begin{bmatrix} e^{\chi_i d_i} & 0 \\ 0 & e^{-\chi_i d_i} \end{bmatrix} \tag{4.45}$$

where $P(i)$ contains information about the transverse field propagation through the i-layer between y_{i-1} and y_i interfaces. Thus, the thickness of the i-layer, d_i, is given by $d_i = y_i - y_{i-1}$. On the other hand, matrix $T(i, i+1)$ transmits the field between consecutive layers through the interface positioned at y_i. The transfer matrix $T(i, i+1)$ is obtained through the continuity of the tangential components of **E** and **H** at $y = y_i$. Particularly, for TM light, Eqs. 4.42 turn into the two following relations:

$$\begin{aligned} A_1^i + A_2^i &= A_1^{i+1} + A_2^{i+1} \\ \frac{n_i^2}{\chi_i}\left(A_2^i - A_1^i\right) &= \frac{n_{i+1}^2}{\chi_{i+1}}\left(A_2^{i+1} - A_1^{i+1}\right) \end{aligned} \tag{4.46}$$

And in the case of TE light, Eqs. 4.43 can be written as:

$$\begin{aligned} A_1^i + A_2^i &= A_1^{i+1} + A_2^{i+1} \\ \frac{1}{\chi_i}\left(A_2^i - A_1^i\right) &= \frac{1}{\chi_{i+1}}\left(A_2^{i+1} - A_1^{i+1}\right) \end{aligned} \tag{4.47}$$

Solving these two equation systems above, the transfer matrix between the i- and $i{+}1$-layers is given by

$$T(i, i+1) = \frac{1}{2} \begin{bmatrix} 1 + \xi_i \dfrac{\chi_i}{\chi_{i+1}} & 1 - \xi_i \dfrac{\chi_i}{\chi_{i+1}} \\ \\ 1 - \xi_i \dfrac{\chi_i}{\chi_{i+1}} & 1 + \xi_i \dfrac{\chi_i}{\chi_{i+1}} \end{bmatrix} \tag{4.48}$$

where $i = [0, 1, ..., N-1]$ and ξ_i is a constant which takes different values for TE and TM. In the case of TE-polarized light, $\xi_{i,TE} = 1$ and for TM light $\xi_{i,TM} = \dfrac{n_{i+1}^2}{n_i^2}$.

Extending this methodology to the whole multilayer structure, the relation between the amplitude of the field in the N-layer (cover) and in the *0*-layer (substrate) can be expressed by

$$\begin{bmatrix} A_1^0 \\ \\ A_2^0 \end{bmatrix} = \prod_{i=0}^{i=N-1} P(i)\, T(i, i+1) \begin{bmatrix} A_1^N \\ \\ A_2^N \end{bmatrix} \tag{4.49}$$

The result of the product of the propagation and transmission matrices can be expressed by the matrix M_κ which is defined by

$$M_\kappa \equiv \begin{bmatrix} m_{11} & m_{12} \\ \\ m_{21} & m_{22} \end{bmatrix} = \prod_{i=0}^{i=N-1} P(i)\, T_\kappa(i, i+1) \tag{4.50}$$

being different depending on the light polarization under study (κ =TE or TM).

The matrix M_κ is especially useful for describing the different light modes which can be supported by the structure, *i.e.*, guided, radiation and evanescent modes, depending on the components format of the matrix. Nevertheless, this work is focused on the modal guiding, hence, just the formalism for guided modes will be detailed.

4.1.2.3 Guided modes

Optically guided modes are characterized by the evanescent behavior of the electromagnetic fields through the outer media of the structure, *i.e.*, at the *0*- and N-layers (substrate and cover, respectively). Thus, in the case of TE-light, it has to be imposed the following conditions to the electric field in the N- and *0*-layers:

$$E_{TE}^{N}(y) \propto e^{-\chi_N (y-y_N)} \rightarrow 0 \qquad for \;\; y \rightarrow \infty \tag{4.51}$$

$$E_{TE}^{0}(y) \propto e^{\chi_0 (y-y_0)} \rightarrow 0 \qquad for \;\; y \rightarrow -\infty \tag{4.52}$$

Hence, considering the field solution given by Eq. 4.40, both A_1^N and A_2^0 amplitudes must be zero. At this point, the matrix M_{TE} must achieve that $m_{22} = 0$ for obtaining a non-trivial solution for the electric field. The same result is reached in the case of TM-light where the magnetic field behaves as given by Eq. 4.38 and both amplitudes A_1^N and A_2^0 must also be zero to fulfill the evanescent behavior of the light at the cover and substrate layers.

Thus, the matrix M_κ for optical guided modes contains a null component m_{22} for both polarizations. The amplitude relation presents the following aspect:

$$\begin{bmatrix} A_1^0 \\ 0 \end{bmatrix} = \begin{bmatrix} m_{11} & m_{12} \\ m_{21} & 0 \end{bmatrix}_\kappa \begin{bmatrix} 0 \\ A_2^N \end{bmatrix} \tag{4.53}$$

Taking into account the relation between amplitudes presented above and the definition of χ_i as

$$\chi_i = \sqrt{\beta^2 - k_0^2 n_i^2} = \beta \sqrt{1 - \frac{n_i^2}{n_{eff}^2}} \tag{4.54}$$

the condition of modal guiding through the waveguide only is reached for a discrete set of values of n_{eff} contained in the range $n_i > n_{eff} > n_0$. When $n_{eff} > n_N$ and $n_{eff} > n_0$ occurs simultaneously, the fields in the cover and the substrate are evanescent.

4.2 Optical waveguide types

Once the planar waveguides have been described obtaining analytic solutions for their guided modes, it has to be noticed that this type of structures only confines light in one direction. Waveguides presenting planar geometry are interesting and easy to solve but they are not efficient guides since their lateral dimension is infinite and light is diffracted along that direction. In practice, most device applications require the confinement of light in both transverse dimensions (x, y). Thus, it is necessary to use a different geometry of waveguides such as nonplanar waveguides which present an index profile $n(x, y)$ depending on both transverse coordinates. The two main groups of nonplanar waveguides are the optical fibers and, on the other hand, the rectangular waveguides. Nevertheless, a clear disadvantage emerges when analyzing modal propagation in nonplanar structures compared to planar ones. It is only possible to reach analytic solutions of the wave equation for a limited number of cases which present easy geometries such as cylindrical symmetry. Hence, numerical methods such as the beam propagation method (BPM), finite element method (FEM) or finite-difference time-domain method (FDTD) are numerical tools generally used for analyzing such nonplanar rectangular waveguides. During this Thesis, a commercial mode solver based on the finite-difference BPM has been used for the analysis of the propagating modes through the waveguides. This method will be briefly described in Section 4.3.

Apart from the classification of the waveguides depending on the geometry (planar or nonplanar), waveguides can also be identified according to the refractive index distribution (step- or gradient-index), the material (glass, polymer, semiconductor, etc.) or the modal structure (single- or multi-mode). Furthermore, symmetric waveguides are considered when the guiding layer is embedded in a unique material and, on the contrary, asymmetric structures present different materials surrounding the guiding layer.

This work is focused on rectangular waveguides. With them, it is possible to obtain a better confinement of the light compared to planar structures, reducing the propagation losses while increasing the power density travelling through them. This better light confinement leads to more efficient nonlinear effects in these structures.

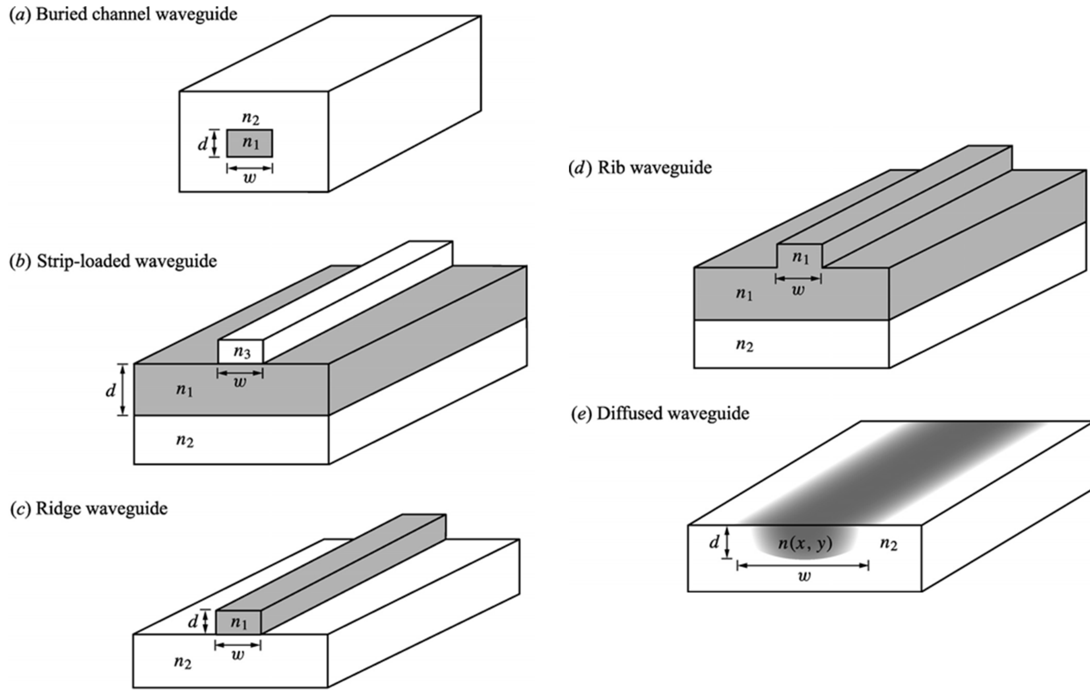

Figure 4.5: Schematic of several designs used for rectangular waveguides.

Figure 4.5 illustrates different representative types of rectangular waveguides. During this Thesis, different types of semiconductor step-index waveguides have been investigated presenting, particularly, ridge, rib and strip-loaded structure geometries.

As commented previously, considering z-direction as the longitudinal direction along which light propagates, the characteristics of a nonplanar waveguide are determined by its transverse index of refraction (which is independent of the z coordinate). When the waveguide is based on optically isotropic materials, it can be simply characterized with a single refractive index which depends on the spatial transverse profiles of the waveguide, $n(x,y)$. However, in the case of waveguides made of optically anisotropic media, we have to consider two different transverse profile of refractive index: the ordinary and the extraordinary refractive index, $n_o(x,y)$ and $n_e(x,y)$, respectively. This latter case is the typical for III-nitrides as commented in Chap. 2.

4.3 Numerical analysis: Finite-difference Beam Propagation Method

The beam propagation method is a mathematical procedure used to study the propagation of electromagnetic fields in arbitrary guiding geometries. As a first approach, it assumes scalar fields (neglecting polarization effects) and paraxiality (propagation restricted to a narrow range of angles, *i.e.*, light propagates predominantly along the z-direction). The scalar treatment of the electromagnetic field given at any point of the structure, represented by the variable $\psi(x, y, z)$ allows the wave equation to be written in the form of the Helmholtz equation as:

$$\frac{\partial^2 \psi}{\partial x^2} + \frac{\partial^2 \psi}{\partial y^2} + \frac{\partial^2 \psi}{\partial z^2} + k_0 n^2(x, y, z)\psi = 0 \tag{4.55}$$

The scalar components of the electromagnetic field can be rewritten from Eq. 4.20 in a general form as:

$$\psi(x, y, z) = u(x, y, z)e^{j\beta z} \tag{4.56}$$

taking into account the rapid variation of the field along the z-direction and the slow variation along the x- and y-directions. When introducing the above expression into the Helmholtz equation, the slowly varying field equation is obtained:

$$\frac{\partial^2 u}{\partial x^2} + \frac{\partial^2 u}{\partial y^2} + \frac{\partial^2 u}{\partial z^2} + 2j\beta\frac{\partial u}{\partial z} + (k_0 n^2 - \beta^2)u = 0 \tag{4.57}$$

This equation above is the wide-angle formulation of the Helmholtz equation. Nevertheless, for simplicity, when assuming the slowly varying envelope approximation (SVEA), the variation of u is considered to be slow enough with z. Thus, the second-order derivative can be neglected leading to the paraxial approximation (narrow-angle formulation) of the Helmholtz equation:

$$\frac{\partial u}{\partial z} = \frac{j}{2\beta}\left[\frac{\partial^2 u}{\partial x^2} + \frac{\partial^2 u}{\partial y^2} + \left(k_0 n^2 - \beta^2\right) u\right] \tag{4.58}$$

In order to solve the previous equation, a finite-difference approach is used to replace the derivatives with finite difference equations. This approach is based on treating the waveguide structure as a mesh in which the field is represented at discrete points on a grid in the transverse (xy)-plane, and at discrete planes along the z-direction (see Fig. 4.6). For example, in the case of the z-dependence, the finite difference approach is given by:

$$\frac{\partial u}{\partial z} \cong \frac{u(z+\Delta z) - u(z)}{\Delta z} \tag{4.59}$$

Given an input field $u(x_m, y_n, z = 0)$, it is possible to calculate the evolution of the field at $z > 0$, *i.e.*, $u(x_m, y_n, z + \Delta z)$.

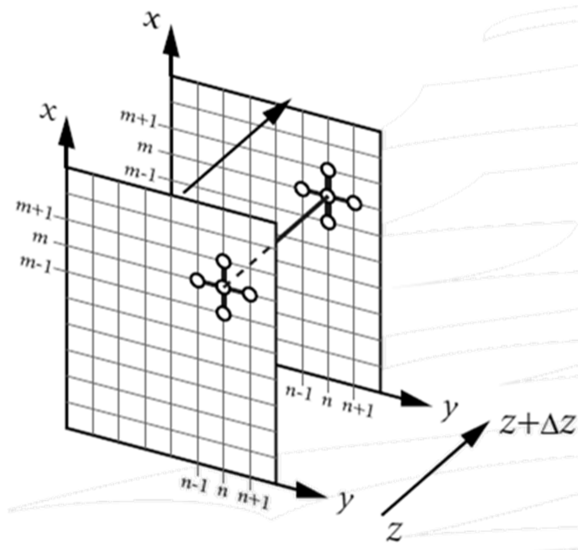

Figure 4.6: Schematic of the transverse grid points and the propagation step in the finite difference method.

The mesh must be chosen in an appropiate way. Mesh sizes widely below the used wavelength are recommended to perform the simulations while large enough to make efficient the computational process. The transversal components of the electromagnetic field can be expressed through a propagator function, $\Gamma(\Delta z)$, taking into account the components at a given position along the z-direction:

$$\psi(x, y, z + \Delta z) = \Gamma_{FD-BPM}(\Delta z)\, \psi(x, y, z) \tag{4.60}$$

For the boundary points, the above equation must be replaced by appropriate boundary conditions which complete the system of equations. It is common to perform the simulations by using the so-called transparent boundary conditions (TBC) [Had91] which assumes that near the boundary the field behaves as an outgoing plane wave avoiding the reflections and allowing radiation to freely escape the computational domain.

Actually, the improved FD-BPM is able to carry out computational processes under several conditions, not only in paraxial approximation and unidirectional propagation. Polarization effects can be included by treating the electromagnetic field as a vector and beginning the derivation from the vector wave equation instead of the scalar Helmholtz equation.
It is also possible to remove the paraxiality of the problem from Eq. 4.57 by considering a differential operator D which denotes $\frac{\partial}{\partial z}$ in the equation. At the same time, $\frac{\partial^2}{\partial z^2}$ is represented by D^2. Thus, the second-order differential equations can be replaced by a quadratic equation which only takes into account the one-way wave equation. The most accurate approach to solve the problem is via the Padé approximants [Had92]. This approach allows the simulation of cases in which light propagates at wide angles or simply structures which present high index contrast [Sca00].
Concerning the direction of propagation, BPM techniques can also take into account simultaneous forward and backward traveling waves. It is assumed that both fields are known at the input of the structure, and taking into account the transfer matrix which describes the whole structure. Thus, both waves are decoupled in the uniform regions along z and are coupled at the interfaces between these regions due to reflection.

All these considerations are included in the propagator function by the commercial mode solvers. Thus, the propagator can take many forms depending on the chosen BPM technique: paraxial or wide-angle, vectorial or scalar, one- or bi-directional propagation, etc. Furthermore, BPM techniques can also include different material effects such as nonlinear and anisotropic behavior.

4.4 Waveguide design and fabrication

This section focuses on the design and fabrication of the ridge/rib-type waveguides. First, the design optimization is carried out by a FD-BPM mode solver. The lithography and etching techniques used in this work are presented here in a general view together with the development of a process for faceting the waveguides.

4.4.1 Optical design

The commercial software used in this work for optical simulations of the waveguides is the BeamProp tool from RSoft. This mode solver implements the BPM method based on an finite-difference scheme. It allows simulations in 2D and 3D, with non-uniform mesh and including anisotropic and nonlinear materials. Polarization effects can be also introduced via a vectorial implementation.

The waveguide design is mainly based on the refractive index distribution together with the structure geometry, *i.e.*, the waveguide height (H), the format of the ridge (width, w, and height, h), the slab thickness (d), etc. (see Fig. 4.7 as an example). Tuning these parameters allows to obtain single- or multimode propagation at a certain wavelength depending on the application. The individual design of the different waveguides under study in this work will be presented in the corresponding chapter.

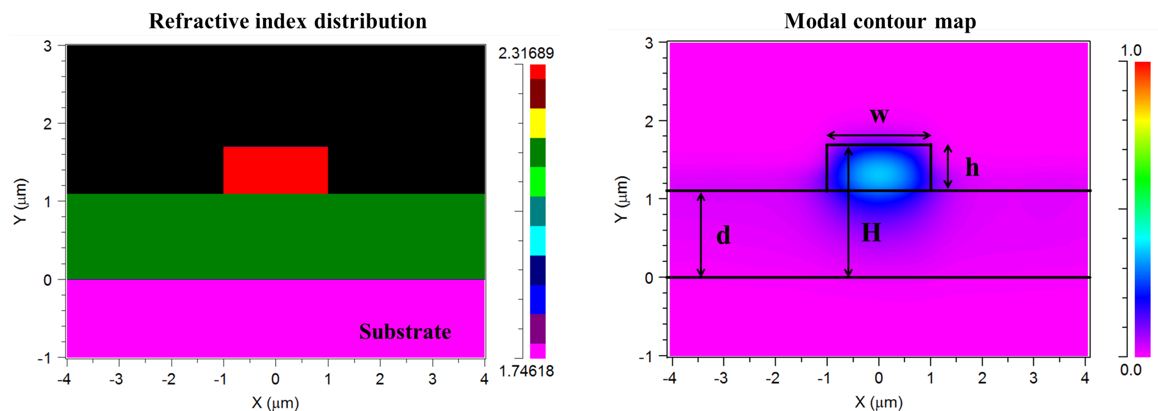

Figure 4.7: (Left) Example of the transverse distribution of the real part of the refractive index at the input facet of a strip-loaded waveguide. (Right) Example of the contour map of the light mode amplitude at the output of the same waveguide.

In the case of multilayer waveguides, as some of the structures contained in this work, the software allows to include a set of materials in the device with the corresponding components of the refractive index and extinction coefficient when the medium is anisotropic. The simulations give information about the amplitude profile of the modes at the output of the waveguide. It is also possible to control the launched power into the waveguide and monitor the light power ratio propagating through the device.

4.4.2 Lithography

Lithography is the process of transferring a designed pattern to a layer or wafer for further device processing. Different types of lithography are used in micro- and nano-device fabrication. Among them, ultraviolet (UV) lithography (or photolithography) and electron beam lithography (EBL) are widely used in semiconductor processing. Both techniques are based on the patterning of a deposited film or a wafer by exposing a resist on top of it.

4.4.2.1 UV lithography or Photolithography

In photolithography techniques, a pattern is transferred from a photomask to a film wafer by exposing a photoresist to UV radiation. This method mainly involves four different steps:

1. Fabrication of the photomask which includes different opaque and transparent zones within a quartz plate. The opaque regions are commonly obtained by using chromium.

2. Deposition of a resist, which is sensitive to light, on the film or wafer by spin-coating.

3. Alignment of the mask and the film and irradiation of the photoresist at the exposure system.

4. Development of the photoresist. The resist can be positive or negative depending on its behavior under the developer action. Actually, the developer makes soluble the photoresist removing, consequently, the exposed regions

when using positive photoresist and the unexposed regions when using negative photoresist.

The exposure technologies can be classified in three types depending on the optical system that transfers the pattern from the mask to the film:

- **Contact exposure:** The film and the mask are in direct contact. Apart from being an inexpensive and simple method, it allows high resolution on the transference of the pattern. Nevertheless, the method induces substantial defect generation on both mask and film.

- **Proximity exposure:** The photomask and the film are separated by a small gap (~10-50 μm) avoiding the defects generated by the contact. Due to the large similarity with the contact exposure, both methods require a precise alignment of the pattern and uniform light intensity all over the film to be patterned.

- **Projection exposure:** Light intensity does not cover the whole film surface. Projection exposure systems (also known as *steppers*) project the mask onto the film by small regions by focusing the light with a lens system in order to create the complete pattern. This is the common technique for large-scale production in the industry.

The three figures of merit in photolithography techniques are the resolution, the registration of one mask to the next (alignment) and the production throughput. Particularly, resolution in photolithography under contact exposure is investigated through the MSF (minimum size feature) being estimated as:

$$MSF \simeq \sqrt{d\,\lambda\,g} \tag{4.61}$$

where d is the thickness of the photoresist film, λ is the exposure wavelength and g is a constant, normally close to 1, that depends on the photoresist and the development procedures.

In UV lithography systems, light at λ=365 nm (i-line emission from a high-pressure mercury lamp) is commonly used for the exposure. The resolution for a constant thickness of the coated photoresist depends directly on the type of the photoresist. The MSF for light at 365 nm is ~0.5 μm when using positive resist and ~2-3 μm

when using negative photoresist. The alternative for reducing the MSF is by using lower exposure wavelengths through exposure processes with low-pressure mercury lamp (235-285 nm) or excimer lasers (KrF at 248 nm, ArF at 193 nm and F_2 at 157 nm). These options raise prices and complexity of the technique.

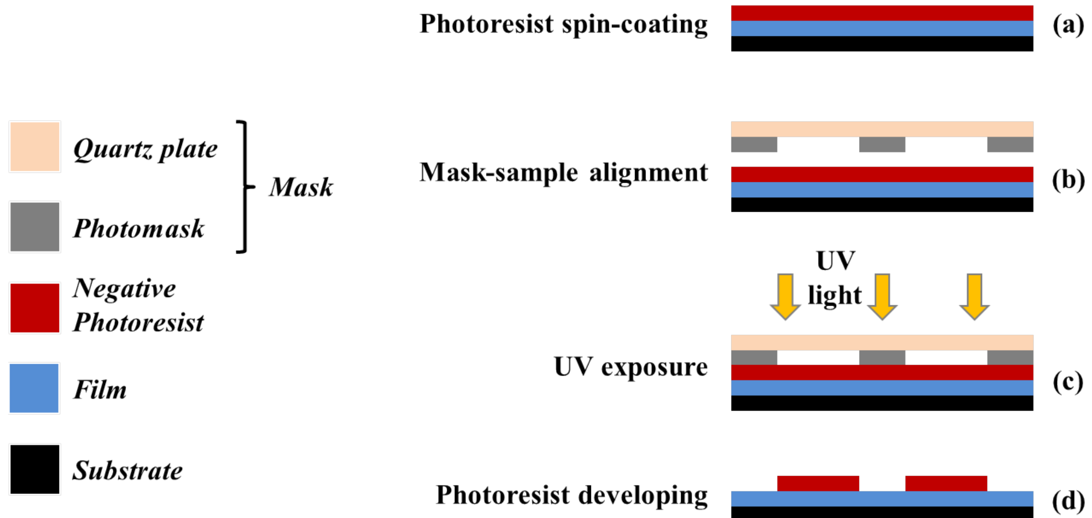

Figure 4.8: Scheme of the UV lithography process using negative photoresist under contact exposured.

As exhibited in Fig. 4.8, the negative photoresist leads to images of the negative of the photomask. Nevertheless, in the case of using positive photoresist, the effect is the opposite.

In this work, UV lithography has been the technique used to perform the patterning of nitride-based films for the further fabrication of the waveguide devices. The characteristics of the photoresists used in this work together with the UV exposure conditions and the photomask designs will be presented in the corresponding chapter for each waveguide device.

4.4.2.2 e-beam lithography

Another lithography method widely used in III-nitride processing is the e-beam lithography (EBL). EBL differs from the photolithography in many aspects. First of all, this technique does not require the patterning of a separate mask since the image or template is directly written into the resist by a scanning e-beam. Hence, e-beam lithography allows patterning the wafer in very flexible way, exposing the resist under

an on/off control and using an accurate positioning stage as it is possible in a scanning electron microscope. Furthermore, the minimum feature sizes are much smaller than with photolithography reaching complex patterned motifs such as 20-nm-wide lines and even isolated features with sub-10 nm resolution [Vie00]. As in the case of the photolithography process, the resolution depends on the used resist together with the accuracy of the lift-off process. In addition, this method avoids the diffraction limits of optical lithography. On the other hand, going against e-beam lithography, writing times for e-beam can be very long depending on the pattern area, dose and current used which induce a very low throughput. This low efficiency together with the need of vacuum makes the technique inappropriate for transferring to the industry.

4.4.3 Etching techniques

Etching is a technological process by which a wafer or film surface is patterned by removing the material restricting the engraving zone by a mask previously defined. The developed photoresist from the lithography can be regarded as the mask. It is also quite common to deposit a metal on top of the developed resist reaching the inversion of the mask. In both cases, it is necessary a lift-off process before the etching. These two possibilities are schemed in Fig. 4.9.

The figures of merit of an etching process are mainly three: uniformity (U), anisotropy (A) and selectivity (S). An ideal etching process requires high values of these three parameters together with a high etching rate (R) which makes possible the automation for industrial processes. The etching figures of merit strongly depend on the used etching techniques and they can be defined as follows:

$$U = \frac{R_{high} - R_{low}}{R_{high} + R_{low}} \qquad \begin{aligned} R_{high} &= \text{Maximum etch rate} \\ R_{low} &= \text{Minimum etch rate} \end{aligned} \tag{4.62}$$

$$A = \frac{R_{vert} - R_{lat}}{R_{vert}} \qquad \begin{aligned} R_{vert} &= \text{Vertical etch rate} \\ R_{lat} &= \text{Lateral etch rate} \end{aligned} \tag{4.63}$$

$$S_{f/m} = \frac{R_f}{R_m} \qquad R_f = \text{Film etch rate}$$
$$S_{f/s} = \frac{R_f}{R_s} \qquad R_m = \text{Mask etch rate} \qquad R_s = \text{Substrate etch rate} \tag{4.64}$$

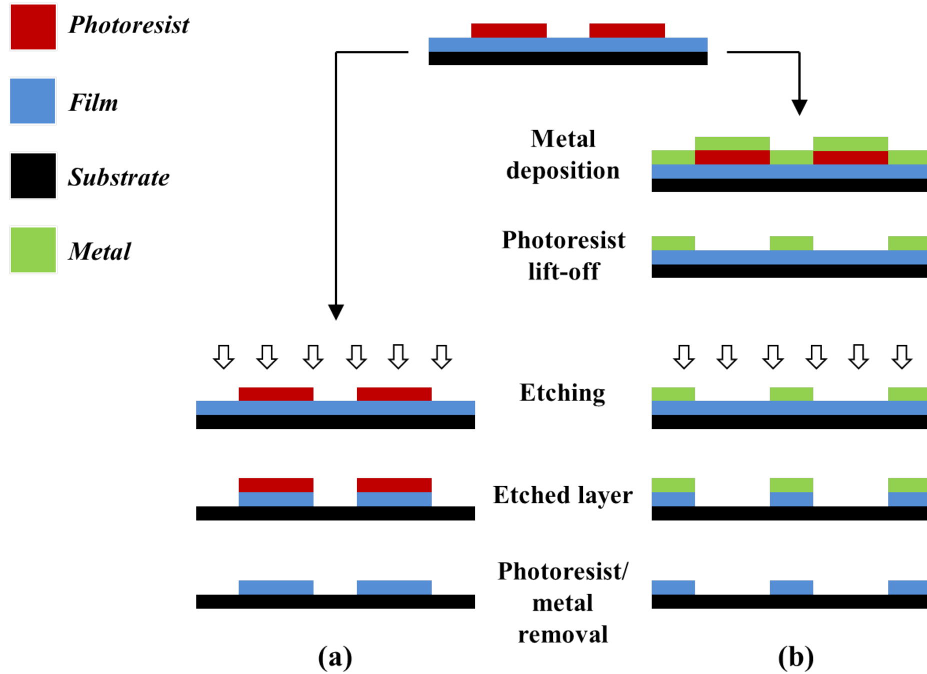

Figure 4.9: Procedure etching for the fabrication of ridge-type waveguides by using as the engraving protection layer (a) the developed photoresist and (b) the deposited metal.

Etching methods are divided in two groups: wet and dry processes. Wet etching is based mainly on chemical processes in which a solvent and the wafer chemically react changing the solid material into soluble. Nevertheless, dry etching is governed by both chemical and physical processes through the removal of wafer material by using reactive or inert ions. On the one hand, wet etching presents high selectivity and the etching rate depends on the reactants concentration. At the same time, the process is isotropic which implies a significant difficulty for obtaining small patterns. By contrast, dry etching can be classified in three types depending on the working pressure and the excitation energy of the plasma as schematized by Fig. 4.10. The most popular methods are the sputtering and ion beam milling (IBM), the reactive ion etching (RIE) and the plasma etching.

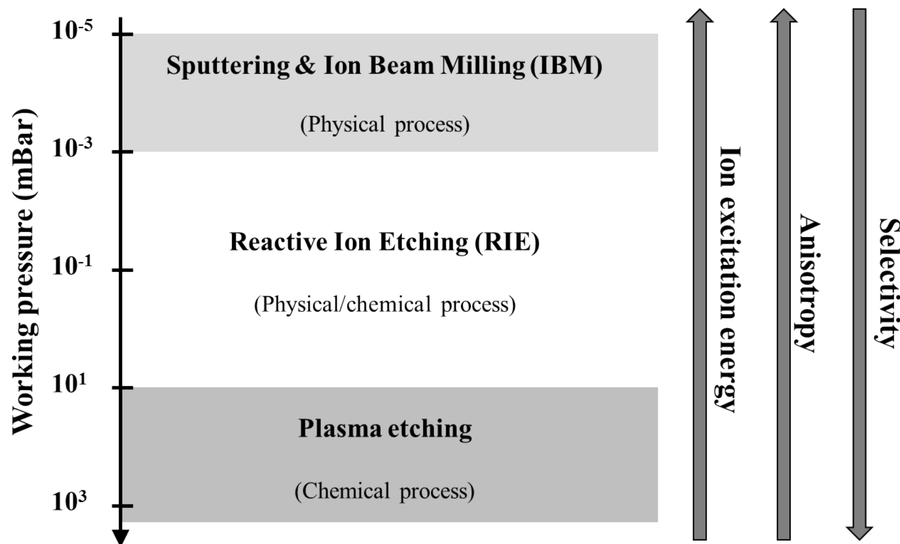

Figure 4.10: Different dry etching techniques depending on the working pressure and the excitation energy of the plasma together with the evolution of the figures of merit such as the etching anisotropy and the selectivity.

In this work, both RIE and sputtering etching techniques are briefly described as they have been used in the fabrication of the waveguides treated in this Thesis. The parameter conditions used in both types of etching techniques are mentioned in the corresponding chapter.

4.4.3.1 ICP-RIE

Regarding the physical/chemical etching process, RIE is considered an attractive solution to attack certain material films through the use of an RF plasma and specific etching gases at low pressure $\sim 10^{-1} - 10^{-3}$ mBar. Etching can be attributed to two distinct mechanisms: chemical etching caused by free radicals and physical etching caused by ion bombardment. The plasma is generated by the application of an RF power source across two electrodes separated in a reactive, gaseous chemical mixture of electrons, ions, and free radicals which produces the distinct plasma glow. Initially, the plasma consists of an equal number of positive and negative charges. Depletion of the charges in the plasma due to diffusion results in a layer of surface charge at the boundary of the plasma. Positive ions are accelerated within the chamber environment and aid in the etching process. The ion bombardment energy

is controlled by the plasma potential which can be estimated from the measurement of the DC potential of the electrodes. This etching technique is mainly characterized by its good anisotropy and selectivity, commonly by using chlorine and fluorine precursors. Nevertheless, it is likely to achieve redeposition of material and trenching zones.

Inductively coupled plasma RIE (ICP-RIE) is a type of RIE system in which the plasma is generated with an RF powered magnetic field. The ICP system creates a high density source of ions which increases the etching rate. At the same time, the RF source is applied to the substrate to enhance the anisotropy of the etching process due to the highly directional electric fields near the substrate.

4.4.3.2 Sputtering etching

Sputtering is the physical etching technique where very energetic ions from noble gases bombard the wafer transferring the momentum and in turn attacking the material. This method is performed at low pressures $\sim 10^{-3} - 10^{-5}$ mBar resulting in an anisotropic removal of material with low selectivity and producing high surface roughness. As in the case of using the RIE technique, sputtering etching likely induces redeposition of etched material and trenching zones.

4.4.4 Facet polishing

Once the ridge-type pattern is transferred to the thin film, the next step is to cut the sample in pieces with the desired size by using a diamond cutter. As the cutting is not absolutely right and flat, cleaving is the preferred method in most semiconductor systems for facets preparation since it is a robust technique for reaching smooth and vertical facets. However, particularly, the formation of facets in III-nitrides grown on sapphire is very difficult because sapphire does not cleave easily. Cleaving c-plane sapphire is hard because sapphire presents many planes which can be cleaved with approximately equal strength and separated each other by a small angular distance. For this reason, facet mechanical polishing is the alternative for device facets preparation.

Facet polishing is required as the last step for the fabrication of the waveguide device. The less the surface roughness of the input and output facets, the less coupling losses

due to scattering. The purpose of this waveguide polishing is to ensure that the facet is uniformly planarized and presents minimum surface roughness. Typically, the polishing process is performed by using a polishing machine or often by hand. In both cases, it is possible to ensure the main direction of polishing by using a piece which holds the sample avoiding the tilt.

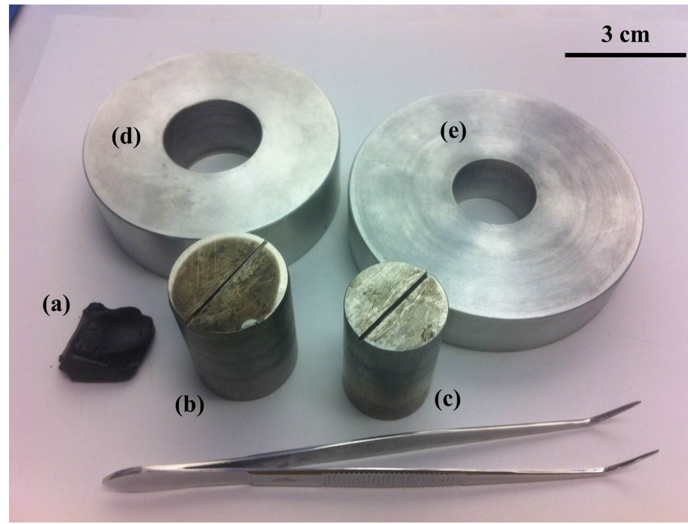

Figure 4.11: Polishing tools used in this work: (a) Apiezon wax piece and metal cylinders with (b) angled and (c) straight slots in which samples are fixed, together with the supporting pieces for the cylinders, (d) and (e).

The experimental polishing tools are presented in Fig. 4.11. In the general case, the sample is inserted and fixed into the straight tiny slot of the cylindrical polishing piece [Fig. 4.11(c)] by using some wax [Fig. 4.11(a)] which has been previously melted with the heater. Afterwards, the cylinder is forced to get cool in order to ensure the fixed position of the sample inside it. The cylinder, which already contains the sample to polish, is coupled into a perforated cylindrical support piece [Fig. 4.11(d),(e)]. The two-pieces system is put downwards to the diamond polishing discs. Since the waveguides present a multilayer structure based on different materials, the choice of the type of abrasive/polishing papers is carried out considering the hardest material. In the case of samples under study in this Thesis, all the waveguides have sapphire substrate which is considered as the hardest material and leads to the use of diamond lapping films as polishing material. The process takes several steps in which the diamond grain size of the discs is always in reduction. During the process, the sample is consistently flushed with water in order to keep the sample clean and minimize

the structure cracking. The highest grain size commonly used is ∼40 μm and the lowest is ∼0.1 μm in order to nearly obtain facets with optical quality. More details of the polishing process of the different waveguides in this work will be presented in the corresponding chapters. After the polishing process, the cylinder is heated again in order to remove the sample. Then, the sample is cleaned in organic solvents: (1) a dichloromethane ultrasonic bath at RT for 10 min, (2) an acetone bath at 40 °C for 10 min and (3) a methanol bath at RT for 10 min. Finally, the sample is blown dry with nitrogen.

Furthermore, an specific oblique facet polishing is carried out simply fabricating the tiny slot with a certain tilt. In this case, the standing cylindrical piece for the sample is designed and fabricated with a slight angle ($\sim 3°$) [see Fig. 4.11(b)]. This procedure is carried out as an alternative for estimating the coupling and propagation losses by the cut-back method as it will be explained in the last section of the current chapter. The rest of the polishing process follows the same protocol as in the case of the straight facet polishing.

4.5 Waveguide optical characterization

The optical characterization of the waveguides is described in this section. The detailed description of the experimental setup is presented together with the protocol used for the optical transmittance measurements of the waveguides. In addition, the estimation of the coupling and propagation losses of the devices through the cut-back method is also summarized.

4.5.1 Experimental setup

The propagation of light was experimentally examined in the linear and nonlinear optical regimes using a mode-locked fiber laser operating at $\lambda = 1.55$ μm with a pulse width of $\Delta t \sim 100$ fs and a repetition rate of $f = 100$ MHz ($T_{rep} = 10$ ns). The light at the output of the laser was coupled into an optical fiber and split using an optical fiber coupler (99/1); *i.e.*, 99 % of the signal is used to perform the linear and nonlinear measurements and the rest is used as a reference. Light, which can be controlled in

polarization, is coupled into the waveguide by means of a ∼2.5-μm-diameter-spot lensed fiber. At the input of the waveguide, the pulse is broadened by the whole optical system up to 150 fs. The waveguide is mounted on a 3-axis positioning stage with tilt and rotation controls. The collection of light at the output of the waveguide is performed with a microscope objective lens to monitor the optical mode by means of an IR camera (see scheme in Fig. 4.12). On the other hand, the output optical power can be measured by replacing the system objective/camera by the system fiber/powermeter which collects the light by a single mode fiber to measure the output optical power (see Fig. 4.13).

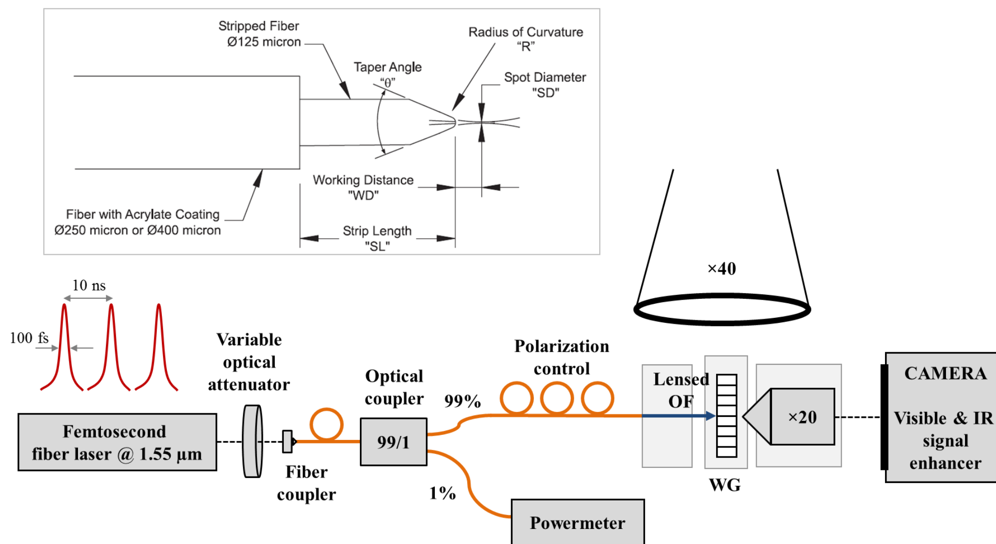

Figure 4.12: Scheme of the experimental setup for optical characterization of the waveguides by monitoring the optical mode at the output of the structure. Inset: Scheme of a typical tapered lensed fiber (supplied by *OZ Optics*) used in this setup.

The experimental system used for carrying out the optical characterization of the different waveguides under study was set up at the Institute of Optics (CSIC) in Madrid under the supervision of Dr. Pedro Corredera.

4.5.2 Optical characterization procedure

The procedure followed for characterizing the optical modal propagation of the light through the fabricated nitride-based waveguides considers both linear and nonlinear regimes. Optical power launched into the waveguide can be controlled by the variable

optical attenuator. The optical attenuator is a circular neutral density filter which continuously varies the optical density when rotating the plate around its axis. It is placed immediately in front of the air/fiber coupler.

In this work, the average incident optical power ranges from a few of μW to ~50 mW (from -12 dBm to 17 dBm) estimated from the 1% output of the optical coupler. Actually, since the light source is a pulsed laser, the pulse powers and pulse energies are of great interest for the measurements. Thus, for the laser used in this work, the relationship between the average power ($P_{average}$) measured by the powermeter and the associated pulse power (P_{pulse}) is given by:

$$P_{pulse} = \frac{T_{rep}}{\Delta t} P_{average} = 10^5 P_{average} \tag{4.65}$$

Another important point of the optical characterization of the waveguides is the choice of the suitable polarization in some cases (as it will be commented in Chap. 5). The polarization of the light at the input of the waveguide can be selected by putting face to face the lensed fiber and the microscope objective to visualize in the IR camera the launched optical fiber mode. Then, this selection is carried out by means of a linear polarization plate which is placed in front of the IR camera together with a polarization control placed before the tapered lensed fiber.

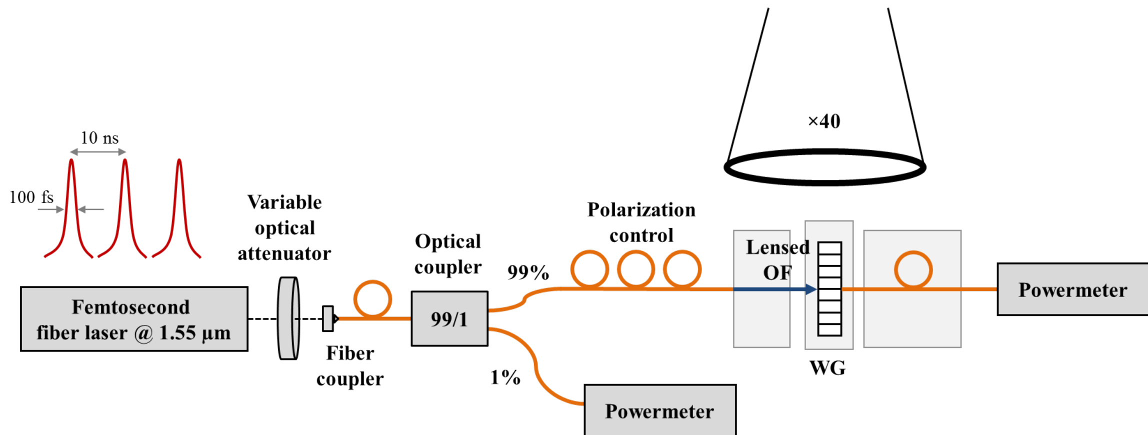

Figure 4.13: Scheme of the experimental setup for linear and nonlinear optical transmittance measurements of the waveguides.

Once the desired light polarization is selected, light is injected into the waveguide and collected at the output by the microscope objective. In this way, optical modes transmitted along the waveguide can be monitored in the IR camera ensuring the suitable propagation of light into the device. After that, the microscope objective is replaced with the single mode optical fiber connected to the powermeter (see Fig. 4.13). Placing the collecting fiber in the good position, optical transmittance measurements can be performed in the linear regime (for low optical power levels) and in the nonlinear regime (for high levels). In this way, it is possible to analyze the nonlinear behavior of the structure.

4.5.3 Propagation and coupling losses: Cut-back method

Up to date, during this Thesis manuscript, the optical waveguides have been considered as ideal lossless structures. Nevertheless, propagation and coupling losses are always present when dealing with real photonic devices.

Concerning the propagation losses, many factors contribute to disturb the light propagation along the waveguide. Among the main sources of propagation losses, it has to be pointed out the conversion of a guided mode into a radiation mode leading to radiation losses or its conversion into a different guided mode resulting in the so-called modal conversion losses. Besides, scattering losses are commonly present due to imperfections of the waveguide structure (see Fig. 4.14) while absorption losses can be obtained when using light absorptive materials.

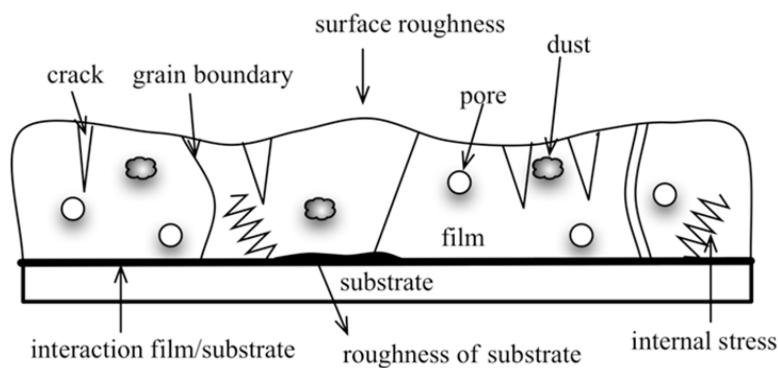

Figure 4.14: Representation of the different scattering sources which likely produce propagation losses [Wu05].

On the other hand, coupling light into- and out-of- the waveguide also leads to the so-called coupling losses. Thus, the injection of light from the optical fiber into the waveguide is a critical step to reach the excitation of a guided mode through the waveguide since commonly the propagated mode coming from the optical fiber can not be propagated directly in the waveguide. Hence, an effective technique to couple and confine the fiber mode into the waveguide is necessary. Several techniques are used for coupling light from an optical fiber to an optical waveguide (regardless of the geometry, *i.e.*, planar, rib, ridge, etc.). In this work, the end-coupling method has been the used technique by which the guided modes from an optical fiber are directly launched into a waveguide facet leading to waveguide mode propagation. As it has been commented previously, in this experiment, light from the optical fiber is coupled into the waveguide by focusing the light using a lensed fiber. Equally important is the collection of light from the output facet of the waveguide and the used technique depends on the experimental goal, *i.e.*, monitoring the transmitted optical mode or measuring the average optical power.

There are different methods for measuring the propagation losses in optical waveguides. Among them, prism-sliding and cut-back methods are widely used. The latter has been used during this work for the estimation of both, separately, propagation and coupling losses [Hun84]. The cut-back method is based on the measurement of the light transmittance through similar waveguides with different lengths. The plot of the experimental optical losses as a function of the waveguide length (L) leads to the estimation of the propagation losses (given by the slope of the linear fit of the experimental points) and the coupling losses due to the two waveguide facets (given by the extrapolation of the linear fit to $L = 0$). This method assumes that the coupling losses into similar waveguides is the same, and that propagation losses are constant with waveguide distance.

The cut-back method presents a disadvantage when dealing with integrated devices such as waveguides since it is usually a destructive method and it is not straightforward to reduce the length of the waveguide by an accurate quantity. An alternative way is to measure the output from a set of waveguides with the same fabrication procedure but with different lengths. Nevertheless, another option has been used in this work to perform the cut-back method. It is based on the polishing of the output facet of the waveguides with a slight angle obtaining different waveguide

lengths. It has to be noticed that this method could lead to an overestimation of the coupling losses since the optical fiber for light collection is not positioned totally perpendicular to the output facet.

Along this manuscript, the term ”incident” is referred to the light without taking into account the coupling losses at the input facet of the guiding devices. Contrarily, the term ”input” already accounts for these losses.

Chapter 5

Nonlinear optical absorption saturation in GaN/AlN QW- and QD-based waveguides

This chapter focuses on the design, fabrication and optical characterization of optical waveguides based on GaN/AlN heterostructures such as quantum wells (QWs) and quantum dots (QDs). These devices are optimized for application in all-optical switching via intersubband/intraband absorption saturation at 1.55 μm.

The first section deals with a brief introduction of the state-of-the-art of different strategies for increasing the optical switching speed by means of interband and intersubband/intraband transitions in several material systems. The second part of the chapter is based on the simultaneous optical design of the waveguide format and the electrical design of the GaN/AlN heterostructures for reaching the most enhanced optical nonlinear effect. Afterwards, the growth of GaN/AlN samples is presented together with their characterization in terms of structural and morphological properties. Besides, the fabrication procedure of the waveguides based on GaN/AlN heterostructures is described. The fourth section is dedicated to the linear and nonlinear optical transmittance measurements of the different optical waveguides highlighting the optical absorption saturation phenomena. Finally, some conclusions are presented. This work has been published as a journal paper in Optics Express [ML13a].

5.1 Introduction

Optical fiber provides a suitable medium for reaching tremendous transmission rates over long distances. Very high data rates can be achieved using a combination of wavelength- and time-division multiplexing techniques (WDM and TDM, respectively) and even larger when implementing space-division multiplexing (SDM) methods. Up to the moment, the capacity record in research for WDM systems over single mode fibers is $\sim$100 Tbps [Ess13]. The improvement has coming through the development of systems based on SDM (via multiple core fibers) which has lead to data transmission rates up to $\sim$1 Pbps per fiber [NTT12]. Despite the extremely large bandwidth reached in optical fibers, the agility of the current optical networks is limited by the electronic behavior of the data signals processing. Among other, signal processing such as switching and routing of data within the communication networks are carried out electronically requiring the conversion of the optical information into electrical signals, processing in the electronic domain, and converting back to the optical domain before retransmission. This process is required at each network node, making the data transmission slower while raising the price of the network. Thus, the increasing demand of bandwidth in optical communications impels the development of all-optical devices (switches, routers, wavelength converters) which avoid the optical-electrical-optical (OEO) conversions at each node of the network. While state-of-the-art electronic switching networks are approaching their maximum bandwidth, no fundamental bandwidth limit exists for their optical counterparts. Hence, in contrast with electronics, optical signal processing may provide ultrafast subpicosecond switching times [Smi82]. Nowadays, the aim is to develop a new generation of all-optical devices for switching with high operation speed above 1 Tbps while consuming low energy.

All-optical devices are required to work within the C-band of optical fibers (centered at $\sim$1.55 μm), where erbium-doped fiber amplifiers are widely available. They should be capable of sustaining high repetition rates with low switching energy and high contrast ratio, features that lead to consider the use of resonant nonlinearities [Wad04]. Highly nonlinear optical fibers and waveguides have been used for generating nonlinear interactions in this spectral region [Blo00][Alm04]. However, due to the low values of their nonlinear coefficients ($n_2 = 2.5 \times 10^{16}$ cm^2/W at 1.55 μm in silica fibers [Kim94][Vin01]), the implementation of devices often requires long interaction

distances (even kilometers in the case of nonlinear fibers) or high power levels [GH11], making them cumbersome for real systems. An interesting alternative comes through the use of semiconductor third-order nonlinearities, exploiting phenomena like nonlinear absorption, self- and cross-phase modulation, self- and cross-gain modulation, and four-wave mixing [Rad05][Boy08]. In this case, all-optical switching can be achieved through optical absorption saturation by an intense control optical pulse, as originally demonstrated at long infrared wavelengths using GaAs/AlGaAs structures [Nod93].

Different material systems have been investigated for reaching the same goal. Silicon devices play with the refractive index changes and absorption coefficient due to a variation of free carrier concentration leading to a maximum operation speed of ∼40 Gbps. Taking into account the InP-based technology, InGaAs/AlAsSb MQW systems have been investigated obtaining a relaxation time ∼2 ps [Gop02] leading potentially to much larger bandwidths (∼500 Gbps).

From this point of view, III-nitride semiconductors are good candidates since the asymmetry of their crystalline structure contributes to enhance nonlinear phenomena [Mor08]. There are two different approaches to cover the near-infrared spectral range using nitride semiconductors. A first strategy is the use of InN, which presents a room temperature direct band gap of ∼0.64 eV (∼1.94 μm). For this purpose, Naranjo *et al.* explored the potential of InN films and InN/InGaN MQW structures with interband transitions (between the conduction and the valence bands involving two types of carriers, *i.e.*, electron and holes) at 1.55 μm, by analyzing their third-order nonlinear susceptibility ($\chi^{(3)}$) [Nar07] and their nonlinear absorption coefficient (α_2) [Nar11]. For these structures, a minimum recovery time in the range of tens of ps can be achieved [VF12a].

At this point, the suitable alternative to increase the operation speed is working with systems which present intersubband/intraband transitions (both between different energy levels within the conduction band in the case of n-type semiconductors and within the valence band when dealing with p-type structures). These optical transitions are differently named depending on the type of the involved energy levels. In a QD, the previously mentioned transitions occur between discrete energy levels and are called intraband transitions. Nevertheless, in QWs, the transitions

take place between different subbands within the conduction or the valence band. The transitions in these structures between two subbands are called intersubband transitions (ISBT) [Tan10]. For writing simplicity, both types of transitions are referred along this work as intersubband transitions when treating them in a general formalism.

ISB transitions lead to recovery times at least one order of magnitude lower than that corresponding to systems exhibiting interband transitions. In optoelectronic devices, widely explored material systems via ISB transitions have been GaAs/AlGaAs and InGaAs/InAlAs compound systems which can be lattice-matched to GaAs and InP substrates, respectively. In other respects, as commented previously, by using interband transitions in InN-based structures the response speed is determined by the electron-hole recombination lifetime generally in the over-picoseconds range. Contrarily, ISBT in the conduction band can exhibit an ultrafast relaxation time (from few picoseconds to femtoseconds range).

Nevertheless, there are only a few semiconductor systems which act as active layers capable of producing ISB transitions at telecom wavelength such as InGaAs/AlAsSb, CdS/ZnSe/BeTe and GaN/AlN heterostructures. Among them, GaN/AlN systems are of great interest due to their likely modeled ISBT at 1.55 μm by controlling the size and composition of the QWs and QDs nanostructures, but also since they present large conduction band offset in the GaN/AlN system (difference between the band gap energy of the well and barrier materials, ΔE_C ~1.8 eV [Tch06]). The suitability of these material systems for potential application in ultrafast all-optical switching devices at 1.55 μm is totally justified due to their ISB relaxation times in the range of 150-400 fs [Suz97][Iiz00][Heb02][Rap03][Ham04][VF08], being the fastest transition among those reported for the rest of the material systems thanks to the strong electron-phonon interaction in wurtzite structures. This ISB transition corresponds to the electron passage from the ground electronic state to the first excited level ($e_1 - e_2$) in QWs, or to the first state confined along the [0001] growth axis ($s - p_z$) in QDs [Bee13]; both ISB transitions are only allowed for TM-polarized light (exhibiting a strong polarization selection rule by which only the z-component of the electric field couples to the ISB transition). Hence, light with polarization in which the electric field is in the plane of the layers of the sample (TE) is not absorbed while waves polarized parallel to the c-axis growth direction (TM) are absorbed.

Nonlinearities are enhanced by quantum confinement in nanostructures, as already demonstrated by second-harmonic generation in GaN/AlN QWs [Nev06], and measurements of the high third-order nonlinear susceptibility in GaN/AlN QWs [Ham04] and QDs [VF08]. Thus, the onset of nonlinear interactions in these confined structures is expected at lower power levels than in bulk materials.

In terms of all-optical device applications, the use of ISBT in GaN/AlGaN QWs for the implementation of all-optical modulators at telecommunication wavelengths was first proposed by Suzuki *et al.* [Suz97][Suz00]. Since then, all-optical switching at 1.55 μm with sub-picosecond response time has been demonstrated by several groups. In general, these devices consist of GaN/AlN multi-QWs embedded in a rib/ridge waveguide. Control switching energies as low as 38 pJ for 10 dB modulation depth [Li07a] and 25 pJ for 5 dB contrast [Iiz09] have been reported using a waveguide with an AlN cladding below the active GaN/AlN QWs, and GaN or Si_xN_y as the upper cladding layer, respectively. Concerning the GaN/AlN nanostructures efficiency, comparative studies using the forward degenerate four-wave mixing technique in a boxcar configuration point to an increase of $\chi^{(3)}$ by a factor of five in GaN/AlN QDs compared to GaN/AlN QWs [VF08]. Furthermore, the $s - p_z$ intraband absorption saturation of GaN/AlN QDs is achieved for a saturation intensity <1.4 W/μm^2 (<0.27 pJ/μm^2) [Nev09], significantly smaller than the value reported for GaN/AlN QWs (9.6 W/μm^2 [Li07a]).

Taking into account the state-of-the-art of the optical behavior of GaN/AlN-based heterostructures, the objective of this investigation is the fabrication of GaN/AlN waveguides which present the capability for application in nonlinear all-optical switching at 1.55 μm via the saturation of the ISBT. The GaN/AlN heterostructures and the waveguide format are designed aiming this device as an alternative for high operation speed ($\sim$10 THz) while using relatively low energy ($\sim$3 pJ for 3-dB change in optical transmittance).

5.2 Optical and electrical design

The active region of the GaN/AlN waveguides investigated in this work is achieved by introducing low-dimensional GaN/AlN heterostructures such as QWs and QDs. These nanostructures induce quantum confinement of the carriers in the material leading to specific electronic and optical properties depending, mainly, on their geometry, size and composition. The dynamics of the electron in free space is given by its energy E and its momentum **p**, both related with the magnitude of the wavevector, k, associated with the electron wave function.

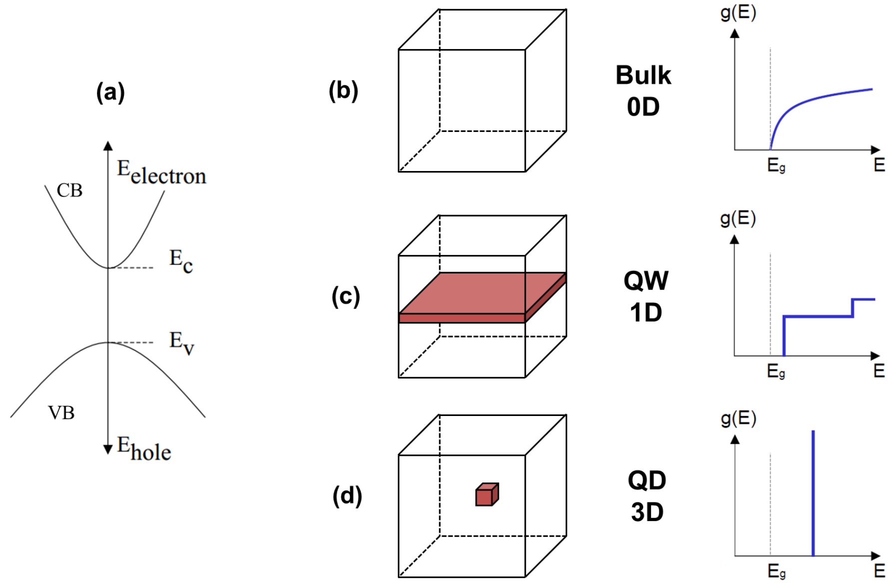

Figure 5.1: (a) Scheme of the parabolic CB and VB in a semiconductor. Confinement geometric format and plot of the density of states, *g(E)*, as a function of the excitation energy for (b) bulk material (0D), (c) QW nanostructure (1D) and (d) QD nanostructure (3D).

In case of a bulk semiconductor, conduction (CB) and valence (VB) bands can be approximated to a parabolic function, considering that electrons (e) and holes (h) move like free particles with effective masses which takes into account the interaction between the carrier and the crystal, m_e^* and m_h^*, respectively. Thus, referring to Fig. 5.1(a), the energies in the CB (E_{CB}) and the VB (E_{VB}) can be approximated by:

$$E_{CB} \simeq E_C + \frac{\hbar^2 k^2}{2m_e^*} \qquad E_{VB} \simeq E_V - \frac{\hbar^2 k^2}{2m_h^*} \tag{5.1}$$

The density of states, *g(E)*, of a system describes the number of states per interval of energy (ΔE) at each energy level (E) that are available to be occupied by electrons. Thus, $g(E) = 0$ corresponds to a gap region in which electrons can not exist. In bulk systems, the g(E) is proportional to $\sqrt{E - E_g}$, as shown in Fig. 5.1(b).

Concerning low-dimensional structures, a QW is a nanostructure which confines electrons in one dimension. A semiconductor QW is obtained by a thin film embedded in other semiconductor layers of larger band gap energy (barriers). The QW confines carriers in the dimension perpendicular to the layer surface allowing the free mobility in the other dimensions, *i.e.*, 2 degrees of freedom). Different from the carrier confinement in a large piece of material (bulk) where the *g(E)* is represented as a continuum range, QWs exhibit a step *g(E)* as shown in Fig. 5.1(c). These nanostructures are typically grown by the Frank van der Merwe method, previously described in Chap. 2.

On the other hand, a QD is a tiny punctual structure, embedded in another material with larger band gap, which confines electrons in 3D leading to zero degrees of freedom. QDs exhibit discrete energy levels corresponding to a delta-shaped density of states function which is exhibited in Fig. 5.1(d). In general, semiconductor-based QDs are grown by MBE or MOCVD by the Stranski-Krastanov growth mode (briefly described in Chap. 2).

In both cases, by changing the QW heterostructure size, *i.e.*, well and barriers thickness and depth (composition), or the QD height and diameter, the electronic and optical characteristics of the structure can be controlled leading to tunable interband and ISB transitions. These changes are critical to obtain the ISB transition at the desired working wavelength. Furthermore, for taking advantage of the low recovery time of the ISB transition previously mentioned ($e_1 - e_2$ and $s - p_z$), it is required to ensure the electronic population in the first confined electronic level in the QW (e_1 level) and the QD (s electronic state), respectively. Figure 5.2(a) depicts the ideal conduction and valence bands (without taking into account the internal electric field effects) of a QW embedded within the barriers along the growth direction. In addition, the equivalent energy levels as a function of the magnitude of the wavevector is exhibited in Fig. 5.2(b).

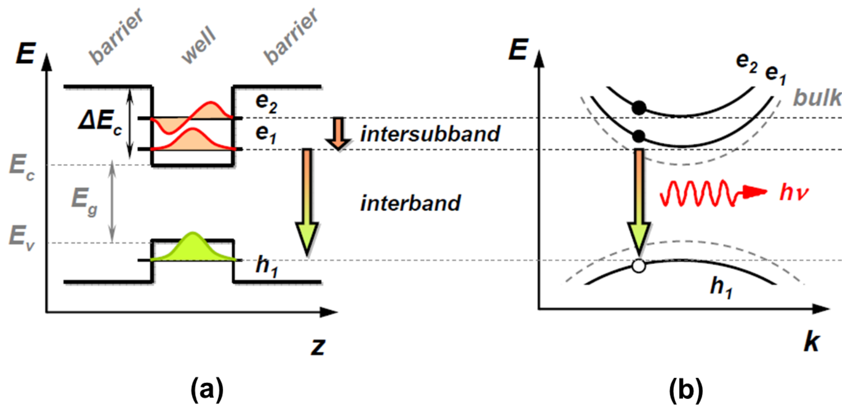

Figure 5.2: (a) Scheme of the energy levels for electron and holes in an ideal QW system along the confinement direction, z. (b) Cross-section of the E-k relation of a QW compared to that of the semiconductor bulk (dashed line). The energy levels in the CB are labeled as e_1 and e_2, and h_1 in the VB [VF11].

The electrical design of the active region was carried out taking into account both optical and electrical considerations. On the one hand, the optical design was performed by using a commercial finite-difference beam-propagation mode solver, particularly, the RSoft BeamProp software. The optical modes propagated through the waveguides were calculated at $\lambda_0 = 1.55$ μm assuming 1.746, 2.120 and 2.317 as the theoretical real part of the refractive indices for sapphire, AlN and GaN, respectively. The electronic properties of the GaN/AlN heterostructures were modeled using the Nextnano^3 8-band k.p. Schrödinger-Poisson solver [Bir07] with the material parameters described in ref. [Kan08].

In this work, there are two different samples which are widely investigated. They consist of three layers of GaN/AlN QDs or QWs active region embedded in a guiding structure based on a 600-nm-thick GaN layer deposited on a 1.1-μm-thick AlN-on-sapphire template. The choice of AlN-template as a substrate is due to the smaller in-plane lattice constant of AlN in comparison with GaN, which keeps the structure under compressive strain preventing the formation of cracks in the active region. Furthermore, the smaller refractive index of AlN in comparison to GaN pushes the optical modes towards the GaN layer, keeping them away from the highly-dislocated sapphire/nitride interface reducing in that way the propagation losses.

Concerning the optical design of the waveguide, firstly, it is important to choose the format of the initial rib-type waveguide device by performing different optical simulations in order to reach the desired theoretical modal propagation. Optical simulations bring out the amplitude of the transverse profile of the optical mode at any distance z, $E(x,y)$. It has to be noticed that, from these values, the effective mode area (A_{eff}) can be defined in a practical way as:

$$A_{eff} = \frac{\left(\int |E(x,y)|^2 dA\right)^2}{\int |E(x,y)|^4 dA} \tag{5.2}$$

where $E(x,y)$ is the amplitude of the electric field and A is the transversal area under consideration. This equation is used mainly for optical modes propagating through single mode waveguides. It takes into account that the transverse field amplitude is not distributed equally all over the guiding layer but slightly decays being considerably lower near the interfaces with the cladding layers. Hence, the effective mode area represents an average area that an optical mode covers when propagating through a waveguide. This parameter is crucial in the case of nonlinear optical investigations, in the sense that lower A_{eff} values lead to higher optical power densities reached inside the waveguide considering the same incident power and coupling.

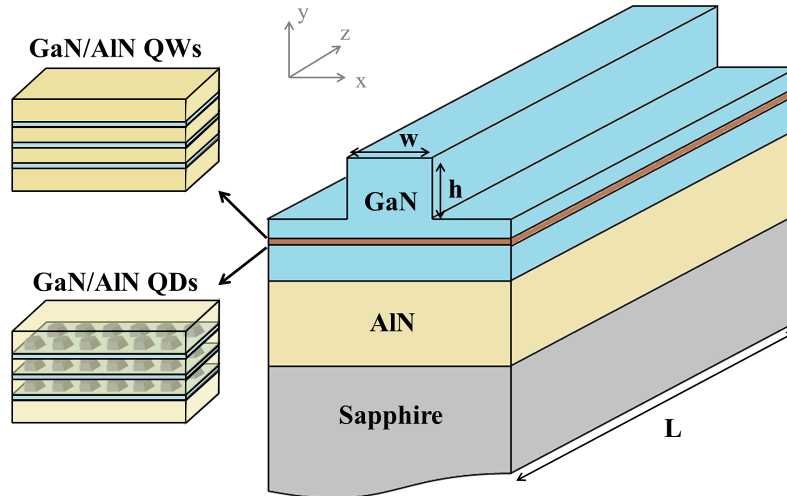

Figure 5.3: Scheme of the GaN/AlN waveguide format together with the dimensions susceptible to optimize. The active region can be based on QWs or QDs of GaN embedded in AlN barriers.

Considering the typical rib/ridge format of the waveguides under study as that depicted in Fig. 5.3, it must be pointed out that single mode waveguides should be preferable as they reduce the coupling losses between the optical fiber and the waveguide. They also reduce the propagation losses in terms of better confinement of the optical mode making them, in turn, more attractive for nonlinear optical investigations. Thus, the GaN layer thickness was chosen so as to achieve single mode light guiding at 1.55 μm for widths of the ridge (w) affordable with optical lithography ($\sim$2 μm in this case) as will be presented in next section. The dimensions of the ridge are critical for the modal propagation, thus, a set of simulations varying the ridge width (from 2 μm to 50 μm) and the ridge height (h), commonly known as etching depth (from 50 nm to 600 nm) was performed.

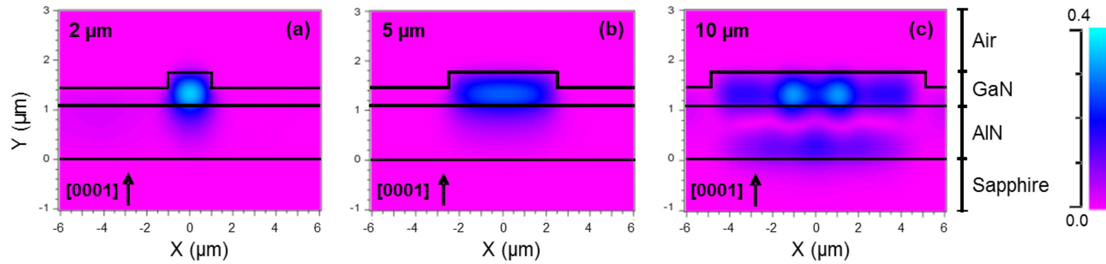

Figure 5.4: (a-c) Cross-section of the waveguide and normalized modal amplitude color maps at the output of GaN/AlN waveguides with different ridge widths: 2, 5 and 10 μm, respectively.

Figure 5.4 exhibits several results obtained from the optical simulations. Devices presenting ridge widths of 2 μm can be considered single mode waveguides, while others with widths of 5 μm can be dealt as quasi-single mode for waveguide lengths in the range of 1-2 mm. Strong multimode propagation is obtained when increasing the waveguide width above 5 μm. At the same time, simulations of the ridge height are exhibited in Fig. 5.5(left) illustrating some representative curves of the evolution of the modal profile when increasing the etching depth of a 2-μm-wide and 2-mm-long waveguide. It must be pointed out that the etching depth from 250 nm to 550 nm has no relevant impact on the output modal profile, presenting in all cases a reduced modal guiding through the GaN-AlN-slab. An etching depth of 350 nm is chosen for the fabrication of the waveguides since it provides the lowest theoretical effective mode area in the range under study [as demonstrated by Fig. 5.5(right)].

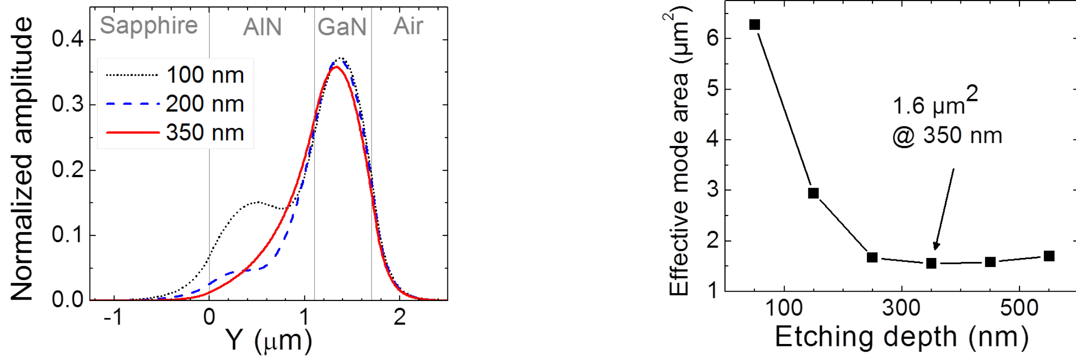

Figure 5.5: Representative optical simulations which demonstrate the optimized ridge height for a 2-μm-wide waveguide leading to 350 nm. (Left) Normalized output modal amplitude profile with different ridge etching depths: 100, 200 and 350 nm. (Right) Estimated effective mode area as a function of the etching depth.

Figure 5.6(left) reveals information about the light amplitude distribution at the different material layers at the output of the device of 2-μm- and 5-μm-wide and 350-nm-deep ridge. It has to be pointed out that ~1% of the total amplitude in both cases is lost through the sapphire substrate. These simulations also exhibit the difference in light confinement between the 2-μm- and the 5-μm-wide waveguides. An increase of ~20% of the output peak amplitude is estimated for 2-μm-wide waveguides with respect to 5-μm-wide ones. For similar coupling losses, the 2-μm-wide waveguide should therefore exhibit lower saturation input power.

Considering the two active devices under study (see Fig. 5.3), the active region is limited to only 3 periods of GaN/AlN QWs/QDs heterostructures in order to ensure a measurable transmittance in 2-mm-long waveguides. The QW-based structures consist of 1.5 nm (6 ML) of Si-doped GaN wells embedded in 3-nm-thick AlN barriers. Instead, the QD-based structure is based on ~1-nm-high (~4 ML) Si-doped GaN QDs separated by 3 nm AlN barriers. In both cases, these dimensions are defined so as to tune the ISB absorption to 1.55 μm (as ideally exhibited in Fig. 5.2 for the QW case), in agreement with previous results [Gui06][Kan08].

Regarding the location of the active nanostructures within the GaN guiding layer, in the case of QWs, they are placed at the modal amplitude maximum, *i.e.*, 250 nm above the AlN-template/GaN interface. In the case of QDs, a certain compressive strain is required to activate the 3D growth. Thus, the best choice from the epitaxial viewpoint would be their deposition directly on the AlN template, profiting from the

2.5% lattice mismatch between GaN and AlN. This location would imply a decrease of the modal overlap with the active layer of ∼22% [see Fig. 5.6(left)], which could be compensated if needed by increasing the number of QD periods.

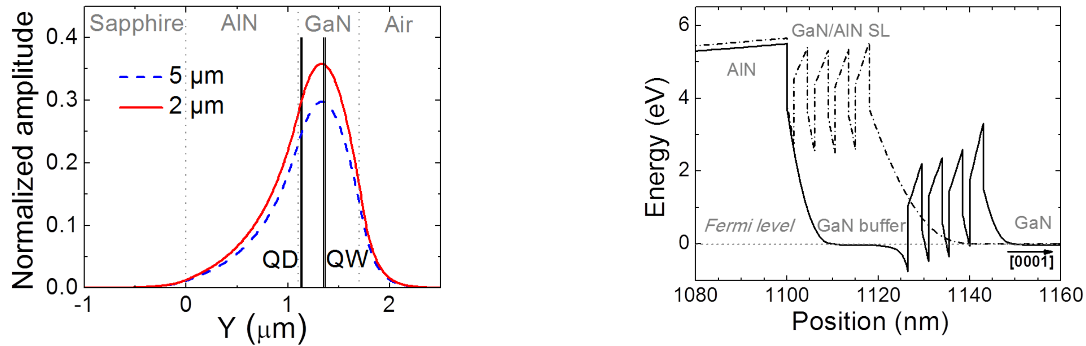

Figure 5.6: (Left) Normalized output modal amplitude profile for both 5-μm- and 2-μm-wide waveguides with 350-nm-deep ridges. Black vertical lines indicate the location of the QD/QW regiones in the experimental structures. (Right) Conduction band profile of the active GaN/AlN superlattice considering the whole waveguide structure designed to obtain a resonant ISB transition at ∼ 1.55 μm. Dot-dashed line shows the depletion of the active structure when growing the QWs directly on the AlN template. Solid line illustrates the avoiding of the depletion of the QWs when introducing a minimum GaN buffer layer ∼25 nm.

However, theoretical calculations of the electronic profile show that the difference of spontaneous and piezoelectric polarization between GaN and AlN leads to a total depletion of the QDs when growing them directly on top of the AlN-on-sapphire substrate, as illustrated by dot-dashed line in Fig. 5.6(right). Therefore, a minimum GaN buffer layer of ∼25 nm is deposited prior to the growth of the QDs, thick enough to obtain flat-band conditions in the QDs [see solid line in Fig. 5.6(right)], while keeping enough elastic energy to induce the QD formation.

5.3 Structure growth and waveguide fabrication

Once the electrical and optical simulations have been completed for the design of the material structure and the waveguide format, the next step of the investigation is the growth of the samples and the fabrication of the waveguides.

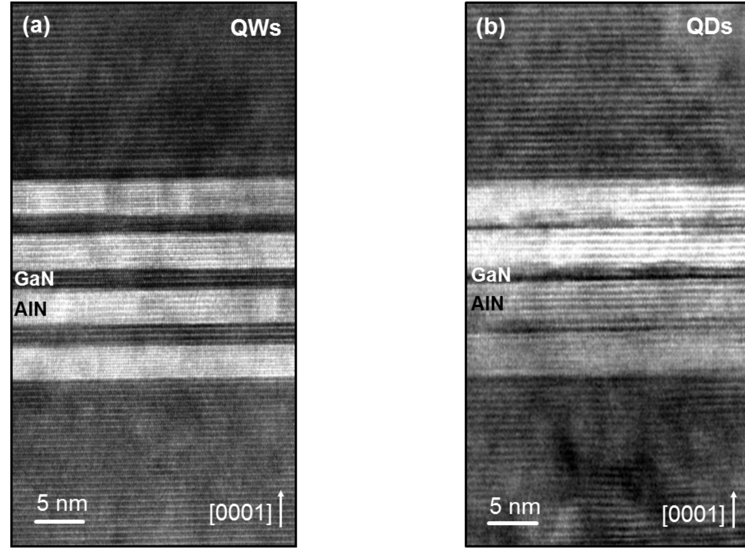

Figure 5.7: HRTEM images of the active region of the samples containing 3 layers of (a) Si-doped GaN/AlN QWs and (b) Si-doped GaN/AlN QDs.

The samples were synthesized by PAMBE using 1.1-μm-thick AlN-on-sapphire commercial substrates. The growth rate was $\sim$280 nm/h and the growth temperature was 720 °C, low enough to ensure a negligible GaN decomposition and to prevent a thickness reduction of the GaN nanostructures during AlN capping process ($\leq$730 °C) [Gog04]. The QW-containing structure was deposited under Ga-rich conditions, without growth interruptions. In the case of the QD-based structure, the AlN barriers were synthesized under Al-rich conditions, followed by nitrogen exposure to consume the Al excess. Then, the GaN QDs are formed by deposition of 3 ML of GaN under N-rich conditions (N/Ga flux ratio = 0.8), followed by a 15 s growth interruption in vacuum. These growth conditions result in a high density (10^{11}-10^{12} cm^{-2}) of small QDs (1-1.5 nm high) connected to the underlying AlN by a 2 ML thick defect-free GaN wetting layer [Gui06]. The dots are subsequently capped with 3 nm of AlN, which rapidly recovers a planar surface. Both QWs and QDs were Si doped ($\sim 10^{20}$ cm^{-3}) in order to populate the first confined electronic level and enable efficient ISB absorption. For both QW- and QD-based samples, the top GaN surface presents a flat morphology with atomic terraces and an rms surface roughness of $\sim$1.0 nm, measured by AFM over an area of 5$\times$5 μm^2.

The active regions were studied by high resolution transmission electron microscopy (HRTEM), as illustrated in Figs. 5.7(a),(b) for GaN/AlN QWs and QDs, respectively. The images show the different morphology of QW and QD layers, both displaying

chemically sharp GaN/AlN interfaces at the atomic scale. The QDs present a height of ∼1 nm and a base diameter of ∼7 nm.

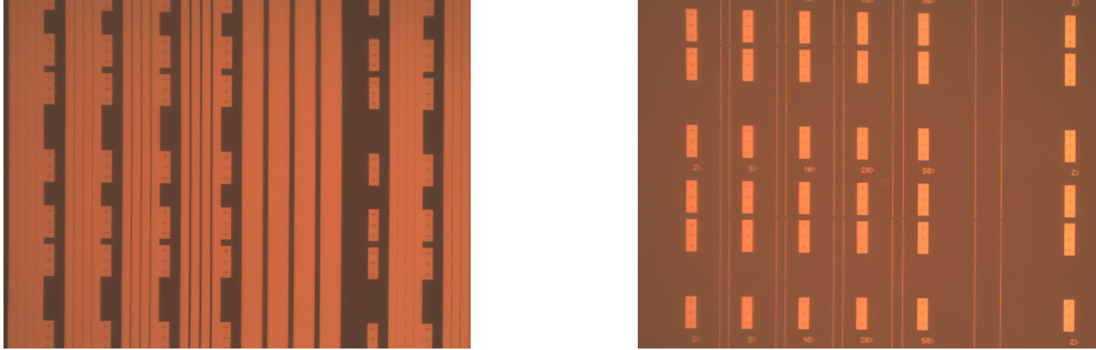

Figure 5.8: Photolithography masks used for the definition of (left) the waveguide patterns and (right) the metallization patterns of the GaN/AlN-based waveguides. Orange regions correspond to the UV opaque chrome zones of the masks.

Concerning the device fabrication, the waveguides were defined by UV lithography with different widths: 2, 5, 10, 20 and 50 μm. The investigations in this work are primarily focused on the two first types of waveguides because of the single mode or quasi-single mode behavior as mentioned before. Two different photolithography mask have been used. The first one for the definition of the optical waveguides on the sample and the other one for defining a metallization in order to easily reference each analyzed waveguide. A negative photoresist has been used in both UV lithography processes leading to a minimum feature size ∼2 μm. The followed procedure is summarized in Fig. 4.8. Images taken by the magnifying glass of both mask are shown in Fig. 5.8. Dark regions correspond to the quartz plate which is transparent to UV light whereas orange zones are the transferring photomask based on chrome patterns (opaque to UV radiation).

The 350-nm-deep ridge was patterned by ICP-RIE using $SiCl_4$ and N_2 plasma at RT taking advantage of its good etching anisotropy and selectivity. The waveguides were cut using an automated dicing saw. After dicing, the samples were mechanically polished to obtain mirror-like facets. A Megapol P200 polishing machine was used for performing a series with diamond polishing films containing different grain size: 30, 15, 9, 6, 3 and 1 μm.

Figures 5.9(a),(b) show the FESEM images of a 2-μm-wide GaN/AlN waveguide tilted 45° and in plane view, respectively.

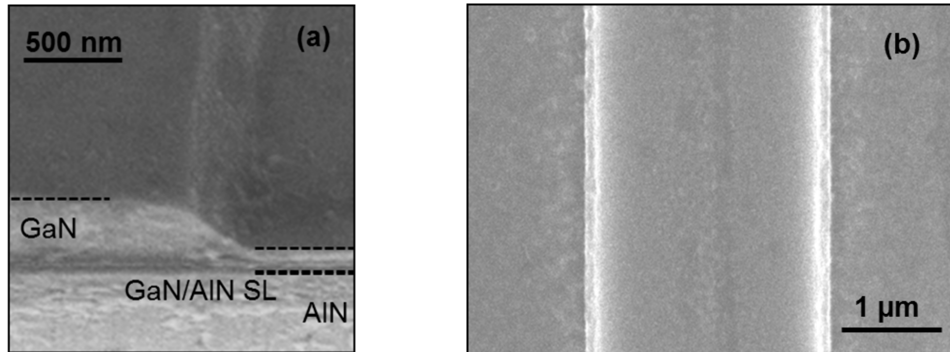

Figure 5.9: FESEM images of a 2-μm-wide GaN/AlN waveguide (a) tilted 45° and (b) in plane view.

5.4 Linear and nonlinear optical measurements

5.4.1 Theory of nonlinear optical absorption

Nomenclature and formalism of light propagation in the linear regime have been previously treated in Chap. 4 in which the optical properties of the material do not depend on the intensity of the excitation field and, thus, the material susceptibility tensor is independent on the applied electric field, $\mathbf{E}(\mathbf{r},t)$. In this situation, polarization vector $\mathbf{P}(\mathbf{r},t)$ is represented by Eq. 4.13.

Contrarily to light propagation in linear regime, nonlinear optics deals with the phenomena that occur as a consequence of the change of the optical properties of a material system by the presence of, typically, intense light provided by a laser. In order to explain the nonlinear behavior of the light propagating through the material, it has been demonstrated that for small nonlinearities, $\mathbf{P}(\mathbf{r},t)$ can be expressed as a function of the applied electric field $\mathbf{E}(\mathbf{r},t)$ by superposing both linear, $\mathbf{P}_L(\mathbf{r},t)=\mathbf{P}^{(1)}$, and nonlinear polarization, $\mathbf{P}_{NL}(\mathbf{r},t)=\mathbf{P}^{(2)}+\mathbf{P}^{(3)}+\cdots$, components [Boy08][GH11]:

$$\begin{aligned}
\mathbf{P} &= \mathbf{P}_L + \mathbf{P}_{NL} = \\
&= \epsilon_0 \int_{-\infty}^{+\infty} \tilde{\chi}^{(1)}(\mathbf{r}, t-t') \cdot \mathbf{E}(\mathbf{r}, t')\, dt' + \\
&+ \epsilon_0 \int\int_{-\infty}^{+\infty} \tilde{\chi}^{(2)}(\mathbf{r}, t-t_1, t-t_2) : \mathbf{E}(\mathbf{r}, t_1)\mathbf{E}(\mathbf{r}, t_2)\, dt_1 dt_2 + \\
&+ \epsilon_0 \int\int\int_{-\infty}^{+\infty} \tilde{\chi}^{(3)}(\mathbf{r}, t-t_1, t-t_2, t-t_3) \vdots \mathbf{E}(\mathbf{r}, t_1)\mathbf{E}(\mathbf{r}, t_2)\mathbf{E}(\mathbf{r}, t_3)\, dt_1 dt_2 dt_3 + \\
&+ \cdots
\end{aligned} \tag{5.3}$$

It has to be noticed that each element $\tilde{\chi}^{(i)}$ is a tensor of rank i and therefore the products inside the integrals are tensor products. The first term of the series is associated to $\tilde{\chi}^{(1)}$ corresponding to the linear response of the material. The second contribution becomes important when dealing with non-centro-symmetric materials. Although III-nitrides do not present inversion symmetry, this work is not focused on the second-order phenomena but just on the third-order phenomena associated with the third-order nonlinear susceptibility $\tilde{\chi}^{(3)}$.

In the linear optical regime, the wave equation in the frequency domain for the electric field has been previously given by Eq. 4.26, where the contribution of the linear polarization $\mathbf{P}^{(1)}$ induced in the medium is included in the parameter $k_0^2 n_i(\omega)^2 - \beta(\omega)^2$. Nevertheless, in nonlinear regimes the wave equation includes the third order nonlinear polarization $\mathbf{P}^{(3)}$ as follows:

$$\nabla^2 \mathbf{E} + (k_0^2 n_i^2 - \beta^2)\mathbf{E} = k_0^2 \mathbf{P}_{NL}^{(3)}(\omega) \tag{5.4}$$

where the nonlinear polarization $\mathbf{P}_{NL}^{(3)}(\omega)$ acts as a source term at the given frequency.

Assuming the light linearly polarized along the x-direction [$\chi_{xxxx}^{(3)}(\omega) = \chi^{(3)}(\omega)$], the total polarization can be described by a scalar expression as [GH11]:

$$\mathbf{P}(\omega) = \epsilon_0 \left(\chi^{(1)}(\omega) + 3\chi^{(3)}(\omega)|E|^2 \right) \mathbf{E}(\omega) = \epsilon_0 \chi(\omega) \mathbf{E}(\omega) \tag{5.5}$$

where $|E|^2$ is the amplitude of the electric field and $\chi^{(3)}(\omega)$ is the complex third-order

susceptibility components with degeneracy of 3. Thus, the total susceptibility contribution is given by:

$$\chi(\omega) = \chi^{(1)}(\omega) + 3\chi^{(3)}(\omega)|E|^2 \quad (5.6)$$

As it can be seen, the nonlinear term can be treated as a correction to the linear susceptibility that depends on the input intensity ($|E|^2 \propto I$). The third-order nonlinear polarization $\mathbf{P}_{NL}^{(3)}(\omega)$ induces a change on the linear refractive index (Δn) and, in addition, on the linear absorption coefficient ($\Delta\alpha$) of the material that depends on the intensity of the input light beam. It is considered that the material responds instantaneously to the applied electric field. The changes introduced by the nonlinear refractive index, n_2, and the nonlinear absorption coefficient, α_2, on the optical properties of the medium are given by:

$$n(I) = n_0 + \Delta n = n_0 + n_2 I \quad (5.7)$$

$$\alpha(I) = \alpha_0 + \Delta\alpha = \alpha_0 + \alpha_2 I \quad (5.8)$$

As the nonlinear polarization depends on the frequency, the $\chi^{(3)}$ value is enhanced when the input light frequency coincides with a resonant frequency of the material.

For transparent media ($\alpha_0 = 0$), the real part of the $\chi^{(3)}$ addresses to the nonlinear refraction whereas the imaginary one drives to the nonlinear absorption as:

$$n_2 = \frac{3}{4}\frac{1}{n_0^2\epsilon_0 c}\Re[\chi^{(3)}] \quad (5.9)$$

$$\alpha_2 = \frac{3\pi}{\lambda}\frac{1}{n_0^2\epsilon_0 c}\Im[\chi^{(3)}] \quad (5.10)$$

For absorptive media ($\alpha_0 \neq 0$), the $\chi^{(3)}$ value quantifies whether light is refracted or absorbed and how much:

$$n_2 = \frac{3}{4}\frac{1}{(n_0^2 + k_0^2)\epsilon_0 c}\left(\Re[\chi^{(3)}] + \frac{k_0}{n_0}\Im[\chi^{(3)}]\right) \quad (5.11)$$

$$\alpha_2 = \frac{3\pi}{\lambda} \frac{1}{(n_0^2 + k_0^2)\epsilon_0 c} \left(\Im[\chi^{(3)}] + \frac{k_0}{n_0} \Re[\chi^{(3)}] \right) \tag{5.12}$$

Among the third-order nonlinear effect, just two types of nonlinear absorptive phenomena have been studied in this work: saturable absorption (SA) which is treated in this current chapter and two-photon absorption (TPA) which will be studied in Chap. 7.

Saturable absorption ($\alpha_2 < 0$)

Figure 5.10 presents a scheme of a system of two electronic levels in which the influence of an intense light beam on the carrier population at the valence band and the conduction band of the material can lead to the reduction of the absorption, even reaching the complete saturation of the absorption.

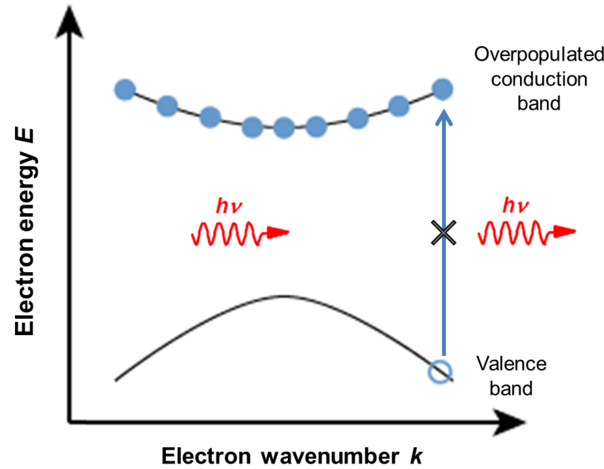

Figure 5.10: Scheme of the optical absorption saturation phenomenon in a two-electronic-level system at resonant energies ($E_{gap} \sim h\nu$).

When the lowest level of the electronic transition is depopulated (whereas the highest level is overpopulated), the probability of absorption decreases due to the non-possible electron-hole recombination and, thus, the optical absorption is completely saturated leading to a total transmission of the input light. Hence, saturable absorbers have an absorption coefficient that decreases when increasing the input light intensity. This

phenomenon is represented by negative values of the nonlinear absorption coefficient ($\alpha_2 < 0$).

The total absorption (α) of the material in the saturation regime shows a dependency with the linear absorption (α_0), the input beam intensity (I) and the material saturation intensity (I_{sat}) given by:

$$\alpha(I) = \frac{\alpha_0}{1 + \frac{I}{I_{sat}}} \tag{5.13}$$

Thus, taking into account Eq. 5.8, the equation which relates the saturation intensity and the nonlinear absorption coefficient is the following:

$$\alpha_2 = -\alpha_0 \left(\frac{1}{I + I_{sat}} \right) \tag{5.14}$$

Hence, for input intensities well below the saturation intensity ($I << I_{sat}$), the nonlinear absorption coefficient is given by $\alpha_2 = -\alpha_0/I_{sat}$. Furthermore, it has to be noticed that for an input intensity equal the saturation, $I = I_{sat}$, $\alpha_2 = -\alpha_0/2I_{sat}$, leading to a value of the total absorption of the material corresponding to half of the linear absorption coefficient value, $\alpha = \alpha_0/2$.

5.4.2 Optical results at linear and nonlinear regimes

Three sets of GaN/AlN-based waveguides have been investigated: 5-μm-wide QW-based waveguide, and 5-μm-wide and 2-μm-wide QD-based waveguides (S1, S2 and S3 in Table 5.1, respectively). The propagation of both TE- and TM-polarizations of light was experimentally examined in the linear and nonlinear optical regimes using the experimental procedure described in Chap. 4.

Coupling and propagation losses of the different waveguides were estimated from the cut-back method under linear optical regime while the optical absorption saturation was investigated under nonlinear optical conditions.

Sample #	Active nanostructures	Ridge width (μm)
S1	QWs	5
S2	QDs	5
S3	QDs	2

Table 5.1: Summary of the GaN/AlN-based waveguides under study concerning the implemented active nanostructures and ridge widths.

5.4.2.1 Linear optical experiments: Cut-back method

The near-field images of the transmitted light in the linear regime can be obtained for each waveguide under study by means of the experimental setup exhibited in Fig. 4.12, collecting the light at the output of the waveguides by using a microscope objective and monitoring it with the help of an IR camera. The near-field images achieved when guiding light at 1.55 μm are shown in Fig. 5.11(a),(b) for the 5-μm- and 2-μm-wide QD-based waveguides, respectively.

Figure 5.11: Near-field images taken with the IR camera of the obtained optical modes at the output of the (a) 5-μm-wide and (b) 2-μm-wide QD-based waveguides.

In other respects, the cut-back method is performed for the estimation of both propagation and coupling losses [Hun84], measuring the transmittance of TE- and TM-polarized light through similar waveguides with different lengths, under low incident power conditions (-12 dBm, well below the absorption saturation level). It has to be pointed out that, in this case, the different lengths of the waveguides have been obtained by polishing the output facet with a slight angle ($\sim$3°). Thus, for all the waveguides under study, coupling losses obtained through the cut-back method are expected to be overestimated.

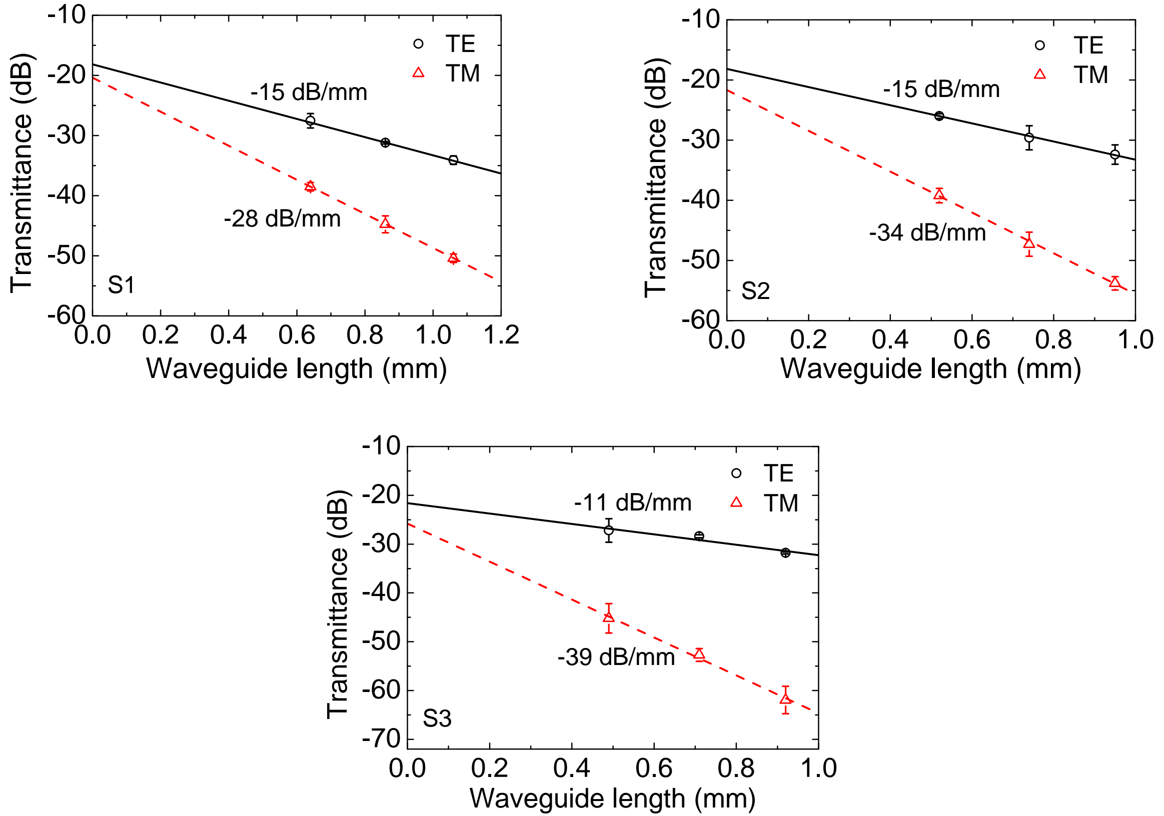

Figure 5.12: Cut-back method: Experimental TE-TM transmittance at minimum incident power (-12 dBm) as a function of the waveguide length for the devices under study (S1-S3). The experimental points correspond to the average of transmittance measurements in three waveguides for each waveguide length.

Figure 5.12 shows the variation of the transmittance as a function of the waveguide length for the three samples. From data obtained for sample S1, propagation losses in the range of ~28 dB/mm for TM-polarized light are extracted, including saturable and non-saturable losses. The 2 dB difference between TM and TE coupling losses is likely due to the asymmetry of the waveguide geometry. Since all the waveguides under study present asymmetry in their transverse profile (wider than higher GaN ridge), a difference in coupling losses between TM- and TE-polarized propagating light always exists. On the other hand, the propagation losses for TM-polarized light increase up to ~34 dB/mm when using QDs in the active region (S2) which reveals that QDs are more absorptive than QWs. Coupling and propagation losses for TE-light are similar (18 dB and 15 dB/mm, respectively) in samples S1 and S2 since this polarization of light is only affected by the waveguide transverse dimensions and not by the active region. Finally, propagation losses for TM-light increase up to ~39 dB/mm when reducing the ridge width to 2 μm (S3) leading to a better

confinement of the optical mode making more efficient the absorption at the active region. However, the propagation losses for TE-light decrease to 11 dB/mm due to the better confinement of the coupled light through the waveguide which gets the light mode away from the ridge sidewalls. At the same time, coupling losses for both polarizations increase in 4 dB (up to 22 dB for TE-light and 26 dB for TM-light) due to the worse injection of light into the waveguide.

In the following transmittance measurements performed in isolated optical waveguides, we have considered that the measured coupling losses are equally distributed between both facets.

5.4.2.2 Nonlinear optical absorption saturation measurements

Figure 5.13(a) illustrates the transmittance measurements for TE- and TM-polarized light as a function of the incident optical power and the input pulse energy for a 1-mm-long S1 waveguide. The transmittance of TE-polarized light is constant for the analyzed power range. In contrast, the transmitted TM light increases with the incident optical power due to the saturation of the $e_1 - e_2$ ISB absorption in the waveguides. Taking into account the coupling losses at the input facet, the input pulse energy required for reaching 10 dB contrast for TM-polarized light is taken as the figure of merit in order to evaluate the efficiency of the absorption saturation of the different devices and compare the obtained results in this work to others reported previously. Table 5.2 summarizes the input pulse energy required for reaching 3-dB- and 10-dB-transmittance contrast for TM polarization between linear and nonlinear optical regimes. These values are highlighted in Figs. 5.13(right) for the three devices under study.

Sample #	**Active nanostructures**	**Ridge width (μm)**	**Energy for 3 dB TM contrast (pJ)**	**Energy for 10 dB TM contrast (pJ)**
S1	QWs	5	8	24
S2	QDs	5	5	13
S3	QDs	2	3	8

Table 5.2: Summary of the experimental input pulse energy required for reaching 3-dB and 10-dB of optical transmittance contrast for TM light for the three samples under study.

Then, in the case of the 5-μm-wide QW-based waveguide (S1), a 10 dB change in the TM transmittance is achieved for input pulse energies of $\sim$24 pJ with 150-fs pulses [see Fig. 5.13(b)], lower than the 38 pJ reported by Li *et al.* [Li07a][Li07b][Li08] in a similar waveguide structure (600 nm GaN on AlN, 1-mm-long waveguide and 3-μm-wide ridge) but incorporating 30 GaN/AlN QWs. In this latter structure, the QWs were inserted between the AlN and the GaN layers without using any GaN buffer layer. Our achievement of similar (or even slightly better) results with only 3 QWs could be explained by the partial depletion of the 30-QW structure due to piezoelectric and spontaneous polarization presenting the active region far away from the Fermi level, as exhibited in Fig. 5.6(right). Thus, only a few of the 30 QWs would participate to the ISB absorption in ref. [Li07a].

Figures 5.13(c),(d) depict the optical TE and TM transmittance and the transmittance increase for TM-polarized light, respectively, as a function of the input pulse energy for a 5-μm-wide QD-based waveguide (S2) with a length of 1.5 mm. In this case, input pulse energies of $\sim$13 pJ are required to obtain a 10 dB change in the TM light transmittance, assuming similar coupling losses as those estimated for both 5-μm-wide QW- and QD-based waveguides. The improvement obtained in comparison to the QW structure might be explained by the three dimensional confinement in the QDs, which prevents lateral escape of carriers, thus favoring absorption saturation.

The transmittance contrast for TM-polarized light can be further enhanced by reducing the waveguide ridge to 2 μm (S3) to obtain single mode propagation, as illustrated in Figs. 5.13(e),(f). In this case, the input pulse energy required for 10 dB absorption saturation is as low as $\sim$8 pJ with 150 fs pulses while just 3 pJ of input pulse energy is required for reaching a transmittance contrast of 3 dB. This reduction in the required energy is attributed to the more efficient light pumping of the QDs active region due to the better confinement of light in the single mode structure. This 2-μm-wide GaN/AlN QD-based waveguide presents the most suitable behavior for application in ultrafast all-optical switching since it shows the highest transmittance contrast for the lowest required input pulse energy.

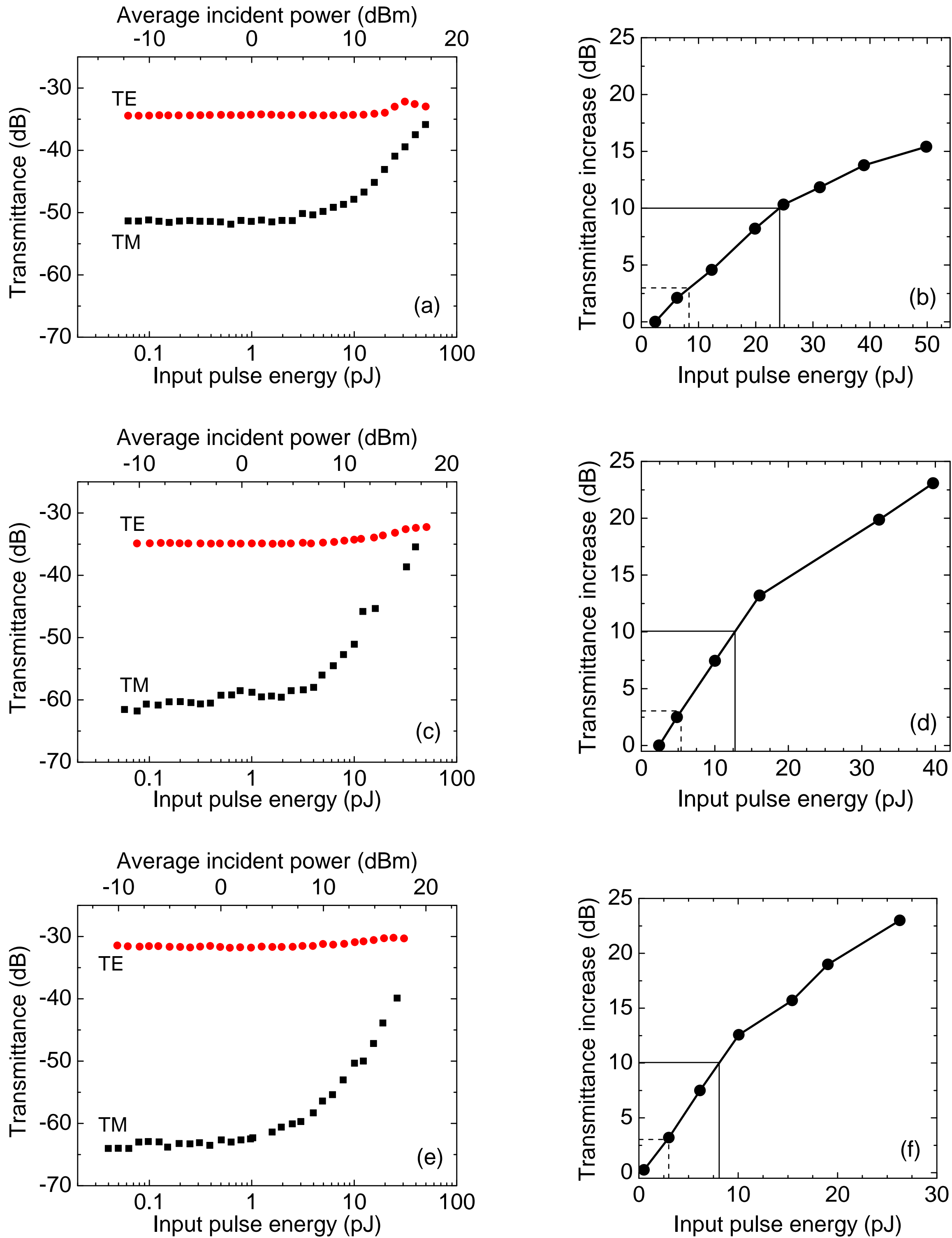

Figure 5.13: Transmittance for TE- and TM-polarized light (left) and transmittance increase for TM-polarized light (right) versus control pulse energy in (a,b) a 1-mm-long 5-μm-wide QW-based WG (S1), (c,d) a 1.5-mm-long 5-μm-wide QD-based WG (S2), and (e,f) a 1.5-mm-long 2-μm-wide QD-based WG (S3).

5.5 Conclusions

In this chapter, three different types of GaN-on-AlN optical waveguides based on quantum heterostructures have been developed and characterized. They have been demonstrated as saturable absorbers at 1.55 μm via their ISB transition only accessible for TM-light. This absorptive nonlinear optical behavior makes them suitable for application in all-optical switching at 1.55 μm.

Two different samples of GaN layers grown on 1.1-μm-thick AlN-on-sapphire substrates were obtained by PAMBE, while embedding 3 periods of GaN/AlN QWs or QDs, respectively. The band gap energy of the heterostructures can be tuned at 1.55 μm through band gap engineering. Electrical simulations provide the optimized GaN QWs thickness ($\sim$1.5 nm) and the GaN QDs height and diameter ($\sim$1 nm and $\sim$7 nm, respectively). At the same time, AlN barriers thickness was fixed to $\sim$3 nm. Furthermore, the optimized position of the active region was at least 25 nm on top of the AlN-template, ensuring the population in the first confined electronic level.

The GaN guiding layer thickness was optimized by optical simulations to 600 nm ensuring the modal guiding when considering a minimum ridge width of the further waveguide of 2 μm. The optimized etching depth was 350 nm for which the 2-μm-wide waveguides were single mode while devices with widths of 5 μm and larger behave as multimode waveguides. Considering the position of the maximum of the mode amplitude through the waveguide (250 nm above the AlN-template) and, in addition, the limitations for locating the active region (given by electrical simulations), QWs were placed at 250 nm and QDs just at 25 nm above the substrate.

All the GaN/AlN samples were waveguide patterned with widths of 2 μm and 5 μm by UV lithography. Furthermore, they were etched by ICP-RIE using $SiCl_4$ and N_2 plasma at RT. The polishing procedure was carried out by using diamond lapping films with grain sizes ranging from 30 μm to 1 μm.

Optical transmittance measurements were performed for the three following GaN/AlN-based devices: 5-μm-wide QW-based, 5-μm-wide QD-based and 2-μm-wide QD-based waveguides.
The cut-back method performed for all the GaN/AlN waveguides indicates that

optical coupling losses for TE- and TM-light increase when reducing the width of the ridge from 5 μm to 2 μm due to the reduction of the coupling area. When considering both QD-based waveguides, the coupling losses increase 4 dB from the 5-μm-wide waveguide to the 2-μm-wide one, particularly, from 18 dB to 22 dB for TE light and from 22 dB to 26 dB for TM polarization.
Propagation losses for TE light are kept constant when replacing the QWs by QDs (15 dB/mm) as the active region. However, they are reduced (from 15 dB/mm to 11 dB/mm) when decreasing the ridge width from 5 μm to 2 μm, due to the better confinement of light. However, for TM light, the propagation losses increase from 28 dB/mm to 34 dB/mm when replacing the QWs by QDs, enhancing the absorptive effect due to the 3D carrier confinement. Furthermore, these losses are even more increased up to 39 dB/mm when reducing the width of the waveguide to 2 μm, inducing the single mode propagation condition.
Nonlinear optical transmittance measurements at 1.55 μm for all the GaN/AlN-based devices show a constant transmittance for TE-light from low to high incident optical power (from -12 dBm to 17 dBm). Contrarily, high transmittance changes for TM-polarized light are obtained within this range of power due to the activation of the ISB transition. In the case of 5-μm-wide QW-based waveguides (S1), the transmitted TM-light increases with the incident optical power due to the saturation of the $e_1 - e_2$ ISB absorption in the QWs. A 10 dB change in the transmittance of TM-polarized light is achieved for input pulse energies of ~24 pJ with 150 fs pulses. This value is improved by almost a factor of 2 (~13 pJ) by the replacement of QWs by QDs as active media (via the $s - p_z$ transition) maintaining the same waveguide width (5 μm), thanks to their three-dimensional carrier confinement. In addition, the reduction of the ridge width from 5 μm to 2 μm results in a further decrease of the required input pulse energy to ~8 pJ for 10-dB-modulation, taking advantage of the single mode propagation along the waveguide. In this latter device, the input pulse energy required for reaching the 3-dB change of transmittance is 3 pJ. Thus, the developed 2-μm-wide GaN/AlN QD-based waveguide is considered the best in terms of further application in all-optical switching since it presents the highest transmittance contrast for the lowest required input pulse energy with 150-fs pulses.

Chapter 6

Passive sputtered-AlN-based optical waveguides

This chapter deals with the growth, characterization and optical response of AlN films deposited on (0001)-oriented sapphire by RF reactive sputtering. Furthermore, the capability of sputtered-AlN optical waveguides acting as passive light pathways is demonstrated aiming at their further integration within III-nitride-based PICs working at telecom wavelengths.

The first section focuses on the state-of-the-art of both the deposition of AlN films by RF reactive sputtering and the use of the AlN waveguide devices in photonic circuits. The next section contains the followed approach for the optimization of AlN films grown on sapphire in terms of structural, morphological and optical quality. Within this framework, different deposition parameters such as RF power, substrate temperature and substrate bias are investigated. Once the AlN layer is optimized for the required application by using a developed two-step deposition method, the third part of this Chapter presents the optical design and the fabrication procedure of the waveguides based on sputtered-AlN layers. Finally, optical characterization results of the optimized AlN-based waveguides are shown. Part of the work presented in this chapter has been reported as a journal paper in Thin Solid Films [ML13b].

6.1 Introduction

As it has been explained in Chap. 1, the achievement of promising PIC technology requires the development of both active and passive devices. The use of structures based on group III-nitrides such as GaN/AlN heterostructures has already been demonstrated suitable for all-optical data processing in a PIC operating at 1.55 μm, as it has been seen in Chap. 5. It would be desirable that the whole PIC device was developed using the same semiconductor family in order to reduce the interconnection losses between the different active elements while minimizing the lattice mismatch between the different materials. For this reason, taking profit of the non-absorptive optical behavior of AlN at 1.55 μm (due to its wide direct optical band gap energy of $\sim$6.2 eV [Gil98]), passive AlN-based waveguides can be suitably designed and fabricated to act as optical passive light pathways within the III-nitride-based PIC.

It must be pointed out that, in addition to its large band gap which prevents the signal absorption via multiple photon processes at 1.55 μm, AlN also presents high mechanical and thermal robustness together with a very low rms surface roughness. This material flatness will improve the light guiding by maintaining a nearly constant air-AlN contrast throughout the whole device.

Most reported works on AlN photonic devices are focused on the AlN-on-insulator platform which can implement linear and nonlinear functions within a silicon-based PIC. This system is widely used instead of silicon, which presents a small band gap ($\sim$1.1 eV), leading to wavelength restriction operations above 1100 nm. Particularly, reported AlN-on-silicon-based structures have been optimized for different photonic devices via linear phenomena in the visible/NIR range and also nonlinear processes such as second harmonic generation at 1.55 μm. Among the passive functions performed by AlN-based structures, optical waveguide directional couplers together with variable ratio beam splitters [Ste13a], optical microring resonators [Per12] and passive interconnecting waveguides [Alv14] have been reported. On the other hand, electro-optical modulators and second harmonic generators via $\chi^{(2)}$ nonlinear optical phenomena have been implemented by active AlN-based devices [Xio12].

Contrarily to the common use of AlN-on-silicon-based devices, this work is focused on AlN-on-sapphire structures for further implementation within III-nitride-based

PICs. In this case, the nitride structure will be used as a passive optical waveguide. Since the AlN-based optical pathways would interconnect different devices grown on sapphire platform (for example the previously optimized active GaN/AlN structures in Chap. 5), it is required that the substrate keeps the same in order to reduce interconnection losses.

Focusing on the AlN material, AlN is considered attractive due to its interesting combination of properties which entails a large field of application. Its wide direct band gap makes AlN a suitable semiconductor for application in several optoelectronic active devices in the ultraviolet spectral region, such as light emitting diodes [Tan06][Gra12]. On the contrary, AlN is transparent in the visible and infrared regions presenting high optical transmittance. AlN also presents high acoustic velocity being essential for the fabrication of surface acoustic wave devices [Ass04] together with a strong piezoelectricity which makes it suitable for application in micro-electro-mechanical systems [Gio09]. Besides, AlN is a good electrical insulator while exhibiting low material density (3.27 g/cm^3 [Drü00]), high thermal conductivity and mechanical hardness. Considering also its chemical stability, AlN is a suitable candidate for protective optical coatings and surface passivating layers. It is also widely used as buffer layer for the growth of GaN, in order to reduce the lattice mismatch, stabilize the metal polarity and prevent unwanted reactions between GaN and the substrate [Luo08][Yan09][Yen12]. It is worthy to comment that AlN thin films are also commonly used for application as buffer layers for InN deposition. Since the lattice mismatch between InN and AlN is significantly lower than that between InN and sapphire substrate, the use of an AlN buffer leads to an improvement of the crystalline quality of the on-top InN film [Kis93][Lu01].

AlN films have been grown by different techniques such as metalorganic vapor phase epitaxy (MOVPE) [Tan07][Lob08], hydride vapor phase epitaxy (HVPE) [Kam06], molecular beam epitaxy (MBE) [Kar97][Kob03] and laser pulsed deposition [Cib04], most of them requiring expensive technology and high substrate temperature. RF reactive magnetron sputtering represents an attractive low-cost technique to synthesize AlN films, allowing deposition in a wide range of temperatures and in both rigid and flexible substrates. Furthermore, reactive sputtering can be easily transferred from small scale in laboratories to large size in industries maintaining the layer properties. Although, nowadays, $\sim$2″-diameter free-standing AlN substrates are

commercialized [Nit14], they are not cost-effective enough. Thus, highly *c*-oriented AlN films deposited on different substrates are often used as the alternative for obtaining large-sized AlN films. The most common substrates used for the deposition of AlN layers are SiC, Si and sapphire [Tun00][Xu01][Hut02][Che03][Zha05][Guo06]. Among them, 6H-SiC(0001) substrate is the most suitable for growing AlN films due to the low lattice mismatch (∼1.0% at RT) [Man00] and the very similar thermal expansion coefficients between AlN and SiC. Nevertheless, regarding technological cost-efficiency, SiC substrates are costly. On the other hand, Si is the cheapest substrate while the lattice mismatch between AlN and Si(111) is quite larger (∼19%) than that between AlN and sapphire (∼13%) (see Table 2.6).

Several papers in the literature deal with the optimization of the sputtering parameters for AlN deposition. Nevertheless, a general influence of these deposition parameters on the orientation of the AlN layers, the crystal quality or the growth rate has not been established. Many parameters are also intrinsic of the sputtering system and its related equipment such as the used substrate, base pressure or target-substrate distance.

In the case of the sputtering chamber pressure, it seems to be established that low pressures induce a preferential growth orientation of AlN films along the *c*-axis evolving to (10-10)-oriented films when increasing the deposition pressure [Xu01][Che03]. The structural quality of *c*-AlN suffers in turn a worsening when raising the sputtering pressure [Seo10][Iri10]. At the same time, several groups have demonstrated with their respective experimental equipment that the growth rate of AlN films by reactive sputtering increases as the pressure decreases [Ekp05][Chi07].

Furthermore, concerning the influence of mixture of N_2 and Ar as the process gas, whereas Clement *et al.* observe that the AlN(0002) orientation tends to disappear when increasing the ratio of N_2/Ar [Cle03], other authors deposit *c*-AlN at high N_2/Ar ratio [Ver04][Chi07]. Nevertheless, among these latter reports, Vergara *et al.* improve the AlN crystal quality when raising the N_2/Ar ratio while Chiu *et al.* do not obtain a clear tendency of the FWHM of the rocking curve around the AlN(0002) diffraction peak with the N_2/Ar ratio. However, in terms of deposition rate, it can be noticed that most of researches are in agreement with the lowering of the growth rate with the increase of the N_2/Ar ratio. This is justified mainly on the likely nitridation of the target in reactive sputtering.

Something similar can be pointed out when investigating the power applied to the

target. In this case, some authors present a reduction of the FWHM of the AlN(0002) rocking curve when increasing the power [Iri10]. Nevertheless, other investigations do not reach a clear tendency within the analyzed range [Aki98][Chi07]. Anyway, it has to be noticed that in general terms, AlN growth rate increases with the power applied to the target [Guo06][You07].
Finally, the influence of substrate temperature on the crystal quality of *c*-AlN films lead to controversial results depending on the research group. Iriarte *et al.* achieve an improvement of the structural quality of the AlN layers when raising the substrate temperature [Iri10] while Guo *et al.* obtain the opposite effect [Guo03] when investigating a similar range of temperatures.

In this work, the influence of several deposition parameters on the AlN film properties is investigated with the aim of clarifying some of those aspects when growing on *c*-sapphire by RF reactive sputtering.

6.2 AlN films synthesized by RF reactive sputtering

The deposition of AlN layers during this Thesis was carried out by using the RF magnetron sputtering system presented in Chap. 2. In all cases, the growth proceeded in high-purity (6N) N_2 atmosphere using a 2-inch Al target (5N). The distance between target and substrate/substrate holder was kept constant at 10.5 cm. Prior to growth, the substrates were cleaned for 10 min in organic solvents (acetone at ~40 °C followed by methanol at RT) and outgassed in the deposition chamber for 30 min at a substrate temperature of 550 °C (100 °C above the growth temperature). This outgassing procedure was optimized to ensure a base pressure of $\sim 10^{-5}$ Pa for all the sputtering processes presented in this Thesis. Then, the Al target was cleaned for 10 min with Ar (5N) plasma at 150 W of RF power and a chamber pressure of 0.67 Pa. This step was carried out before each deposition in order to remove the likely contamination of the target surface induced during the substrate loading process. Additionally, the substrates were cleaned for 5 min with Ar plasma at 20 W and 1.33 Pa.

The sputtering parameters studied were the RF power (P_{RF}), substrate temperature (T_{subs}) and substrate bias (V_S) over the range of values summarized in Table 6.1. Other parameters such as the 0.47 Pa of sputtering pressure and the pure N_2 atmosphere were kept constant for all the AlN growth processes considering previous results in InN layers using the same sputtering system [VF10]. The choice of the nitrogen atmosphere is also supported by previous experiments for AlN growth with different N_2/Ar atmospheres, showing the best crystal quality for samples deposited in pure nitrogen, despite the associated reduction of the growth rate. This reduction is attributed to a likely nitridation of the target together with the lowering of the sputtering yield by the N_2 plasma compared to the Ar plasma [Rav99]. However, a reduced deposition rate is not always a drawback since it allows AlN films to be used in a further implementation as thin buffer layers for the deposition of InN by RF sputtering as will be presented in Chap. 7.

Parameter	**Value**
Deposition pressure	0.47 Pa
Reactive gas, N_2	100 %
RF power	100, 125, 150, 175 W
Substrate temperature	350, 400, 450, 500 °C
Substrate bias	Floating, +5, -5, -15, -25, -35 V
Deposition time	2 h

Table 6.1: Sputtering parameters investigated for the deposition of AlN films.

6.2.1 Effect of RF power

A set of AlN samples was deposited on *c*-sapphire at T_{subs} = 400 °C and ranging the RF power from 100 W to 175 W. Considering the magnetron dimensions and the power density tolerated by the Al target used in this Thesis (~15 W/cm^2), the maximum theoretical power level supported by the Al target without inducing any damage is ~300 W [Les10]. This maximum value is large enough compared to the power range under study. For this set of samples, the substrate was not externally biased during the deposition process, *i.e.*, the growth is carried out under floating substrate (F.S.) configuration.

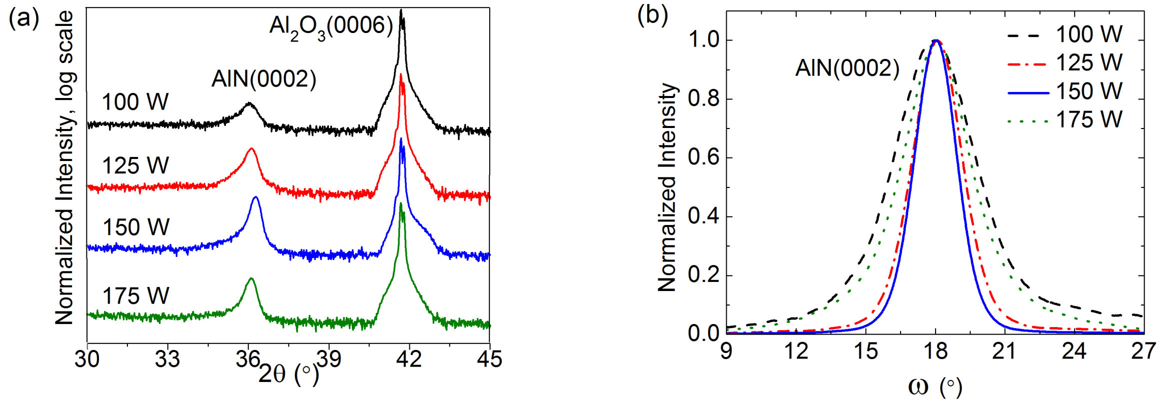

Figure 6.1: (a) HRXRD $2\theta/\omega$-scans and (b) ω-scans of AlN films deposited on *c*-sapphire substrates at 100% N_2, 0.47 Pa, 400 °C and floating substrate as a function of the RF power.

Figure 6.1(a) illustrates the HRXRD $2\theta/\omega$-scans for this set of AlN samples. All the AlN films under study present *c*-axis preferred growth orientation showing the AlN(0002) diffraction peak with the absence of reflections related to any other crystal orientation. The structural quality is estimated from the FWHM of the ω-scan around the AlN(0002) x-ray reflection peak. Figure 6.1(b) exhibits the evolution of the FWHM of the rocking curve as a function of P_{RF} for this set of samples. As it can be observed, the structural quality of the AlN layer is enhanced when increasing the RF power applied to the Al target from 100 W to 150 W, decreasing the FWHM of the rocking from 4.26° to 2.18°. This improvement is attributed to the increase in the energy of the Al species arriving to the substrate. At the same time, the target sputtering rate raises inducing, consequently, an increase in the AlN deposition rate from 45 nm/h to 63 nm/h (obtained from XRR measurements) within that P_{RF} range with an estimated error of ∼5 nm/h. This amelioration of crystal quality and increase of growth rate with the power is in agreement with results presented by other authors both on sapphire and other different substrates [Chi07][Vas09][Iri10][Jin12]. In contrast, further increase of P_{RF} up to 175 W leads to a higher AlN deposition rate (88 nm/h) (see Fig. 6.2) together with a degradation of the structural quality presented by the increase of the FWHM of the AlN(0002) rocking curve up to 3.80°. The likely re-sputtering process of the atoms of the growing-layer due to the highly energetic impinging species could explain this degradation of the crystalline quality. In the range of RF power under study, the energy of the species arriving at the

growing-layer is not significantly affected by successive collisions with the filling gas in the chamber since the mean free path of the particles at the deposition pressure of 0.47 Pa is ∼0.2 m, twice the distance between the target and the substrate in our sputtering system.

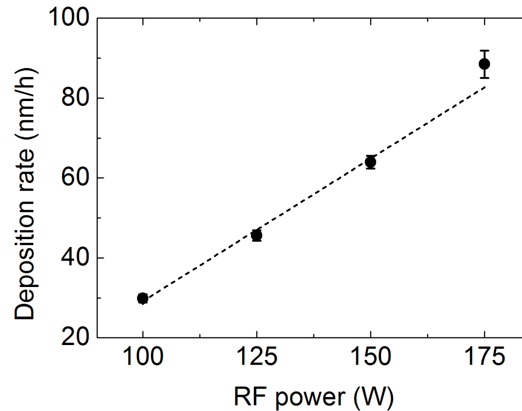

Figure 6.2: Growth rate for AlN films deposited on *c*-sapphire at a sputering pressure of 0.47 Pa, T_{subs} = 400 °C and pure nitrogen atmosphere as a function of the RF power applied to the Al target.

Figure 6.2 demonstrates that the AlN growth rate depends linearly on the RF power applied to the Al target. It has to be noticed that effects linked to high density plasma conditions such as rarefaction can be neglected, as it induces a nonlinear dependence of deposition rate with power [Ros88][Ekp05][And09]. Furthermore, it must be pointed out that the rarefaction is particularly important for sputtering pressures well above 1 Pa [Kol08] and for atoms flux arriving to the growing surface above 5×10^{19} atoms/m^{2}s [Pal06]. In this case, the largest deposition rate obtained for the AlN films studied in this Thesis is ∼90 nm/h which leads to an atom flux of $\sim1.2\times10^{19}$ atoms/m^{2}s. This estimated atom flux together with the used sputtering pressure of 0.47 Pa support the gas rarefaction to be negligible.

Figure 6.3 shows the measured rms surface roughness as a function of the RF power together with the corresponding AFM images taken on 1×1 μm^2 scanned areas. The evolution is similar as in the case of the FWHM of the AlN(0002) rocking curve. As it has been commented previously, the increase of P_{RF} from 100 W to 150 W induces an increase of the energy of the impinging species resulting in turn in a higher mobility of the atoms on the growing surface. This enhanced adatoms mobility leads to extremely

flat films decreasing the rms surface roughness of the AlN layers from 1.8 nm to 0.3 nm. It must be pointed out that the rms roughness value of the used two-face-polished c-sapphire substrate is also ∼0.3 nm [see AFM image in Fig. 2.16(a)].

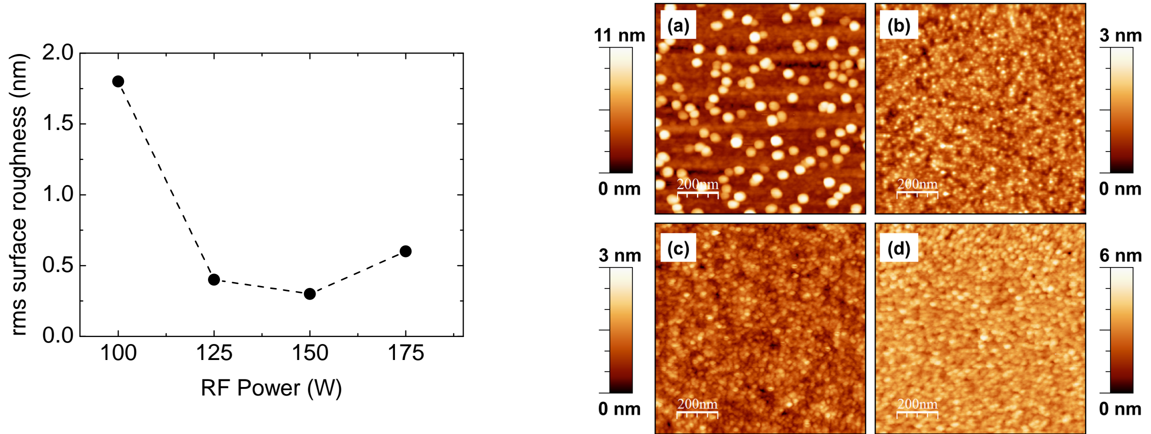

Figure 6.3: (Left) rms surface roughness measured by AFM on 1×1 μm^2 scanned area as a function of the RF power for the AlN layers under study. (Right) AFM images depending on the RF power: (a) 100 W, (b) 125 W, (c) 150 W and (d) 175 W.

Nevertheless, a further increase of the RF power up to 175 W results in a slight degradation of the surface morphology of the layer obtaining, in this case, AlN layers with rms roughness of 0.6 nm. For all the analyzed samples, results achieved in 1×1 μm^2 surface areas are consistent with measurements carried out in larger (2×2 μm^2) and lower (0.5×0.5 μm^2) scanning scales.

Concerning the optical properties of the AlN samples under study, Fig. 6.4 shows the linear optical transmittance (Tr) spectrum of the AlN layer deposited at 150 W. The absorption coefficient of the sample was derived from Tr using the relation $\alpha(\lambda) \propto$ -ln(Tr), which neglects the losses introduced by interfaces reflection and optical scattering. The obtained absorption was modeled using a sigmoidal approximation given by Eq. 3.7. The band gap energy estimation is then obtained by the intersection of the linear fitting to α^2(E) with the x-axis (see Fig. 6.4). This linear fitting leads to an estimated optical band gap of ∼6.02 eV for the AlN film deposited at 150 W. It has to be noticed that all the AlN samples of this set present similar band gap energies ∼6.0 eV which is in good agreement with the previously reported value in the literature for AlN samples deposited by RF sputtering [Gue11].

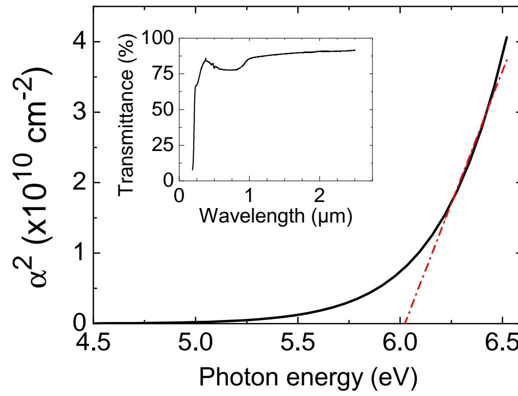

Figure 6.4: Linear fitting of the experimental square absorption coefficient of the optimized AlN layer deposited at 150 W presenting an estimated band gap energy of 6.02 eV. Inset: Linear optical transmittance spectrum of the AlN sample in the wavelength range from 190 nm to 2500 nm.

These linear transmittance measurements were performed in the 190-2500 nm spectral range under normal incidence and at RT using a UV/VIS/NIR Perkin-Elmer Lambda 1050 scanning spectrophotometer. This optical characterization was carried out in collaboration with Dr. Susana Fernández from the Centro de Investigaciones Energéticas, Medioambientales y Tecnológicas (CIEMAT) in Madrid.

6.2.2 Effect of substrate temperature

Once the RF power has been optimized to 150 W, the next step is to investigate the influence of the substrate temperature on the properties of sputtered AlN films. A set of AlN samples was deposited at substrate temperatures ranging from 350 °C to 500 °C, keeping P_{RF} = 150 W, a sputtering pressure of 0.47 Pa and pure N_2 atmosphere. Similarly to the set of samples deposited by varying the RF power, HRXRD $2\theta/\omega$-scans reveal that all AlN films of this set maintain the orientation along the c-axis without any other crystal orientation.

Concerning the structural quality of the layers, Fig. 6.5 exhibits the FWHM of the rocking curve of the AlN(0002) x-ray reflection and the estimated grain size as a function of the substrate temperature. As it can be observed, an improvement of the crystal quality of AlN films is achieved when growing at 400 °C and 450 °C with the minimum value of the FWHM of the rocking curve of 1.91°, being obtained for the sample deposited at 450 °C.

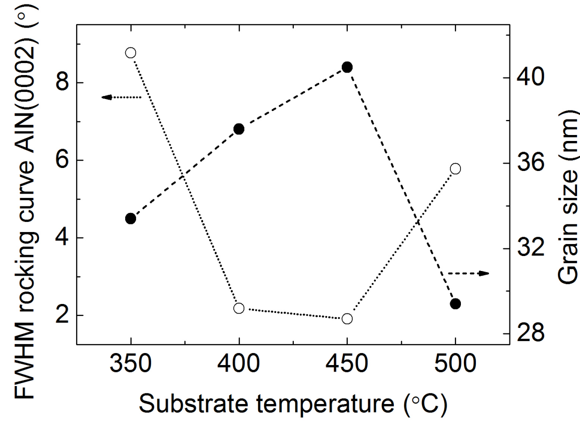

Figure 6.5: FWHM of the rocking curve of the AlN(0002) x-ray reflection and grain size as a function of substrate temperature for AlN layers deposited at 150 W, 0.47 Pa and 100% N_2.

However, both AlN layers deposited at 350 °C and 500 °C show larger values of the FWHM. Thus, on the one hand, the worsening in the case of deposition at 350 °C is attributed to the reduction of the mobility of the impinging species at low substrate temperatures. By contrast, the degradation of the layer when growing AlN at 500 °C is associated to the increase of the desorption rate of physi-adsorbed atoms from the substrate at high substrate temperature as observed by Guo *et al.* [Guo03]. This desorption enhancement leads to a decrease of the gran size, obtained from the FWHM of the HRXRD $2\theta/\omega$-scan by Scherrer's formula (see Eq. 3.2), for $T_{subs} = 500$ °C. This effect is also supported by a reduction of the growth rate from ∼64 nm/h estimated for the AlN deposited at 400 °C to ∼52 nm/h being the lowest value corresponding to the layers grown at 500 °C. In relation to the surface morphology of the AlN films obtained by varying the substrate temperature, the rms roughnesses measured by AFM on 1×1 μm^2 area remain in the range from 0.3 nm to 0.6 nm. At the same time, the band gap energies estimated by the sigmoidal model for all the films are kept without variation at ∼6.0 eV.

From these results, the optimized substrate temperature was 450 °C.

6.2.3 Effect of substrate bias

The third deposition parameter investigated for the AlN film growth optimization is the DC bias applied to the substrate during the sputtering deposition process. The

adequate tuning of the substrate bias during deposition can be a critical parameter to improve the crystalline quality of the AlN layer [Cle03]. The effect of the substrate bias on the layer quality was investigated by applying a DC voltage to the substrate during deposition. In these experiments, the substrate bias was varied from +5 V to -35 V keeping constant the rest of the growth conditions: 150 W, 0.47 Pa, 450 °C and 100% N_2. It is worth saying that the AlN deposition under floating substrate conditions leads to a substrate DC self biasing of -3.8 V.

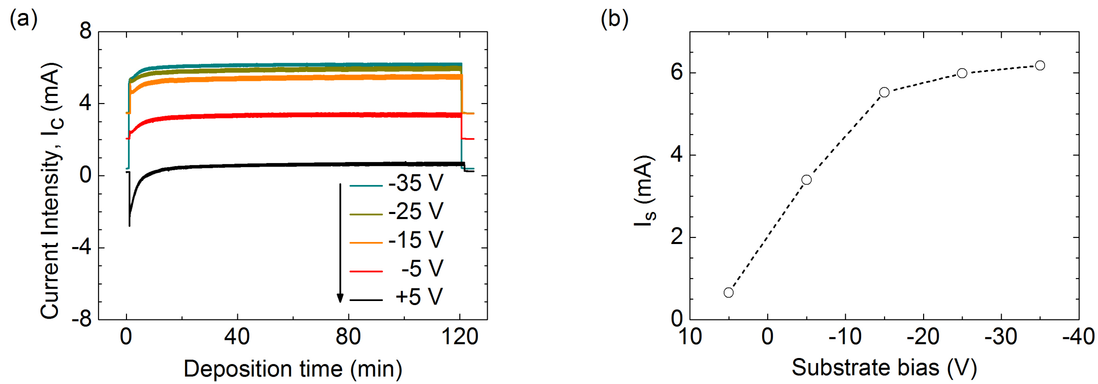

Figure 6.6: (a) Real-time evolution of the current I_c during the AlN deposition process for 2 h for different values of substrate bias. (b) Saturation intensity, I_s, as a function of the bias applied to the substrate during the AlN deposition process.

Considering the circuit formed by the biased substrate, the plasma environment and the grounded sputtering chamber in the experimental setup, the current intensity, I_c, flowing through the circuit was monitored during the AlN deposition (see the scheme of the substrate biasing method in Fig. 2.12). As illustrated in Fig. 6.6(a), the time-dependent evolution of I_c follows the characteristic behavior of a capacitor charging process, with a transient time during which the arrival of positively charged ions partially compensates the externally negative bias applied to the substrate. After this transient time, I_c saturates to a value I_s. Figure 6.6(b) shows that the I_s value linearly increases with DC bias from +5 V to -15 V while tends to saturate when biasing at -25 V and -35 V.

Concerning the surface morphology, the AlN films under study present rms roughnesses in the range of (0.6±0.1) nm for 1×1 μm^2 scanning area.

Figure 6.7 shows that the deposition rates of all the AlN films are within the range of (60±5) nm/h, obtained from XRR measurements. The film density of this set of samples was also estimated from XRR measurements (from scans similar to that shown in Fig. 3.5 and by using Eq. 3.3). Figure 6.7 shows that the film density increases with the substrate bias from +5 V to -15 V and strongly decreases when biasing at -25 V and -35 V. It is worth saying that for the sample deposited at -15 V of substrate bias, the estimated film density is 3.24 g/cm^3, close to the AlN bulk density of 3.27 g/cm^3 [Drü00]. Measurements of the saturation intensity values, growth rates, grain sizes and the estimation of film densities lead to the understanding of the evolution of the AlN layers within this set.

Within the range from -5 V to -15 V and taking into account the substrate self-biasing at floating conditions (-3.8 V), the deposition rate linearly increases together with the film density inducing the increase of both the number and energy of the adatoms reaching the substrate. This presence of higher number of available ions is supported by the raising evolution of the measured saturation intensity values within the range of bias under study [see Fig. 6.6(b)]. Thus, without variation of temperature, it is possible to enhance the adatom mobility at the substrate leading to larger grain size of the AlN layer while improving its structural quality (see Fig. 6.8).

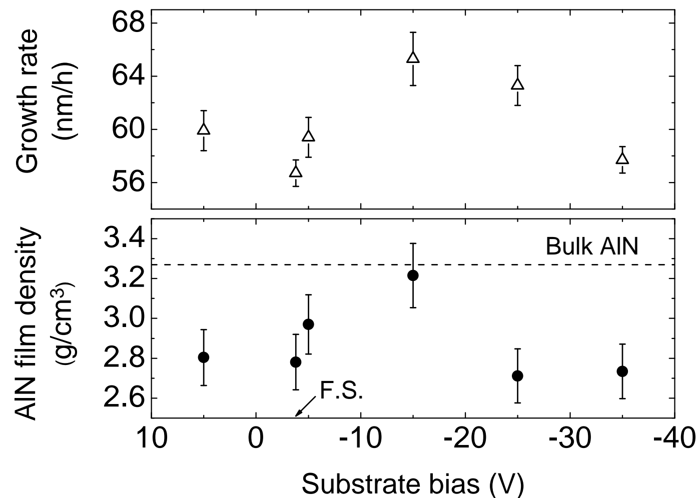

Figure 6.7: Estimated growth rate and film density by means of XRR measurements of the AlN samples deposited under different substrate bias.

On the other hand, Fig. 6.6(b) also shows a saturation of the I_s values within the range of bias from -15 V to -35 V. These values without significant variation imply a

constant number of ions but with higher energy, when reaching the substrate. This fact is accompanied by a decrease of both the growth rate and the film density shown in Fig. 6.7. For substrate bias above -15 V, the high kinetic energy of the adatoms impinging the substrate could lead to a desorption of the growing layer. This likely desorption is supported by the reduction of the AlN grain size (see Fig. 6.8) and could be accompanied by re-sputtering of the material from the substrate when applying an excessive DC voltage which is significantly pronounced in the AlN layer deposited at -35 V of substrate bias. The significant decrease of the film density could be also attributed to a change in stoichiometry.

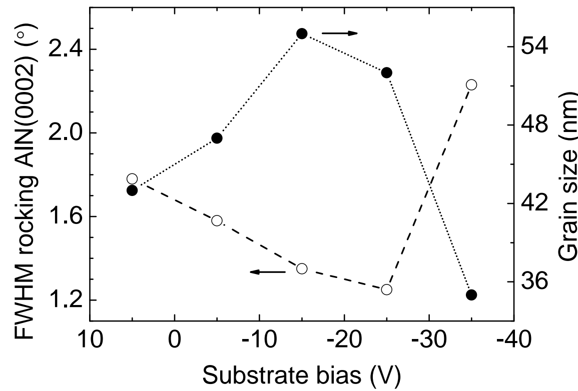

Figure 6.8: FWHM of the rocking curve of the AlN(0002) reflection and grain size as a function of the substrate bias. Best results of the FWHM and grain size for AlN deposited under unbiased conditions are 1.91° and 40.5 nm, respectively.

Regarding the crystal orientation of the AlN layer under study, Fig. 6.9(a) displays the HRXRD $2\theta/\omega$-scans for this set of samples. All the diffractograms exhibit the AlN(0002) reflection peak being the unique growth orientation. Nevertheless, a broad reflection at $2\theta \sim 35°$ is observed for negative bias from -5 V to -25 V. This parasitic reflection is attributed to lattice disorder at the AlN/sapphire interface originated by the highly accelerated positive ions (Al^+, N^+, N_2^+) impinging the substrate at the initial stages of the deposition process, during the charging transient observed in Fig. 6.6(a). Hence, a sample based on a thin AlN buffer layer deposited at -15 V followed by an unbiased AlN film with a nominal thickness of ~240 nm was synthesized in order to verify that the broad reflection at $2\theta \sim 35°$ was originated by interface damage. The HRXRD characterization of this sample lead to a $2\theta/\omega$ diffractogram presented in Fig. 6.9(b) in comparison with the unbiased AlN samples.

The AlN(0002) diffraction peak together with the reflection at $2\theta \sim 35°$ can be clearly observed. Since this reflection is not observed in any unbiased AlN layer, it can be confirmed the presence of lattice disorder at the AlN/substrate interface attributed to the negative biasing of the substrate.

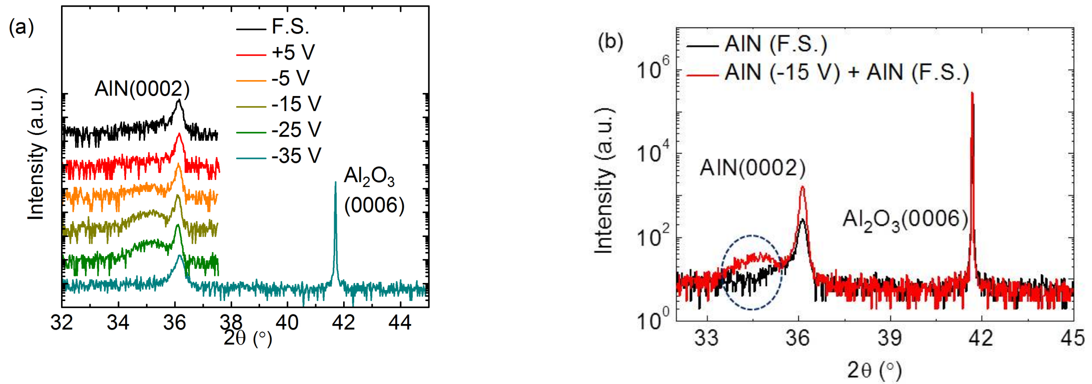

Figure 6.9: (a) HRXRD $2\theta/\omega$-scans of AlN films deposited at T_{subs} = 450 °C and P_{RF} = 150 W as a function of the substrate bias together with the unbiased AlN layer (F.S.). (b) HRXRD $2\theta/\omega$-scan of the AlN sample consisting of a thin buffer layer (30 nm) biased at -15 V followed by a 240-nm-thick unbiased AlN layer (red line). This diffractogram is shown in comparison to the 120-nm-thick unbiased AlN film (black line).

Concerning the rocking curves of the AlN(0002) diffraction peak, Fig. 6.8 shows that the FWHM decreases monotonously when increasing negative bias up to -25 V reaching a best value of 1.25°. The higher negative bias addresses to an increase of the kinetic energy of the impinging ions, hence increasing the mobility of the adatoms at the growing surface [Seo10]. This is consistent with the estimated increase of the grain size, as it is exhibited in Fig. 6.8. A maximum grain size of ~55 nm is achieved for the AlN sample deposited with a substrate bias of -15 V. AlN films deposited at a substrate bias of -35 V show the maximum value of FWHM of the rocking curve around the AlN(0002) reflection peak in the studied range, namely 2.23°. In this case, the worsening of the structural quality of the sample is attributed to a re-sputtering of the growing surface by the highly accelerated ions as commented previously [Cle03]. This explanation is supported by the low value of grain size, ~35 nm presented by this AlN layer.

In addition, Fig. 6.9(a) shows that there is no reflection peak around $2\theta \sim 35°$ related to the interface damage for the AlN film deposited at -35 V. This behavior

could be explained by the clear reduction of the film density which could lead to changes in stoichiometry for AlN deposited at DC bias above -15 V. Particularly, the biasing at -35 V implies the arrival to the substrate of too high energetic particles which could induce the re-sputtering even at the beginning of the process (see the reduction of growth rate in Fig. 6.7) making difficult the sustaining of the theoretical initial lattice disorder.

After the analysis of the influence of substrate bias on the crystal quality of the sputtered AlN films, it has to be noticed that the observed trend with negative bias is somehow similar to the one described as a function of the RF power (presented in Subsection 6.2.1). In both cases, increasing negative bias and P_{RF} results in an enhancement of the mobility of the adatoms and thus an improvement of the layer quality, until a certain threshold (-35 V and P_{RF} = 175 W, respectively) where degradation is associated to the onset of the re-sputtering process.

6.2.4 Two-step deposition method

In the previous subsections, optimized conditions for the deposition of AlN films have been presented. In summary, within the range of analyzed parameters, the optimized conditions in terms of the FWHM of the AlN(0002) x-ray reflection for AlN growth are: P_{RF} = 150 W, T_{subs} = 450 °C and V_S = -15 V. For this substrate bias, the AlN layers show the largest grain size (∼55 nm) while keeping low values of both the FWHM of the x-ray rocking curve (1.35°) and the rms surface roughness (∼0.6 nm for a 1×1 μm^2 analyzed area). Besides, these AlN films present values of density similar to the theoretical one. Nevertheless, the improvement of the crystalline quality of the layers under negative substrate bias is accompanied by a degradation of the AlN/sapphire interface. Thus, in this subsection, a two-step deposition method is developed in order to prevent the lattice disorder previously observed by HRXRD measurements whereas maintaining the structural and morphological quality of the AlN films.

Different two-step methods for sputtered AlN growth have been previously reported in the literature by using AlN films both as buffer and layer but changing sputtering pressure or RF power [Wil01][Cho04][Che08].

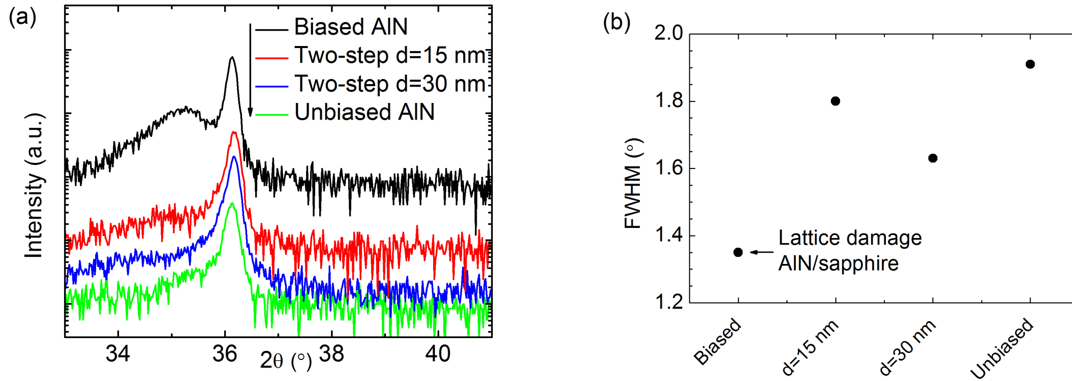

Figure 6.10: (a) HRXRD $2\theta/\omega$-scans of AlN films deposited under various substrate bias conditions: 120-nm-thick AlN at -15 V, two-step AlN with 15-nm and 30-nm-thick unbiased buffer layer followed by 120-nm-thick AlN at -15 V, and 120-nm-thick unbiased AlN. (b) HRXRD rocking curve around the AlN(0002) reflection peak for all the AlN films described in the previous caption.

The two-step deposition method presented in this Thesis is based on the deposition of AlN buffer and layer by applying different bias to the substrate. It consists firstly on the nucleation of an AlN buffer grown under unbiased substrate conditions, followed by the deposition of negatively biased AlN at -15 V. The use of an AlN unbiased buffer suppresses the damage at the AlN/sapphire interface while the deposition of AlN at -15 V induces an improvement of the crystal quality. The buffer thickness, d, is a crucial parameter in this two-step growth process. It must be optimized to prevent the interface degradation while keeping it as thin as possible taking advantage of the structural improvement under negative bias. Thus, two different buffer thicknesses were analyzed evaluating the prevention of the initial lattice disorder. Figure 6.10(a) shows the HRXRD $2\theta/\omega$-scan of two-step AlN samples with 120-nm-thick AlN layer on top of an unbiased buffer layer with thicknesses of ~15 nm and ~30 nm, compared to the optimized unbiased AlN and a biased layer deposited at V_S = -15 V (both 120 nm thick). The use of an unbiased 15-nm-thick buffer does not fully avoid the formation of lattice disorder. This is noticeable through a weak and broad peak at $2\theta \sim 35°$ and can be understood by the fact that the grain size obtained in thick AlN layers deposited using the same conditions as the buffer layer is ~40 nm, significantly larger than the buffer layer thickness. Thus a non-homogeneous surface coverage can be expected in a three dimensional growth model [Kis93]. The increase of the buffer layer thickness to 30 nm enables the total suppression of the interface damage and leads to a reduction of the FWHM of the AlN(0002) rocking curve to 1.63° compared to that corresponding to the optimized unbiased layer (1.91°) [see Fig. 6.10(b)].

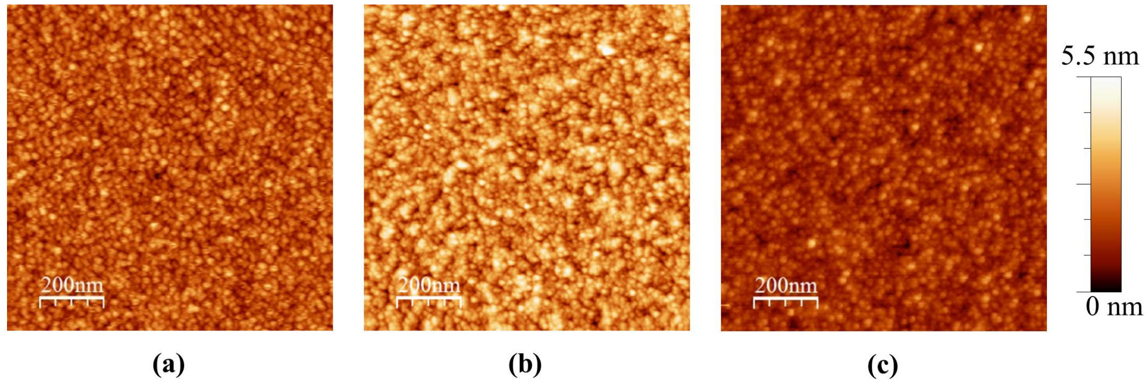

Figure 6.11: AFM images of 120-nm-thick AlN deposited on *c*-sapphire (a) at floating substrate conditions; (b) at -15 V of substrate bias; and (c) at -15 V biased substrate conditions on top of 30-nm-thick unbiased AlN buffer layer (optimized two-step method). The rms surface roughness of the layers is 0.6, 0.7 and 0.4 nm, respectively.

In summary, the two-step method allows the deposition of AlN on *c*-sapphire without any lattice disorder at the AlN/sapphire interface while maintaining the layer quality. In the case under study, the AlN film deposited using a 30-nm-thick unbiased AlN followed by a 120-nm-thick biased AlN at -15 V presents a FWHM = 1.63°, ∼40 nm of grain size and an rms surface roughness of ∼0.4 nm measured in a 1×1 μm^2 area. This rms surface roughness value is even lower than the values obtained for both the optimized unbiased and biased AlN layers (see AFM images in Fig. 6.11).

6.3 Sputtered-AlN-based optical waveguides

As previously introduced in Chap. 1, the objective of the optimization of AlN layers on *c*-sapphire by RF sputtering is, mainly, its further use for developing passive optical waveguides at 1.55 μm. In addition, optimized AlN films will be used as buffer layers for the deposition of InN layers by the same growth technique inducing an enhancement of the crystal quality of the top InN material (see Chap. 7).

As presented in Chap. 5, the capability of GaN/AlN-based QWs and QDs for all-optical switching has been demonstrated. These active devices can be implemented within a III-nitride-based PIC. It must be pointed out that passive pathways for light between different elements are also needed. The ideal solution for implementing these

optical pathways is by using a material from the group-III-nitrides family to reduce interconnection losses and enhance the material quality by avoiding lattice mismatch between layers in the overgrowth processes. Thus, since GaN/AlN heterostructures were grown on AlN-on-sapphire templates, the AlN overgrowth for passive channels can be ideally lattice-matched to the active part of the device. Hence, concerning a III-nitride-based PIC development, AlN deposited by RF-sputtering can be considered as one of the best candidates for passive interconnections between active devices operating at 1.55 μm. Sputtered AlN material takes profit of its wide band gap and its low cost deposition process combined with the relatively low T_{subs} used for AlN deposition, well below the T_{subs} used in epitaxial techniques. Hence, sputtering technique enables the regrowth of AlN material on previously deposited III-nitride-based active devices avoiding any damage likely associated with high temperatures.

This section presents the suitability of sputtered-AlN films deposited on sapphire for application in passive AlN optical waveguides. Optical design and fabrication of the device, together with optical transmittance measurements under low and high incident optical power are described in this section.

6.3.1 Waveguide optical design

Different optical simulations have been performed for optimizing the AlN guiding layer thickness and the dimensions of the waveguide ridge (width and etching depth) considering ordinary refractive indices of 1.740 and 2.127 for sapphire and AlN at 1.55 μm, respectively. The calculated AlN guiding layer thickness was fixed to 600 nm to enhance the light coupling to the previously developed GaN/AlN-based active waveguides presented in Chap. 5. At the same time, optical simulations via the RSoft BeamProp software point to modal guiding for waveguides with ridge widths of 2 μm and this optimized AlN layer thickness.

On the other hand, the optimization of the waveguide format to obtain single mode propagation for 2-mm-long waveguides while reaching the minimum slab modal guiding is also achieved from optical simulations varying the ridge width and etching depth, simultaneously. It has to be noticed that the optimized waveguide format must be experimentally affordable with the etching technique used. The investigated

dimensions were ridge widths of 2 μm and 5 μm while etching depth was ranged from 100 nm to 600 nm. Single mode propagation of light at 1.55 μm was obtained for 2-μm-wide ridges and etching depths below 200 nm and above 500 nm. In this study, the etching depth was set to 150 nm due to technical limitations imposed by the metal mask used during the waveguides processing since it was too thin for etching the 570-nm-thick AlN layer down to the substrate.

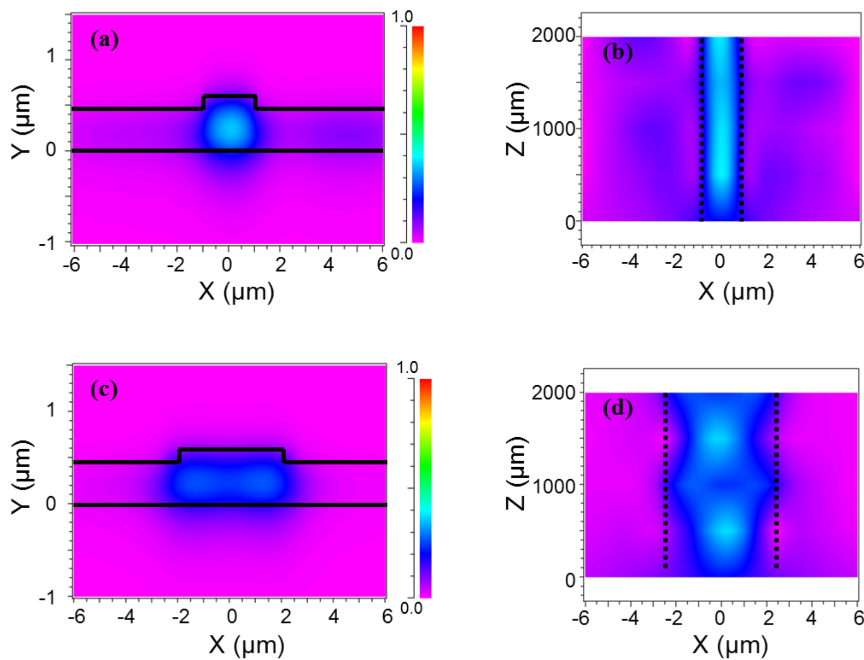

Figure 6.12: (a),(c) Simulated waveguide cross-sections and normalized transverse modal amplitudes at the output facet for 2-μm- and 5-μm-wide waveguides, respectively. (b),(d) Normalized light amplitude color maps when propagating along the waveguide for 2-μm- and 5-μm-wide waveguides, respectively.

Figures 6.12(a),(b) show the single mode behavior at 1.55 μm of the 2-μm-wide AlN waveguide with 150 nm of etching depth. At the same time, 5-μm-wide waveguide is multimode regardless of the etching depth. Figures 6.12(c),(d) exhibit the simulation of light propagation through the 2-μm-wide and 5-μm-wide waveguides, respectively, pointing to multimode propagation behavior in the case of the 5-μm-wide waveguide with the optimized 150 nm of etching depth.

6.3.2 AlN film deposition

The optimized nominally 600-nm-thick compact AlN guiding layer was deposited on *c*-sapphire by RF sputtering using the two-step deposition method explained in Subsection 6.2.4. The designed AlN layer consists of a bilayer of 30 nm deposited under floating substrate conditions and 570 nm under biased substrate at -15 V.

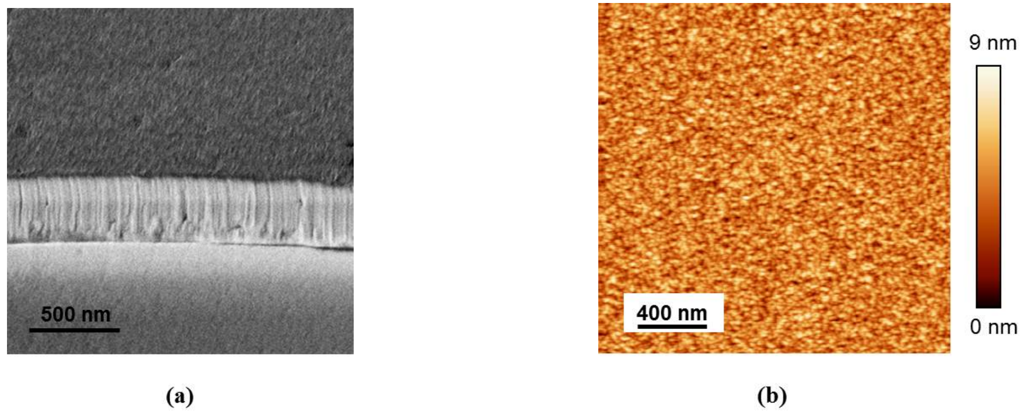

Figure 6.13: (a) 45°-tilted FESEM and (b) 2×2 μm^2 AFM images of the 570-nm-thick AlN layer deposited on sapphire for the development of the waveguides. The obtained rms is ~1 nm.

The synthesized AlN films present a thickness of ~570 nm with an expected optical band gap of ~6.0 eV ensuring their transparency at 1.55 μm with high transmittance level ~85 %. The layer thickness is estimated through the 45°-tilted FESEM image shown by Fig. 6.13(a). Figure 6.14 shows the experimental linear optical transmittance of the optimized AlN bulk material (black line) together with the theoretical calculations using the transfer matrix method [Nar07] (red line). From the fitted curve, it is possible to obtain estimated values of the band gap wavelength, λ_g, ordinary refractive index, $n_o(\lambda)$, and the absorption coefficient, $\alpha_o(\lambda)$. First-order Sellmeier dispersion formula was considered for refractive index calculation in the range under study [350-1700] nm whereas the sigmoidal approximation was used for the absorption coefficient estimation [Nar07]. The obtained dispersion relation is also plotted in Fig. 6.14 leading to a value of the ordinary refractive index of n_o=1.85 at 1.55 μm being lower than others reported, for instance, ~2.1 [Ste13b]. Concerning this difference, this 570-nm-thick AlN layer presents an estimated material density of ~3.11 g/cm^3 below the theoretical one, which likely induces a reduction

of the refractive index. Besides, the observed deviation might be related to impurity incorporation during deposition changing the optical properties of the layer.

Regarding the structural analysis of the optimized AlN layers, their crystal quality is improved when increasing the thickness of the biased top AlN films. The FWHM of the rocking curve of the AlN(0002) reflection peak decreases from 1.6° to 1.2° when increasing the upper AlN thickness from 120 nm to 540 nm. At the same time, 570-nm-thick AlN layers maintain a smooth surface roughness presenting a slightly higher rms ~1 nm compared to the corresponding one for the 150-nm-thick ones. AFM image of the AlN layers deposited for the development of the waveguides is shown in Fig. 6.13.

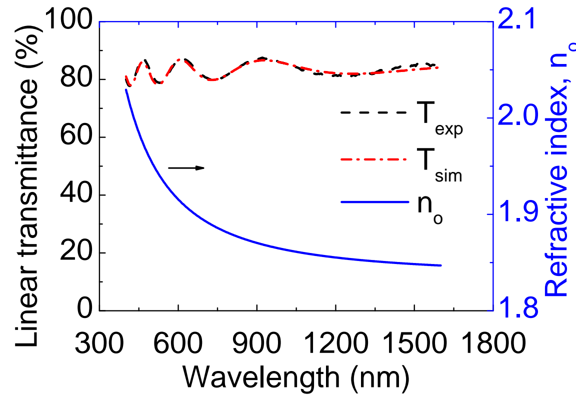

Figure 6.14: Linear optical transmittance of the optimized AlN bulk material (black line) and theoretical calculations (red line) together with the dispersion relation for the ordinary refractive index estimated for this AlN layer.

6.3.3 Waveguide fabrication

The fabrication of the AlN waveguides has been mainly based on three steps: patterning of the guiding structures, etching of the AlN layer and mechanical polishing of the facets. Firstly, the lithography process was carried out by following the procedure schemed in Fig. 4.8 but using positive resist. Thus, the AlN films were covered with the positive photoresist Shipley S1813 and the waveguide pattern was transferred by contact exposure UV lithography at 365 nm for 3.5 s. After the photoresist developing with MF319 for 1 min, a ~80-nm-thick Al layer was deposited by DC magnetron sputtering as the metal mask for the further etching process. Finally, the resist is removed by a lift-off process based on an acetone solution.

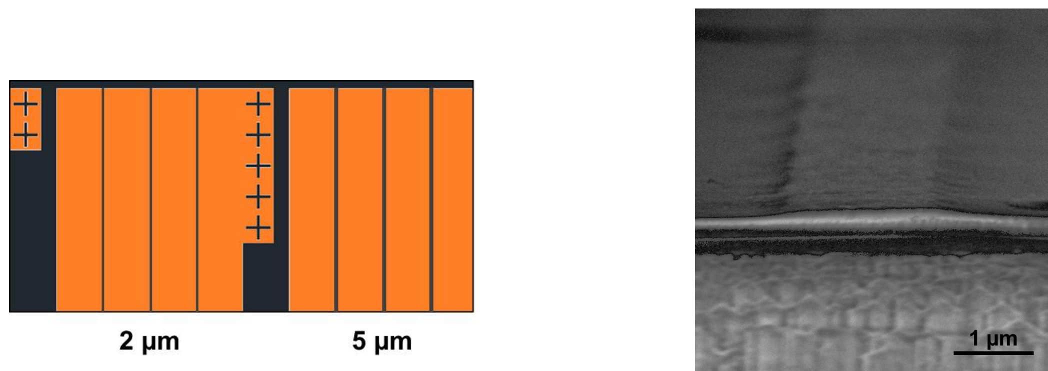

Figure 6.15: (Left) Scheme of the photomask used in the UV lithography process for the patterning of the AlN waveguides. (Right) FESEM image of the cross-section and surface of the fabricated 2-μm-wide AlN waveguide.

AlN waveguides of 2 μm and 5 μm widths were patterned. Figure 6.15(left) shows the design of the photomask used for the patterning of the AlN waveguide structures. Dark zones correspond to regions which are transparent to UV exposure whereas orange parts represent the chroming pattern of the photomask which is opaque to UV light.

To etch the waveguides, Ar sputtering was attempted. This technique did not result in an efficient etching process for compact sputtered-AlN-material due to its extremely low etching rate ~10 nm/h. Thus, the ridge format was actually reached by etching the patterned AlN in a reactive atmosphere using ICP-RIE based on SF_6 and O_2 plasma at RT. The developed etching depth was ~125 nm confirmed by the profilometer. Figure 6.15(right) shows a FESEM image of the cross-section and surface of the fabricated 2-μm-wide AlN waveguide.

Finally, facets have been mechanically polished through a series of diamond lapping films with different grain sizes from 40 μm to 0.1 μm.

6.3.4 Optical transmittance at 1.55 μm at linear and nonlinear regimes

Optical characterization at 1.55 μm of the AlN waveguides has been carried out by using the experimental setup introduced in Chap. 4 and depicted in Fig. 4.13.

Only 2-μm-wide AlN-on-sapphire waveguides have been investigated in terms of optical transmittance measurements at linear and nonlinear regimes due to their characteristic single mode condition and compatibility with the GaN/AlN waveguides developed in Chap. 5.

Figure 6.16(a) shows the optical transmittance measured in these 2-μm-wide and 1.8-mm-long AlN waveguides for TE- and TM-light. Experimental results show the constant optical transmittance of these devices at 1.55 μm for both polarizations and average incident optical powers ranging from -12 dBm to 17 dBm, confirming their non-absorptive and highly linear behavior.

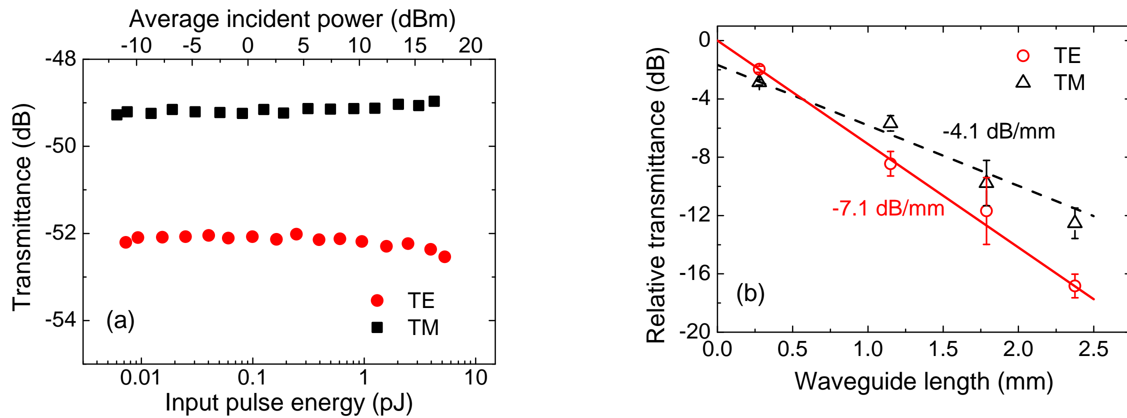

Figure 6.16: (a) Experimental optical transmittance of the 2-μm-wide and 1.8-mm-long AlN waveguides for TE- and TM-polarizations at linear and nonlinear regimes at 1.55 μm. (b) Cut-back method: Experimental relative optical transmittance between TE and TM polarizations at minimum incident optical power (-12 dBm) as a function of the waveguide lengths under study.

Since the interest of these AlN waveguides is focused on the low-loss propagation of light, the cut-back method was performed to estimate the linear losses of the waveguides. This is done by measuring four similar waveguides with different lengths at low incident optical powers (-12 dBm) [see Fig. 6.16(b)]. It has to be pointed out that, contrarily to the GaN/AlN-based waveguides, in this case, the different waveguide lengths have been reached by removing material of the output facet by straight polishing. The propagation losses obtained for both polarizations are 7.1 dB/mm for TE-light and 4.1 dB/mm for TM-light. The difference between them can be probably due to diffraction effects along the *(x,z)*-plane associated with the

low-confinement of light along the x-axis. A difference of ∼8 dB/mm is estimated in propagation losses for TE-polarized light between GaN/AlN and AlN waveguides, it being lower for the latter case. This difference can be attributed to the AlN buffer layer contained in the GaN/AlN waveguides which guides a significant part of the light inducing higher diffraction losses for TE polarization which vibrates along the non-confining direction of the AlN slab.

On the other hand, optical coupling losses estimated considering both input and output facets are 40.1 dB for the TE polarization and 41.7 dB for TM light, which are significantly large, approximately twice than those obtained for the GaN/AlN-based waveguides. The difference of ∼2 dB in coupling losses between TE and TM light polarizations (estimated from the interception with the y-axis of the linear fit) is attributed to the waveguide asymmetry. This 2-dB difference obtained in AlN waveguides is similar to that achieved in the case of GaN/AlN waveguides.

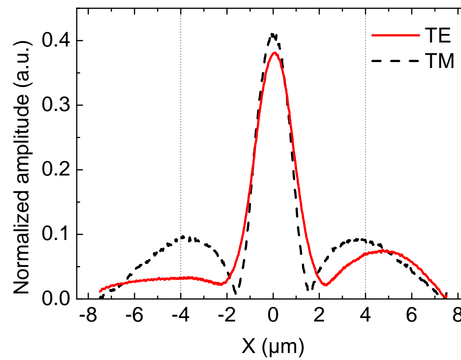

Figure 6.17: Normalized amplitude at the output of the 2-μm-wide and 1.8-mm-long AlN waveguide exhibiting lower collected output light with the 8-μm-diameter-core optical fiber in the case of TE polarization compared to propagated TM light.

In addition, it is worthy to remark that optical simulations for AlN waveguides lead to a higher amplitude for TM-light reaching the output facet and collected by the output optical fiber than in the case of TE-light. It has to be noticed that the collection of light in the experiment is performed by means of a ∼8-μm-diameter-core optical fiber. Thus, some part of the light propagated through the slab and outside the ridge is also collected by the optical fiber. This amount of collected light is estimated by the area below the simulated amplitude curves. Experimental results

for devices with lengths above 1 mm are in agreement with the theoretical analysis which demonstrates that this amount of collected light is higher in the case of TM polarization. As an example, Fig. 6.17 shows the simulated case of the 2-μm-wide and 1.8-mm-long AlN waveguides.

6.4 Conclusions

In this chapter, the development of sputtered-AlN waveguides has been presented together with the optical measurements which demonstrate their capability of working as passive optical pathways at 1.55 μm.

The optimization of *c*-oriented AlN films deposited on *c*-sapphire by RF reactive sputtering has been carried out. RF power applied to the target, substrate temperature and external substrate biasing have been the investigated parameters.
The best structural quality of the layers has been obtained for 150 W within the range from 100 W to 175 W. Smooth surface roughness with rms of ~0.3 nm and an optical band gap energy of ~6.0 eV have been obtained for this AlN layer.
The variation of the substrate temperature from 350 °C to 500 °C leads to an enhanced structural quality of the layer for 450 °C. However, AlN films grown at 350 °C and 500 °C present a worsening of the crystal quality which is attributed to the low adatom mobility and desorption processes, respectively. On the other hand, it has not been observed a clear influence of the substrate temperature on the surface roughness and the apparent optical band gap energy.
Regarding the application of an external bias to the substrate from +5 V to -35 V, a lattice disorder coming from the AlN/sapphire interface is observed when biasing from -5 V to -25 V which is attributed to the highly accelerated target species arriving to the substrate. This lattice disorder does not appear in AlN layers grown under floating substrate conditions or deposited at -35 V. Re-sputtering processes of the layer could emerge for high substrate bias (-25 V and -35 V) due to the highly accelerated atoms arriving to the substrate. The optimized substrate bias is found to be -15 V which induces an AlN layer with the largest grain size, the highest growth rate and a film density almost similar to the theoretical one, while presenting better structural quality than the unbiased AlN layer.

To combine the benefits of optimized biased and unbiased conditions, a two-step deposition method for sputtered-AlN films has been developed. It is based on a double AlN layer consisted on a first 30-nm-thick unbiased AlN buffer (to avoid the lattice disorder at the AlN/sapphire interface) followed by an AlN layer deposited under -15 V biased substrate condition (to improve the crystal quality of the material). The optimized AlN layer presents compactness, an rms below 1 nm and an apparent optical band gap of ∼6.0 eV.

Optimized sputtered-AlN films have been synthesized via the two-step deposition method for waveguide fabrication. Optical simulations via a finite-difference beam-propagation mode solver lead to an optimized 600-nm-thick AlN guiding layer to ensure the optical modal guiding for the minimum waveguide width of ∼2 μm. Furthermore, theoretically, widths of 2 μm lead to single mode devices for etching depths below 200 nm and above 500 nm at 1.55 μm, while 5-μm-wide waveguides present multimode behavior regardless of the etching depth. Hence, the optimized ridge height has been chosen to be ∼150 nm considering technological limitations. Concerning the fabrication, AlN films with a thickness of 570 nm have been patterned with widths of 2 μm and 5 μm by UV lithography and ∼125 nm etching depth achieved by ICP-RIE using SF_6 and O_2 as the reactants.

Sputtered-AlN waveguides have shown constant optical transmittance behavior for both TE- and TM-light polarizations at linear and nonlinear regimes at 1.55 μm. The cut-back method has been performed for the estimation of coupling and propagation losses of the AlN waveguides.
A difference of ∼2 dB in coupling losses has been obtained between both polarizations, being attributed to the waveguide asymmetry.
The optical propagation losses are higher for TE-light (7.1 dB/mm) compared to those obtained for TM polarization (4.1 dB/mm). This difference can be due to the low-confinement of the optical mode along the x-axis.

The sputtered-AlN waveguides developed in this work open the possibility of using this low-cost technique for the overgrowth without thermal damage of AlN-based passive interconnections in III-nitride-based PICs operating at 1.55 μm.

Chapter 7

Nonlinear TPA process in sputtered-InN-based waveguides

This chapter focuses on the design, fabrication and optical characterization of InN-based optical waveguides for application in nonlinear all-optical devices working at 1.55 μm. For this purpose, InN films deposited by RF reactive sputtering on *c*-sapphire are investigated through the use of different AlN buffer layers in terms of structural, morphological and optical quality. Two types of sputtered-InN layers have been processed in a waveguide format exhibiting two-photon absorption (TPA) phenomena at 1.55 μm.

A brief introduction dealing with the state-of-the-art of the growth of InN by RF sputtering is presented in the first section. After that, the influence of different AlN buffer layers on the properties of the on-top deposited InN layers is analyzed. The third section contains the optical design and the fabrication of the InN-based optical waveguides. Finally, nonlinear optical response via TPA process of the optimized InN-based waveguides is demonstrated, addressing their application in all-optical limitation at 1.55 μm. All the work presented in this chapter has been submitted for publication as journal papers [ML14a][ML14b].

7.1 Introduction

InN has been attracted much attention as material for the development of optical coatings, low-resistance ohmic contacts and optoelectronic devices such as solar cells or opto-chemical sensors [Bhu03][Wu09]. This interest has arisen due to its room temperature direct optical band gap in the NIR range (~0.7 eV) [Bhu03], its high electron mobility and its radiation resistance. Among the different growth techniques for InN films, high-quality material is obtained mainly by MBE [Lu03][Wan07][Yam09][Che13] and MOVPE [Sui06][Bri09][Ruf09]. In both deposition methods, the optimal substrate temperature for the InN growth is closed to the decomposition temperature of the material (~500 °C) [Gal07]. These two techniques are the best assessed for the deposition of InN films with high electron mobility and low carrier concentration.

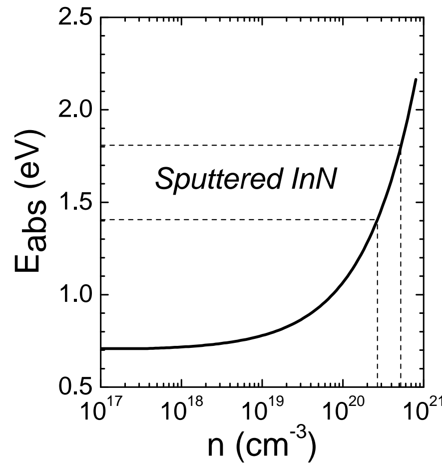

Figure 7.1: Calculated apparent optical band gap as a function of the free carrier concentration by considering the Burstein-Moss effect and including the conduction band nonparabolicity [Wal04]. Typical limit values of the band gap for the sputtered InN films are also shown.

Nevertheless, RF reactive sputtering can be considered the low-cost solution for the synthesis of relatively-high-quality InN layers taking profit of the possibility of deposition at lower T_{subs} than that used by MBE or MOVPE, even at RT. Furthermore, this technique also allows the material growth on a wide range of rigid (glass, silicon, sapphire, GaN-on-sapphire) [Guo98][She02][Guo09][VF10], and flexible

[Zoi08][Fer09][Est11] substrates. Sputtered-InN is mainly characterized by its large RT direct optical band gap between 1.4 eV (∼890 nm) [Sas10] and 1.8 eV (∼690 nm) [Pu06] compared to that obtained by MBE or MOVPE. This large apparent optical band gap value is attributed to the polycrystalline nature of the InN material and the Burstein-Moss effect induced by high carrier concentration of the layers in the range of 10^{20} cm^{-3}. Figure 7.1 shows the simulated apparent optical band gap as a function of the free carrier concentration by considering the Burstein-Moss effect and including the conduction band nonparabolicity [Wal04].

It is well-known that the use of an optimized intermediate buffer layer can improve the quality of the InN films in MBE, MOVPE and RF sputtering by minimizing the lattice mismatch between the InN layer and the substrate. Several studies have been reported considering different buffer layers: AlN [Kis93][Lu01][Wal12], GaN [Gal06][Shi06], low-temperature InN [Gra05][Wan09], low-growth-rate InN [VF12c] and ZnO:Al [Fer10]. Within this Thesis, it has also been presented that biasing the substrate can lead to an improvement of the crystalline quality of RF-sputtered AlN material through the increase of the kinetic energy of the impinging ions [ML13b]. In this work, a study of the effect of AlN buffers deposited under different substrate bias on the InN layer quality is presented.

On the other hand, the large value of the apparent optical band gap of InN deposited by sputtering opens the possibility of using this material in nonlinear optical applications via TPA processes at 1.55 μm (0.8 eV). In fact, nonlinear optical response of RF-sputtered InN films deposited on GaN-template substrates was successfully demonstrated at 1.55 μm in our group [VF12b]. This behavior was demonstrated via femtosecond time-resolved pump and probe transmittance measurements. An increase of the nonlinear contribution of the absorption ($\alpha_2 > 0$) when increasing the excitation optical power was achieved, associated to a resonant reverse saturable absorption (RSA) process. The TPA effect arises as the most likely responsible of the nonlinear absorption.

At the moment of writing this manuscript, we have not found any report on the sputtered-InN optical waveguides development. Thus, considering the previous nonlinear optical results obtained for InN layers by sputtering in our laboratory [VF12b], a similar behavior can be expected for this material in a waveguide format.

In this case, optical active devices based on sputtered-InN could be developed for further application in a III-nitride-based PIC acting as all-optical power limiters. For this purpose, the InN films deposited as the guiding layer for the fabricated optical device require a resonant band gap energy around 1.6 eV in order to reach an efficient TPA effect at 1.55 μm. Besides, the material within the optical waveguide should present smooth surface roughness and low propagation losses.

7.2 InN deposition using AlN buffers by RF reactive sputtering

This section focuses of the investigation of InN films deposited on AlN buffer layers by RF reactive sputtering. As in the case of AlN deposition presented in Chap. 6, the InN samples under study were deposited on (0001)-oriented sapphire substrates using the sputtering system introduced in Chap. 2. The In target was of 4N5 purity whereas the Al target and the reactive gas were 5N and 6N, respectively. The distance between both targets and the substrate was kept at 10.5 cm.

Four different buffers were investigated for the growth of InN layers. The InN top layers in all samples under study (S1-S4) were deposited using an RF power of 40 W with the sample holder unbiased. It must be pointed out that the maximum power density which can be applied to the In target used in this Thesis (2 W/cm^2) leads to a maximum theoretical power level supported by the target without inducing any damage of $\sim$50 W [Les10]. Besides, the deposition of all the buffers and InN layers was performed in a pure nitrogen atmosphere keeping constant the sputtering pressure at 0.47 Pa and the substrate temperature at 450 °C. As summarized in Table 7.1, four different buffer layers for the deposition of samples S1-S4 were investigated:

- **S1:** a 30-nm-thick low-growth-rate InN (*LGR-InN*) buffer layer grown at P_{RF}=20 W (deposited at 60 nm/h) and with the sample holder unbiased, following previous investigations on Si(111) substrates [VF10].

- **S2:** a 30-nm-thick AlN buffer layer grown at P_{RF}=150 W with the sample holder unbiased (*us-AlN*).

- **S3:** a 30-nm-thick AlN buffer layer grown at P_{RF}=150 W with the sample holder biased at -15 V (*bs-AlN*). This bias value was previously optimized for the deposition of RF sputtered AlN films, as justified in Chap. 6 [ML13b].

- **S4:** a double AlN buffer layer consisting of 30 nm of us-AlN followed by 30 nm of bs-AlN. This growth sequence was formerly reported to provide the best crystalline quality of RF-sputtered AlN [ML13b].

The initial growth procedure is the same as in the case of the AlN deposition including the chemical cleaning of the substrates, their outgassing at 100 °C above the deposition temperature inside the chamber and the targets pre-sputtering with Ar (5N) plasma.

	S1	**S2**	**S3**	**S4**
Buffer	LGR-InN	us-AlN	bs-AlN	Double AlN (us-AlN+bs-AlN)
Buffer P_{RF} (W)	20	150	150	150
Buffer thickness (nm)	30	30	30	60

Table 7.1: Summary of the conditions for the four buffers under study: type of buffer, RF power applied to the substrate during the buffer layer deposition and buffer thickness. The sputtering pressure and substrate temperature are kept at 0.47 Pa and 450 °C for all the material deposition in this study together with the nitrogen atmosphere. The optimized substrate bias for the biased-AlN buffer is -15 V.

7.2.1 Structural, morphological and optical characterization

S1-S4 samples have been characterized in detail in terms of structural quality and morphological and optical properties. The structural analysis was mainly based on the study of symmetric $2\theta/\omega$-scans spanning the sapphire(0006) and InN(0002) reflections as well as rocking curves around the InN(0002) reflection. AFM measurements were carried out for characterizing the surface morphology whereas FESEM images were taken for studying the films morphology and thickness. Finally, linear transmittance measurements in the visible/NIR range and PL experiments, both at RT, were performed in order to investigate the optical properties of the InN layers.

7.2.1.1 Structural characterization

All the analyzed InN films (S1-S4) present wurzite crystallographic structure with (0001)-preferred growth orientation. For all samples, a single peak corresponding to InN(0002) reflection is observed in the HRXRD $2\theta/\omega$-diffractograms. Particularly, in sample S4, it is also observed a peak related to the AlN buffer at $2\theta \sim 36°$ [see Fig. 7.2(a)] corresponding to the thickest AlN buffer layer among the analyzed samples.

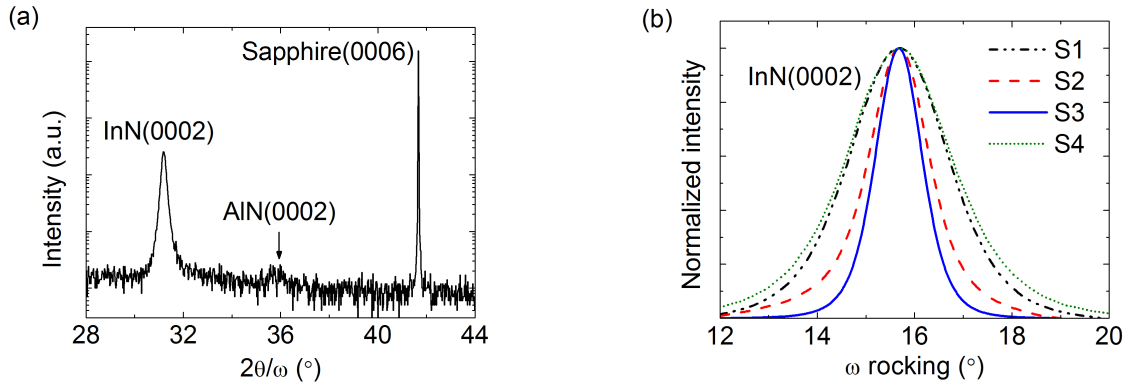

Figure 7.2: (a) HRXRD $2\theta/\omega$-scan of sample S4 showing the (0001)-preferred growth orientation together with the AlN(0002) reflection corresponding to the thickest AlN buffer layer among the analyzed samples. (b) HRXRD rocking curves of the InN(0002) reflection peak of the InN layers (S1-S4).

Regarding the crystal quality of the InN films, Fig. 7.2(b) shows the ω-scans of the InN(0002) reflection of all the samples. The values of the FWHM of the rocking curve around the InN(0002) reflection are summarized in Table 7.2. A remarkable improvement of the InN crystal quality is obtained when using a single AlN buffer layer (30 nm thick), compared to the use of the LGR-InN buffer. The value of the FWHM decreases from 2.4° when using the LGR-InN buffer (S1), to 1.5° and 1.2°, in the case of using us-AlN (S2) and bs-AlN (S3) buffer layers, respectively, resulting the latter in the best crystal quality among the InN films under consideration. On the contrary, a clear degradation is achieved when using a double AlN (S4) buffer, raising the FWHM of the InN(0002) rocking curve up to 2.7°.

	S1	S2	S3	S4
Buffer	LGR-InN	us-AlN	bs-AlN	Double AlN (us-AlN+bs-AlN)
FWHM InN(0002) rocking curve (°)	2.4	1.5	1.2	2.7
Column surface density ratio with respect to S1	1	1.5	-	6.4
Column diameter (nm)	176±20	170±25	-	87±9
rms surface roughness (nm)	71±2	49±4	32±3	6.6±0.1

Table 7.2: Summary of the structural and morphological properties of the analyzed InN films depending on the buffer used in terms of crystal quality, density of columns, columns size and rms surface surface.

7.2.1.2 Morphological analysis

Figure 7.3 exhibits the AFM images of the InN films under study scanned in a 2×2 μm^2 surface area.

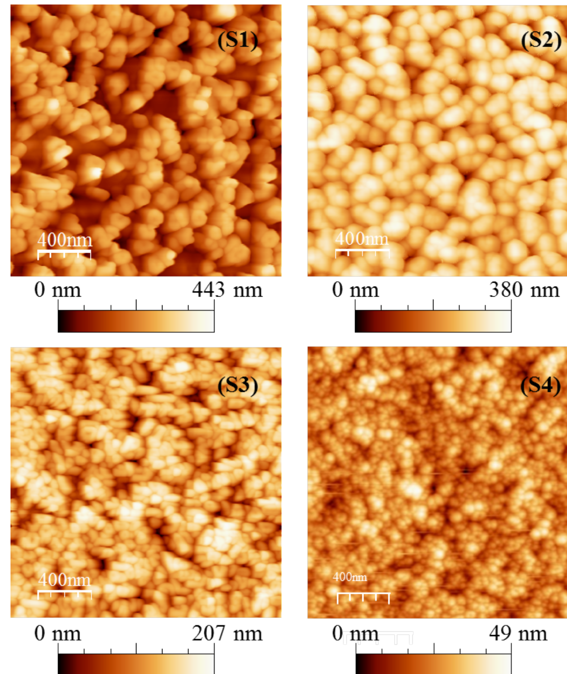

Figure 7.3: AFM images (2×2 μm^2 scanned area) of the InN layers under study (S1-S4).

As it can be seen in the AFM images, the InN layers show nanostructured morphology. The size of the nanostructures is reduced by one-half, from a diameter of (176±20) nm corresponding to the InN deposited by using the LGR-InN buffer to a diameter of (87±9) nm associated to the InN layer grown on the double AlN buffer. At the same time, an increase of the nanostructure density from 2.5×10^{9} cm^{-2} (sample S1) to 16×10^{9} cm^{-2} (sample S4) is achieved. Accordingly, the rms surface roughness decreases from ∼71 nm to ∼6 nm. AFM image of sample S4 exhibits the InN smoothest surface while presents the smallest nanostructures together with the highest density of them. Nevertheless, it shows the broadest x-ray rocking curve in Fig. 7.2(b).

On the other hand, FESEM images exhibit the surface and cross-section of the InN layers under study (see Fig. 7.4). These images clearly show that the nanostructured nature of the InN layers observed in the AFM images corresponds to columnar-like morphology in all cases except for S3 which can be considered 3D-like. It is possible to explain the large broadening of the rocking curve in sample S4 from the corresponding FESEM image. It can be clearly observed the small diameter of the columns which results in larger variations of their tilt being reflected in a uniform growth front with low surface roughness.

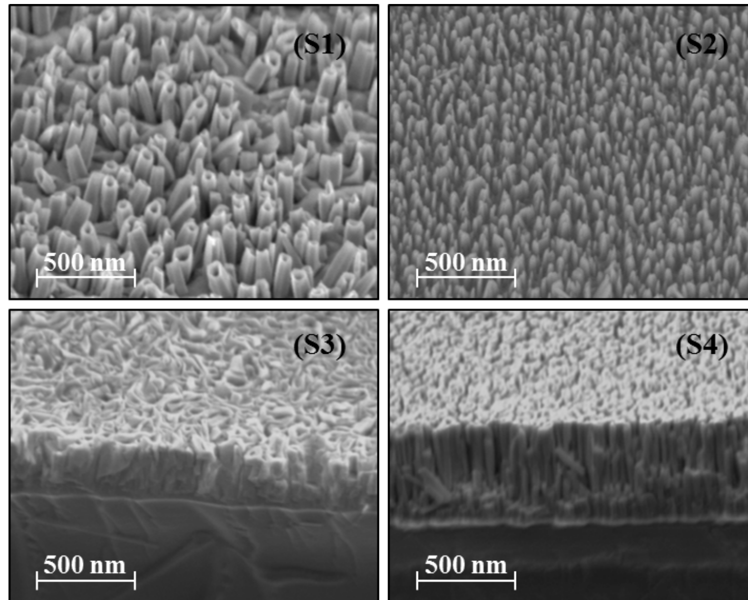

Figure 7.4: FESEM images of all the InN films deposited on *c*-sapphire.

Table 7.2 summarizes the morphological and structural properties of the analyzed InN layers, *i.e.*, the extracted values of rms surface roughness of the set of samples together with the column diameters and the column density for all the InN samples compared to that of sample S1.

7.2.1.3 Optical properties

The linear optical transmittance measurements for the InN bulk material were performed by using the system shown in Fig. 3.8. The obtained absorption was modeled using the sigmoidal approximation, and the apparent optical band gap energy ($E_{g,opt}$) was estimated by the extrapolation to the x-axis of the linear fit of the squared absorption coefficient (α^2) as a function of the energy (see Fig. 7.5).

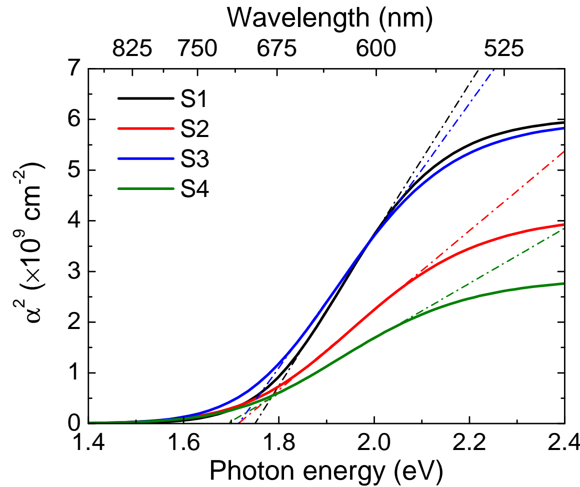

Figure 7.5: RT squared absorption coefficient (solid line) with a linear fit (dot-dashed line) as a function of the photon energy for the set of InN layers under study.

An apparent optical band gap energy in the range of (1.71±0.04) eV ($\lambda_{g,opt}$ ~725 nm) is obtained for all the InN layers (S1-S4) under study (see Table 7.3). This value is in agreement with the results reported by other authors for InN deposited by sputtering [She02][But05][Guo05]. Hence, as pointed out in the introduction of this chapter, these large values of $E_{g,opt}$ in sputtered InN samples have been mainly associated to a free carrier concentration in the InN films which could be estimated in the range of mid-10^{20} cm^{-3} [Wu04]. Besides, the obtained optical band gap is in the range of the one shown by compact InN layers with measured similar carrier concentration deposited in our laboratory [VF12c].

	S1	S2	S3	S4
$E_{g,opt}$ (eV)	1.746	1.714	1.715	1.690
ΔE (meV)	115	148	130	174
E_{PL} (eV)	1.557	1.561	1.583	1.666
FWHM E_{PL} (meV)	301	355	302	415
Stokes shift (meV)	189	153	132	24

Table 7.3: Summary of optical characterization results obtained using transmittance and PL measurements at RT for all the analyzed samples.

Concerning the optical analysis through PL measurements, Fig. 7.6 shows the PL emission spectra at RT for all the analyzed InN films. All the samples present a single PL emission peak (E_{PL}) centered in the range of (1.591±0.075) eV (λ_{PL} ~779 nm), with a FWHM above 300 meV in all cases (see also Table 7.3).

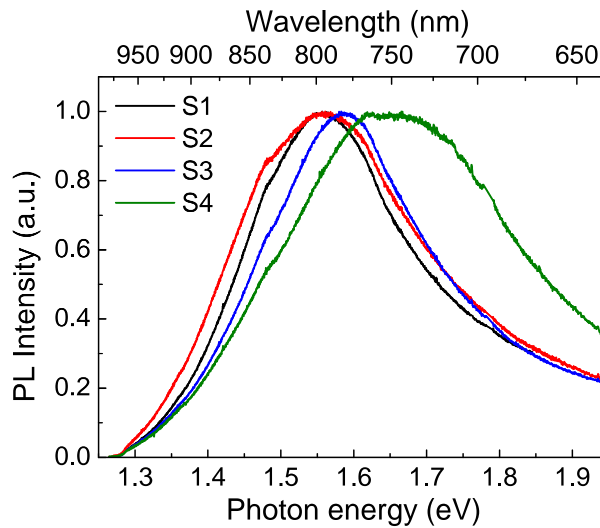

Figure 7.6: Normalized RT PL emission spectra depending on the excitation photon energy for the analyzed InN samples (S1-S4).

All the samples except for S4 present similar optical features with an absorption edge broadening (ΔE) in the range of (130±18) meV, and Stoke's shift from 130 meV

to 190 meV (see Table 7.3), in agreement with results presented by other authors [Bhu03]. These large Stoke's shift together with the high FWHM of the PL emission can be attributed to emission from potential fluctuations due to a non-homogeneous distribution of defects. These defects should be responsible of the high residual carrier level of the samples, as it has been observed by other authors in highly doped samples InN [Liu10]. The non-homogeneous defect distribution would determine the optical properties of the InN sample despite its particular morphology in case of large column diameter (S1 and S2) or 3D morphology (S3). On the contrary, the sample with the lowest column diameter among the analyzed layers (S4) shows the widest optical absorption edge and PL emission, linked to the lowest Stoke's shift (24 meV), which is tentatively attributed to some influence of the columnar size on the defect distribution inside the nanocolumns.

7.3 Sputtered-InN-based optical waveguides

Considering the different structural, morphological and optical properties achieved in the four InN samples under study, it must be pointed out that the application of the InN layers in optical waveguiding requires a transparent material at telecom wavelength together with a smooth surface roughness. Furthermore, the use of these waveguides for nonlinear all-optical limiters at 1.55 μm through two-photon absorption requires an InN layer with a band gap energy around $\sim$1.6 eV (2$\times$0.8 eV). For this reason, among the four analyzed samples, S4 can be considered the best option for the mentioned application. This InN layer grown on the double AlN buffer shows columnar morphology with an rms surface roughness of $\sim$6 nm and an optical band gap energy of 1.69 eV with an absorption band edge of ΔE $\sim$0.174 eV, which enables the TPA process at 0.8 eV.

7.3.1 Waveguide optical design

Two different InN layers are considered for the fabrication of the optical waveguides: an InN/AlN waveguide and an InN waveguide. The first one is the presented in the previous section which is based on a columnar InN film grown on a double AlN buffer (60 nm thick) on sapphire substrate with and optimized thickness of 600 nm in order

to enable its integration with the optical waveguides shown in previous chapters. The other candidate is a 350-nm-thick compact InN layer deposited directly on sapphire.

In order to design the waveguide format basing on both InN-based structures, optical simulations were performed considering 1.740, 2.280 and 2.125 as the refractive indices at 1.55 μm of sapphire, InN and AlN materials, respectively.

7.3.1.1 Columnar InN/AlN waveguide

Taking into account the thickness of the optimized InN layer (S4), *i.e.*, 600 nm, together with the 60-nm-thick double AlN buffer on sapphire, the optical modal guiding is ensured for the minimum ridge widths under study ($\sim$2 μm). At the same time, this guiding layer thickness is similar to that of the active GaN/AlN waveguides and passive AlN waveguides studied in Chaps. 5 and 6, respectively. The similarity of this dimension of the different devices would improve the light coupling between them.

It has to be pointed out that this InN guiding layer is based on columns with diameters $\sim$87 nm. This column dimension allows to consider negligible the optical diffractive effects associated with these nanostructures at 1.55 μm .

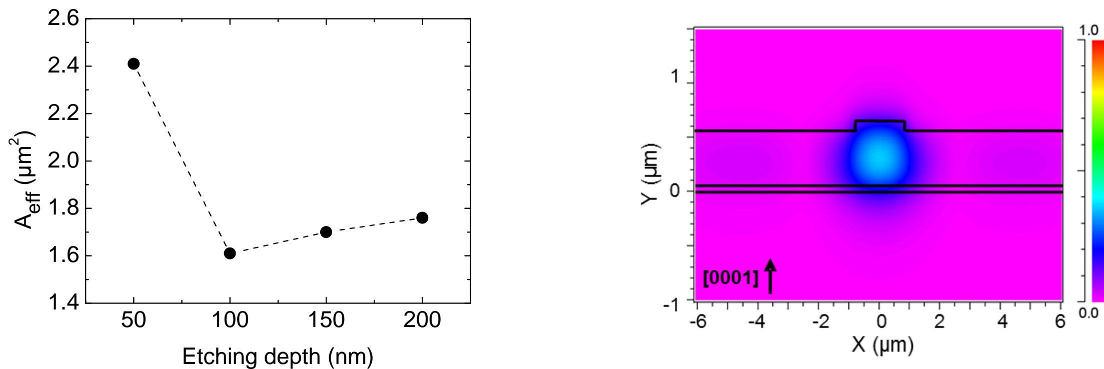

Figure 7.7: Optical simulations for the 2-μm-wide and 2-mm-long columnar InN waveguide: (Left) Effective area of the mode at the output of the single mode waveguide considering etching depths from 50 nm to 200 nm. (Right) Cross-section of the waveguide and normalized modal amplitude color maps at the output of the device considering 100 nm of etching depth.

As previously treated in the case of the AlN waveguide, the optimization of the InN waveguide format comes through optical simulations of the ridge width and etching depth. In order to obtain single mode propagation within the InN waveguides while enhancing the optical coupling between the active and passive devices, the ridge width is optimized to 2 μm for 2-mm-long waveguides. Multimode propagation is obtained for 5-μm-wide (or wider) InN waveguides. On the other hand, etching depth values ranging from 50 nm to 600 nm were investigated for 2-μm-wide waveguides, with the aim at obtaining single mode propagation while avoiding modal guiding through the slab. In this case, optical simulations lead to clear single mode waveguides when considering etching depths from 50 nm to 200 nm. However, multimode propagation is achieved for ridge heights higher than 250 nm.
Among the values which induce single mode propagation, the optimized etching depth is 100 nm since it leads to the highest confinement of light through the waveguide while presenting the lowest mode effective area, A_{eff} ~1.6 μm^2 [see Fig. 7.7(left)]. The normalized modal amplitude at the output of this optimized waveguide together with the device cross-section is shown in Fig. 7.7(right).

7.3.1.2 Compact InN waveguide

The second InN-based waveguide under study is based on a 350-nm-thick compact InN layer deposited by RF reactive sputtering directly on c-sapphire substrate. The growth conditions were pure nitrogen atmosphere, P_{RF} = 40 W, 0.47 Pa of chamber pressure and T_{subs} = 300 °C which were previously optimized in our laboratory. The obtained InN film presents high crystal quality in terms of the FWHM of the InN(0002) rocking curve, it being 2.2° and the rms surface roughness is ~6 nm. Concerning the optical properties, the InN-on-sapphire layer exhibits an apparent optical absorption edge of ~1.77 eV with an absorption band edge of ~0.133 eV, estimated from linear transmittance measurements of the bulk material. Figure 7.8 shows the AFM image of this InN layer on sapphire in a 2×2 μm^2 area and its FESEM image exhibiting its compactness.

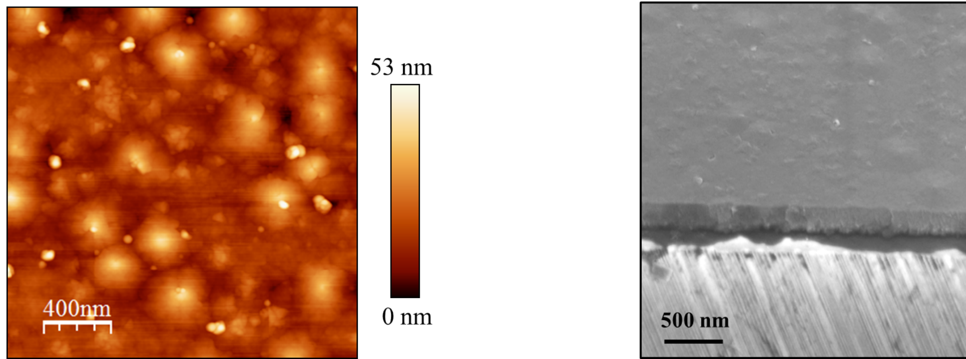

Figure 7.8: (Left) AFM and (Right) FESEM images of the compact InN layer deposited directly on the sapphire substrate by RF reactive sputtering.

Concerning the design of the optical waveguide based on this compact InN layer, first of all, a width of 2 μm is considered for the device in order to ensure single mode propagation as in the case of the previously optimized GaN/AlN- and AlN-based waveguides. The next step is the optimization of the etching depth of the waveguide.

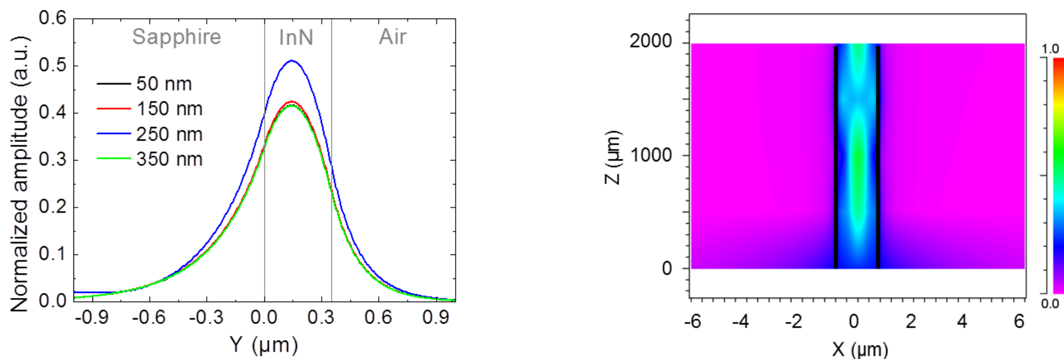

Figure 7.9: Optical simulations for the 2-μm-wide and 2-mm-long compact InN waveguide: (Left) Normalized output modal amplitude profile for different etching depths from 50 nm to 350 nm. (Right) Plane view of the waveguide format together with the color maps of the normalized modal amplitude of light propagating along the 250-nm-deep waveguide confirming its multimode behavior.

Figure 7.9(left) plots the normalized output modal amplitude profile for different etching depths for a 2-μm-wide and 2-mm-long waveguide. The analyzed values range from 50 nm to 350 nm. As it can be seen, the best etching value in terms of modal amplitude at the output of the device is 250 nm, but it leads to multimode propagation

as shown in Fig. 7.9(right). The optimized etching depth is then considered to be 350 nm since it induces single mode propagation with the lowest effective mode area (A_{eff} ∼0.9 μm^2) within the analyzed etching depth range. At the same time, this waveguide etching has the advantage of presenting the easiest technological process since it is only required to etch down to the substrate. The cross-section of the waveguide and normalized modal amplitude color maps at the output of the waveguide with the optimized etching depth can be observed in Fig. 7.10(left).

It has to be noticed that from optical calculations, the waveguide based on the optimized compact InN deposited directly on sapphire would have a more efficient response in nonlinear optical experiments than that based on the columnar InN on sapphire using a double AlN buffer. The difference comes from the theoretically more intense (higher maximum modal amplitude) and confined (lower A_{eff}) optical mode at the output of the compact InN waveguide compared to that achieved for the columnar one, as can be observed in Fig. 7.10(right). A maximum normalized modal amplitude of 42% and a mode effective area ∼0.9 μm^2 are theoretically obtained for the light propagating through the compact InN waveguide whereas the values achieved for the columnar InN device are 37% and ∼1.6 μm^2, respectively.

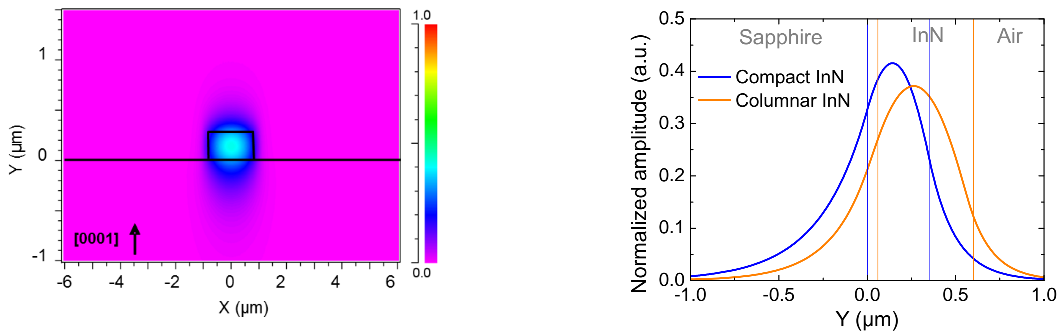

Figure 7.10: (Left) Cross-section of the waveguide and normalized modal amplitude color maps at the output of the deviced with the optimized etching depth of 350 nm. (Right) Normalized modal amplitude profile obtained at the output of the two optimized InN-based waveguides. Vertical solid lines indicate the thickness for the InN layer in each case.

Thus, considering both structures presenting a similar nonlinear absorption coefficient, a more enhanced nonlinear response should be expected for the waveguide based on the compact InN film.

Finally, Fig. 7.11 shows the designed format of both optical InN-based waveguides for their fabrication.

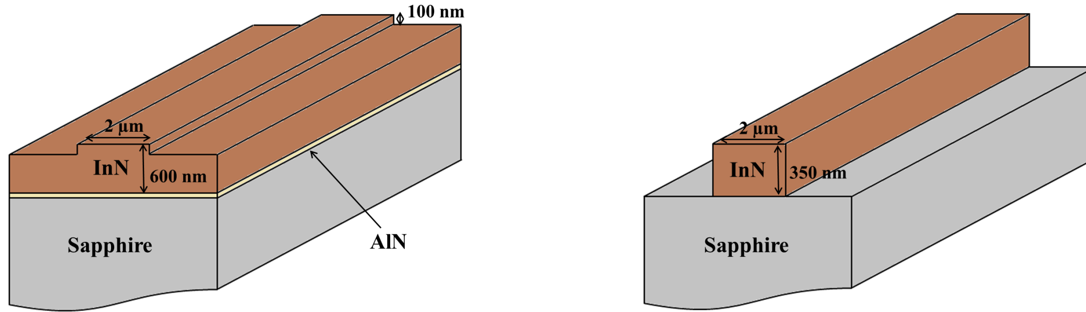

Figure 7.11: Designed InN-based waveguides with the detailed dimensions: (Left) Columnar InN on double AlN buffer waveguide and (Right) Compact InN waveguide.

7.3.2 Waveguide fabrication

The patterning of the InN guiding structures was carried out simultaneously with the sputtered-AlN-based structures and, consequently, under the same process conditions (see Subsection 6.3.3). Concerning the etching technique used, the physical etching by sputtering using Ar plasma was successfully performed for both columnar and compact InN films. The process was carried out by using the sputtering system in our laboratory. As it was presented in Chap. 6, this etching technique was not efficient for sputtered-AlN films. However, it works well for sputtered-InN due to the lower hardness of InN compared to AlN (11.2 Gpa [Edg97] and 18 GPa [Yon02], respectively, measured by nanoindentation) together with the lower cation-nitrogen bond energy in the case of InN (42.5 kcal/mol) compared to that of AlN (63.5 kcal/mol) [Kas07]. Hence, the physical etching process was performed at RT in pure Ar atmosphere with 40 W of RF power applied to the substrate and 0.47 Pa of chamber pressure. Under these conditions, it is possible to obtain highly enough energetic ions in order to etch the material placed on the substrate holder. Slightly different etching rates were experimentally obtained for compact InN and columnar InN being 5 nm/min and 7 nm/min, respectively.

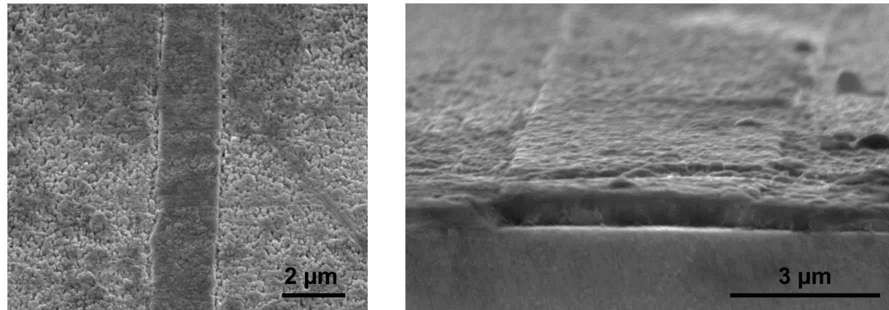

Figure 7.12: FESEM images of the fabricated columnar InN/AlN waveguides: (Left) surface view of the 2-μm-wide waveguide and (Right) cross-section and suface view of the 5-μm-wide waveguide.

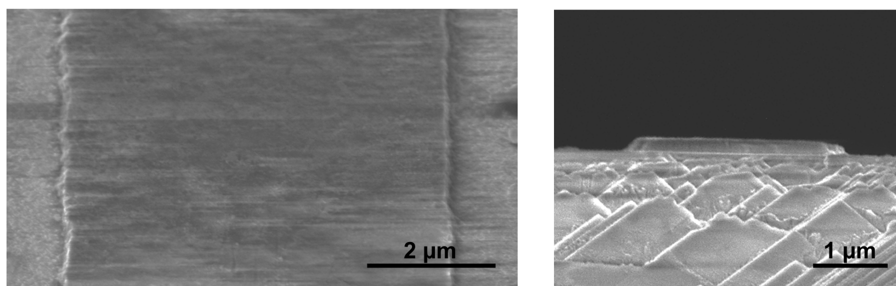

Figure 7.13: FESEM images of the fabricated compact InN waveguides: (Left) surface view of the 5-μm-wide waveguide and (Right) cross-section of facet of the 2-μm-wide waveguide.

The likely remaining non-etched Al metal mask [see the last step process in Fig. 4.9(b)] is removed by using a 20% HCl solution at 40 °C for 60 min followed by a cleaning with organics, firstly, a bath in acetone at the same temperature for 30 min and, after that, methanol in ultrasonics at RT for 10 min. Figures 7.12 and 7.13 shows the FESEM images of the fabricated columnar and compact InN-based optical waveguides, respectively, with different widths, 2 μm and 5 μm.

The etching down to the substrate of the compact-InN material has been also checked by linear optical transmittance investigations. Figure 7.14 shows the Tr spectra of an InN test layer, a sapphire substrate and the InN sample after etching.

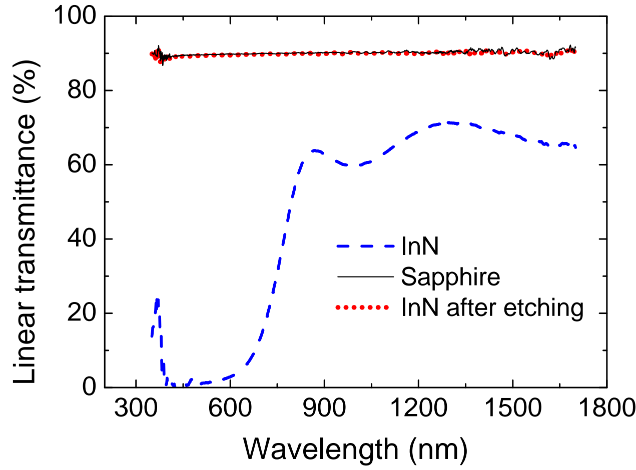

Figure 7.14: Comparison of the linear optical transmittance of the original InN layer grown on sapphire, the single sapphire substrate and the InN layer after the Ar plasma etching. The agreement between the spectra of the etched InN and that of the sapphire substrate confirms the total etching of the original InN layer.

As in the case of the AlN-based waveguide fabrication, the last step is focused on the facets polishing. The followed procedure in the case of the InN-based waveguides is the same by mechanically polishing with different diamond lapping films ranging the grain size from 40 μm to 0.1 μm.

7.4 Linear and nonlinear optical characterization of sputtered-InN-based waveguides

Optical characterization at 1.55 μm of the two developed InN-based waveguides has been carried out by using the experimental setup exhibited in Fig. 4.13 but replacing the output single mode optical fiber by a single mode lensed fiber with a spot size diameter of $\sim$2.5 μm similar to that used at the input facet of the waveguide. The optical investigations have only been performed for 2-μm-wide InN waveguides since these devices present single mode behavior and their width is compatible to both GaN/AlN-based and AlN-based waveguides.

This section is focused on the study of the nonlinear optical behavior of the developed InN waveguides. Hence, both columnar- and compact-InN-based waveguides are

investigated with the subsequent comparison between the optical results achieved. Taking into account that another third-order nonlinear effect was demonstrated for the sputtered-InN bulk material in terms of nonlinear response via the two-photon absorption [VF12b], a brief explanation of this nonlinear effect is introduced for supporting this investigation.

Two-photon absorption ($\alpha_2 > 0$)

Among the different phenomena based on the reverse saturable absorption (RSA), TPA is a process where two photons are simultaneously absorbed at resonant wavelengths.

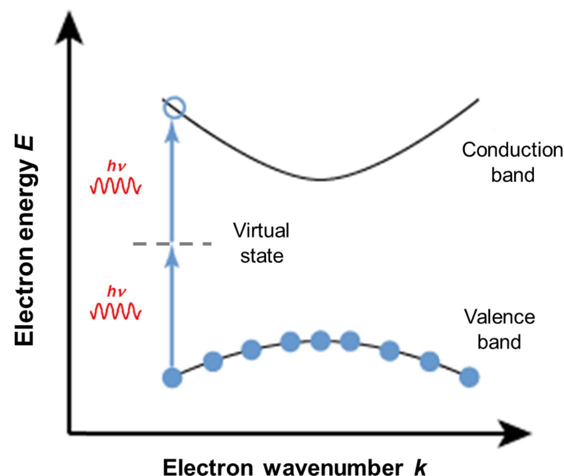

Figure 7.15: Scheme of the TPA process in a two-electronic-level semiconductor.

Considering an electron transition from the ground state to a higher available state, the sum of the incident photon energies must be equal to that of the upper level, being the photon energy half of the band gap energy, at least. Figure 7.15 schemes the TPA process in a system of two electronic levels. The optical transition can take place only when the two photons are present together. The first photon induces the electron to perform a virtual transition to a forbidden state (virtual state within the band gap). Hence, if the second photon pumps the material within the lifetime of the virtual state, the electron will move to the upper level and the absorption process will

be completed. If not, the virtual transition collapses, the electron goes back to the ground state and the absorption process does not take place. TPA process is more efficient when photons are supplied at high pumping rates to ensure the presence of two photons at the virtual state within its virtual lifetime.

In order to establish the mathematical formalism of the process within the semiconductor, just the nonlinear TPA process will be considered. The formalism comes from the generalization of the Lambert-Beer's Law including the nonlinear absorption contribution through the TPA nonlinear absorption coefficient, α_2.

$$\frac{dI}{dz} = -\alpha_0 I - \alpha_2 I^2 \tag{7.1}$$

Hence, integrating the above equation as a function of z (the longitudinal dimension of the waveguide), the intensity at the output of an optical waveguide with length L is given by:

$$I = I_0 \frac{\alpha_0 e^{-\alpha_0 L}}{\alpha_0 + \alpha_2 I_0 \left(1 - e^{-\alpha_0 L}\right)} \tag{7.2}$$

where I_0 is the input intensity at z=0. Finally, the transmittance considering both linear absorption and TPA effect is given by the following equation:

$$T_{TPA} = \frac{e^{-\alpha_0 L}}{1 + \alpha_2 I_0 L_{eff}} \tag{7.3}$$

being $L_{eff} = \left(1 - e^{-\alpha_0 L}\right)/\alpha_0$ the effective length of the device.

Hence, materials which present two-photon absorption exhibit a reduction in the transmitted light at resonant wavelengths for high intensity excitation acting as the contrary effect to the absorption saturation phenomena.

It has to be noticed that the nonlinear optical properties such as TPA effect is highly dependent on the incident light polarization and the orientation of the sample due to the anisotropy of the semiconductor crystals [Wan12].

7.4.1 Linear optical experiments: Cut-back method

As widely commented along this Thesis, the experimental measurement of both coupling and propagation losses for each device under study is crucial. Thus, both InN-based waveguides are investigated through the cut-back method at 1.55 μm for both TE- and TM-light polarization at relatively low incident power conditions (-2 dBm). As in the case of the AlN-based waveguides characterization, different waveguide lengths required for performing the cut-back method have been achieved by straight polishing, progressively removing material of the output facet. Figure 7.16 plots the variation of the optical transmittance as a function of the waveguide length for the two sputtered-InN-based waveguides: (left) the columnar InN/AlN waveguide and (right) the compact InN waveguide.

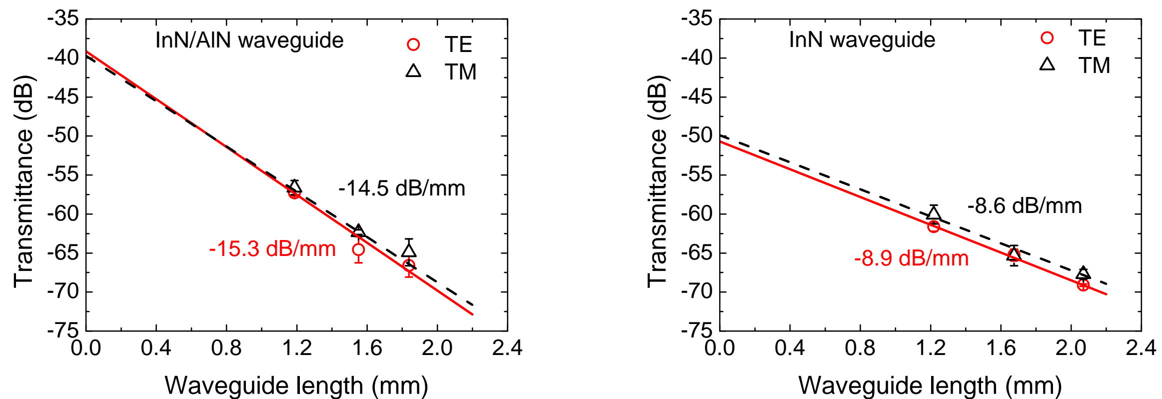

Figure 7.16: Cut-back method: Experimental TE-TM transmittance at low incident optical power (-2 dBm) as a function of the device length for (Left) the columnar InN/AlN waveguide and (Right) the compact InN waveguide. The experimental points correspond to the average of transmittance measurements in three similar waveguides for each length.

It can be clearly observed that the difference in coupling and propagation losses between both TE- and TM-polarizations is almost negligible for each type of waveguide. A more noticeable polarization dependence of the transmittance should be expected due to geometrical asymmetry of the waveguides, but Rayleigh scattering effects due to the post-etching residual sidewall roughness could be hiding it.

On the other hand, regarding the losses at both input and output facets, coupling losses in the compact InN waveguide (~50 dB) are much larger than those in the columnar one (~40 dB). This difference can be attributed to the waveguide geometry since the columnar InN/AlN waveguide presents an InN guiding layer

thicker (600 nm) than the compact one (350 nm), maintaining both the same ridge width; thus the light coupling is easier for the columnar InN/AlN waveguide.

Concerning the propagation losses within both optical devices, these are much higher in the case of the columnar InN/AlN waveguide (∼15 dB/mm) compared to those corresponding to the compact InN device (∼8.7 dB/mm). This difference can be attributed to the better 2D confinement (x- and y-axis) provided by the total etching of the compact InN layer down to the sapphire substrate for the latter case. This transversal confinement avoids the likely diffractive effects along the x-axis while reducing the optical losses due to surface roughness at the guiding layer/substrate and guiding layer/air interfaces. Furthermore, the presence of nanocolumns within the InN/AlN waveguide compared to the bulk InN devices could lead to a larger contribution of Rayleigh scattering effects within the columnar device attributed to its nanostructured morphology. At the same time, this nanostructured morphology could imply a reduction of the effective refractive index of InN material with the subsequent reduction of the optical confinement due to the lower refractive index contrast within the structure.

7.4.2 Nonlinear optical measurements

Nonlinear optical measurements have been performed in the InN-based waveguides with the femtoseconds laser at 1.55 μm described in Chap. 4 using average incident optical powers up to 17 dBm (∼50 mW).

Figures 7.17(a),(c) show the evolution of the optical transmittance for TE- and TM-polarizations as a function of the average incident power and the input pulse energy (obtained taking into account the optical coupling losses at the input facet), for the columnar InN/AlN waveguide and the compact InN one, respectively. It can be clearly observed a reduction of transmittance for high input pulse energies. This nonlinear response is attributed to TPA process which is dependent of the light polarization. It has to be noticed that for both devices the transmittance contrast between linear and nonlinear regimes is estimated to be ∼6 dB for TE light and ∼4.5 dB for TM polarization.

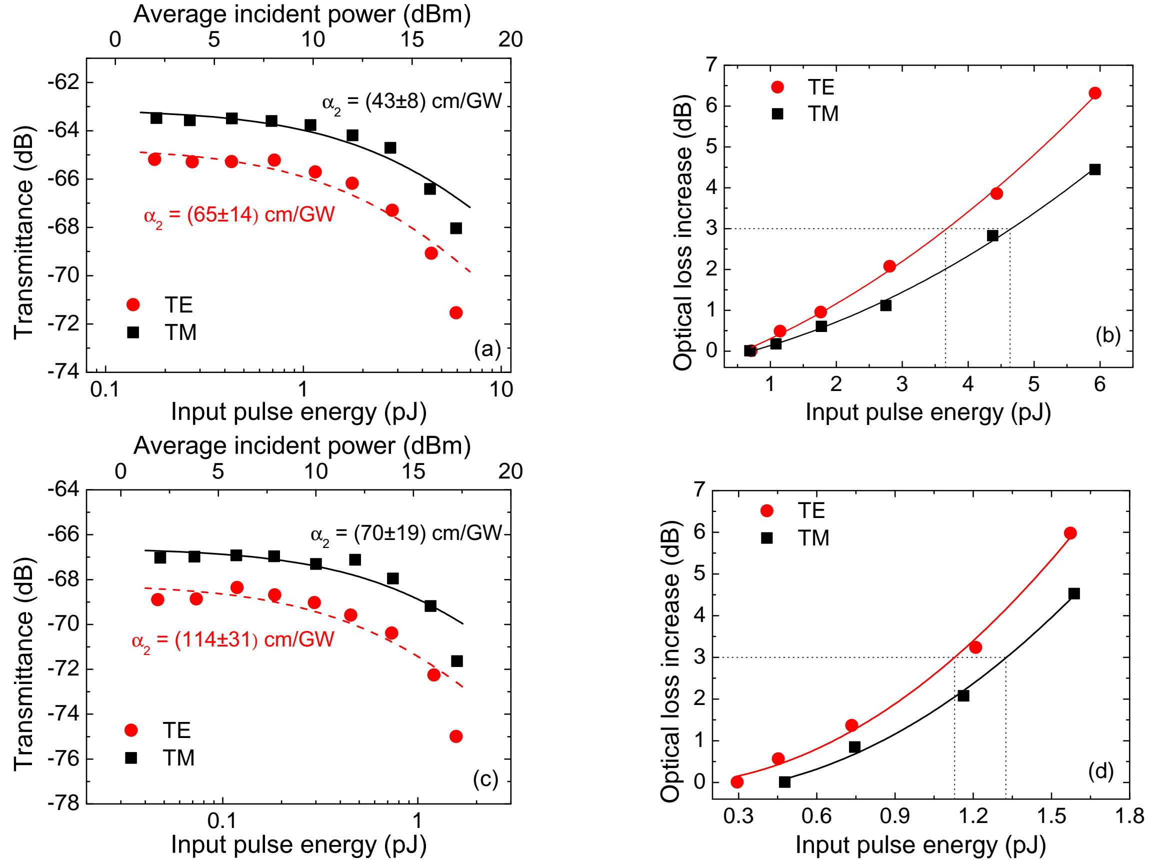

Figure 7.17: (Left) Transmittance and (Right) optical loss increase for TE- and TM-polarized light versus the input pulse energy in (a,b) a 1.84-mm-long columnar InN-on-double-AlN waveguide and (c,d) a 2.07-mm-long compact InN waveguide.

Experimental results from Figs. 7.17(a),(c) can be fitted to the transmittance equation (Eq. 7.3) introducing the dependence on the input pulse energy by considering $I_0 = E_{pulse}/(A_{eff}\Delta t)$:

$$T_{TPA} = \frac{e^{-\alpha_0 L}}{1 + \frac{\alpha_2}{A_{eff}\Delta t}\left(\frac{1-e^{-\alpha_0 L}}{\alpha_0}\right) E_{pulse}} \tag{7.4}$$

where Δt is the temporal pulse width entering the optical devices, 150 fs in our case, and A_{eff} is the effective area (taken as the mode area obtained from simulations). Hence, both linear and nonlinear values of the absorption coefficient can be extracted from the fitting curves [solid line for TM-light and dash line for TE-light in Figs. 7.17(a),(c)]. The obtained values together with the estimated L_{eff} are presented

in Table 7.4. In all cases, the transmittance obtained for the maximum input power significantly differs from the calculated expected value from data fitting to Eq. 7.4. This increased absorption at the highest input pulse intensity analyzed ($\sim$2.7 GW/cm^2) could be attributed to a likely contribution of nonlinear free carrier absorption (FCA) effect by the free electrons excited in TPA process. This phenomenon is enhanced at high optical intensities following a cubic dependence on the input power (within the generalized Lambert-Beer's Law, Eq. 7.2) when free carriers are generated by TPA process [TF10]. All the values of α_2 obtained at 1.55 μm in this work are highly dependent on the polarization excitation reaching larger values for TE-light than for TM-light in both InN-based devices. The ratios between both nonlinear absorption coefficients are estimated to be $\sim$1.5 and $\sim$1.6, for the columnar InN/AlN waveguide and the compact InN one, respectively.

The obtained values are also larger than that reported for InP (24-33 cm/GW) with a recovery time in the subpicoseconds range [Vig04] and those of Si(111) and GaAs of $\sim$0.88 cm/GW and $\sim$10.2 cm/GW, respectively [Din03], also at $\sim$1.55 μm. On the other hand, the nonlinear coefficient values estimated for these InN-based devices are lower than the obtained through Z-scan measurements for sputtered-bulk InN in our group (167 $\pm$ 30 cm/GW with a recovery time of 380 fs) [VF12b]. In the case of the bulk InN material analyzed by Z-scan, light always pumped the sample directly onto the xy-surface (TE-light), *i.e.*, the basal crystallographic plane of the InN hexagons. Because of the isotropy in the xy-plane, only one component of the third-order susceptibility tensor is excited, $\chi^{(3)}_{xxxx}$ [Wan12]. However, when performing this type of measurement with the optical waveguide, the c-axis of the hexagons is also accessible with TM-light exciting, in this case, the $\chi^{(3)}$ tensor component along the growth direction, *i.e.*, $\chi^{(3)}_{zzzz}$. Hence, just the α_2 value obtained for the TE polarization of light can be compared with results achieved via Z-scan experiments. Thus, the difference between both values could be introduced by a slight overestimation of the coupling losses within both InN-based optical waveguides.

The efficiency of both InN-based waveguides is investigated by considering the 3-dB of optical loss increase as the figure of merit [see Figs. 7.17(b),(d)]. Solid and dashed lines have been introduced as guides for the eyes. Particularly, the input pulse energies required for reaching a 3-dB change for TE- and TM-light excitation within the columnar InN/AlN waveguide and the compact InN devices are presented

in Table 7.4. The compact InN waveguide can be considered more efficient than the columnar InN/AlN one since it requires lower input pulse energy to achieve a 3-dB transmittance contrast.

It must be pointed out that for all the measured waveguide lengths corresponding to both InN-based waveguides under study, the obtained transmittance contrast is similar for each structure since the effective length in both cases (∼0.12 mm for the columnar InN/AlN waveguide and ∼0.14 mm for the compact one) is lower than the analyzed lengths of the two devices, 1.84 mm and 2.07 mm, respectively.

	InN/AlN waveguide		**InN waveguide**	
	TM	**TE**	**TM**	**TE**
α_0 (cm^{-1})	80.7±0.2	82.7±0.3	74.1±0.3	75.9±0.3
L_{eff} (mm)	0.12	0.12	0.14	0.13
α_2 (cm/GW)	43.4±8.3	65.2±14.0	69.6±18.7	113.6±30.6
Energy for **3 dB** contrast (pJ)	4.6	3.6	1.3	1.1

Table 7.4: Results for the parameters related to the linear and nonlinear optical absorption for both sputtered-InN-based waveguides under study.

7.5 Conclusions

In this chapter, the development of sputtered-InN-based waveguides has been presented. All the steps for developing them have been described covering the synthesis of the material, the design of the optical waveguide and the fabrication process, together with the optical measurements. Results from the nonlinear optical characterization demonstrate that these sputtered-InN based waveguides present nonlinear TPA effect at 1.55 μm which makes them attractive for their further use in all-optical applications acting as optical limiters within a III-nitride-based PIC working at the resonant wavelengths.

The influence of the AlN buffer deposited by RF sputtering under different substrate bias configurations for the growth of InN layers on *c*-sapphire has also been investigated. Three AlN buffers have been studied: deposited at floating substrate conditions, with optimized substrate bias (-15 V) and the last one based on an AlN-bilayer (an unbiased AlN film followed by a -15 V-biased AlN layer). For comparison, an InN layer grown on a low-growth-rate InN buffer has also been analyzed.
All the InN samples under study present *c*-axis preferred growth orientation with a structural quality enhanced when polarized the substrate during the single AlN buffer deposition. On the other hand, the worst result in terms of crystal quality of the InN films is obtained when using the double AlN buffer.
All the samples under study present a columnar-like nature except for the InN grown on the biased AlN buffer, which can be considered 3D-like. The density of columns, their diameter and the surface roughness of the InN layer can be controlled by changing the different buffer used. The lowest rms surface roughness is achieved for the InN grown on the double AlN buffer ($\sim$6 nm) together with the lowest column diameter (87$\pm$9 nm) and the highest column density among the studied layers. Concerning this latter InN layer, the mentioned worsening of the crystal quality of these InN films, estimated by the broadening of the rocking curve around the InN(0002) peak reflection, is attributed to an increase of the tilt of the nanocolumns. An apparent optical absorption edge within the range of (1.71$\pm$0.04) eV and PL emission peak at (1.591$\pm$0.075) eV have been observed for all the InN samples at room temperature. The PL emission characteristics are attributed to defects responsible of the high residual carrier concentration of the layers, although some influence of column size is pointed out for the sample with the lowest column diameter.

Sputtered-InN films deposited on the double AlN buffer (columnar InN) together with optimized sputtered-InN directly on the sapphire substrate (compact InN) have been investigated for waveguide fabrication. The optimized InN/AlN structure has 600 nm of columnar InN guiding layer and a width of 2 μm and 100 nm of etching depth. On the other hand, the InN waveguide presents 350 nm of compact InN guiding layer, a ridge width of 2 μm and a total etching down to the substrate, *i.e.*, 350 nm of etching depth. The patterning of the waveguides was performed by UV lithography and the etching process was carried out by physical sputtering with Ar plasma.

Single mode 2-μm-wide InN-based waveguides were optically characterized at 1.55 μm for TE- and TM-light at linear and nonlinear regimes (from -2 dBm to 17 dBm of average incident optical power).
Optical transmittance is significantly reduced when injecting light at high input pulse energies. The observed nonlinear behavior is attributed to an interband transition in InN material by the absorption of two photons of the same energy (0.8 eV). This phenomenon occurs for both TE- and TM-polarizations.
Cut-back method experiments have also been performed for both types of waveguides. There is no clear change in coupling losses for both polarizations in each waveguide. Besides, this is also observed in the case of propagation losses. The expected polarization dependence of the transmittance due to the geometrical asymmetry of the waveguides could be hidden by scattering effects associated with their residual sidewall roughness.
On the other hand, a significant difference of optical losses between the two different waveguides has been achieved. Coupling losses in the compact InN waveguide are much larger than those in the columnar one, ~50 dB and ~40 dB, respectively. This difference is attributed to the difference in waveguide dimensions since the columnar InN/AlN waveguide presents 600 nm of columnar InN guiding layer and the compact InN structures only presents 350 nm, maintaining both the same ridge width of 2 μm. Propagation losses are much higher in the case of the columnar InN/AlN waveguide (~15 dB/mm) compared to those corresponding to the compact InN device (~8.7 dB/mm). The lower value corresponding to the compact InN waveguide can be associated to the better light confinement provided by the total etching of the compact InN layer (with an effective mode area of $A_{eff} \sim 0.9$ μm^2 compared to the 1.6 μm^2 of the columnar InN/AlN waveguide). This better confinement of the light can contribute to minimize the optical losses due to surface roughness at the guiding layer/substrate and guiding layer/air interfaces. Furthermore, the larger scattering effects within the columnar InN waveguide could contribute to the difference in propagation losses between both devices. At the same time, a reduction of the effective refractive index could be expected together with the subsequent reduction of the optical light confinement.

Nonlinear absorption coefficient values of ~43 cm/GW and ~65 cm/GW have been reached for the columnar InN/AlN device for TM- and TE-light, respectively. On the other hand, values of ~70 cm/GW and ~114 cm/GW for TM and TE polarizations

have also been obtained for the compact InN waveguide. All the estimated values are larger than those reported for InP, Si(111) and GaAs at $\sim$1.55 μm.
The difference between the experimental nonlinear transmittance results obtained in columnar InN/AlN waveguides and compact InN ones lies in the input pulse energy required in each case for obtaining a reduction of the transmittance of 3 dB at nonlinear regime. Thus, these required energies are estimated to be 3.6 pJ for TE- light and 4.6 pJ for TM polarization in the columnar InN/AlN waveguide and 1.1 pJ and 1.3 pJ in the compact InN device for TE- and TM-light, respectively. These results make the compact InN-based device more efficient in terms of nonlinear behavior than the columnar InN-based waveguide.

Finally, these results open the possibility of using a low-cost deposition technique such as RF sputtering for the successful development of InN-based optical waveguides in a thermal harmless procedure. The capability of the developed sputtered-InN-based devices (both based on columnar and compact InN layers) for acting as reverse saturable absorbers via TPA processes has been demonstrated. These InN-based devices could work as all-optical limiters within a III-nitride-based PIC operating at 1.55 μm.

Chapter 8

Conclusions and future work

8.1 Conclusions

This section presents the conclusions extracted from the results obtained in this work. They are divided in three parts directly related to the three main objectives pursued in this Thesis. In a general view, this work has demonstrated the possibility of achieving different optical waveguide components based on III-nitrides, even using a low cost technology, which present specific linear and nonlinear optical responses. These behaviors are attractive for performing different all-optical functions such as switching, passive interconnection and power limitation within a PIC operating at 1.55 μm.

GaN/AlN QW- and QD-based optical waveguides

Optical waveguides based on GaN/AlN quantum heterostructures have been demonstrated as saturable absorbers at 1.55 μm via their ISB transition only accessible for TM-polarized light.

Two different optimized samples were synthesized by PAMBE consisting of a GaN guiding layer on 1.1-μm-thick AlN-on-sapphire commercial substrates and containing 3 periods of GaN/AlN QWs and QDs, respectively. Electrical simulations determines that the tuning of the band gap energy at 1.55 μm is obtained by

~1.5-nm-thick GaN QWs and ~1-nm-high GaN QDs, both of them embedded in ~3-nm-thick AlN barriers.
In order to ensure the population in the first confined electronic level of both involved transitions, it is required to grow a 25-nm-thick GaN buffer layer on top of the AlN-template.

It is determined from optical simulations that a 600-nm-thick GaN guiding layer ensures the modal guiding at 1.55 μm at the minimum ridge width affordable by optical lithography.
Ridge widths from 2 μm to 50 μm and etching depths between 50 nm and 600 nm were investigated. The optimized ridge height was 350 nm inducing single mode propagation for 2-μm-wide waveguides and multimode propagation for ridges wider than 5 μm. This etching depth also exhibits the maximum theoretical modal amplitude 250 nm above the AlN-template. Thus, QWs were placed at 250 nm and QDs just 25 nm above the AlN-template, leading to a more efficient light pumping at 1.55 μm in the case of QWs compared to QDs.

The patterning of 2-μm- and 5-μm-wide waveguides was performed by UV lithography. The GaN guiding layers were 350-nm-etched by the ICP-RIE technique using $SiCl_4$ and N_2 plasma at RT. Both input and output waveguide facets were mechanically polished with diamond lapping films with grain sizes from 30 μm to 1 μm.

Linear and nonlinear optical experiments at 1.55 μm were carried out for the characterization of three different GaN/AlN-based devices: 5-μm-wide QW-based, 5-μm-wide QD-based and 2-μm-wide QD-based waveguides.
As expected, optical coupling losses for TE- and TM-light suffer an increase when decreasing the width of the QD-based waveguides from 5 μm to 2 μm since the material coupling region has been reduced.
Propagation losses for TE- and TM-polarizations follow a different evolution. In the case of TE-light, propagation losses are not affected by the change of QWs by QDs as active region but they are reduced when decreasing the ridge width from 5 μm to 2 μm among the QD-based waveguides. This reduction is attributed to the single mode behavior of the 2-μm-wide waveguide which provides a better confinement of light within the narrowest device.

By contrast, these waveguides demonstrate their absorptive behavior at low incident optical power for TM light regardless of the embedded quantum region. The propagation losses increase when replacing the QWs by the QDs heterostructure. Furthermore, these losses are even more increased when propagating through the single mode waveguide with ridge width of 2 μm due to the better confinement of the optical mode making more efficient the absorption at the active region.

Regarding the transmittance measurements as a function of the input pulse energy, constant transmittance is observed for TE-light in the range of optical power under study (from -12 dBm to 17 dBm). However, a high increase of optical transmittance is obtained when raising the input pulse energies for TM-light due to the saturation of the ISB transition in QWs and QDs.

The three waveguides under study are considered very attractive for nonlinear applications due to the absorption saturation they present, reaching up to $\sim$25 dB of transmittance increase from low to high input powers. Among them, the 2-μm-wide GaN/AlN QD-based waveguide can be considered as the most efficient saturable absorber device. It presents the highest optical transmittance contrast for TM light for the lowest required input pulse energy (3 dB of transmittance change for 3 pJ of input pulse energy with 150-fs pulses).

These three types of optical waveguides have been demonstrated to act as saturable absorbers at 1.55 μm. All-optical switching functions could be reached with this type of devices basing on their ISB absorption saturation effect.

Sputtered-AlN-based optical waveguides

The development of sputtered-AlN waveguides has also been presented in this work. For these structures, it has been demonstrated a non-absorptive behavior at 1.55 μm at low and high incident optical power.

Firstly, AlN films deposited on *c*-sapphire by RF sputtering were optimized by analyzing the influence of the RF power applied to the Al target, the substrate temperature and the external substrate biasing on the AlN layer properties.

The optimized sputtered-AlN films were achieved following a two-step deposition method. They were based on a double AlN layer consisted on a first 30-nm-thick unbiased AlN buffer followed by an AlN layer deposited under -15 V biased substrate condition. Apart from the followed sequence, the RF power was kept at 150 W, 450 °C of substrate temperature, 0.47 Pa of pressure and pure nitrogen atmosphere.

The AlN-waveguide format was designed by optical simulations. The thickness of the AlN guiding layer was optimized to ~600 nm for ensuring the modal guiding for ridge widths as low as 2 μm while facilitating the integration with the previously presented GaN/AlN structures. Ridges of 5 μm and wider lead to multimode propagation at 1.55 μm regardless of the considered etching depth. AlN waveguides with ridge widths of 2 μm are single mode for etching depths below 200 nm and above 500 nm.

The deposited 570-nm-thick AlN used for the fabrication of the waveguide presents the following material properties: compact morphology, high crystal quality (FWHM of the AlN(0002) rocking curve of 1.2°), rms surface roughness around 1 nm and apparent optical band gap of ~6.0 eV with high optical transmittance at 1.55 μm (~85 %).

The patterning of the 2-μm- and 5-μm-wide waveguides was performed by UV lithography. The AlN layers were 125-nm-etched due to technological limitations by means of the ICP-RIE technique using SF_6 and O_2 plasma at RT. Etching depth was limited by the technological process in relation to the maximum thickness of the Al metal mask deposited during the lithography process. Waveguide facets were polished with diamond lapping films with grain sizes ranging from 40 μm to 0.1 μm.

Sputtered-AlN waveguides have shown constant optical transmittance for both TE- and TM polarizations in the whole range of optical powers studied at 1.55 μm.
Coupling losses in the range from 40 dB to 42 dB are estimated for both polarizations, being 2 dB larger for TM light with respect to TE polarization. This difference is attributed to the waveguide asymmetry.
The optical propagation losses are higher for TE-light (7.1 dB/mm) compared to those obtained for TM polarization (4.1 dB/mm). This difference can be due to the low-confinement of the optical mode along the x-axis.
The sputtered-AlN-based waveguides developed in this work open the possibility

of using this low-cost technique for the overgrowth at non-harmful temperatures of AlN-based passive interconnections at 1.55 μm.

Sputtered-InN-based optical waveguides

Two different sputtered-InN-based optical waveguides were developed during this Thesis. In both cases, it has been demonstrated their nonlinear optical response via TPA process at 1.55 μm, being novel results for these type of optical waveguides.

Both InN guiding layers used for the fabrication of the optical waveguides were deposited by RF reactive sputtering on *c*-sapphire substrates.

- **Columnar InN guiding layer on AlN buffer**

  This InN layer was deposited on a previously optimized 60-nm-thick double AlN buffer layer following the two-step method for AlN films. The deposition conditions for the InN film were 40 W of RF power applied to the In target, 450 °C of substrate temperature, 0.47 Pa of sputtering pressure and pure nitrogen atmosphere. InN layers grown under these conditions show columnar morphology with diameter of the nanocolumns of ∼87 nm.

  Optical simulations lead to 600 nm of AlN thickness to ensure the modal guiding at 1.55 μm for ridge widths of 2 μm while enabling the coupling to the GaN/AlN-based and AlN-based waveguides presented in this Thesis. On the other hand, etching depths from 50 nm to 200 nm induce single mode propagation. The optimized ridge height was 100 nm since it leads to the lowest mode effective area (∼1.6 μm^2) among the analyzed range and, in turn, the highest confinement of light through the waveguide.

  A 600-nm-thick columnar InN guiding layer was deposited for the fabrication of the columnar InN waveguide. This guiding layer presents an apparent optical band gap of 1.69 eV with an absorption band edge of ∼174 meV. Besides, the columnar InN film presents good crystal quality (FWHM of the AlN(0002) rocking curve of 2.7°) and an rms surface roughness of ∼6 nm.

- **Compact InN guiding layer**

  A 350-nm-thick compact InN film was deposited directly on the sapphire substrate under the following deposition conditions: 40 W of RF power, 300 °C of substrate temperature, 0.47 Pa of pressure and pure nitrogen. This InN film shows similar rms as the columnar one (∼6 nm), but larger optical band gap of 1.77 eV with an absorption band edge of ∼133 meV. Futhermore, it presents good crystal quality showing a FWHM of the AlN(0002) rocking curve of 2.2°.

  Optical simulations for 2-μm-wide compact InN waveguides lead to choose 350 nm as the best etching depth due to its single mode condition at 1.55 μm while presenting the lowest effective mode area (∼0.9 μm^2) in the range under study. Besides, it implies the easiest technological etching process.

The patterning of both InN-based waveguides with widths of 2 μm and 5 μm was also performed by UV lithography. The InN layers were etched by sputtering with Ar plasma and 40 W of RF power applied to the substrate, with the substrate kept at RT and 0.47 Pa of chamber pressure. The facets of the waveguides were polished using diamond lapping films with different grain sizes ranging from 40 μm to 0.1 μm.

Single mode 2-μm-wide InN-based waveguides were optically characterized at 1.55 μm for TE- and TM-light at linear and nonlinear regimes. Coupling and propagation losses are, respectively, similar for both polarizations in each type of waveguide. The expected polarization dependence of the linear transmittance due to geometrical asymmetry of the waveguides could be hidden by the scattering effects attributed to the post-etching residual sidewall roughness.
A significant difference in optical losses between the two InN-based waveguides was achieved. Coupling losses in the compact InN waveguide (∼50 dB) are much larger than those in the columnar one (∼40 dB), being attributed to the difference in waveguide dimensions.
Propagation losses are much higher in the case of the columnar InN/AlN waveguide (∼15 dB/mm) compared to those corresponding to the compact InN device (∼8.7 dB/mm). It can be explained by the better light confinement provided by the

total etching of the compact InN layer which can contribute to minimize the optical losses at the guiding layer/substrate and guiding layer/air interfaces due to surface roughness. Furthermore, a larger contribution of Rayleigh scattering effects due to the nanocolumns could be expected within the columnar InN waveguide leading to higher propagation losses. This columnar morphology could reduce the effective refractive index inducing a reduction of the optical modal confinement in the columnar InN waveguide.

Optical transmittance is significantly reduced in both devices when injecting light at high input pulse energies at resonant wavelength (∼1.55 μm). This reduction is achieved via the TPA process for both TE- and TM-polarizations showing ∼6 dB and ∼4.5 dB of contrast, respectively. The input pulse energy required for reaching these total contrasts is ∼6 pJ in the case of the columnar InN waveguide and ∼1.6 pJ for the compact InN one.
Nonlinear absorption coefficient values of ∼43 cm/GW and ∼65 cm/GW have been obtained for the columnar InN/AlN device for TM- and TE-light, respectively. At the same time, values of ∼70 cm/GW and ∼114 cm/GW for TM and TE polarizations, respectively, have also been estimated for the compact InN waveguide. All these values are larger than the reported for InP, Si(111) and GaAs at ∼1.55 μm. A ratio of ∼3.5 between the largest value achieved in this work and the highest value reported corresponding to InP material (33 cm/GW) has been obtained.
The input pulse energy required for reaching 3 dB of transmittance change is lower in the case of the compact InN waveguide than for the columnar InN one. This result leads to consider the compact InN-based waveguide as the most efficient InN-based device in terms of nonlinear behavior at 1.55 μm.

Taking into account that both the growth of the InN guiding layers and the etching process of the waveguides were performed by RF sputtering, the obtained results open the possibility of using this low-cost and thermally harmless technique for reaching reverse saturable absorbers via the TPA process at 1.55 μm.

8.2 Future work

This section focuses on the new ideas which have emerged during the development of this Thesis. It includes the possible improvements of the structures, the methodology to develop them and also new applications to take into account as future work.

GaN/AlN QW- and QD-based optical waveguides

The efficiency of these devices for further application in all-optical switching could be improved by different possibilities:

- Making more absorptive the QD-based device while ensuring the non-total vanishing of light transmittance. This goal could be reached by an optimum trade-off between the number of periods of the QD structure and the waveguide length.

- Fitting the QD location with the maximum of the mode amplitude into the waveguide in order to make more efficient the light pumping of the active region. It would be required to optimize both the thickness of the GaN guiding layer and the etching depth of the waveguide format to fit the maximum modal amplitude to the QDs location (in this case 25 nm above the AlN-template).

- Following a less harmful polishing procedure for the waveguide facets in order to reduce the coupling losses. The series of diamond grain sizes used should begin with a size lower than 30 μm and finish the process using a diamond lapping film with grain size of 0.1 μm to reach a better optical quality of the input and output facets of the waveguide.

- Improving the coupling technique by investigating other methods different from the end-coupling method used in this work. Advantages and disadvantages of other methods in terms of alignment complexity and coupling- and cost-efficiency should be analyzed. Methods such as tapered-coupling method or grating coupling method could be investigated.

Concerning new fields of application, apart from the possibility of using these devices in all-optical switching applications at 1.55 μm, wavelength conversion process through cross-absorption-modulation phenomena at 1.55 μm could be explored. Furthermore, these optical waveguides can be also used as the saturable absorber element of a SESAM (*i.e.*, semiconductor saturable absorber mirror) introduced within an optical resonator for the development of ultrafast mode-locked lasers emitting at 1.55 μm. However, it has to be noticed that for these applications, coupling losses should be extremely reduced.

Sputtered-AlN-based optical waveguides

The efficiency of these sputtered-AlN-waveguides for further application in all-optical interconnections at 1.55 μm is limited by the optical losses. These losses could be reduced by means of:

- Optimizing the technological process to allow the etching of the AlN guiding layer down to the substrate would be possible. Thus, a better confinement of light along the waveguide and a reduction of the propagation losses due to interfaces roughness could be reached.
- Performing a better polishing procedure as in the case of the GaN/AlN-based optical waveguides to reduce the coupling losses at both input and output facets of the devices.
- Improving the coupling technique as in the case of GaN/AlN-based waveguides.

Considering the established basis of passive AlN optical waveguides obtained in this work, a low-cost optical coupler device could be implemented by using this type of low-cost AlN waveguides. The structure could be designed by using two waveguides and, depending on the gap distance between them, the etching depth and the coupling length, light could be coupled from one to the other at a certain amplitude relation. Other different photonic devices such as passive optical ring resonators could be also implemented within the visible/NIR range.

Sputtered-InN-based optical waveguides

As in the case of the sputtered-AlN-based waveguides, the efficiency of the sputtered-InN-based optical devices could be improved in terms of nonlinear optical efficiency by the following ways:

- Synthesizing sputtered-InN guiding layers which present an apparent optical band gap closer to 1.6 eV in order to provide a more enhanced resonant effect at 1.55 μm (0.8 eV) for TPA process.
- Optimizing the polishing procedure to make it less harmful.
- Improving the coupling technique as in the rest of waveguides under study.

Apart from the mentioned application in all-optical limiters within a III-nitride-based PIC, these InN-based waveguides could be used to develop opto-chemical sensors by investigating the influence of the surrounding medium on the modes propagating through the optical waveguide.

Furthermore, the optimization of both AlN and InN films by RF sputtering in our group opens the possibility to study the growth of AlInN alloys. These materials are of wide interest for application in sensors and low-cost solar cells working within the visible/NIR range of the solar spectrum.

Bibliography

[Agr04] G. P. Agrawal, *Lightwave technology: components and devices*, vol. 1 (Wiley-Interscience, 2004).

[Aki98] M. Akiyama, C.-N. Xu, K. Nonaka, K. Shobu, and T. Watanabe, *Statistical approach for optimizing sputtering conditions of highly oriented aluminum nitride thin films*. Thin Solid Films **315**(1), 62 (1998).

[Alb03] J. M. Albella, *Láminas delgadas y recubrimientos: preparación, propiedades y aplicaciones*, vol. 11 (CSIC, 2003).

[Alm04] V. R. Almeida, C. A. Barrios, R. R. Panepucci, and M. Lipson, *All-optical control of light on a silicon chip*. Nature **431**(7012), 1081 (2004).

[Alv14] M. Alvarado, M. Pelegrini, I. Pereyra, T. d. Assumpção, L. Kassab, and M. Alayo, *Fabrication and characterization of aluminum nitride pedestal-type optical waveguide 1*. Can. J. Phys. **92**(999), 1 (2014).

[And09] A. Anders and G. Y. Yushkov, *Plasma "anti-assistance" and "self-assistance" to high power impulse magnetron sputtering*. J. Appl. Phys. **105**(7), 073301 (2009).

[Ane99] E. Anemogiannis, E. N. Glytsis, and T. K. Gaylord, *Determination of guided and leaky modes in lossless and lossy planar multilayer optical waveguides: reflection pole method and wavevector density method*. J. Lightwave Technol. **17**(5), 929 (1999).

[Ass04] M. Assouar, M. El Hakiki, O. Elmazria, P. Alnot, and C. Tiusan, *Synthesis and microstructural characterisation of reactive RF magnetron sputtering AlN films for surface acoustic wave filters*. Diam. Relat. Mater. **13**(4), 1111 (2004).

[Bar73] A. Barker and M. Ilegems, *Infrared lattice vibrations and free-electron dispersion in GaN*. Phys. Rev. B **7**(2), 743 (1973).

[Bau07] E. Baumann, *Near infrared intersubband absorption and photovoltaic detection in GaN/AIN multi quantum well structures*. Ph.D. thesis, Institut de Physique de l'Université de Neuchâtel (2007).

[Bee13] M. Beeler, E. Trichas, and E. Monroy, *III-nitride semiconductors for intersubband optoelectronics: a review*. Semicond. Sci. Tech. **28**(7), 074022 (2013).

[Ber99] M. J. Bergmann, U. Özgür, H. C. Casey, J. F. Muth, Y. C. Chang, R. M. Kolbas, R. A. Rao, C. B. Eom, and M. Schurman, *Linear optical properties of a heavily Mg-doped* $Al_{0.09}Ga_{0.91}N$ *epitaxial layer*. Appl. Phys. Lett. **74**(21), 3188 (1999).

[Bhu03] A. G. Bhuiyan, A. Hashimoto, and A. Yamamoto, *Indium nitride (InN): A review on growth, characterization, and properties*. J. Appl. Phys. **94**(5), 2779 (2003).

[Bir07] S. Birner, T. Zibold, T. Andlauer, T. Kubis, M. Sabathil, A. Trellakis, and P. Vogl, *Nextnano: General purpose 3-D simulations*. IEEE T. Electron. Dev. **54**(9), 2137 (2007).

[Blo00] N. Bloembergen, *Nonlinear optics: past, present, and future*. IEEE J. Sel. Top. Quant. **6**(6), 876 (2000).

[Bor99] M. Born and E. Wolf, *Principles of optics: electromagnetic theory of propagation, interference and diffraction of light* (CUP Archive, 1999).

[Boy08] R. W. Boyd, *Nonlinear optics* (Academic press, 2008).

[Bri09] O. Briot, S. Ruffenach, M. Moret, B. Gil, C. Giesen, M. Heuken, S. Rushworth, T. Leese, and M. Succi, *Growth of InN films and nanostructures by MOVPE*. J. Cryst. Growth **311**(10), 2761 (2009).

[But05] K. Butcher and T. Tansley, *InN, latest development and a review of the band-gap controversy*. Superlattice Microst. **38**(1), 1 (2005).

[Che03] H. Cheng, Y. Sun, and P. Hing, *The influence of deposition conditions on structure and morphology of aluminum nitride films deposited by radio frequency reactive sputtering*. Thin Solid Films **434**(1), 112 (2003).

[Che08] J. Cherng, C. Lin, and T. Chen, *Two-step reactive sputtering of piezoelectric AlN thin films*. Surf. Coat. Tech. **202**(22), 5684 (2008).

[Che13] W. C. Chen, S. Y. Kuo, F. I. Lai, W. T. Lin, and C. N. Hsiao, *Effect of substrate temperature on structural and optical properties of InN epilayer grown on GaN template*. Thin Solid Films **529**, 169 (2013).

[Chi07] K.-H. Chiu, J.-H. Chen, H.-R. Chen, and R.-S. Huang, *Deposition and characterization of reactive magnetron sputtered aluminum nitride thin films for film bulk acoustic wave resonator*. Thin Solid Films **515**(11), 4819 (2007).

[Cho04] D.-H. Cho, D.-Y. Kim, B.-H. Kim, J.-P. Jun, J.-S. Park, and J.-B. Lee, *Properties of AlN films grown by two-step deposition and characteristics of AlN-FBAR devices*. In *IEEE Ultrasonics Symposium, 2004*, vol. 3, pp. 1702–1705 (2004).

[Cib04] C. Cibert, F. Tétard, P. Djemia, C. Champeaux, A. Catherinot, and D. Tétard, *Mechanical and physicochemical properties of AlN thin films obtained by pulsed laser deposition*. Superlattice Microst. **36**(4), 409 (2004).

[Cle03] M. Clement, E. Iborra, J. Sangrador, A. Sanz-Hervas, L. Vergara, and M. Aguilar, *Influence of sputtering mechanisms on the preferred orientation of aluminum nitride thin films*. J. Appl. Phys. **94**(3), 1495 (2003).

[Das12] A. Das, *Boîtes quantiques de semi-conducteurs nitrures pour des applications aux capteurs opto-chimiques*. Ph.D. thesis, Université de Grenoble (2012).

[Dav02] V. Y. Davydov, A. Klochikhin, R. Seisyan, V. Emtsev, S. Ivanov, F. Bechstedt, J. Furthmüller, H. Harima, A. Mudryi, J. Aderhold *et al.*, *Absorption and emission of hexagonal InN. Evidence of narrow fundamental band gap*. Phys. Status Solidi B **229**(3), r1 (2002).

[Dim00] R. Dimitrov, M. Murphy, J. Smart, W. Schaff, J. Shealy, L. Eastman, O. Ambacher, and M. Stutzmann, *Two-dimensional electron gases in Ga-face and N-face AlGaN/GaN heterostructures grown by plasma-induced molecular*

beam epitaxy and metalorganic chemical vapor deposition on sapphire. J. Appl. Phys. **87**(7), 3375 (2000).

[Din03] M. Dinu, F. Quochi, and H. Garcia, *Third-order nonlinearities in silicon at telecom wavelengths*. Appl. Phys. Lett. **82**(18), 2954 (2003).

[Drü00] T. P. Drüsedau and J. Bläsing, *Optical and structural properties of highly c-axis oriented aluminum nitride prepared by sputter-deposition in pure nitrogen*. Thin Solid Films **377**, 27 (2000).

[Edg97] J. H. Edgar, C. Wei, D. Smith, T. Kistenmacher, and W. Bryden, *Hardness, elastic modulus and structure of indium nitride thin films on AlN-nucleated sapphire substrates*. J. Mater. Sci.-Mater. El. **8**(5), 307 (1997).

[Ekp05] S. D. Ekpe, L. W. Bezuidenhout, and S. K. Dew, *Deposition rate model of magnetron sputtered particles*. Thin Solid Films **474**(1), 330 (2005).

[Ess13] R.-J. Essiambre, R. Ryf, N. Fontaine, and S. Randel, *Breakthroughs in photonics 2012: Space-division multiplexing in multimode and multicore fibers for high-capacity optical communication*. IEEE Photonics J. **5**(2), 0701307 (2013).

[Est06] Ó. Esteban, *Desarrollo y caracterización de sensores de fibra óptica para control medioambiental*. Ph.D. thesis, Universidad Complutense de Madrid (2006).

[Est11] Ó. Esteban, F. B. Naranjo, N. Díaz-Herrera, S. Valdueza-Felip, M.-C. Navarrete, and A. González-Cano, *High-sensitive SPR sensing with Indium Nitride as a dielectric overlay of optical fibers*. Sensor. Actuat. B-Chem. **158**(1), 372 (2011).

[Fen08] Z. C. Feng, *III-nitride Devices and Nanoengineering* (Imperial College Press, 2008).

[Fer09] S. Fernández, A. Martínez-Steele, J. Gandía, and F. B. Naranjo, *Radio frequency sputter deposition of high-quality conductive and transparent ZnO: Al films on polymer substrates for thin film solar cells applications*. Thin Solid Films **517**(10), 3152 (2009).

[Fer10] S. Fernández, F. B. Naranjo, S. Valdueza-Felip, and O. De Abril, *Applications of ZnO: Al deposited by RF sputtering to InN low-cost technology*. Phys. Status Solidi A **207**(7), 1717 (2010).

[Fra49] F. Frank and J. H. van der Merwe, *One-dimensional dislocations. I. Static theory*. Proc. Royal Soc. London. Series A. Mathematical and Physical Sciences **198**(1053), 205 (1949).

[Gal06] C. S. Gallinat, G. Koblmüller, J. S. Brown, S. Bernardis, J. S. Speck, G. D. Chern, E. D. Readinger, H. Shen, and M. Wraback, *In-polar InN grown by plasma-assisted molecular beam epitaxy*. Appl. Phys. Lett. **89**(3), 032109 (2006).

[Gal07] C. Gallinat, G. Koblmüller, J. Brown, and J. Speck, *A growth diagram for plasma-assisted molecular beam epitaxy of In-face InN*. J. Appl. Phys. **102**(6), 064907 (2007).

[GH11] M. González-Herráez and T. Sylvestre, *Advanced fiber optics: concepts and technology*, chap. 5 (EPFL Press, 2011).

[Gil98] B. Gil, *Group III nitride semiconductor compounds: physics and applications* (Clarendon, 1998).

[Gio09] C. Giordano, I. Ingrosso, M. Todaro, G. Maruccio, S. De Guido, R. Cingolani, A. Passaseo, and M. De Vittorio, *AlN on polysilicon piezoelectric cantilevers for sensors/actuators*. Microelectron. Eng. **86**(4), 1204 (2009).

[Gog04] N. Gogneau, D. Jalabert, E. Monroy, E. Sarigiannidou, J. Rouviere, T. Shibata, M. Tanaka, J. Gerard, and B. Daudin, *Influence of AlN overgrowth on structural properties of GaN quantum wells and quantum dots grown by plasma-assisted molecular beam epitaxy*. J. Appl. Phys. **96**(2), 1104 (2004).

[Gop02] A. V. Gopal, H. Yoshida, A. Neogi, N. Georgiev, T. Mozume, T. Simoyama, O. Wada, and H. Ishikawa, *Intersubband absorption saturation in InGaAs-AlAsSb quantum wells*. IEEE J. Quantum Elect. **38**(11), 1515 (2002).

[Gra05] J. Grandal and M. Sánchez-García, *InN layers grown on silicon substrates: effect of substrate temperature and buffer layers*. J. Cryst. Growth **278**(1), 373 (2005).

[Gra12] J. R. Grandusky, Z. Zhong, J. Chen, C. Leung, and L. J. Schowalter, *Manufacturability of high power ultraviolet-C light emitting diodes on bulk aluminum nitride substrates*. Solid State Electron. (2012).

[Gue11] J. Guerra, L. Montañez, O. Erlenbach, G. Galvez, F. De Zela, A. Winnacker, and R. Weingärtner, *Determination of the optical bandgap and disorder energies of thin amorphous SiC and AlN films produced by radio frequency magnetron sputtering*. In *J. Phys.: Conf. Ser.*, vol. 274, p. 012113 (IOP Publishing, 2011).

[Gui06] F. Guillot, E. Bellet-Amalric, E. Monroy, M. Tchernycheva, L. Nevou, L. Doyennette, F. Julien, L. S. Dang, T. Remmele, M. Albrecht *et al.*, *Si-doped GaN/ AlN quantum dot superlattices for optoelectronics at telecommunication wavelengths*. J. Appl. Phys. **100**(4), 044326 (2006).

[Guo98] Q. Guo, N. Shingai, M. Nishio, and H. Ogawa, *Deposition of InN thin films by radio frequency magnetron sputtering*. J. Cryst. Growth **189**, 466 (1998).

[Guo03] Q. Guo, K. Yahata, T. Tanaka, M. Nishio, and H. Ogawa, *Low-temperature growth of aluminum nitride on sapphire substrates*. J. Cryst. Growth **257**(1), 123 (2003).

[Guo05] Q. Guo, T. Tanaka, M. Nishio, H. Ogawa, X. Pu, and W. Shen, *Observation of visible luminescence from indium nitride at room temperature*. Appl. Phys. Lett. **86**(23), 231913 (2005).

[Guo06] Q. Guo, T. Tanaka, M. Nishio, and H. Ogawa, *Growth properties of AlN films on sapphire substrates by reactive sputtering*. Vacuum **80**(7), 716 (2006).

[Guo09] Q. Guo, M. Ogata, Y. Ding, T. Tanaka, and M. Nishio, *Heteroepitaxial growth of InN layers on (111) silicon substrates*. J. Cryst. Growth **311**(10), 2783 (2009).

[Had91] G. R. Hadley, *Transparent boundary condition for beam propagation*. Opt. Lett. **16**(9), 624 (1991).

[Had92] G. R. Hadley, *Wide-angle beam propagation using Padé approximant operators*. Opt. Lett. **17**(20), 1426 (1992).

[Ham04] J. Hamazaki, S. Matsui, H. Kunugita, K. Ema, H. Kanazawa, T. Tachibana, A. Kikuchi, and K. Kishino, *Ultrafast intersubband relaxation and nonlinear susceptibility at 1.55 μm in GaN/AlN multiple-quantum wells*. Appl. Phys. Lett. **84**(7), 1102 (2004).

[Heb02] J. Heber, C. Gmachl, H. Ng, and A. Cho, *Comparative study of ultrafast intersubband electron scattering times at 1.55 μm wavelength in GaN/AlGaN heterostructures*. Appl. Phys. Lett. **81**(7), 1237 (2002).

[Hof03] D. Hofstetter, S.-S. Schad, H. Wu, W. J. Schaff, and L. F. Eastman, *GaN/AlN-based quantum-well infrared photodetector for 1.55 μm*. Appl. Phys. Lett. **83**(3), 572 (2003).

[Hor07] I. Horcas, R. Fernández, J. M. Gómez-Rodríguez, J. Colchero, J. Gómez-Herrero, and A. M. Baro, *WSXM: A software for scanning probe microscopy and a tool for nanotechnology*. Rev. Sci. Instrum. **78**, 013705 (2007).

[Hui03] R. Hui, S. Taherion, Y. Wan, J. Li, S. Jin, J. Lin, and H. Jiang, *GaN-based waveguide devices for long-wavelength optical communications*. Appl. Phys. Lett. **82**(9), 1326 (2003).

[Hun84] R. G. Hunsperger, *Integrated optics: theory and technology*, vol. 2 (Springer, 1984).

[Hut02] Y. Huttel, H. Gomez, A. Cebollada, G. Armelles, and M. Alonso, *Epitaxial growth of AlN on sapphire (0001) by sputtering: a structural, morphological and optical study*. J. Cryst. Growth **242**(1), 116 (2002).

[Iiz00] N. Iizuka, K. Kaneko, N. Suzuki, T. Asano, S. Noda, and O. Wada, *Ultrafast intersubband relaxation ($\leq$150 fs) in AlGaN/GaN multiple quantum wells*. Appl. Phys. Lett. **77**(5), 648 (2000).

[Iiz02] K. Iizuka, *Elements of photonics* (Wiley-Interscience, 2002).

[Iiz09] N. Iizuka, H. Yoshida, N. Managaki, T. Shimizu, S. Hassanet, C. Cumtornkittikul, M. Sugiyama, and Y. Nakano, *Integration of GaN/AlN all-optical switch with SiN/AlN waveguide utilizing spot-size conversion*. Opt. Express **17**(25), 23247 (2009).

[Iri10] G. Iriarte, J. Rodriguez, and F. Calle, *Synthesis of c-axis oriented AlN thin films on different substrates: A review*. Mater. Res. Bull. **45**(9), 1039 (2010).

[Jin12] H. Jin, J. Zhou, S. Dong, B. Feng, J. Luo, D. Wang, W. Milne, and C. Yang, *Deposition of c-axis orientation aluminum nitride films on flexible polymer substrates by reactive direct-current magnetron sputtering*. Thin Solid Films **520**(15), 4863 (2012).

[Kam06] D. S. Kamber, Y. Wu, B. A. Haskell, S. Newman, S. P. DenBaars, J. S. Speck, and S. Nakamura, *Direct heteroepitaxial growth of thick AlN layers on sapphire substrates by hydride vapor phase epitaxy*. J. Cryst. Growth **297**(2), 321 (2006).

[Kan08] P. K. Kandaswamy, F. Guillot, E. Bellet-Amalric, E. Monroy, L. Nevou, M. Tchernycheva, A. Michon, F. Julien, E. Baumann, F. Giorgetta *et al.*, *GaN/AlN short-period superlattices for intersubband optoelectronics: A systematic study of their epitaxial growth, design, and performance*. J. Appl. Phys. **104**(9), 093501 (2008).

[Kar97] S. Karmann, H. Schenk, U. Kaiser, A. Fissel, and W. Richter, *Growth of columnar aluminum nitride layers on Si (111) by molecular beam epitaxy*. Mater. Sci. Eng. B-Adv. **50**(1), 228 (1997).

[Kas01] S. O. Kasap, *Optoelectronics & Photonics: Principles & Practices* (Prentice-Hall, 2001).

[Kas07] S. Kasap and P. Capper, *Springer handbook of electronic and photonic materials* (Springer, 2007).

[Kaw04] K. Kawano and T. Kitoh, *Introduction to Optical Waveguide Analysis: Solving Maxwell's Equation and the Schrödinger Equation* (John Wiley & Sons, 2004).

[Kil64] J. S. Kilby, *Miniaturized electronic circuits* (1964). US Patent 3,138,743.

[Kim94] K. Kim, W. Reed, K. Quoi, and R. Stolen, *Measurement of the nonlinear index of silica-core and dispersion-shifted fibers*. Opt. Lett. **19**(4), 257 (1994).

[Kis93] T. Kistenmacher, S. Ecelberger, and W. Bryden, *Structural and electrical properties of reactively sputtered InN thin films on AlN-buffered (00.1)*

sapphire substrates: Dependence on buffer and film growth temperatures and thicknesses. J. Appl. Phys. **74**(3), 1684 (1993).

[Kob03] G. Koblmueller, R. Averbeck, L. Geelhaar, H. Riechert, W. Hosler, and P. Pongratz, *Growth diagram and morphologies of AlN thin films grown by molecular beam epitaxy*. J. Appl. Phys. **93**(12), 9591 (2003).

[Kol08] I. Kolev and A. Bogaerts, *Calculation of gas heating in a dc sputter magnetron*. J. Appl. Phys. **104**(9), 093301 (2008).

[Lah09] L. Lahourcade, *Plasma-assisted molecular beam epitaxy of (11-22)-oriented III-nitrides*. Ph.D. thesis, Institut Polytechnique de Grenoble (2009).

[Lal11] V. Lal, P. Evans, M. Fisher, R. Malendevich, A. James, P. Studenkov, G. Goldfarb, T. Vallaitis, M. Kato, P. Samra *et al.*, *Terabit photonic integrated circuits in InP: 10-channel coherent PM-QPSK transmitter and receiver PICs operating at 100 Gb/s per wavelength*. In *Photonics Society Summer Topical Meeting Series, 2011 IEEE*, pp. 117–118 (IEEE, 2011).

[Les10] K. J. Lesker, *Practical Process Tips*. Lesker-Tech. **7**, 1 (2010).

[Li07a] Y. Li, A. Bhattacharyya, C. Thomidis, T. D. Moustakas, and R. Paiella, *Ultrafast all-optical switching with low saturation energy via intersubband transitions in GaN/AlN quantum-well waveguides*. Opt. Express **15**(26), 17922 (2007).

[Li07b] Y. Li, A. Bhattacharyya, C. Thomidis, T. D. Moustakas, and R. Paiella, *Nonlinear optical waveguides based on near-infrared intersubband transitions in GaN/AlN quantum wells*. Opt. Express **15**(9), 5860 (2007).

[Li08] Y. Li, A. Bhattacharyya, C. Thomidis, Y. Liao, T. D. Moustakas, and R. Paiella, *Refractive-index nonlinearities of intersubband transitions in GaN/AlN quantum-well waveguides*. J. Appl. Phys. **104**(8), 083101 (2008).

[Liu05] J.-M. Liu, *Photonic devices* (Cambridge University Press, 2005).

[Liu10] B. Liu, Z. Zhang, R. Zhang, D. Fu, Z. Xie, H. Lu, W. Schaff, L. Song, Y. Cui, X. Hua *et al.*, *Electron concentration dependence of exciton localization and freeze-out at local potential fluctuations in InN films*. Appl. Phys. A-Mater. **99**(1), 139 (2010).

[Lob08] A. Lobanova, E. Yakovlev, R. Talalaev, S. Thapa, and F. Scholz, *Growth conditions and surface morphology of AlN MOVPE*. J. Cryst. Growth **310**(23), 4935 (2008).

[Lu01] H. Lu, W. J. Schaff, J. Hwang, H. Wu, G. Koley, and L. F. Eastman, *Effect of an AlN buffer layer on the epitaxial growth of InN by molecular-beam epitaxy*. Appl. Phys. Lett. **79**(10), 1489 (2001).

[Lu03] H. Lu, W. J. Schaff, L. F. Eastman, and C. Stutz, *Surface charge accumulation of InN films grown by molecular-beam epitaxy*. Appl. Phys. Lett. **82**(11), 1736 (2003).

[Luo08] W. Luo, X. Wang, L. Guo, H. Xiao, C. Wang, J. Ran, J. Li, and J. Li, *Influence of AlN buffer layer thickness on the properties of GaN epilayer on Si (111) by MOCVD*. Microelectron. J. **39**(12), 1710 (2008).

[Mal72] I. Malitson and M. Dodge, *Refractive-index and birefringence of synthetic sapphire*. In *J. Opt. Soc. Am.*, vol. 62, p. 1405 (1972).

[Man00] M. O. Manasreh, *III-Nitride Semiconductors: Electrical, Structural and Defects Properties: Electrical, Structural and Defects Properties* (Elsevier, 2000).

[Mas05] M. Mastro, O. Kryliouk, T. Anderson, A. Davydov, and A. Shapiro, *Influence of polarity on GaN thermal stability*. J. Cryst. Growth **274**(1), 38 (2005).

[Mat02] T. Matsuoka, H. Okamoto, M. Nakao, H. Harima, and E. Kurimoto, *Optical bandgap energy of wurtzite InN*. Appl. Phys. Lett. **81**(7), 1246 (2002).

[ML13a] L. Monteagudo-Lerma, S. Valdueza-Felip, F. B. Naranjo, P. Corredera, L. Rapenne, E. Sarigiannidou, G. Strasser, E. Monroy, and M. González-Herráez, *Waveguide saturable absorbers at 1.55 μm based on intraband transitions in GaN/AlN QDs*. Opt. Express **21**(23), 27578 (2013).

[ML13b] L. Monteagudo-Lerma, S. Valdueza-Felip, A. Núñez-Cascajero, M. González-Herráez,E. Monroy and F. B. Naranjo, *Two-step method for the deposition of AlN by radio frequency sputtering*. Thin Solid Films **545**, 149 (2013).

[ML14a] L. Monteagudo-Lerma, S. Valdueza-Felip, A. Núñez-Cascajero, A. Ruiz, M. González-Herráez, E. Monroy, and F. B. Naranjo, *Morphology and arrangement of InN nanocolumns deposited by radio-frequency sputtering: effect of the buffer layer*. J. Cryst. Growth (2015, Submitted).

[ML14b] L. Monteagudo-Lerma, F. B. Naranjo, P. Postigo, E. Barrios, P. Corredera, and M. González-Herráez, *InN-based optical waveguides by RF sputtering for all-optical applications at 1.55 μm*. Appl. Phys. Lett. (2015, Submitted).

[Mor08] H. Morkoc, *Handbook of nitride semiconductors and devices, Vol. 2 Electronic and optical processes in nitrides* (John Wiley & Sons, 2008).

[Nar03] F. B. Naranjo, *Crecimiento, fabricación y caracterización de diodos electroluminiscentes basados en pozos cunticos de InGaN*. Ph.D. thesis, Universidad Politécnica de Madrid (2003).

[Nar07] F. B. Naranjo, M. Gonzalez-Herraez, H. Fernández, J. Solis, and E. Monroy, *Third order nonlinear susceptibility of InN at near band-gap wavelengths*. Appl. Phys. Lett. **90**(9), 091903 (2007).

[Nar11] F. B. Naranjo, P. Kandaswamy, S. Valdueza-Felip, V. Calvo, M. González-Herráez, S. Martin-Lopez, P. Corredera, J. A. Mendez, G. Mutta, B. Lacroix, P. Ruterana, and E. Monroy, *Nonlinear absorption of InN/InGaN multiple-quantum-well structures at optical telecommunication wavelengths*. Appl. Phys. Lett. **98**(3), 031902 (2011).

[Nev06] L. Nevou, M. Tchernycheva, F. Julien, M. Raybaut, A. Godard, E. Rosencher, F. Guillot, and E. Monroy, *Intersubband resonant enhancement of second-harmonic generation in GaN/AlN quantum wells*. Appl. Phys. Lett. **89**(15), 151101 (2006).

[Nev09] L. Nevou, J. Mangeney, M. Tchernycheva, F. Julien, F. Guillot, and E. Monroy, *Ultrafast relaxation and optical saturation of intraband absorption of GaN/AlN quantum dots*. Appl. Phys. Lett. **94**(13), 132104 (2009).

[Nit14] Nitride-Crystals, `www.nitride-crystals.com` (2014).

[Nod93] S. Noda, T. Yamashita, M. Ohya, Y. Muromoto, and A. Sasaki, *All-optical modulation for semiconductor lasers by using three energy levels in n-doped quantum wells*. IEEE J. Quantum Elect. **29**(6), 1640 (1993).

[NTT12] NTT, *World Record One Petabit per Second Fiber Transmission over 50-km: Equivalent to Sending 5,000 HDTV Videos per Second over a Single Fiber*. Press Release (2012).

[Ozg01] U. Ozgur, G. Webb-Wood, H. O. Everitt, F. Yun, and H. Morkoç, *Systematic measurement of Al x Ga 1-x N refractive indices*. Appl. Phys. Lett. **79**(25), 4103 (2001).

[Pal06] A. Palmero, H. Rudolph, and F. Habraken, *Study of the gas rarefaction phenomenon in a magnetron sputtering system*. Thin Solid Films **515**(2), 631 (2006).

[Pas66] J. Pastrňák and L. Roskovcova, *Refraction index measurements on AlN single crystals*. Phys. Status Solidi B **14**(1), K5 (1966).

[Pat39] A. L. Patterson, *The Scherrer formula for X-ray particle size determination*. Phys. Rev. **56**(10), 978 (1939).

[Per12] W. H. Pernice, C. Xiong, and H. X. Tang, *High Q micro-ring resonators fabricated from polycrystalline aluminum nitride films for near infrared and visible photonics*. Opt. Express **20**(11), 12261 (2012).

[Pu06] X. Pu, W. Shen, Z. Zhang, H. Ogawa, and Q. Guo, *Growth and depth dependence of visible luminescence in wurtzite InN epilayers*. Appl. Phys. Lett. **88**(15), 151904 (2006).

[Rad05] S. Radic and C. J. McKinstrie, *Optical amplification and signal processing in highly nonlinear optical fiber*. IEICE T. Electron. **88**(5), 859 (2005).

[Rap03] R. Rapaport, G. Chen, O. Mitrofanov, C. Gmachl, H. Ng, and S. Chu, *Resonant optical nonlinearities from intersubband transitions in GaN/AlN quantum wells*. Appl. Phys. Lett. **83**(2), 263 (2003).

[Rav99] A. Raveh, M. Weiss, M. Pinkas, D. Rosen, and G. Kimmel, *Graded Al–AlN, TiN, and TiAlN multilayers deposited by radio-frequency reactive magnetron sputtering*. Surf. Coat. Tech. **114**(2), 269 (1999).

[Ros88] S. Rossnagel and H. Kaufman, *Current–voltage relations in magnetrons*. J. Vac. Sci. Technol. A **6**(2), 223 (1988).

[Ruf09] S. Ruffenach, M. Moret, O. Briot, and B. Gil, *Ammonia: A source of hydrogen dopant for InN layers grown by metal organic vapor phase epitaxy*. Appl. Phys. Lett. **95**(4), 042102 (2009).

[Sai01] N. Saito and Y. Igasaki, *Electrical and optical properties of InN films prepared by reactive sputtering*. Appl. Surf. Sci. **169**, 349 (2001).

[Sai02] Y. Saito, H. Harima, E. Kurimoto, T. Yamaguchi, N. Teraguchi, A. Suzuki, T. Araki, and Y. Nanishi, *Growth Temperature Dependence of Indium Nitride Crystalline Quality Grown by RF-MBE*. Phys. Status Solidi B **234**(3), 796 (2002).

[Sal91] B. Saleh and M. Teich, *Fundamentals of photonics*, vol. 1 (Wiley-Interscience, 1991).

[Sas10] T. Sasaoka, M. Mori, T. Miyazaki, and S. Adachi, *Room-temperature infrared photoluminescence from sputter-deposited InN films*. J. Appl. Phys. **108**(6), 063538 (2010).

[Sca00] R. Scarmozzino, A. Gopinath, R. Pregla, and S. Helfert, *Numerical techniques for modeling guided-wave photonic devices*. IEEE J. Sel. Top. Quant. **6**(1), 150 (2000).

[Seo10] H.-C. Seo, I. Petrov, and K. Kim, *Structural Properties of AlN Grown on Sapphire at Plasma Self-Heating Conditions Using Reactive Magnetron Sputter Deposition*. J. Electron. Mater. **39**(8), 1146 (2010).

[Ses02] K. Seshan, *Handbook of thin film deposition processes and techniques: Principles, Methods, Equipment and Applications* (Noyes Publications, 2002).

[She02] W. Shen, L. Jiang, H. Yang, F. Meng, H. Ogawa, and Q. Guo, *Bandtail characteristics in InN thin films*. Appl. Phys. Lett. **80**(12), 2063 (2002).

[Shi06] H. Shinoda and N. Mutsukura, *Structural and optical properties of InN films prepared by radio frequency magnetron sputtering*. Thin Solid Films **503**(1), 8 (2006).

[Smi82] P. Smith, *On the physical limits of digital optical switching and logic elements*. Bell Syst. Tech. J. **61**(8), 1975 (1982).

[Ste13a] M. Stegmaier and W. H. Pernice, *Broadband directional coupling in aluminum nitride nanophotonic circuits*. Opt. Express **21**(6), 7304 (2013).

[Ste13b] M. Stegmaier and W. H. Pernice, *Mode control and mode conversion in nonlinear aluminum nitride waveguides*. Opt. Express **21**(22), 26742 (2013).

[Str38] I. Stranski and L. Krastanow, *Zur Theorie der orientation Ausscheidung von Ionenkristallen aufeinander*. Math.-Naturwiss. K1 Abt. IIb **146**, 797 (1938).

[Sui06] S. Suihkonen, J. Sormunen, V. Rangel-Kuoppa, H. Koskenvaara, and M. Sopanen, *Growth of InN by vertical flow MOVPE*. J. Cryst. Growth **291**(1), 8 (2006).

[Suz97] N. Suzuki and N. Iizuka, *Feasibility study on ultrafast nonlinear optical properties of 1.55-μm intersubband transition in AlGaN/GaN quantum wells*. Jpn. J. Appl. Phys. **36**(0 Pt 2), 8A (1997).

[Suz00] N. Suzuki, N. Iizuka, and K. Kaneko, *Intersubband transition in AlGaN-GaN quantum wells for ultrafast all-optical switching at communication wavelength*. In *Proc. SPIE 3940, Ultrafast Phenomena in Semiconductors IV*, p. 127 (SPIE, 2000).

[Tan86] T. Tansley and C. Foley, *Optical band gap of indium nitride*. J. Appl. Phys. **59**(9), 3241 (1986).

[Tan06] Y. Taniyasu, M. Kasu, and T. Makimoto, *An aluminium nitride light-emitting diode with a wavelength of 210 nanometres*. Nature **441**(7091), 325 (2006).

[Tan07] Y. Taniyasu, M. Kasu, and T. Makimoto, *Threading dislocations in heteroepitaxial AlN layer grown by MOVPE on SiC (0001) substrate*. J. Cryst. Growth **298**, 310 (2007).

[Tan10] S. F. Tang, T. C. Chen, S. Y. Lin, and H. Y. Tu, *Intersubband Transitions in the Quantum Dot Layers for Quantum Confined Photodetector*. Cutting Edge Nanotechnology, Intechopen (2010).

[Tch06] M. Tchernycheva, L. Nevou, L. Doyennette, F. Julien, E. Warde, F. Guillot, E. Monroy, E. Bellet-Amalric, T. Remmele, and M. Albrecht, *Systematic experimental and theoretical investigation of intersubband absorption in Ga N/ Al N quantum wells*. Phys. Rev. B **73**(12), 125347 (2006).

[TF10] A. C. Turner-Foster, M. A. Foster, J. S. Levy, C. B. Poitras, R. Salem, A. L. Gaeta, and M. Lipson, *Ultrashort free-carrier lifetime in low-loss silicon nanowaveguides*. Opt. Express **18**(4), 3582 (2010).

[Tun00] S. Tungasmita, J. Birch, P. Persson, K. Jarrendahl, and L. Hultman, *Enhanced quality of epitaxial AlN thin films on 6H–SiC by ultra-high-vacuum ion-assisted reactive dc magnetron sputter deposition*. Appl. Phys. Lett. **76**(2), 170 (2000).

[Var67] Y. Varshni, *Temperature dependence of the energy gap in semiconductors*. Physica **34**(1), 149 (1967).

[Var08] A. Vardi, N. Kheirodin, L. Nevou, H. Machhadani, L. Vivien, P. Crozat, M. Tchernycheva, R. Colombelli, F. Julien, F. Guillot *et al.*, *High-speed operation of GaN/AlGaN quantum cascade detectors at $\lambda \approx 1.55$ μm*. Appl. Phys. Lett. **93**(19), 193509 (2008).

[Vas09] Z. Vashaei, T. Aikawa, M. Ohtsuka, H. Kobatake, H. Fukuyama, S. Ikeda, and K. Takada, *Influence of sputtering parameters on the crystallinity and crystal orientation of AlN layers deposited by RF sputtering using the AlN target*. J. Cryst. Growth **311**(3), 459 (2009).

[Ver04] L. Vergara, M. Clement, E. Iborra, A. Sanz-Hervas, J. García López, Y. Morilla, J. Sangrador, and M. Respaldiza, *Influence of oxygen and argon on the crystal quality and piezoelectric response of AlN sputtered thin films*. Diam. Relat. Mater. **13**(4), 839 (2004).

[VF08] S. Valdueza-Felip, F. B. Naranjo, M. Gonzalez-Herraez, H. Fernández, J. Solis, F. Guillot, E. Monroy, L. Nevou, M. Tchernycheva, and F. Julien, *Characterization of the Resonant Third-Order Nonlinear Susceptibility of Si-Doped GaN–AlN Quantum Wells and Quantum Dots at 1.5 μm*. IEEE Photon. Technol. Lett. **20**(16), 1366 (2008).

[VF10] S. Valdueza-Felip, F. B. Naranjo, M. González-Herráez, L. Lahourcade, E. Monroy, and S. Fernández, *Influence of deposition conditions on*

nanocrystalline InN layers synthesized on Si (111) and GaN templates by RF sputtering. J. Cryst. Growth **312**(19), 2689 (2010).

[VF11] S. Valdueza-Felip, *Nitride-based semiconductor nanostructures for applications in optical communications at 1.5 μm*. Ph.D. thesis, Universidad de Alcalá (2011).

[VF12a] S. Valdueza-Felip, L. Rigutti, F. B. Naranjo, P. Ruterana, J. Mangeney, F. Julien, M. González-Herráez, and E. Monroy, *Carrier localization in InN/InGaN multiple-quantum wells with high In-content*. Appl. Phys. Lett. **101**(6), 062109 (2012).

[VF12b] S. Valdueza-Felip, L. Monteagudo-Lerma, J. Mangeney, M. Gonzalez-Herraez, F. H. Julien, and F. B. Naranjo, *Nonlinear Absorption at Optical Telecommunication Wavelengths of InN Films Deposited by RF Sputtering*. IEEE Photon. Technol. Lett. **24**(22), 1998 (2012).

[VF12c] S. Valdueza-Felip, J. Ibáñez, E. Monroy, M. González-Herráez, L. Artús, and F. B. Naranjo, *Improvement of InN layers deposited on Si (111) by RF sputtering using a low-growth-rate InN buffer layer*. Thin Solid Films **520**(7), 2805 (2012).

[Vie00] C. Vieu, F. Carcenac, A. Pepin, Y. Chen, M. Mejias, A. Lebib, L. Manin-Ferlazzo, L. Couraud, and H. Launois, *Electron beam lithography: resolution limits and applications*. Appl. Surf. Sci. **164**(1), 111 (2000).

[Vig04] D. Vignaud, J. Lampin, and F. Mollot, *Two-photon absorption in InP substrates in the 1.55 μm range*. Appl. Phys. Lett. **85**(2), 239 (2004).

[Vin01] C. Vinegoni, M. Wegmuller, and N. Gisin, *Measurements of the nonlinear coefficient of standard, SMF, DSF, and DCF fibers using a self-aligned interferometer and a Faraday mirror*. IEEE Photon. Technol. Lett. **13**(12), 1337 (2001).

[Vol26] M. Volmer and A. Weber, *Nucleus formation in supersaturated systems*. Z. Phys. Chem **119**(1926) (1926).

[Vur01] I. Vurgaftman, J. Meyer, and L. Ram-Mohan, *Band parameters for III–V compound semiconductors and their alloys*. J. Appl. Phys. **89**(11), 5815 (2001).

[Vur03] I. Vurgaftman and J. Meyer, *Band parameters for nitrogen-containing semiconductors*. J. Appl. Phys. **94**(6), 3675 (2003).

[Wad04] O. Wada, *Femtosecond all-optical devices for ultrafast communication and signal processing*. New J. Phys. **6**(1), 183 (2004).

[Wal04] W. Walukiewicz, S. Li, J. Wu, K. Yu, J. Ager Iii, E. Haller, H. Lu, and W. J. Schaff, *Optical properties and electronic structure of InN and In-rich group III-nitride alloys*. J. Cryst. Growth **269**(1), 119 (2004).

[Wal12] R. Walther, D. Litvinov, M. Fotouhi, R. Schneider, D. Gerthsen, R. Vöhringer, D. Hu, and D. Schaadt, *Microstructure of PAMBE-grown InN layers on Si (111)*. J. Cryst. Growth **340**(1), 34 (2012).

[Wan07] X. Wang, S.-B. Che, Y. Ishitani, and A. Yoshikawa, *Growth and properties of Mg-doped In-polar InN films*. Appl. Phys. Lett. **90**(20), 201913 (2007).

[Wan09] Y.-H. Wang and W.-L. Chen, *The influence of the LT-InN buffer growth conditions on the quality of InN films grown on Si (111) substrate by MBE*. Physica E **41**(5), 848 (2009).

[Wan12] K. Wang, J. Zhou, L. Yuan, Y. Tao, J. Chen, P. Lu, and Z. L. Wang, *Anisotropic third-order optical nonlinearity of a single ZnO micro/nanowire*. Nano Lett. **12**(2), 833 (2012).

[Web10] M. J. Weber, *Handbook of optical materials* (CRC press, 2010).

[Wil01] I. Wilke, R. King, and H. Kieu, *Two-step AIN-PVD for improved film properties* (2001). US Patent 6,312,568.

[Wu02] J. Wu, W. Walukiewicz, K. Yu, J. Ager Iii, E. Haller, H. Lu, W. J. Schaff, Y. Saito, and Y. Nanishi, *Unusual properties of the fundamental band gap of InN*. Appl. Phys. Lett. **80**, 3967 (2002).

[Wu03] J. Wu, W. Walukiewicz, W. Shan, K. Yu, J. Ager, S. Li, E. Haller, H. Lu, and W. J. Schaff, *Temperature dependence of the fundamental band gap of InN*. J. Appl. Phys. **94**(7), 4457 (2003).

[Wu04] J. Wu, W. Walukiewicz, S. Li, R. Armitage, J. Ho, E. Weber, E. Haller, H. Lu, W. J. Schaff, A. Barcz *et al.*, *Effects of electron concentration on the optical absorption edge of InN*. Appl. Phys. Lett. **84**(15), 2805 (2004).

[Wu05] Y. Wu, *Guides d'onde planaires de Y_2O_3, Y_2O_3: Tb^{3+} et de YAG élaborés par voie sol-gel: analyse structurale et optique*. Ph.D. thesis, Université Claude Bernard - Lyon 1 (2005).

[Wu09] J. Wu, *When group-III nitrides go infrared: New properties and perspectives*. J. Appl. Phys. **106**(1), 011101 (2009).

[Xio12] C. Xiong, W. H. Pernice, X. Sun, C. Schuck, K. Y. Fong, and H. X. Tang, *Aluminum nitride as a new material for chip-scale optomechanics and nonlinear optics*. New J. Phys. **14**(9), 095014 (2012).

[Xu01] X.-H. Xu, H.-S. Wu, C.-J. Zhang, and Z.-H. Jin, *Morphological properties of AlN piezoelectric thin films deposited by DC reactive magnetron sputtering*. Thin Solid Films **388**(1), 62 (2001).

[Yam09] T. Yamaguchi, D. Muto, T. Araki, and Y. Nanishi, *Growth and characterization of N-polar and In-polar InN films by RF-MBE*. J. Cryst. Growth **311**(10), 2780 (2009).

[Yan09] J. Yang, S. Kang, D. Dinh, and D. Yoon, *Influence of AlN buffer layer thickness and deposition methods on GaN epitaxial growth*. Thin Solid Films **517**(17), 5057 (2009).

[Yas10] M. Yasaka, *X-ray thin-film measurement techniques*. V. X-ray reflectivity measurement. The Rigaku Journal **26**, 1 (2010).

[Yen12] C.-H. Yen, W.-C. Lai, Y.-Y. Yang, C.-K. Wang, T.-K. Ko, S.-J. Hon, and S.-J. Chang, *GaN-based light-emitting diode with sputtered AlN nucleation layer*. IEEE Photon. Technol. Lett. **24**(4), 294 (2012).

[Yon02] I. Yonenaga, T. Shima, and M. H. Sluiter, *Nano-indentation hardness and elastic moduli of bulk single-crystal AlN*. Jpn. J. Appl. Phys. **41**(7R), 4620 (2002).

[You07] Y. Z. You and D. Kim, *Influence of incidence angle and distance on the structure of aluminium nitride films prepared by reactive magnetron sputtering*. Thin Solid Films **515**(5), 2860 (2007).

[Zha05] J. Zhang, H. Cheng, Y. Chen, A. Uddin, S. Yuan, S. Geng, and S. Zhang, *Growth of AlN films on Si (100) and Si (111) substrates by reactive magnetron sputtering*. Surf. Coat. Tech. **198**(1), 68 (2005).

[Zoi08] N. Zoita, C. Besleaga, L. Braic, T. Mitran, C. Grigorescu, and L. Nedelcu, *InN thin films deposited on flexible substrates by reactive RF-magnetron sputtering*. Optoelectron. Adv. Mat. **2**(11), 719 (2008).